Effective Date: April 22, 2011
Revision -

GSFC JPSS CMO
07/19/2011
Released

Joint Polar Satellite System (JPSS) Ground Project
Code 474
474-00029

Joint Polar Satellite System (JPSS) OMPS NADIR Total Column Ozone Algorithm Theoretical Basis Document (ATBD)

For Public Release

The information provided herein does not contain technical data as defined in the International Traffic in Arms Regulations (ITAR) 22 CFC 120.10. This document has been approved For Public Release.

National Aeronautics and Space Administration

Goddard Space Flight Center
Greenbelt, Maryland

This page intentionally left blank.

Joint Polar Satellite System (JPSS)
OMPS NADIR Total Column Ozone
Algorithm Theoretical Basis Document (ATBD)

JPSS Electronic Signature Page

Prepared By:

Neal Baker
JPSS Data Products and Algorithms, Senior Engineering Advisor
(Electronic Approvals available online at https://jpssmis.gsfc.nasa.gov/mainmenu_dsp.cfm)

Approved By:

JPSS Ground System

Heather Kilcoyne
JPSS Data Products and Algorithms Manager
(Electronic Approvals available online at https://jpssmis.gsfc.nasa.gov/mainmenu_dsp.cfm)

Goddard Space Flight Center
Greenbelt, Maryland

This page intentionally left blank.

Preface

This document is under JPSS Ground Algorithm configuration control. Once this document is approved, JPSS approved changes are handled in accordance with Class I and Class II change control requirements as described in the JPSS Configuration Management Procedures, and changes to this document shall be made by complete revision.

Any questions should be addressed to:

JPSS Ground Project Configuration Management Office
NASA/GSFC
Code 474
Greenbelt, MD 20771

This page intentionally left blank.

Change History Log

Revision	Effective Date	Description of Changes (Reference the CCR & CCB/ERB Approve Date)
Original	04/22/2011	**474-CCR-11-0044**: This version baselines D43774, OMPS NADIR Total Column Ozone Algorithm Theoretical Basis Document ATBD (ref Raytheon doc), Rev D dated 10/28/2009 as a JPSS document, version Rev –.. This is the version that was approved for NPP launch. Per NPOESS CDFCB - External, Volume V – Metadata, doc number D34862-05, this has been approved for Public Release into CLASS. This CCR was approved by the JPSS Ground Algorithm ERB on April 22, 2011.

This page intentionally left blank.

Northrop Grumman Space & Mission Systems Corp.
Space Technology
One Space Park
Redondo Beach, CA 90278

Engineering & Manufacturing Development (EMD) Phase
Acquisition & Operations Contract

CAGE NO. 11982

OMPS NADIR Total Column Ozone Algorithm Theoretical Basis Document ATBD (ref Raytheon doc)

Document Number: D43774

Document Date: 10/28/2009 **Revision: D**

Point of Contact: Bhaswar Sen, , Modeling and Simulation Team
Megan Novicki, Modeling and Simulation Team

ELECTRONIC APPROVAL SIGNATURES:

Bruce Hauss, Algorithms, Calibration and Validation IPT Lead

Prepared by
Northrop Grumman Space Technology
One Space Park
Redondo Beach, CA 90278

Prepared for
Department of the Air Force
NPOESS Integrated Program Office
C/O SMC/CIK
2420 Vela Way, Suite 1467-A8
Los Angeles AFB, CA 90245-4659

Under
Contract No. F04701-02-C-0502

Northrop Grumman Space & Mission Systems Corp.
Space Technology
One Space Park
Redondo Beach, CA 90278

NORTHROP GRUMMAN

Raytheon

Revision/Change Record

Document Number D43774

Revision	Document Date	Revision/Change Description	Pages Affected
---	02/12/2007	Initial PCIM Release to bring document into Matrix Accountability. Reference original Raytheon document (no document number) delivered in 2005	All
A	10/23/2007	Document changes reflect changes to algorithm. ECR A136 Removed reference to “CMIS”. Changed reference to “CrIS” to “CrIMSS”	All
B	07/17/2008	Revision of SDR algorithm description to reflect changes described in ECR-A-158A . Affected section 3.1. Added missing equations. Affected section 2.3	42-120 10-20
C	01/21/2009	Revision of the SDR algorithm description to be consistent with the software updates by ECR-A-191. Corrected typos. Added system level reference documents. Affected sections 1, 2, and 3.1.	1-103
D	10/28/2009	Revision of the EDR algorithm description to be consistent with the software updates by ECR-A-260B.	All

TABLE OF CONTENTS

Page

LIST OF FIGURES ..... **v**

LIST OF TABLES ..... **viii**

1 Introduction **1**

1.1 SYSTEM DESCRIPTION 1

1.2 SCOPE AND OBJECTIVES 2

1.3 OVERVIEW 3

1.4 DATA PRODUCTS 3

1.5 APPLICABLE DOCUMENTS 3

1.5.1 NPOESS system level documents: 3

1.5.2 OMPS system level documents 4

1.5.2.1 Controlling Documents 4

1.5.2.2 OMPS Reference Documents 4

1.6 REVISION HISTORY 4

1.7 CONTRIBUTING AUTHORS 6

2 Scientific Basis **8**

2.1 PHYSICAL DESCRIPTION 8

2.2 SENSOR DESCRIPTION 9

2.3 FORWARD MODEL 9

2.3.1 Radiative Transfer Tables 10

2.3.1.1 Standard Ozone and Temperature Profile Determination 13

2.3.1.2 Sensor Table Generation 15

2.3.2 Sensitivity Table 16

2.3.3 Rotational-Raman Scattering 17

2.4 RETRIEVAL 18

2.4.1 Overview 18

2.4.2 OMPS Reflectivity (Cloud Fraction) 19

2.4.3 Initial Estimate of Ozone 20

2.4.4 Linear Correction 21

2.4.5 Profile Selection 22

2.4.6 Correction for Tropospheric Aerosols and Sun Glint 24
2.4.7 Correction for Temperature and Ozone Profile Shape 26
2.4.8 Correction for Tropospheric Ozone 27
2.4.9 Multiple Triplet Formulation 29
2.4.10 OMPS Channel Selection 31
2.4.11 Volcanic SO_2 34
2.5 ERROR SOURCES 38

3 Algorithm Description 40
3.1 SDR DATA PRODUCTION 40
3.1.1 SDR algorithm Inputs and Outputs 41
3.1.1.1 Inputs to the SDR algorithm 41
3.1.1.2 Outputs from the SDR algorithm 43
3.1.2 Earth View Processing 48
3.1.2.1 Database Input 51
3.1.2.2 CCD Spectral and Spatial Registration 51
3.1.2.3 Housekeeping Data 52
3.1.2.4 Solar Irradiance Spectrum 52
3.1.2.5 Geolocation 53
3.1.2.6 Signal Corrections 69
3.1.2.7 Radiometric Correction 71
3.1.2.8 Stray Light Correction 71
3.1.2.9 Match-up with Limb Profile EDR 73
3.1.2.10 External Data Match-up 74
3.1.2.11 Data Quality Checks 78
3.1.3 Calibration 79
3.1.3.1 Theoretical Basis: Radiometric Calibration 80
3.1.3.2 Theoretical Basis: Diffuser Degradation 81
3.1.3.3 Theoretical Basis: Wavelength Registration 83
3.1.3.4 Calibration Record Processing 85
3.1.3.5 Calibration Trending 93
3.2 EDR PRODUCTION 104
3.2.1 Retrieval Algorithm Description 111

4 Assumptions 133

5 Input Data Requirements 134
5.1 PRIMARY SENSOR REQUIREMENTS 134
5.2 OTHER OMPS SENSOR DATA REQUIREMENTS 134
5.3 OTHER NPOESS SENSOR DATA REQUIREMENTS 135
5.4 CLIMATOLOGY DATA REQUIREMENTS 135

6 Output Data Description 136

6.1 EDRS 136

6.2 ADDITIONAL DATA PRODUCTS 136

6.3 EDR CONTENT 137

7 System Accuracy and Precision 139

7.1 SYSTEM ACCURACY 139

7.1.1 Sensor Accuracy 140

7.1.1.1 Initial Albedo Calibration, Wavelength-Independent 141

7.1.1.2 Initial Albedo Calibration, Wavelength-Dependent 141

7.1.1.3 Long-term Albedo Calibration 142

7.1.1.4 Pixel-to-Pixel Radiometric Calibration 142

7.1.1.5 Wavelength Calibration Accuracy 142

7.1.1.6 Intra-orbital Wavelength Shift Sensitivity 145

7.1.1.7 Polarization Sensitivity 145

7.1.1.8 Stray Light, Out of Field 148

7.1.1.9 Stray Light, Out of Band 148

7.1.2 Algorithm Accuracy Errors 149

7.1.2.1 Rayleigh Scattering Coefficients 150

7.1.2.2 Ozone Absorption Coefficients, Absolute 150

7.1.2.3 Ozone Absorption Coefficients, Temperature Dependence 150

7.1.2.4 Tropospheric Aerosol Correction 151

7.1.2.5 Cloud Top Pressure 151

7.1.2.6 Pressure Table Interpolation 151

7.1.2.7 Non-Homogeneous Scene (Snow/Ice/Cloud Cover) 151

7.1.2.8 Ozone Profile Shape Errors 153

7.1.2.9 Multiple Scattering 153

7.1.2.10 Ring Effect Correction 153

7.2 LONG TERM STABILITY 154

7.2.1 Reference Deployment Schedule 154

7.2.2 Radiometric Uncertainty Allocation 158

7.3 SYSTEM PRECISION 159

7.3.1 Sensor Precision Errors 160

7.3.1.1 Sensor Noise 160

7.3.1.2 Spectral Calibration 162

7.3.1.3 Radiometric Calibration 165

7.3.2 Algorithm Precision Allocations 169

7.3.2.1 Ozone Absorption Coefficients, Temperature Dependence 169

7.3.2.2 Cloud Top/Surface Pressure 169

7.3.2.3 Cloud Fraction (Non-Homogeneous Scene) 170

7.3.2.4 Ozone Profile Shape Errors 170
7.3.2.5 Tropospheric Aerosol Correction 170
7.3.2.6 Tropospheric Ozone 170
7.3.3 Global Distribution of Total Column Precision Errors 177
7.3.3.1 Global Allocations for Temperature Dependence, Cloud Fraction, and Tropospheric Aerosols 178
7.3.3.2 Global Allocations for Sensor Noise and Profile Shape 178
7.3.3.3 Global Allocations for Cloud Top / Surface Pressure and Tropospheric Ozone 179
7.4 MAPPING UNCERTAINTY 181
7.5 VERIFICATION AND VALIDATION 182
8 References 183

LIST OF FIGURES

Page

Figure 1.1-1. Overview of the data flow from sensors input to the generation of RDR, SDR and EDR/IP data products 2

Figures 2.4-1 and 2.4-2: Quadratic fits of percent error in Ω_{V7} as a function of $R_{336\text{-}377}$ for path lengths below and above 4.5 25

Figure 2.4-3. Impact of temperature changes on OMPS triplet channels 32

Figure 2.4-4. Impact of temperature changes on OMPS derived total ozone 32

Figure 2.4-5. Impact of wavelength shift on OMPS derived total ozone 33

Figure 2.4-6. Impact of Ring effect on the OMPS channels 34

Figure 2.4-7. Distribution of SOI for ADEOS TOMS, Mar. 20, 1997 37

Figure 2.4-8. Percentage of ADEOS TOMS daily retrievals flagged as SO_2 contaminated 38

Figure 3.1-1. Schematic Showing SDR Generation 40

Figure 3.1-2. Schematic showing Earth View SDR generation process 49

Figure 3.1-3. OMPS geolocation elements 53

Figure 3.1-4. OMPS geolocation coordinate systems 54

Figure 3.1-5. Instrument Coordinate System 55

Figure 3.1-6. Orbital Coordinate System 56

Figure 3.1-7. ECI Coordinate System 57

Figure 3.1-8. ECEF Coordinate System 58

Figure 3.1-9. CCD focal plane to the ground view 59

Figure 3.1-10. Cross-Track view angles α (Azimuth) 60

Figure 3.1-11. Along-track view angle β (Elevation) 60

Figure 3.1-12. Ground Trace of TC with respect to spacecraft ground track 61

Figure 3.1-13. Ellipsoidal viewing vector intersection 65

Figure 3.1-14. CrIMSS External Data Match-up 76

Figure 3.1-15(a). SDR processing flow for calibration records 86

Figure 3.1-15(b). SDR processing flow for calibration records (continued) 87

Figure 3.1-16 (a). SDR flow for trending calibration data 94

Figure 3.1-16 (b). SDR flow for trending calibration data 95

Figure 3.2-1. EDR Production 105

Figure 3.2-1. EDR Production (cont) 106

Figure 3.2-1. EDR Production (cont) 107

Figure 3.2-1. EDR Production (cont) 108

Figure 7.1-1. OMPS Total Column accuracy error allocations and performance. 140

Figure 7.1-2. Simulated Retrievals of Ozone 144

Figure 7.1-3. Ozone Error Due to Polarization Sensitivity 147

Figure 7.1-4. Ozone error in DU using the TOMS pressure node points (TOP) and the new OMPS pressure node points (BOTTOM). Note the difference in the vertical scales. 152

Figure 7.2-1. TOMS Earth Probe Working/Reference solar measurement ratio ... 155

Figure 7.2-2. Diffuser degradation rates for TOMS and SBUV instruments. 157

Figure 7.2-3. Estimated Radiometric Drift Uncertainties 159

Figure 7.3-1. OMPS Total Column precision error allocations and performance. 160

Figure 7.3-2. Ozone error due to sensor SNR = 1000 for a wide range of scenes. 162

Figure 7.3-3. Results of Thermal and Mechanical Modeling on Spectral Registration 163

Figure 7.3-4. Deviations From Actual Wavelength Shifts 164

Figure 7.3-5. TOMS Earth Probe operational calibration for the A triplet 165

Figure 7.3-6. TOMS Earth Probe Working diffuser solar signal 166

Figure 7.3-7. Standard Deviation of Predicted Calibrations About the "True" Sensor Calibration of Figure 7.3-6 167

Figure 7.3-8. Trended irradiance errors resulting from the spectral trend errors of Figure 7.3-4 168

Figure 7.3-9 (a),(b) Temperature Sensitivity for (a) Low and (b) mid 172

Figure 7.3-9(c) Ozone Temperature Sensitivity for (c) High 173

Figure 7.3-10. Error due to cloud top pressure error for (a) low, (b) mid, and (c) high latitude ozone. 176

Figure 7.3-11. Systematic Ozone Error 177

Figure 7.4-1. Error tree addressing the mapping uncertainty of the nadir total column measurements 182

LIST OF TABLES

Page

Table 1.6-1. Revision History of This Document....4

Table 1.6-2. Revision History of This Document Prior to PICM Release 6

Table 2.3-1. Table Node Points....12

Table 2.3-2. Umkehr Layers Used for Ozone Profiles....13

Table 2.3-3. OMPS Standard Ozone Profiles (in Dobson Units) 14

Table 2.3-4. OMPS Standard Temperature (in Kelvin) 15

Table 2.4-1 Aerosol model parameters....24

Table 2.4-2. Selection of the Multiple Triplets Available to OMPS 30

Table 2.5-1. Factors Contributing to the Accuracy and Precision Error Budgets .38

Table 3.1-1. CrIMSS Horizontal Cell Size....75

Table 3.1-2. VIIRS Horizontal Cell Size 77

Table 3.1-3. Signal corrections applied to various data types....88

Table 3.2-1. List of Variables Used in the Algorithm Flow Diagrams....109

Table 4-1. List of Assumptions Made in Forward Model and in Retrieval 133

Table 5.1-1. Sensor Parameters and Performance Requirements 134

Table 5.2-1. Other OMPS Data Required by the Total Column Ozone Algorithm.134

Table 5.3-1. Data Products from Other NPOESS Sensor Systems That Are Used by the Total Column Ozone Algorithm....135

Table 5.4-1. Climatology Databases Used by the Total Column Ozone Algorithm 135

Table 6.1-1. Total Column Ozone EDR Specifications 136

Table 6.2-1. Additional, Non-Baseline Data Products Available from the Total Ozone Algorithm....136

Table 7.1-1. OMPS System Accuracy Requirements....139

Table 7.1-2. Allocation for sensor contributions to retrieved ozone accuracy.... 140

Table 7.1-3. Allocation for algorithm contributions to retrieved ozone accuracy 150

Table 7.3-1. Limb retrieval precision 171

Table 7.3-2. Distribution of total column ozone amount..... 178

Table 7.3-3. Solar zenith angle distributions 179

Table 7.3-4. Cloud fraction distribution..... 179

Table 7.3-5. Cloud fraction distribution..... 180

Table 7.3-6. Distribution of errors in tropospheric ozone 180

Table 7.3-7. Global sensor and algorithm precision error allocations 181

1 Introduction

The Ozone Mapping and Profiler Suite (OMPS) is an important component of the National Polar-Orbiting Operational Environmental Satellite System (NPOESS). The OMPS mission is to provide the NPOESS users with data products that describe the vertical, horizontal, and temporal distribution of ozone in the Earth's atmosphere. These data (or Environmental Data Records—EDRs) are derived from the spaceborne ultraviolet, visible, and near infrared observations of a two-sensor system.

1.1 SYSTEM DESCRIPTION

The nadir system has two focal planes: one operating from 300 to 380 nm for total column ozone observations, and the other operating at 250 to 310 nm for profile ozone observations. Together with the interface and control electronics they are the OMPS sensor suite. For the NPP mission, the OMPS sensor suite also contains a limb system that has a focal plane operating from 290 to 1000 nm for high vertical resolution profile ozone observations. The ground processing system will receive and process the sensor data into Raw Data Records (RDRs), Sensor Data Records (SDRs) and EDRs or Intermediate Products (IPs). These data products will be delivered to the NPOESS users in pre-defined format and contents. The limb system SDRs will not be part of the NPOESS operational system, and will be generated by NASA/SDS.

The EDR requirements thresholds listed in section 40.3.2 of the NPOESS system specification, document SY15-0007, shall be met when data from OMPS is processed using the operational algorithms described in these ATBDs.

The OMPS algorithms include the following:

1 The **Nadir Total Column Ozone SDR algorithm** was originally developed by the OMPS sensor subcontractor and significantly improved by NGST to meet the NPOESS program need.

2 The **Nadir Profile Ozone SDR algorithm** was originally developed by the OMPS sensor subcontractor and significantly improved by NGST to meet the NPOESS program need.

3 The **Nadir Total Column Ozone Algorithm** is adapted from the heritage TOMS version 7 algorithm. We have included modular enhancements to meet EDR requirements and to provide for graceful degradation.

4 The **Nadir Profile Ozone Algorithm** is adopted from the heritage SBUV/2 operational algorithm. The ozone profile from this algorithm provides a link to the heritage twenty-year ozone profile data set.

Figure 1.1-1 maps the flow of the OMPS data from the sensors through the RDR, SDR, and EDR algorithms. For the SDR algorithm, the figure identifies the required inputs as the external EDRs, the climatological databases, and the calibration data. For the EDR algorithms, this figure also identifies the connection between the algorithms.

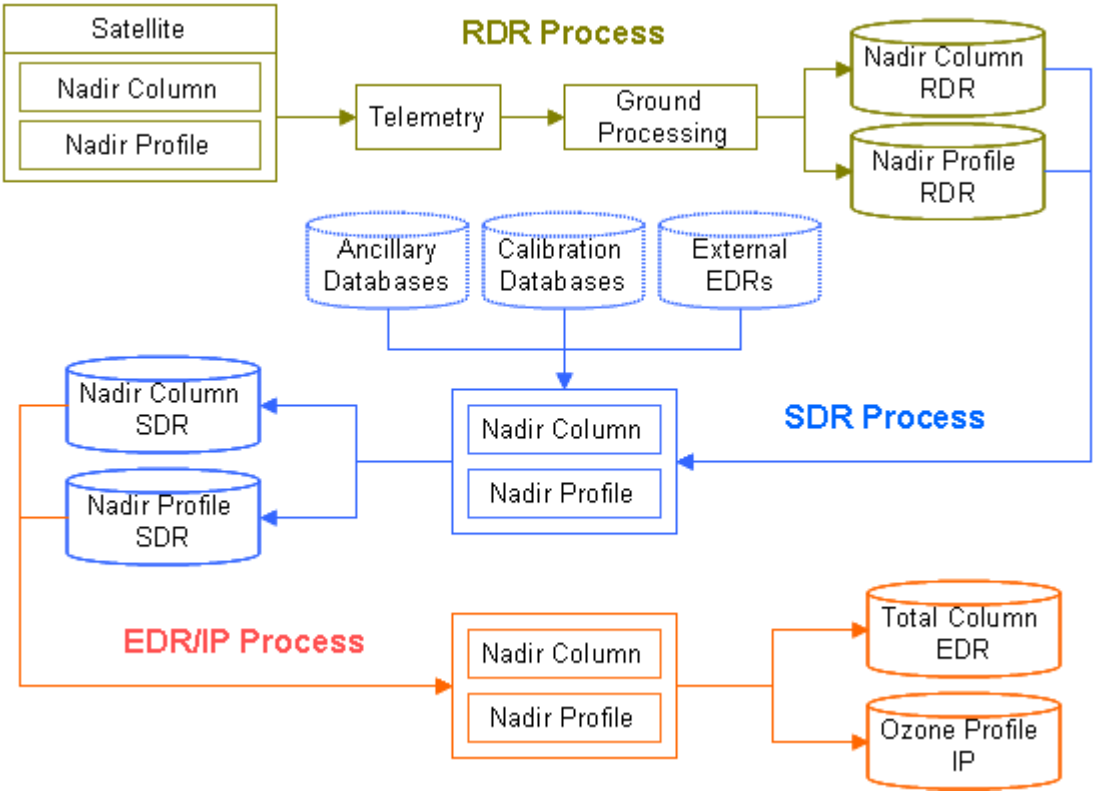

Figure 1.1-1. Overview of the data flow from sensors input to the generation of RDR, SDR and EDR/IP data products

1.2 SCOPE AND OBJECTIVES

This Algorithm Theoretical Basis Document (ATBD) describes the OMPS Total Column Ozone SDR algorithm and the OMPS Total Column Ozone EDR algorithm. The Total Column (TC) EDR product consists of the total ozone in a column of air

from 0 to 60 km and observed for all solar zenith angle viewing conditions less than or equal to 80 degrees.

This document identifies the sources of input data that are required by the algorithm; provides the physical theory and mathematical background underlying the use of this information; describes practical considerations affecting the detailed algorithm development; lists any assumptions employed in the algorithm retrieval process, describes the SDR and EDR products and additional algorithm by-products; details expected sensor and algorithm errors (accuracy and precision); and discusses the use of calibration data sets.

1.3 OVERVIEW

The Ball Team's Total Column Ozone Algorithm is adapted from the Total Ozone Mapping Spectrometer (TOMS) Version 7 Algorithm (McPeters et al., 1996). The algorithm is based on the comparison of measured normalized radiance to calculated normalized radiance (using a standard UV radiative transfer model) for specific measurement geometry, viewing conditions, and surface conditions. The algorithm takes the IFOV information from the SDR, determines the viewing geometry, and characterizes the scene from either external EDR information or climatological data. It then constructs the normalized radiance as the ratio of measured radiance to irradiance. From a radiative transfer model, the normalized radiances are calculated for the given viewing conditions. These are compared to the measured values and an ozone estimate is determined. This estimate is refined for effects from aerosols and other contaminants. After data quality flags are set the EDR output file is constructed.

1.4 DATA PRODUCTS

The main data products are the earth view radiance SDRs in the unit of W/cm3/sr and the total column ozone amount in Dobson Units (DU), equivalent to milli-atm-cm of ozone, for solar zenith angles < 80°.

1.5 APPLICABLE DOCUMENTS

1.5.1 NPOESS system level documents:

1. NPOESS System Specification, DOC SY15-0007, Rev N
2. Operational Algorithm Description Document for the OMPS Total Column SDR algorithm Software (D39310)
3. Operational Algorithm Description Document for the OMPS Total Column EDR algorithm Software (D37031)
4. NPP EDR Production Report, Document Number D37005

5. EDIR Interdependency Report, Document Number **Error! Unknown document property name.**
6. NPOESS Common Data Format Control Book, Document Number D34862

1.5.2 OMPS system level documents

1.5.2.1 Controlling Documents

7. OMPS System Specification – Document Number 542798
8. OMPS Algorithm Development Specification – Document Number 542808

1.5.2.2 OMPS Reference Documents

9. OMPS Algorithm Theoretical Basis Document: Nadir Total Column Ozone Algorithm—Document Number D43774
10. OMPS Algorithm Theoretical Basis Document: UV/VIS Limb Profile Ozone Algorithm—Document Number IN0092-107.
11. OMPS Algorithm Theoretical Basis Document: Nadir Profile Ozone Algorithm—Document Number D43775
12. OMPS Algorithm Theoretical Basis Document: IR Total Column Ozone Algorithm—Document Number IN0092-109.
13. OMPS Algorithm Test and Verification Plans and Procedures (ATVPP) – Document Number IN0092-124.

1.6 REVISION HISTORY

The original version of this document was dated March 1, 1999. This was a working document that was finalized just prior to the critical design review (CDR), although many of the sections remain unchanged. Revisions to this document were made as the nadir total column sensor design and algorithm matured, and as performance information was verified and validated.

In February 12, 2007, this document was re-baselined and checked into the NPOESS Matrix system by NGST. Subsequent revisions since this initial PCIM release are recorded in Table 1.6-1. Change and revision history prior to the PCIM release is documented in Table 1.6-2.

Table 1.6-1. Revision History of This Document

Revision	Document Date	Revision/Change Description	Pages Affected
---	02/12/2007	Initial PCIM Release to bring document into Matrix Accountability. Reference original Raytheon document (no document number) delivered in 2005	All

Revision	Document Date	Revision/Change Description	Pages Affected
A	10/23/2007	Document changes reflect changes to algorithm. ECR A-136. Removed reference to “CMIS”. Changed reference to “CrIS” to “CrIMSS”	All
B	07/17/2008	Revision of SDR algorithm description to reflect changes. Affected section 3.1. Adding missing equations. Affected section 2.3	42-120 10-20
C	01/21/2009	Revision of the SDR algorithm description to be consistent with the software updates by ECR-A-191. Corrected typos. Added system level reference documents. Affected sections 1, 2, and 3.1.	1-103
D	10/28/2009	Revision of the EDR algorithm description to be consistent with software updates referenced in ECR A-260. Corrected typos in the SDR algorithm description section.	All

Table 1.6-2. Revision History of This Document Prior to PICM Release

Revision	Release Date	Section	Change Type
Draft	March 1, 1999		
CFI	April 6, 1999		
RRR1	February 15, 2000	Table of Contents	Update to reflect new Section 8
		2.3.2	Correct equation defining Q_2
		8	Revise section to reflect AVTPP
		9	Added missing reference
Initial Release	July 24, 2000	2.4.9	Correction to sensitivity derivation
		8.4.2	Correction to precision comparison
RRR2	November 5, 2000	3	Updated SDR earth view and calibration
		1.8	Updated contributing author list
		All	Corrected typographical and grammar
RRR3	July 23, 2001	3	Further updated SDR description, reviewed and corrected EDR description
		8	Deleted Section 8
		A	Deleted Appendix A (now described in Version Description Document)
		B	Deleted Appendix B
		All	Corrected typographical and grammar
TC CDR	November 22, 2002	2.3.1.2	Revise description of sensor table
		2.4.6	Revise description of aerosol correction
		2.4.7	Revise description of temperature profile shape correction
		2.4.8	Revise description of tropospheric ozone correction
		3	Revise description of SDR algorithm
		3	Revise description of EDR algorithm
Rev C	December 19, 2003	2.3	Revise Eq.(2) p.7
Rev D	15-July-04		Updated for V4.4 SDR algorithm release
		3.1.2.5, 3.1.3.4.4	Removed attitude correction section
		3.1.2.6, 3.3.3.4.5	Revised geolocation section
Rev E	December xx, 2004	ALL	SPCT ALG00000594
Rev F	April 6, 2005	2.4.11,3.1.3.1,3.2.1	SPCR ALG00000781

1.7 CONTRIBUTING AUTHORS

The following people have contributed to the development of the algorithm software and documentation for the production of the NPOESS ozone data products (including the IR Ozone product):

Colin Seftor	Raytheon
Igor Shimansky	Raytheon
Lack Larson	Raytheon
Hilary Snell	AER, Inc
John Pickle	AER, Inc

Richard Buss	Raytheon
Brent Canova	Ball
Kelly Chance	Harvard-Smithsonian
James Done	Northrop Grumman
David Flittner	University of Arizona
Jeffrey Hayes	Raytheon
Jennifer Hegarty	AER, Inc.
Benjamin Herman	University of Arizona
Glen Jaross	Raytheon
Vlad Kondratovich	Raytheon
James Leitch	Ball
Jean-Luc Moncet	AER, Inc.
Juan Rodriguez	Ball
James Russell	Hampton University
Thomas Samec	Northrop Grumman
Richard Slonaker	Raytheon
Thomas Swissler	Swissler InfoTech
Lisa Wait	Northrop Grumman
Karen Jordan	Northrop Grumman
Megan Novicki	Northrop Grumman
Degui Gu	Northrop Grumman
Noah Anderson	Raytheon
Bhaswar Sen	Northrop Grumman
Hélène Rieu	AER, Inc

2 Scientific Basis

2.1 PHYSICAL DESCRIPTION

Interpretation of the radiance measurements made by the OMPS nadir total column sensor requires an understanding of how the Earth's atmosphere scatters ultraviolet radiation as a function of solar zenith angle. Incoming solar radiation undergoes absorption and scattering in the atmosphere by atmospheric constituents such as ozone and aerosols, and radiation that reaches the ground is scattered by surfaces of widely varying reflectivity.

The backscattered radiance at a given wavelength depends, in principle, upon the entire ozone profile from the top of the atmosphere to the surface. For the ozone absorbing wavelengths in the OMPS sensor, the backscattered radiance consists primarily of solar radiation that penetrates the stratosphere and is reflected back by dense tropospheric air, clouds, aerosols, and the Earth's surface. The total optical depth above the scattering layer in the troposphere primarily determines the intensity. The amount of ozone below the scattering layer is small and can be estimated with sufficient accuracy to permit derivation of total column. Because most of the ozone is in the stratosphere, the principal effect of atmospheric ozone at these wavelengths is to attenuate both the solar flux going to the troposphere and the component reflected back to the satellite.

Derivation of atmospheric ozone content from measurements of the backscattered radiances requires a treatment of the reflection from the Earth's surface and of the scattering by clouds and other aerosols. These processes are not isotropic; the amount of light scattered or reflected from a given scene to the satellite depends on both the solar zenith angle and view angle, the angle between the nadir and the scene as seen at the satellite.

Early versions of the algorithm used for Total Ozone Mapping Spectrometer (TOMS) sensors based their calculation of reflectivity on the treatment of Dave (1978). He represented the contribution of clouds and aerosols to the backscattered intensity by assuming that radiation is reflected from a particular pressure level called the "scene pressure," with a Lambert-equivalent "scene reflectivity," R. When this method was applied at the non-ozone-absorbing wavelengths the resulting reflectivity exhibited wavelength dependence correlated with partially clouded scenes.

To remove this wavelength dependence, the OMPS algorithm (as well as the latest version of the TOMS algorithm) uses a simple physical model that assumes the scene can be well characterized using two separate reflecting surfaces, one representing the ground and the other representing clouds. The fractional contribution of each to the reflectivity is obtained by comparing the measured radiances with the values calculated for pure ground and pure cloud origin.

2.2 SENSOR DESCRIPTION

The NPOESS satellite will operate in a near circular, sun-synchronous orbit. The nominal orbit for the satellite is 833 km altitude, 98.7 degree inclination. The orbit will be a "precise" orbit (i.e., altitude maintained to ± 17 km, ± 0.05 degrees inclination, nodal crossing times maintained to 10 minutes throughout the mission lifetime) to minimize orbital drift (precession). The NPOESS platform will be capable of flying at any equatorial node crossing time. However, the nominal configuration will be a nodal crossing time of 1330.

The grating spectrometer and focal plane for total column measurements provide 0.45 nm spectral sampling across the wavelength range of 300 to 380 nm. The IFOV for the nadir cell of the total column measurement is 49.5 km cross track with an along-track reporting interval of 50 km. The total FOV cross track is 110 degrees to provide daily global coverage.

The signal-to-noise ratio (SNR), derived from a sensitivity analysis of the total column algorithm, requires end-of-life performance for all 22 spectral channels used in the total column measurements.

Sensor Calibration. On-orbit calibration is provided by weekly solar irradiance measurements with a reflective diffuser at the entrance aperture. The albedo calibration, defined as the ratio of radiance calibration to irradiance calibration at the same wavelength, will be determined to an accuracy greater than or equal to 2% at all wavelengths from 300-380 nm. Working and reference diffusers are used to monitor diffuser degradation. The reference diffuser comparisons will measure working diffuser reflectance changes to provide good long-term stability of sensor measurements.

2.3 FORWARD MODEL

The intensity of radiation as it passes through a region where it is absorbed and scattered can be described using a simplified form of Beer's Law that assumes a pure Rayleigh scattering atmosphere with ozone absorption:

$$I = Fe^{-s(\alpha\Omega+\beta p)} \tag{1}$$

where

I	=	radiance (Watts / cm^3-steradian)
F	=	solar flux (Watts / cm^3)
Ω	=	total column ozone amount (atm-cm)
s	=	path length (unitless)

α = ozone absorption coefficient (1 / atm-cm)

β = Rayleigh scattering coefficient (1 / atm)

p = pressure (atm)

Taking the log of both sides:

$$N = -100 \log_{10} \frac{I}{F} = 43.43 s\alpha\Omega + 43.43 s\beta p = C_1\Omega + C_2 \quad (2)$$

The term I/F is known as the normalized radiance, NR. The N value provides a unit for NR that has a scaling comparable to the total column ozone; the factor of 100 is to produce a convenient numerical range.

The basic approach of the algorithm is to use the radiative transfer code TOMRAD to calculate the N values that should be measured for different ozone amounts given the location of the measurement, viewing conditions, and surface properties. The column ozone amount that yields calculated N values that match the measured N values is then determined.

In practical application, rather than calculate NRs (in the form of N values) separately for each scene, detailed calculations of N values are performed for a grid of total column ozone amounts, vertical distributions of ozone, solar and satellite zenith angles, and four choices of pressure at the reflecting surface. The calculated N value for a given scene is obtained by interpolation in this grid of calculated N values.

2.3.1 Radiative Transfer Tables

The calculation of NRs at each pressure level follows the formulation of Dave (1964), with the addition of a spherical correction for the incident beam and the incorporation of molecular anisotropy (Ahmad and Bhartia, 1995).

Consider an atmosphere bounded below by a Lambertian reflecting surface of reflectivity R. The backscattered radiance emerging from the top of the atmosphere as seen by a UV sensor, I_m, is the sum of purely atmospheric backscatter I_a, and reflection of the incident radiation from the reflecting surface I_s,

$$I_m(\lambda,\theta,\theta_0,\Omega,P_0,R) = I_a(\lambda,\theta,\theta_0,\phi,\Omega,P_0) + I_s(\lambda,\theta,\theta_0,\Omega,P_0,R) \quad (3)$$

where

λ = wavelength (nm)

θ = satellite zenith angle, as seen from the ground (degrees)

θ_0 = solar zenith angle (degrees)

φ = azimuth angle (degrees)

Ω = column ozone amount (DU or atm-cm)

P_0 = pressure at the reflecting surface (atm)

R = effective reflectivity at the reflecting surface (unitless)

The intensity due to atmospheric scattering can be expressed as a harmonic series in azimuth as:

$$I_a(\lambda,\theta_0,\theta,\phi,\Omega,P,R) = \sum_{m=0}^{N} I_m(\lambda,\theta_0,\theta,\phi,\Omega,P,R)\cos(m\phi) \tag{4}$$

N=2 for Rayleigh scattering, yielding two azimuthally dependent terms and one azimuthally independent term:

$$I_a = I_0 + I_1\cos\phi + I_2\cos 2\phi \tag{5}$$

The surface reflection term, I_s, can be expressed as:

$$I_s(\lambda,\theta_0,\theta,\Omega,P_0) = \frac{RT(\lambda,\theta_0,\theta,\Omega,P_0)}{1-RS_b(\lambda,\Omega,P_0)} \tag{6}$$

$$T(\lambda,\theta,\theta_0,\Omega,P_0) = I_d(\lambda,\theta,\theta_0,\Omega,P_0)\,f(\lambda,\theta,\Omega,P_0) \tag{7}$$

where

S_b = fraction of radiation reflected from surface that atmosphere reflects back to surface

I_d = total amount of direct and diffuse radiation reaching surface at P_0

f = fraction of radiation reflected toward satellite in direction θ that reaches the satellite.

The denominator accounts for multiple reflections between the ground and atmosphere, where S_b is the fraction of the reflected radiation scattered back to the surface by the atmosphere.

The total intensity seen by the satellite (I_m or I_t) can now be written as:

$$I_t = I_0 + I_1\cos\phi + I_2\cos 2\phi + \frac{RT}{1-RS_b} \tag{8}$$

Part of the angular dependence of I_1 and I_2 can be factored out as:

$$I_1 = Q_1(\theta_0, \theta) \cdot Z_1; \text{ and } I_2 = Q_2(\theta_0, \theta) \cdot Z_2 \quad (9)$$

where

$$Q_1(\theta_0, \theta) = -\frac{3}{8}\cos\theta_0 \sin\theta_0 \sin\theta, \text{ and} \quad (10)$$

$$Q_2(\theta_0, \theta) = \frac{3}{32}\frac{\sin^2\theta_0 \sin^2\theta}{\cos\theta} \quad (11)$$

Z_1 and Z_2 are better-behaved angular functions and are therefore used in table interpolations instead of I_1 and I_2.

(Note: the actual angular interpolations are performed on the quantities $\log(I_0)$, Z_1/I_0, Z_2/I_0, T/I_0. The interpolated values are converted to I_0, I_1, I_2, T and, along with S_b, are used to calculate I.)

A "master table" containing I_0, Z_1, Z_2, T, and S_b was generated using TOMRAD for the conditions shown in **Table 2.3-1**. The entire table is calculated for the size satellite zenith angles for the two sides of the CCD independently.

Table 2.3-1. Table Node Points

Quantity	Number	Values
Wavelength	3047	From 248 to 401 nm in steps of ~0.05 nm
Solar Zenith Angle	10	0, 30, 45, 60, 70, 77, 81, 84, 86, 88°
Satellite Zenith Angle	6x2	0, 15, 30, 45, 60, 70°
Pressure	4	1.0, 0.7, 0.4, 0.1 atm
Ozone Profiles	26	6 low, 10 mid, and 10 high latitude

For each wavelength, TOMRAD requires as input an ozone and temperature profile, the Rayleigh scattering coefficient, the molecular anisotropy factor, and the ozone absorption coefficient at 0 °C. The temperature profile is used, along with the absorption coefficient at 0 °C (α_0), to determine the absorption coefficient at each of the 11 ozone and profile layers. If T_{layer} is the temperature for the atmospheric layer, then

$$\alpha_{layer} = \alpha_0 + c_1 T_{layer} + c_2 T_{layer}^2 \quad (12)$$

The coefficients c_1 and c_2 are also provided for each wavelength.

The six low-latitude profiles range from 225 to 475 Dobson Units (DU) in steps of 50 DU. The ten mid- and ten high-latitude profiles range from 125 to 575 DU in steps of 50 DU. These standard ozone and temperature profiles were determined from an Empirical Orthogonal Function (EOF) analysis of the entire SAGE II data set.

2.3.1.1 Standard Ozone and Temperature Profile Determination

The OMPS total column algorithm's table is based on a set of climatological ozone profiles that account for the dependence of the measured radiances on the total amount of ozone and its vertical distribution (Klenk et al., 1982). To develop this set of standard profiles, empirical orthogonal functions (EOF) were derived for an external data set comprising SAGE II profiles over the period from launch in October 1984 through June 1991 (when the eruption of Mt. Pinatubo began to impact the SAGE II ozone retrieval). This problem is bounded by using only the first two EOFs to define a two-dimensional space that explains most of the variability in the ozone profile. To provide statistically consistent lower layers for SAGE II profiles, a set of balloonsonde profiles in the period from November 1978 through 1987 for 20 ground sites distributed about the globe were used in conjunction with the SAGE II profiles. The derived climatology spans the ensemble of possible profiles. For details of the analysis, see Wellemeyer et al. (1997). The standard OMPS profiles are defined in Umkehr layers (**Table 2.3-2**), so the SAGE II profiles are converted to pressure coordinates using the National Centers for Environmental Prediction (NCEP) temperature profiles provided with the SAGE II data and integrated into Umkehr layers. The resulting standard ozone and temperature profiles are given in **Tables 2.3-3** and **2.3-4**.

Table 2.3-2. Umkehr Layers Used for Ozone Profiles

Umkehr Layer No.	Layer Pressure (mb)	Pressure at Altitude of Midpoint (mb)	Layer Midpoint (km)
12	0.000 – 0.247	–	–
11	0.247 – 0.495	0.350	56.5
10	0.495 – 0.990	0.700	51.0
9	0.990 – 1.980	1.40	45.5
8	1.980 – 3.960	2.80	40.2
7	3.960 – 7.920	5.60	35.2
6	7.920 – 15.80	11.2	30.4
5	15.80 – 31.70	22.4	25.8
4	31.70 – 63.30	44.8	21.3
3	63.30 – 127.0	89.6	17.0
2	127.0 – 253.0	179.0	12.5
0 and 1	253.0 – 1013	507.0	5.5

Table 2.3-3. OMPS Standard Ozone Profiles (in Dobson Units)

Prof	Umkehr Layer Number										
	0	1	2	3	4	5	6	7	8	9	> 9
225L	15.0	9.0	5.0	7.0	25.0	62.2	57.0	29.4	10.9	3.2	1.3
275L	15.0	9.0	6.0	12.0	52.0	79.2	57.0	29.4	10.9	3.2	1.3
325L	15.0	9.0	10.0	31.0	71.0	87.2	57.0	29.4	10.9	3.2	1.3
375L	15.0	9.0	21.0	53.0	88.0	87.2	57.0	29.4	10.9	3.2	1.3
425L	15.0	9.0	37.0	81.0	94.0	87.2	57.0	29.4	10.9	3.2	1.3
475L	15.0	9.0	54.0	108.0	100.0	87.2	57.0	29.4	10.9	3.2	1.3
125M	6.0	5.0	4.0	6.0	8.0	31.8	28.0	20.0	11.1	3.7	1.4
175M	8.0	7.0	8.0	12.0	26.0	41.9	33.6	22.3	11.1	3.7	1.4
225M	10.0	9.0	12.0	18.0	44.0	52.1	39.2	24.5	11.1	3.7	1.4
275M	16.0	12.0	15.0	29.0	58.0	63.7	40.6	24.5	11.1	3.7	1.4
325M	16.0	14.0	26.0	45.0	74.7	66.9	41.7	24.5	11.1	3.7	1.4
375M	16.0	16.0	39.0	64.0	85.7	71.1	42.5	24.5	11.1	3.7	1.4
425M	16.0	18.0	54.0	84.0	97.7	71.7	42.9	24.5	11.1	3.7	1.4
475M	16.0	22.0	72.0	107.7	101.0	72.6	43.0	24.5	11.1	3.7	1.4
525M	16.0	26.0	91.0	127.7	108.0	72.6	43.0	24.5	11.1	3.7	1.4
575M	16.0	30.0	110.0	147.7	115.0	72.6	43.0	24.5	11.1	3.7	1.4
125H	9.5	7.0	18.3	7.6	8.2	28.6	22.0	12.4	7.7	2.5	1.2
175H	9.5	8.0	22.8	22.0	26.9	32.3	26.8	15.0	8.0	2.5	1.2
225H	10.0	9.0	27.6	45.7	41.0	35.0	28.8	15.4	8.3	2.9	1.3
275H	14.0	12.0	34.0	66.9	54.2	36.0	28.8	15.4	8.9	3.4	1.4
325H	14.0	15.0	46.8	82.6	65.2	41.7	28.8	17.2	8.9	3.4	1.4
375H	14.0	20.0	61.2	93.8	75.2	45.9	32.5	18.7	8.9	3.4	1.4
425H	14.0	25.0	76.2	104.9	84.2	51.4	35.6	20.0	8.9	3.4	1.4
475H	14.0	32.0	91.0	117.1	93.0	55.8	37.5	20.9	8.9	3.4	1.4
525H	14.0	41.0	107.1	128.1	101.0	60.2	38.2	21.7	8.9	3.4	1.4
575H	14.0	49.0	123.2	142.2	111.0	60.6	38.8	22.5	8.9	3.4	1.4

Table 2.3-4. OMPS Standard Temperature (in Kelvin)

	Umkehr Layer Number										
Prof	**0**	**1**	**2**	**3**	**4**	**5**	**6**	**7**	**8**	**9**	**> 9**
225L	283.0	251.0	215.6	200.7	210.7	221.6	231.1	245.3	258.7	267.4	265.4
275L	283.0	251.0	215.9	203.5	211.9	222.5	231.1	245.3	258.7	267.4	265.4
325L	283.0	251.0	216.5	207.0	213.6	223.0	231.1	245.3	258.7	267.4	265.4
375L	283.0	251.0	216.0	210.0	216.0	224.0	231.1	245.3	258.7	267.4	265.4
425L	283.0	251.0	216.0	213.0	217.0	224.5	231.1	245.3	258.7	267.4	265.4
475L	283.0	251.0	216.0	216.0	219.0	225.0	231.1	245.3	258.7	267.4	265.4
125M	237.0	218.0	196.0	191.0	193.0	210.0	227.6	239.4	253.6	263.9	262.6
175M	260.0	228.0	201.7	198.0	202.1	214.3	227.6	239.4	253.6	263.9	262.6
225M	273.0	239.0	213.3	207.5	211.7	219.1	227.6	239.4	253.6	263.9	262.6
275M	273.0	239.0	217.1	212.2	214.9	220.4	227.6	239.4	253.6	263.9	262.6
325M	273.0	239.0	219.1	216.6	217.0	220.8	227.6	239.4	253.6	263.9	262.6
375M	273.0	239.0	220.2	219.0	219.0	221.9	227.6	239.4	253.6	263.9	262.6
425M	273.0	239.0	220.9	220.7	221.0	223.7	227.6	239.4	253.6	263.9	262.6
475M	273.0	239.0	221.5	222.5	222.7	224.4	227.6	239.4	253.6	263.9	262.6
525M	273.0	239.0	222.3	224.8	225.5	225.8	227.6	239.4	253.6	263.9	262.6
575M	273.0	239.0	225.0	227.0	227.0	227.0	227.6	239.4	253.5	263.9	262.6
125H	237.0	218.0	196.0	191.0	193.0	210.0	223.3	237.1	251.6	262.4	265.6
175H	260.0	228.0	201.7	198.0	202.1	214.3	223.3	237.1	251.6	262.4	265.6
225H	260.0	228.0	209.7	208.5	212.5	222.0	228.0	237.1	251.6	262.4	265.6
275H	260.0	228.0	222.6	223.4	223.8	226.5	231.6	237.1	251.6	262.4	265.6
325H	260.0	228.0	222.6	223.4	223.8	226.5	231.6	237.1	251.5	262.4	265.6
375H	260.0	228.0	222.6	223.4	223.8	226.5	231.6	237.1	251.5	262.4	265.6
425H	260.0	228.0	222.6	223.4	223.8	226.5	231.6	237.1	251.5	262.4	265.6
475H	260.0	228.0	222.6	223.4	223.8	226.5	231.6	237.1	251.5	262.4	265.6
525H	260.0	228.0	222.6	223.4	223.8	226.5	231.6	237.1	251.5	262.4	265.6
575H	260.0	228.0	222.6	223.4	223.8	226.5	231.6	237.1	251.5	262.4	265.6

2.3.1.2 Sensor Table Generation

The OMPS nadir total column sensor measures UV radiances in the range from 300 to 380 nm. The total column algorithm uses 22 wavelengths from this range (details of the wavelength selection are given in Section 2.4.10).

The OMPS sensor cannot actually measure monochromatic radiance, $I(\lambda)$, because of its finite bandwidth. Therefore, in generating look-up tables for the algorithm, slit-averaged values were computed from the master table for the central value of the 22 wavelengths using slit functions from the OMPS sensor. Mathematically, the slit-average radiance is written as:

$$\bar{I}(\lambda_0) = \frac{\int I(\lambda)S(\lambda)d\lambda}{\int S(\lambda)d\lambda} \text{ , or} \tag{13}$$

$$\bar{I} = \frac{\int NR(\lambda)F(\lambda)S(\lambda)d\lambda}{\int S(\lambda)d\lambda} \text{ ,} \tag{14}$$

where λ_0 is the central slit wavelength, S(λ) is the response function (slit function), and F(λ) is the extraterrestrial solar flux. Similarly, the measured average solar flux F may be expressed as

$$\bar{F}(\lambda_0) = \frac{\int F(\lambda)S(\lambda)d\lambda}{\int S(\lambda)d\lambda} \tag{15}$$

Consequently, the measured NR can be expressed as

$$\bar{NR}(\lambda_0) = \frac{\int NR(\lambda)F(\lambda)S(\lambda)d\lambda}{\int F(\lambda)S(\lambda)d\lambda} \tag{16}$$

Thus, the NR utilized in establishing the ozone look-up tables should be computed following Equation (16). In this equation, NR(λ) now represents the theoretical NR obtained from TOMRAD using a given ozone profile and at a given pressure, solar zenith angle, and satellite zenith angle, and employing the ozone absorption coefficient, $\alpha_{BP}(\lambda)$, provided by Bass and Paur as a parameter at given wavelength λ_{BP} (Bass and Paur, 1984). In the OMPS table, the NRs were derived using Equation (16) and values from the master table. In addition, the high-resolution solar flux measurements from the SOLSTICE instrument were included in the calculation (Woods et al., 1996).

To account for the sensor spectral smile, seven different sets of the 22 wavelengths are used to generate the sensor table, spanning the range of wavelengths from the edges of the CCD to the center. The algorithm then interpolates table values between the two sets of wavelengths that bracket the wavelength values provided by the SDR.

2.3.2 Sensitivity Table

As described above, the sensor table is based on a standard set of ozone and temperature profiles. To correct for deviations between the actual ozone and temperature profiles and the standard ones, the OMPS algorithm uses a sensitivity table to calculate the change in N with layer ozone amount, dN/dx.

dN/dx Table. As in the generation of the master table, TOMRAD was used to generate values of $\log(I_0)$, Z_1/I_0, Z_2/I_0, T/I_0, and S_b for each wavelength, angle, and pressure node point shown in Table 2.3-1. However, TOMRAD was run 12 times for each standard ozone and temperature profile, once unperturbed and 11 times with perturbations about the standard profile. On the first run, the standard ozone profile was used. On the second run, the standard ozone profile was perturbed by increasing ozone in the first layer by 10%. On the third run, the standard profile was perturbed by increasing ozone in the second layer by 10%. This process continued for the 11 layer ozone amounts. A table was generated containing values for the 26 standard profiles as well as all 11 perturbations of each standard profile.

By combining calculated N values for ozone profiles perturbed in different layers with calculated N values for the standard profile, dN/dx values for each of the layers can be generated and used by the algorithm.

A sensor table is generated from the sensitivity "master table" using the same procedure described in Section 2.3.1.2. Because this table is used to determine sensitivities, only wavelengths corresponding to the center of the CCD are used.

2.3.3 Rotational-Raman Scattering

In the algorithm, a correction to the computed table radiances is applied in order to account for the effects of rotational-Raman scattering (RRS), which is also known as the Ring effect. The RRS effect on backscattered ultraviolet (BUV) radiances, which has been modeled and described in detail elsewhere (Joiner et al., 1995) is complex and varies as a function of solar zenith angle, satellite zenith angle, reflectivity, and surface pressure as well as wavelength. The correction is applied to the table radiances after each lookup is performed.

In order to simplify the RRS correction, the dependencies on solar and satellite zenith angle, which are small under most conditions, are ignored. For example, at low reflectivities, the RRS correction varies with solar and satellite zenith angle by less than $\pm$ 0.2% at all wavelengths.

The RRS effect is approximately linear with surface pressure. Therefore, a single correction is applied at each wavelength to the 1.0, 0.7, 0.4, and 0.1 atmospheric pressure tables. These are computed at the surface and cloud reflectivities, respectively, and are chosen consistent with assumptions made in the partial cloud algorithm. All correction factors were computed at a solar zenith angle of 45° and a satellite zenith angle of 0°.

2.4 RETRIEVAL

2.4.1 Overview

As stated previously, the retrieval of ozone is based on a comparison between the measured normalized radiances (NRs) and NRs derived by radiative transfer calculations for different ozone amounts and the conditions of the measurement. It is implemented by using the tables of backscattered NRs described in Section 2.3. Given the computed radiances for the particular observing conditions, the total ozone value can be derived by interpolation of NR as a function of ozone. It is also possible to reverse this process and use the tables to obtain the NRs that would be expected for a given column ozone and conditions of the measurement. The logarithm of the ratio of the measured NR to this calculated NR (or the difference between measured and calculated N values) is the residue.

The retrieval starts out by calculating an effective cloud fraction. The reflecting surface is assumed to consist of two components, a surface component of lower reflectivity and a cloud component of higher reflectivity. By comparing the measured radiance at an ozone-insensitive wavelength with one calculated for cloud and for ground reflection alone, the effective cloud fraction and the contribution from each level can be derived.

Using this effective cloud fraction and the NRs measured at a pair of wavelengths (one strongly sensitive to ozone, one weakly sensitive or insensitive to ozone), an initial ozone estimate is derived by matching the measured N value to N values interpolated from the table using the viewing conditions of the measurement.

This ozone estimate is used to calculate residues for the pair of wavelengths. A linear correction to the initial ozone estimate is then derived from the residues at these two wavelengths. This linear correction accounts for differences between the Rayleigh scattering atmosphere model assumed in constructing the tables and the actual atmosphere measured by the sensor.

Although the linear correction accounts for most differences between the model Rayleigh and actual atmospheres, it overcorrects the amount of total ozone in the presence of tropospheric aerosols or for cases of sun glint. A second adjustment to the ozone value is therefore applied. This adjustment, which is based on the 331-376 nm residue difference, effectively corrects for these effects. A quantity called the aerosol index is based on the 331-376 nm residue difference and represents a separate data product that has proven useful to the science community in the study of tropospheric aerosols.

Since the calculated N values are derived from tables based on a set of standard ozone and temperature profiles, deviations of the actual ozone and temperature profiles from the standard ones produce errors in the ozone retrieval. External data are used to determine the layer deviations between actual and standard profiles. Corrections for these profile differences are calculated by multiplying each layer

deviation with sensitivities determined by table interpolation. These corrections are applied to the retrieved ozone.

Finally, the backscattered radiances at 1 nm resolution are not 100% sensitive to ozone in the troposphere. This inefficiency also produces errors in the retrieved ozone value. The algorithm uses climatological values for the amount of tropospheric ozone (depending on location and time of year) along with layer ozone sensitivities calculated from the dN/dx table to determine tropospheric efficiency. This efficiency factor is used to correct the tropospheric ozone amount and, in turn, the total column ozone amount.

In order to minimize errors due to sensor noise, the above procedure is performed on multiple sets of triplets using 4 different ozone-insensitive wavelengths to determine reflectivity. For each measurement, 12 different wavelength triplets are used (3 different wavelength pairs matched to the 4 different reflectivity wavelengths). The choice of triplets is based upon the optical path length of the measurement.

The ozone retrieval is checked for volcanic SO_2 contamination. If it is contaminated, the retrieval is flagged for post processing. The retrieval is also checked for the occurrence of a solar eclipse and, if affected, it is flagged.

Algorithms for the derivation of other parameters besides ozone have been developed. These include an estimate of UVB flux at the surface and estimates of aerosol loading due to the presence of atmospheric aerosols.

2.4.2 OMPS Reflectivity (Cloud Fraction)

The OMPS algorithm accounts for the presence of clouds using a simple physical model that assumes a scene can be represented by two separate reflecting surfaces, one for the ground and one for clouds. The fractional contribution of each to the reflectivity is obtained by comparing the measured NR with NR values calculated for pure ground and pure cloud scenes.

For a given measurement at a given non-ozone-absorbing wavelength, the NR tables are used along with Equation (16) to determine an NR value corresponding to reflection off of the ground and an NR value corresponding to reflection off of a cloud. The total NR is computed simply as the area weighted average of the terrain and cloud NRs.

In the calculation of the terrain NR, external terrain pressure information from CrIMSS is used. If not available, a data set compiled from the TUG87 geophysical model (Weiser, 1987) is used. This data set contains a 1° latitude by 1° longitude grid of pressure values.

The surface reflectivity is determined from a database of minimum UV surface reflectivity developed using the 15-year Nimbus-7/TOMS data set (Herman and

Celarier, 1997). This data set contains a 1° latitude by 1° longitude grid of minimum UV surface reflectivity for each month.

In the calculation of cloud radiance, external cloud pressure information from VIIRS is used. If not available, a data-set compiled from the International Satellite Cloud Climatology Project (ISCCP) will be used to determine the cloud-top pressure. This data set, similar to the one described above, contains a 1° latitude by 1° longitude grid for each month. A cloud reflectivity of 80 percent is assumed. The cloud top pressure information from VIIRS is determined at IR wavelengths and has shown to have significant error in the UV. This is a subject under review and changes may be implemented for the NPOESS version of the algorithm.

The fractional cloud cover, f, is estimated as:

$$f = \frac{I_{measured} - I_{terrain}}{I_{cloud} - I_{terrain}} \tag{17}$$

where $I_{terrain}$ and I_{cloud} are the terrain and cloud-top NRs, respectively, from the tables, and $I_{measured}$ is the measured NR. An effective reflectivity, R, is calculated as:

$$R = R_{surface} + (0.8 - R_{surface}) * f \tag{18}$$

In cases where the reflectivity is less than $R_{surface}$ or greater than 80%, the effective reflectivity is calculated by inverting Equation (6).

External data from VIIRS is used to determine if snow or ice is on the ground. If there is no snow or ice, then the cloud fraction (determined from the nadir sensor) and the cloud top pressure (VIIRS EDR) and surface pressure (CrIMSS EDR) are used to determine the effective reflectivity and the pressure of the reflecting surface. If there is snow or ice, then the retrieval algorithm will calculate R assuming a clear scene (Ahmad, 2000).

If the external EDRs are unavailable, a snow/ice database is used. As above, it is determined from the database that snow or ice conditions are present, the OMPS algorithm will calculate R assuming a clear scene.

2.4.3 Initial Estimate of Ozone

The OMPS nadir algorithm uses the cloud fraction (or reflectivity) determined from an ozone-insensitive wavelength and the measured N value difference between a pair of closely spaced shorter wavelengths (one strongly ozone absorbing and one ozone insensitive or weakly ozone absorbing) to determine an initial estimate of ozone. The use of a pair difference provides an estimate insensitive to wavelength-independent errors, in particular, calibration errors. The ozone estimate is the ozone value at which, for the derived reflectivity and measurement geometry, the calculated N value difference for the pair of wavelengths best matches the measured N value difference. The pair chosen for this initial estimate is 318/336 nm.

For each measurement, NRs are calculated for a given standard ozone profile at each pressure level using the given viewing conditions. The ozone profile used for the calculation depends on the latitude of the measurement and the total ozone value corresponds to the closest table node point below the ozone amount from the previous measurement. For the ground situation, the surface reflectivity is assumed and terrain pressure is used to interpolate the 0.1, 0.4, 0.7, and 1.0 atm NRs in order to determine a calculated NR for this ozone profile. For the cloud situation, NRs for each ozone value are determined assuming a cloud reflectivity of 80% with the cloud pressure used for the interpolation. An NR is determined for the entire scene as an area-weighted average of the ground and cloud NRs using the fractional cloud cover, f. The NRs are converted into pair N values, and the calculated pair N value is compared to the measured pair N value.

If the calculated N value is lower than the measured N value, another pair N value is calculated (using the procedure just described) for the next higher ozone node point. If it is higher, another pair N value is calculated for the next lower ozone node point. In this way, two calculated pair N values that bracket the measured pair N value are found. An ozone estimate is determined using the measured pair N value to linearly interpolate between calculated N values to find the corresponding ozone amount.

2.4.4 Linear Correction

In the absence of other geophysical phenomena or calibration errors, N values calculated for each of the pair of wavelengths (using the ozone estimate and the reflectivity determined from the reflectivity wavelength) are equal to the measured N values for those wavelengths. Consequently, non-zero values of the difference between measured and calculated N value, or residue, for a given wavelength signifies that either calibration errors or geophysical phenomena are not yet taken into account.

The OMPS algorithm corrects for this error by assuming that the residue dependence in the wavelength triplet is linear. If, for a given OMPS wavelength the measured N value is denoted by N_m, then, using a first order Taylor series expansion:

$$N_m = N_0 + (\Omega - \Omega_0)\frac{dN}{d\Omega} \tag{19}$$

where Ω_0 is an initial estimate of ozone obtained using the pair of wavelengths. N_0 is the N value calculated by using the long wavelength, cloud fraction, and Ω_0 in conjunction with the tables. Ω is the corrected ozone value. By assuming a linear wavelength dependence the above equation becomes:

$$r = N_m - N_0 = (\Omega - \Omega_0)\frac{dN}{d\Omega} + a + b\lambda \tag{20}$$

where r is the residue. Since the long or reflectivity wavelength is insensitive to ozone, dN/dΩ = 0 and

$$r = a + b\lambda = a + b\lambda_R \tag{21}$$

Since the long wavelength is used to determine the cloud fraction (and, therefore, reflectivity), the calculated and measured N values are equal:

$$r_R = 0 \Rightarrow a = -\lambda_R b$$

For ozone-sensitive wavelengths:

$$r_\lambda = (\Omega - \Omega_0)\frac{dN}{d\Omega} + b(\lambda - \lambda_R) \tag{22}$$

Since there are 2 unknowns in Equation (22), Ω and b, the pair of wavelengths in the triplet are used to solve for Ω:

$$\Omega = \Omega_0 + \frac{r_1(\lambda_2 - \lambda_R) - r_2(\lambda_1 - \lambda_R)}{(\frac{dN}{d\Omega})_1(\lambda_2 - \lambda_R) - (\frac{dN}{d\Omega})_2(\lambda_1 - \lambda_R)} \tag{23}$$

where 1 and 2 represent the two different wavelengths.

The triplets used to solve Equation (23) depend on the optical path length of the measurement, which is defined as the path length times ozone amount divided by 1000:

$$s\Omega = \Omega_0 \cdot (\sec\theta_0 + \sec\theta)/1000. \tag{24}$$

This choice of triplets is discussed in Sections 2.4.9 and 2.4.10.

2.4.5 Profile Selection

The radiative transfer tables include ozone and temperature profiles for three broad latitude bands; low, middle, and high. For latitudes ≤ 15°, the retrieval is performed using only the low-latitude profiles. For 15° < latitudes ≤ 45°, retrievals are performed using low- and mid-latitude profiles. For 45° < latitudes < 75°, retrievals are calculated using mid- and high-latitude profiles. And, for latitude ≥ 75°, retrievals are performed for high-latitude profiles. Values of dN/dΩ are calculated, as well.

For retrievals at latitudes where two profiles are used, an ozone value appropriate to the latitude of the measurement is derived from the ozone values for the two profiles, using an equation of the form:

$$\Omega = (1 - f_{prof}) \cdot \Omega_{lower} + f_{prof}\,\Omega_{higher} \tag{25}$$

where

Ω = ozone,

Ω_{lower} = ozone retrieved using lower latitude profile,

Ω_{higher} = ozone retrieved using higher latitude profile, and

f_{prof} = weight given to higher latitude profile.

Thus, f_{prof} will be 0 if only the lower latitude profile is selected, 1 if only the higher latitude profile is selected, and in between for a combination of the two profiles.

For *somega* less than 1.5, a value of f_{prof} obtained by simple linear interpolation in latitude,

$$f_{prof} = \frac{|latitude| - |latitude|_{lower}}{|latitude|_{higher} - |latitude|_{lower}} \tag{26}$$

is used for latitudes between 15 and 75 degrees using the two profiles appropriate for the latitude. The low-latitude profile alone is used from the equator to 15 degrees, and the high-latitude profile alone is used from 75 degrees to the pole.

For longer path lengths, a profile mixing scheme is used to determine the profile mixing factor, f_{prof}. The basic principle is to calculate the residue of a fourth, shorter wavelength that is sensitive to ozone profile shape information. By defining a linear combination of the standard profiles that best explains the radiances at all four wavelengths, the algorithm calculates the profile mixing factor:

$$f_m = \frac{r'(lower)}{r'(lower) - r'(higher)} \tag{27}$$

where lower and higher refer to latitudes of the two profiles used and r′ refers to the residue for the shortest channel among four wavelength channels. In most cases, the appropriate profile will be between the higher and lower latitude profiles, and the residues will be of opposite sign; thus the denominator represents a distance between the residues (or sensitivity to profile shape) and the numerator a fraction of this distance. When the low- and mid-latitude profiles are used, and when the derived value of f_{prof} is greater than 1, the process is repeated using the mid- and high-latitude profiles. Similarly, if f_{prof} is less than zero using mid- and high-latitude profiles, then the process is repeated using the low- and mid-latitude profiles.

The value of Ω as obtained from Equation (25) represents the heritage Version 7 algorithm total ozone and will be reported as a separate data product, Ω_{V7}.

2.4.6 Correction for Tropospheric Aerosols and Sun Glint

Radiative transfer studies performed at NASA/GSFC and Raytheon indicate that in the presence of tropospheric aerosols, the linear assumption does not adequately account for tropospheric aerosols or sun glint. These studies further indicate that the error in retrieved ozone is linearly related to the TOMS aerosol index, AI, defined as the difference between 331 and 360 nm residues. Since the OMPS algorithm does not contain a 331 or 361 nm channel, the difference between the 336 and 377 nm channel residues, $R_{336\text{-}377}$, is used to determine the aerosol correction.

To determine the form of the correction, different aerosol models were used to simulate retrievals of Ω_{V7}. The aerosol model parameters are given in **Table 2.4-1**.

Table 2.4-1. Aerosol model parameters

Type	Model #	Model name	Radius (μm)		Standard Deviation		Fraction	Ref. Index		Optical depth at 551nm	Aerosol height (km)	Total # of cases
			m1	m2	M1	M2	m2	Real	image			
Industrial	1	IS1	0.078	0.497	1.499	2.160	4.36E-04	1.40	0.004			
	2	IS2	0.088	0.509	1.499	2.160	4.04E-04	1.40	0.004			
	3	IS3	0.137	0.567	1.499	2.160	8.10E-04	1.40	0.004	0.3		
	4	IA1	0.085	0.641	1.560	2.004	7.00E-04	1.45	0.012	0.6 0.9	0.0	36
	5	IA2	0.090	0.676	1.560	2.004	6.84E-04	1.45	0.012			
	6	IA3	0.109	0.804	1.560	2.004	6.95E-04	1.45	0.012			
Biomass	7	BL1	0.074	0.511	1.537	2.203	1.70E-04	1.50	0.010			
	8	BL2	0.087	0.567	1.537	2.203	2.06E-04	1.50	0.010			
	9	BL3	0.124	0.719	1.537	2.203	2.94E-04	1.50	0.010	1.0	1.0	
	10	BH1	0.076	0.665	1.492	2.075	2.07E-04	1.50	0.020	2.0 3.0 5.0	3.0 5.0	144
	11	BH2	0.080	0.705	1.492	2.075	2.05E-04	1.50	0.020			
	12	BH3	0.097	0.866	1.492	2.075	1.99E-04	1.50	0.020			
Desert	13	DS1	0.071		1.568			1.53	[1]L		1.0	
	14	DS2	0.071		1.568			1.53	[1]H	0.5 1.0	3.0	72
	15	DL1	0.764		1.822			1.53	[1]L	2.0	.0	

	16 DL2 0.764	1.822	1.53	[1]H	

[1]Wavelength dependent with (H)igh or (L)ow absorbance. The following values from Patterson et al. (1977) are used for high absorption (half of that used for low absorbing case):

λ (μm)	.270	.290	.310	.330	.350	.370	.390	.410	.430	.450	.470	.500
A	.0290	.0265	.0236	.0211	.0188	.0168	.0150	.0134	.0119	.0106	.0095	.0080

The percent error in the Version 7 ozone value was determined and plotted as a function of $R_{336\text{-}377}$. Two different quadratic fits were then made, one for path length less than or equal to 4.5 and one for path length greater than 4.5. **Figures 2.4-1** and **2.4-2** show the two situations.

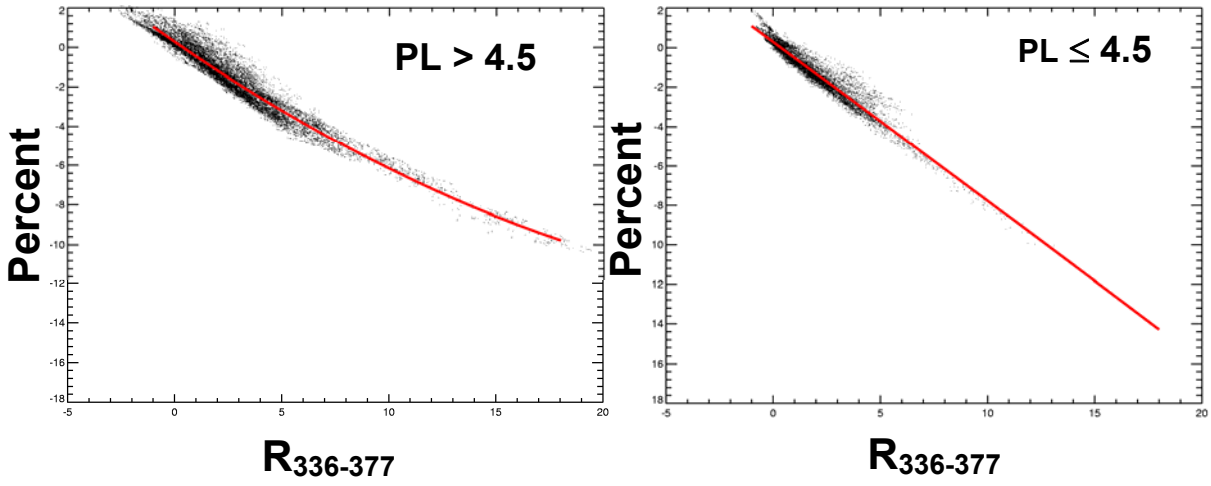

Figures 2.4-1 and 2.4-2. Quadratic fits of percent error in Ω_{V7} as a function of $R_{336\text{-}377}$ for path lengths below and above 4.5

The fits resulted in the following values (the constant term is assumed to be zero; no aerosols equals no error):

$$\Delta\Omega(\%) = -0.75\,R_{336-377} + 0.011\,R_{336-377}^2 \text{ for PL} \le 4.5 \quad (28)$$

$$\Delta\Omega(\%) = -0.80\,R_{336-377} \text{ for PL} > 4.5 \quad (29)$$

To correct for the presence of tropospheric aerosols, the algorithm first calculates $R_{336\text{-}377}$ and then corrects the ozone value using the coefficients from the above two fits:

$$\Omega_{aercor} = \Omega_{V7} + 0.75\,R_{336-377} - 0.011\,R_{336-377}^2 \text{ for PL} \le 4.5 \quad (30)$$

$$\Omega_{aercor} = \Omega_{V7} + 0.80\,R_{336-377} \text{ for PL} > 4.5 \quad (31)$$

The aerosol index is defined as the 331-360 nm residue difference for the TOMS sensor system. To be compatible, an aerosol index is then calculated from $R_{336\text{-}377}$ and reported out in the data record:

$$Aerosol\ Index = \frac{331-360}{336-377} R_{336-377}\,. \quad (32)$$

2.4.7 Correction for Temperature and Ozone Profile Shape

Since the ozone absorption coefficient depends on temperature, differences between the standard temperature profiles and the actual atmospheric temperature profile lead to errors in retrieved ozone. The same is true for differences between the standard ozone profile shape and the actual ozone profile shape, particularly for large path length or large ozone amount.

To correct for these temperature and profile shape errors, two terms are added to the Taylor series expansion given in Equation 20. Expanding around Ω_{aercor}:

$$r = N_m - N_{aercor} = (\Omega - \Omega_{aercor})\frac{dN}{d\Omega} + \sum_{layer}(t_{layer} - t_{layer}^0)\frac{dN}{dt_{layer}} + \sum_{layer}(x_{layer} - x_{layer}^0)\frac{dN}{dx_{layer}} + a + b\lambda \quad (33)$$

where:

t_{layer} = layer temperature obtained from the CrIMSS sensors,

t^0_{layer} = layer temperature used in the standard profile,

x_{layer} = layer ozone amount obtained from the TOMS V8 Climatology, and

x^0_{layer} = layer ozone amount used in the standard profile.

The layer ozone sensitivity, dN/dx_{layer}, is determined from the radiative transfer tables described in Section 2.3.2. The ozone layer sensitivity is only determined for the levels in the stratosphere.

The layer temperature sensitivity, dN/dt_{layer}, is determined using dN/dx_{layer} and the relationship of the ozone absorption coefficient, α, for a given wavelength λ to the temperature, T:

$$\alpha = c_0 + c_1 T + c_2 T^2 \tag{34}$$

where c_1, c_2, c_3 are constants for that wavelength. Using the chain rule:

$$\sum_x \left(\frac{\Delta N_x}{\Delta T}\right)_x = \sum_x \left(\frac{\partial N}{\partial T}\right)_x = \sum_x \left(\frac{\partial N}{\partial x}\right)_x \left(\frac{\partial x}{\partial \alpha}\right)_x \left(\frac{\partial \alpha}{\partial T}\right)_x = \sum_x \left(\frac{\partial N}{\partial x}\right)_x \left(\frac{\partial x}{\partial \alpha}\right)_x \Delta\alpha_x \tag{35}$$

where x is each atmospheric level. From Equation (1):

$$\frac{\Delta I}{I} = -s\Delta(\alpha x) \tag{36}$$

and, from the definition of N value:

$$N_x = -\log_{10}\frac{I}{I_0} = -Cs\alpha x \Rightarrow \Delta N = -Cs\Delta(*\alpha x) = -Cs(\alpha\Delta x + x\Delta\alpha)\,. \tag{37}$$

Combining Equations (35), (36) **a**nd (37):

$$\sum_x \left(\frac{\Delta N}{\partial T}\right)_x = \sum_x \left(\frac{\partial N}{\partial x}\right)_x \frac{x}{\alpha_x}\frac{\partial \alpha}{\partial T} = \sum_x \left(\frac{\partial N}{\partial x}\right)_x \frac{x}{\alpha_x}\left[\alpha(T_x^{stdprf}) - \alpha(T_x^{measured})\right]. \tag{38}$$

The CrIMSS temperature profile information is matched to the 11 layers used in the tables through a spline fitting procedure. A similar procedure would be used to match the OMPS limb retrieval. As the limb retrieval is not part of the NPOESS system, this procedure is not carried out as part of the algorithm.

The ozone solution becomes:

$$\Omega_{tpcor} = \Omega_{aercor} + \frac{r_1(\lambda_2 - \lambda_R) - r_2(\lambda_1 - \lambda_R)}{(\frac{dN}{d\Omega})_1(\lambda_2 - \lambda_R) - (\frac{dN}{d\Omega})_2(\lambda_1 - \lambda_R)} \tag{39}$$

2.4.8 Correction for Tropospheric Ozone

The OMPS limb retrieval was intended to be used used to correct profile shape errors and to correct for errors due to the insensitivity of the BUV solar radiation (at 1 nm spectral resolution) to tropospheric ozone. The limb retrieval is no longer part of the NPOESS system, and therefore this correction is no longer made on the basis of the limb measurements. The algorithm maintains this correction ability and if called uses the climatology from TOMS V8 to make the appropriate corrections.

The amount of tropospheric ozone that is measured strongly depends on the amount of ozone below 13 km contained in the standard profile, X_{13}^0. We can write the amount of ozone retrieved below 13 km as:

$$X_{retr} = \Omega_{tpcor} - \sum_{13}^{60} x_{limb} \tag{40}$$

where $\sum_{13}^{60} x_{limb}$ is the sum of the V8 Climatology profile from 13 to 60 km. The technique is not applied below 13 km to reduce errors introduced by using the climatology ozone profile and to avoid problems due to clouds. .

If the technique were 100% efficient in measuring ozone in the troposphere, the difference between X_{retr} and X_{13}^{0} would be an accurate measure of the difference between the retrieved amount and the amount in the standard profile below 13 km. Since the technique is less efficient, we need to divide the difference by the measurement efficiency to determine the actual change:

$$\Delta X = \frac{X_{retr} - X_{13}^{0}}{\xi_{13}} \tag{41}$$

We can now write

$$X_{13} = \frac{X_{retr} - X_{13}^{0}}{\xi_{13}} + X_{13}^{0} \tag{42}$$

where X_{13} is the actual amount of ozone below 13 km. The efficiency of measuring ozone below 13 km is:

$$\xi_{13} = \frac{\sum_{13}^{60} \xi_{layer} (x_{climatology} - x_{standard})}{\sum_{13}^{60} (x_{climatology} - x_{standard})} \tag{43}$$

where ξ_{layer} represents the measurement efficiencies in each atmospheric layer up to 13 km, $x_{standard}$ is the amount of ozone in a given layer below 13 km in the standard profile, and $x_{climatology}$ is the amount contained in a climatological database. One should note that the efficiency estimate is weighted by the vertical distribution in layer ozone differences between the climatology and the standard profiles for layers below 13 km and not on the difference between total ozone amounts below 13 km.

The database consists of monthly tropospheric ozone amounts on a 1-degree longitude by 1-degree latitude grid. The initial contents have been generated using ozone profile information obtained from balloonsonde as well as satellites such as SBUV, SBUV/2, MLS, and SAGE, and total ozone information from TOMS instruments. Once the OMPS system is in orbit, the database will be updated as

more accurate tropospheric ozone values are determined by the nadir-mapping sensor.

The individual layer efficiencies are determined from

$$\xi_{layer} = \frac{dN_{triplet} / dx}{dN_{triplet} / d\Omega} \tag{44}$$

The layer sensitivities in the numerator are obtained from the sensitivity tables, and the total column ozone sensitivity is calculated when making the initial ozone estimate.

Once the layer sensitivities and ozone amounts have been determined, Equation (44) can be used to determine the actual ozone amount below 13 km, which is used to correct Ω:

$$\Omega = \Omega - X_{13}^{0} + X_{13} = \Omega_{tpcor} + (1+\xi_{13})\frac{X_{retr} - X_{13}^{0}}{\xi_{13}} \tag{45}$$

In cases of totally clouded scenes, the tropospheric climatology will be used to estimate the amount of ozone below the cloud. Some residual error will remain since the tropospheric ozone amount is dependent on the amount of sunlight and the local circulation, and the climatology is determined using estimates derived from clear sunlit scenes.

2.4.9 Multiple Triplet Formulation

To reduce the effects of sensor noise, the above retrieval process is performed for each sensor measurement using 12 different sets of triplets.

The cloud fraction is determined using 4 different ozone-insensitive wavelengths (364, 367, 372, and 377 nm). Then, each of these reflectivity wavelengths is matched to 3 different pairs of wavelengths that form the wavelength triplets used to determine ozone. The choice of triplets depends on their ability to accurately measure ozone for the viewing conditions of the measurement or, in other words, their ozone sensitivity.

From Beer's Law we know that:

$$A = \frac{I}{F} = e^{-s(\alpha\Omega+\beta p)}; \tag{46}$$

$$\Delta A_{\lambda} = -\alpha s e^{-s(\alpha_{\lambda}\Omega+\beta p)}\Delta\Omega; \tag{47}$$

$$\frac{\Delta A_\lambda}{A} = -\alpha s \Delta\Omega \, . \tag{48}$$

The wavelength sensitivity (percent change in albedo per percent change in ozone) is therefore

$$\frac{\Delta A_\lambda / A_\lambda}{\Delta\Omega / \Omega} = -\alpha s \Omega \tag{49}$$

For a pair of wavelengths

$$\frac{\Delta A_p / A_p}{\Delta\Omega / \Omega} = -\Delta\alpha s \Omega \tag{50}$$

where p represents the wavelength pair. The quantity $\Delta\alpha s\Omega$ can therefore be used to assess the sensitivity of each ozone triplet.

Table 2.4-2 shows $\Delta\alpha s\Omega$ as a function of the path length $s\Omega$ between the wavelengths for each of the wavelength pairs that will be matched to the 4 reflectivity channels (the difference is presented since the algorithm uses a pair of wavelengths matched to the reflectivity wavelengths):

Table 2.4-2. Selection of the Multiple Triplets Available to OMPS

SΩ / λ Pairs	0.75	1.00	1.25	1.50	1.75	2.00	2.50	3.00	3.50	4.00	5.00	6.00
308.5 – 321.0	1.96	2.61	3.26	3.92	4.57	5.22	6.53	7.83	9.14	10.44	13.05	15.66
310.5 – 321.0	1.39	1.85	2.32	2.78	3.24	3.71	4.63	5.56	6.48	7.41	9.26	11.12
312.0 – 321.0	1.06	1.41	1.77	2.12	2.48	2.83	3.54	4.24	4.95	**Too Sensitive**	.07	8.49
312.5 – 321.0	0.92	1.23	1.54	1.85	2.16	2.46	3.08	3.70	4.31		.16	7.39
314.0 – 321.0	0.79	1.05	1.31	1.57	1.83	2.09	2.62	3.14	3.66		.23	6.28
318.0 – 336.0	**Too Insensitive**		1.04	1.24	1.45	1.66	2.07	2.49	2.90		.15	4.97
315.0 – 321.0			0.90	1.09	1.27	1.45	1.81	2.17	2.53		.62	4.34
320.0 – 329.0			0.73	0.88	1.03	1.17	1.47	1.76	2.05	2.35	2.93	3.52
322.5 – 332.0			0.54	0.65	0.76	0.87	1.09	1.30	1.52	1.74	2.17	2.61
325.0 – 336.0			0.45	0.54	0.63	0.72	0.90	1.08	1.25	1.43	1.79	2.15
328.0 – 336.0	0.19	0.25	0.32	0.38	0.45	0.51	0.64	0.76	0.89	1.02	1.27	1.53
331.0 – 336.0	0.11	0.14	0.18	0.21	0.25	0.28	0.35	0.42	0.49	0.56	0.70	0.84
316.0 – 329.0	0.73	0.98	1.22	1.47	1.71	1.96	2.45	2.94	3.43	3.92	4.90	5.88
317.0 – 321.0	0.35	0.47	0.59	0.71	0.82	0.94	1.18	1.41	1.64	1.88	2.35	2.82

The clear area in the table indicates which wavelength pairs have ozone sensitivity needed to accurately determine ozone for each atmospheric condition. The path lengths across the top are the maximums for the corresponding bins.

2.4.10 OMPS Channel Selection

The OMPS channels are selected primarily to minimize temperature dependence in the triplet retrieval. The Huggins bands in the near UV display the periodic temperature dependence shown in **Figure 2.4-3**. By choosing short wavelengths at relative minima in temperature dependence and mid-wavelengths at relative maxima in temperature dependence, the impact of changes in local temperature on triplet ozone are reduced. The lines in the figure indicate the possible values of absorption at different short wavelengths that provide zero triplet dependence on temperature for a given mid- and long-wavelength selection. If the actual absorption is higher than that is indicated at a specific wavelength, then choosing this wavelength as the short-wavelength to form a triplet will have positive temperature dependence. (These channels were selected from an arbitrary scale of 0.5 nm steps at even 0.5 nm. They will be reselected at a particular sensor's absolute wavelength scale and reporting interval.) **Figure 2.4-4** shows the resulting sensitivity of the various triplets to a 10 degree shift in the temperature profile at ozone absorbing altitudes. Note that the selection of 321 nm as a short wavelength creates a triplet with strong temperature dependence that can be used to monitor temperature sensitivity and therefore temperature corrections. The specific choice of long wavelength has little or no effect on these results.

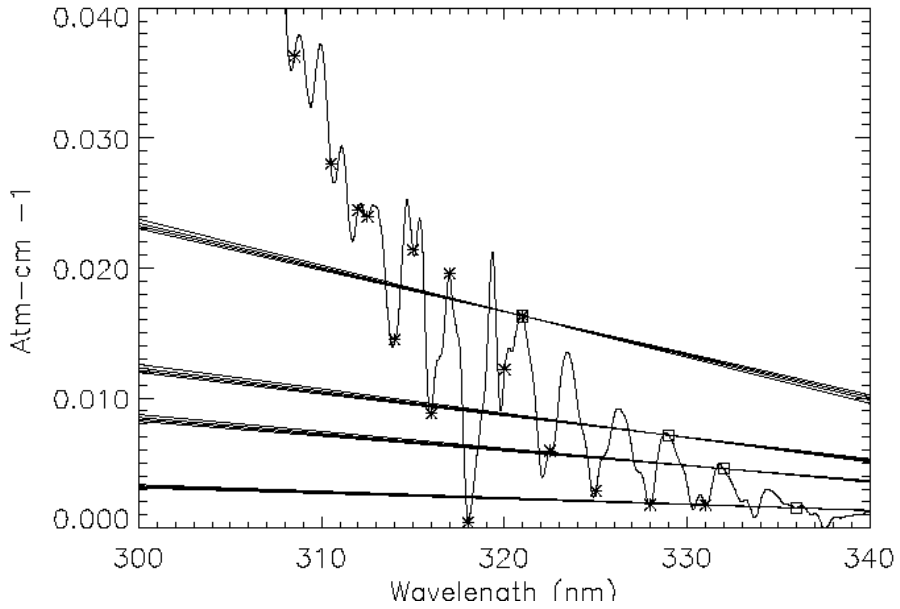

Figure 2.4-3. Impact of temperature changes on OMPS triplet channels

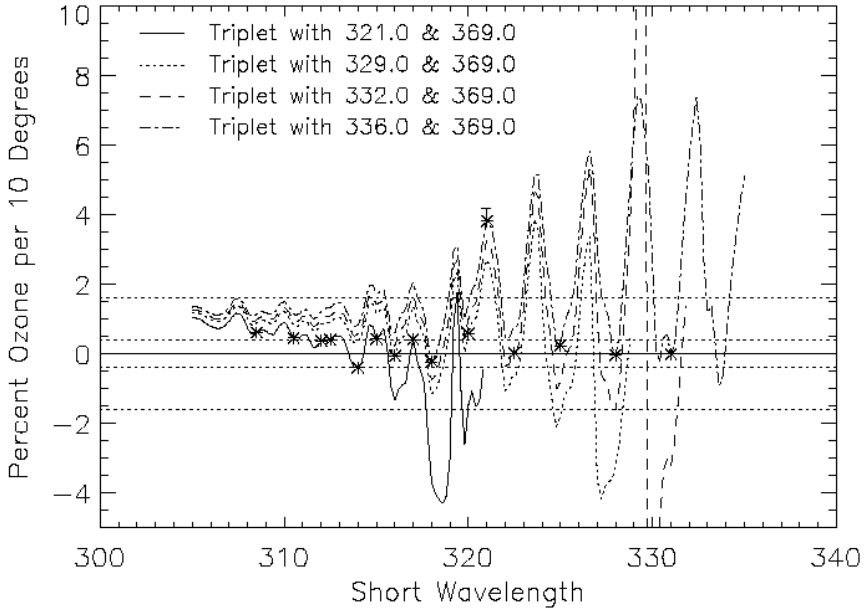

Figure 2.4-4. Impact of temperature changes on OMPS derived total ozone

Since the extreme in the temperature dependence are also extreme in the absorption (local absorption maximum corresponds with local minimum in temperature

dependence), this selection procedure also minimizes sensitivity to shifts in the spectral scale. See **Figure 2.4-5**.

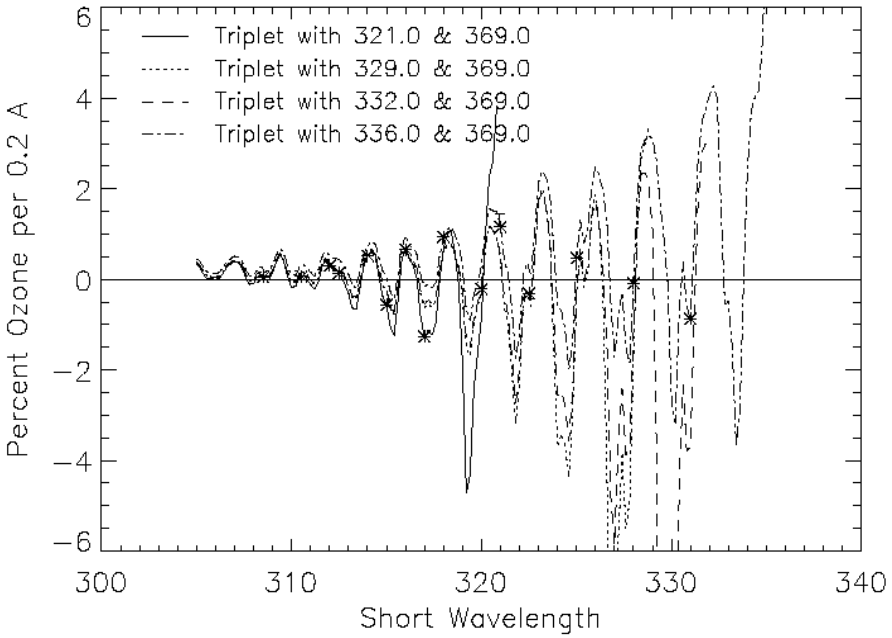

Figure 2.4-5. Impact of wavelength shift on OMPS derived total ozone

A third criterion for channel selection is minimization of the Ring effect. The OMPS channel selection is indicated in **Figure 2.4-6**, which also shows the nominal Ring effect for clear conditions. The Ring effect is the result of rotational Raman scattering, which modifies the wavelength of the scattered light and fills in spectral features (Fraunhofer lines) present in the incoming solar flux. Note that the Ring features are anti-correlated with the features of the relative solar flux included to illustrate this relationship. Because it is scattering induced, the Ring effect is pressure dependent. In general, the Ring effect is quite complicated to model. In the OMPS forward model, only a simple first order correction based on the pressure dependence is made in order to conserve processing time associated with a complete treatment of this complex problem. This is why channels are selected to minimize Ring dependence. As in the case of temperature dependence, two channels (316 and 317 nm) have also been selected to maximize the effect so that the Ring correction can be monitored.

The selection of long wavelength channels is also effected by O_4 absorption. The abundance of O_4 (the O_2 - O_2 collisional complex) is proportional to the pressure squared, so it occurs close to surface. The effect of O_4 absorption has been studied and found to be less than 0.1% for the OMPS wavelengths.

We note that the 360 nm and 380 nm channels are the heritage reflectivity channels for the EP/TOMS and the Nimbus7 TOMS respectively. Since O_4 absorption is affecting both of these channels, it is likely that GSFC/NASA will study these absorption features in the near future and suggest corrections to the retrieved ozone.

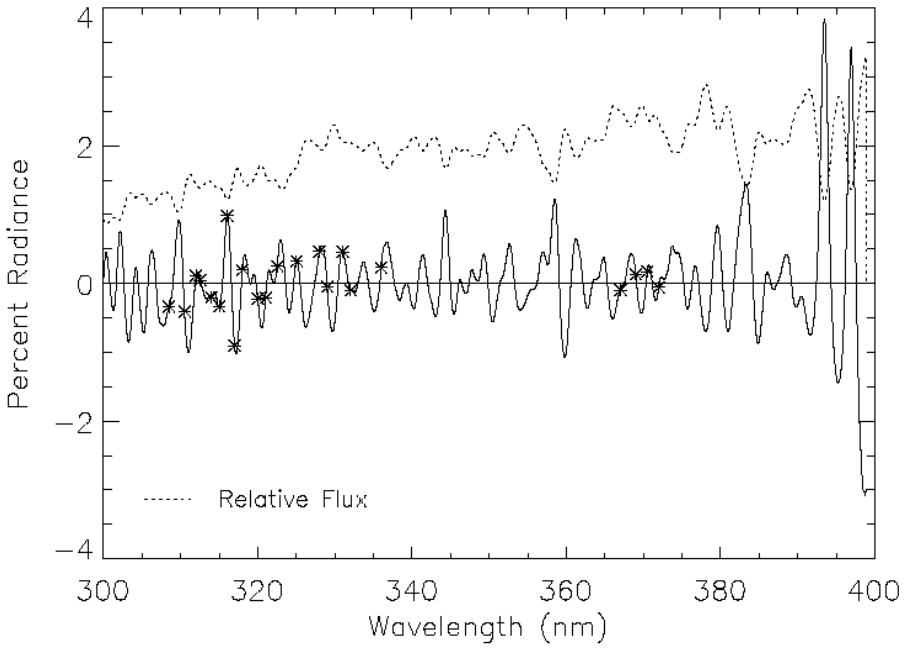

Figure 2.4-6. Impact of Ring effect on the OMPS channels

Our channel selection scheme represents a significant improvement over the heritage channels as well as other potential schemes. Our selections for the OMPS channels have lower sensitivity to temperature effects and wavelength calibration shifts, as well as smaller Ring dependence. They maintain adequate separation between the long- and mid-wavelength channels to give sufficient sensitivity to the wavelength dependent scattering effects of tropospheric aerosols. The 312.0 nm channel provides increased sensitivity to SO_2, which is important for volcanic hazard detection.

2.4.11 Volcanic SO_2

Because of the similarity in absorption coefficients between O_3 and SO_2, the presence of SO_2 due to volcanic eruptions causes an error in determining ozone. The OMPS total column algorithm, while not designed to derive quantitative values for SO_2 amounts, does determine approximate SO_2 amounts. These values serve as

flags to indicate the presence of SO_2 from volcanic eruptions and, therefore, an error in ozone determination.

After performing an ozone retrieval, the algorithm determines if there is any volcanic SO_2 present in the atmosphere by performing a Taylor series expansion about the retrieved ozone amount, Ω_{ret}:

$$r = N_m - N_{ret} = (\Omega - \Omega_{ret})\frac{dN}{d\Omega} + S\frac{dN}{dS} + a + b\lambda \tag{51}$$

where S is the amount of SO_2 in the atmosphere (because there is normally no SO_2 the initial estimate, S_0, is zero), N_m is the measured N value for a given wavelength, N_0 is the N value for that wavelength calculated from the tables, Ω is the true ozone in the atmosphere, and the a + bλ term accounts for linear wavelength dependencies (either from calibration or atmospheric effects). We now have 4 unknowns, and we need 4 wavelengths to construct the 4 equations necessary to solve for S.

Along with one of the reflectivity wavelengths, the 317, 331 and 336 nm wavelengths are chosen to solve for SO_2. These wavelengths occur either at local maxima or minima with respect to the SO_2/O_3 cross-section ratio and were selected based on the conclusions in Gurevich and Krueger (1997) that such a choice optimizes the retrieval of SO_2.

The ozone sensitivities, $dN/d\Omega$, are determined internally in the course of deriving Ω_{ret}. The SO_2 sensitivities are approximated by

$$\frac{dN}{dS} = \frac{\alpha_{SO_2}}{\alpha_\Omega}\frac{dN}{d\Omega} \tag{52}$$

where α_{SO2} and α_Ω are the absorption coefficients for SO_2 and ozone for the given wavelength. Since the algorithm is designed to detect contamination from volcanic eruptions, α_{SO2} and α_Ω are chosen so that the algorithmic sensitivity to SO_2 for a volcanic plume is large. The SO_2 absorption coefficients are therefore chosen for a temperature of 210 K, which is the temperature of many volcanic plumes, and the ozone absorption coefficients are chosen for a temperature of 223 K, which is the nominal temperature of the ozone maximum.

There are four unknowns in the Taylor series expansion (Ω, S, a, and b). Using the OMPS reflectivity wavelengths with no ozone or SO_2 absorption (377 nm, for example), the four unknowns can be reduced to three by writing the a term as a function of the b term. The other 3 wavelengths are then used to solve the resulting three equations for S. Four estimates of S can be made using the 4 reflectivity wavelengths, thereby reducing the effects of sensor noise.

It should be noted that these equations can be used to simultaneously solve for the "uncontaminated" ozone amount Ω as well as S. However, since the SO_2 sensitivities are approximations designed to be most effective for volcanic eruptions, their use leads to errors in the calculation of Ω. Furthermore, the similarity in absorption between ozone and SO_2 also contribute to the errors when simultaneously retrieving both quantities. For these reasons, this algorithm is not used to determine ozone but, rather, to detect the presence of volcanic SO_2.

Because these errors exist in the calculation of S, it is reported not as the actual SO_2 amount but as an index indicating contamination. We call S the SO_2 index (SOI).

Determination of the SO_2 Contamination Flag Value. The calculation of SOI is not exactly zero in the absence of volcanic SO_2 but is, instead, distributed about zero in a peak whose standard deviation (σ) depends on the noise of the algorithm-sensor system and the approximations discussed above.

ADEOS TOMS is an example of a modern TOMS instrument that uses the above algorithm to flag data contaminated with SO_2. Since the calibration has been finalized and the data have been recently archived, we use it to serve as an example of how the data was flagged in the heritage Version 7 algorithm and how we plan to set this flag for OMPS. **Figure 2.4-7** shows a histogram indicating the frequency of SOI values calculated for March 20, 1997. This date, which represents a background day with no volcanic SO_2, was chosen because of the maximum latitudinal coverage of the data. The histogram is sharply peaked about zero with a σ of about 3 Dobson Units. For the TOMS the SO_2 contamination flag was set for any value of SOI greater than 4σ. In the case of ADEOS TOMS, this is 12 Dobson Units.

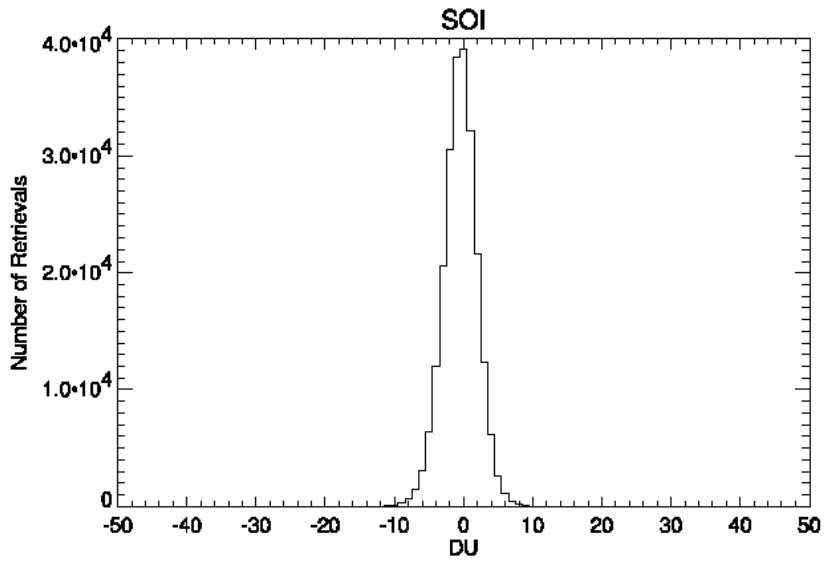

Figure 2.4-7. Distribution of SOI for ADEOS TOMS, Mar. 20, 1997

Figure 2.4-8 shows the number of retrievals flagged as contaminated by SO_2 for each day of the 10 month ADEOS TOMS data record. It indicates that the flagged samples represent less than 0.01% of the total number of samples for a given day.

It should be noted that there was volcanic SO_2 contamination due to the eruption of Nyamuragira in December 1996. The number of retrievals contaminated by SO_2 due to this eruption, however, is small (approximately 10-20 measurements per day) and is barely discernable in Figure 2.4-8. A contaminated plume can be seen on a map showing the global distribution of SO_2 in latitude and longitude. In such a map, the cluster of contaminated values due to the volcanic eruption can be easily picked out from the rest of the flagged values that are scattered randomly.

Simulations of the SOI algorithm using the OMPS algorithm, wavelengths, signal-to-noise ratio, and slit functions indicate an SOI σ of approximately 1.5 DU. With 4 measurements of SOI this value can be further reduced by a factor of 2 to 0.75. An SOI flag set at 3 DU would lead to an equivalent percentage of the data eliminated as in TOMS. It should be emphasized that the SOI algorithm is not precise enough to provide a quantitative correction to the ozone amount. It can, however, be reliably used to flag volcanic SO_2 contaminated retrievals.

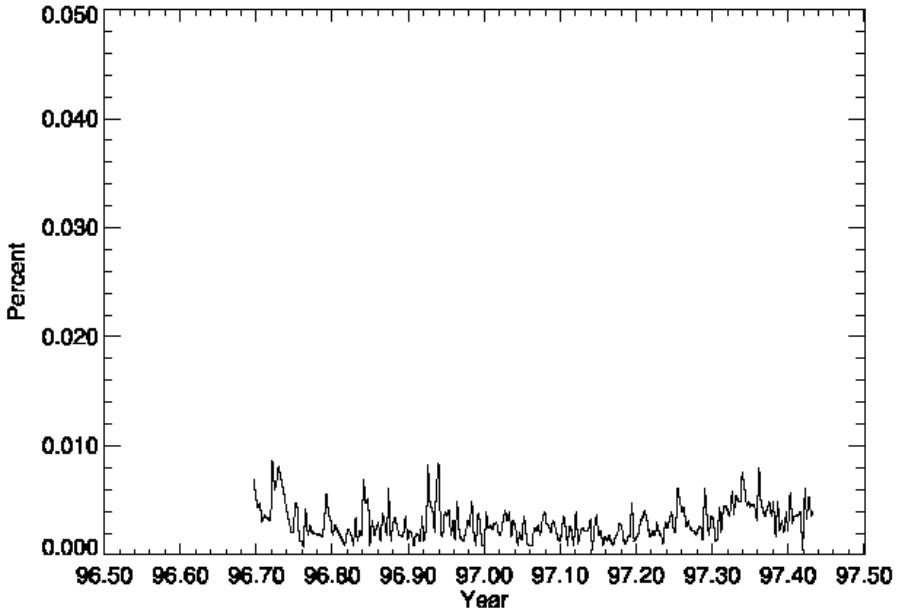

Figure 2.4-8. Percentage of ADEOS TOMS daily retrievals flagged as SO_2 contaminated

2.5 ERROR SOURCES

Table 2.5-1 summarizes the sources of error in the total column algorithm. Section 7 provides more detail about each error and how it affects the algorithm.

Table 2.5-1. Factors Contributing to the Accuracy and Precision Error Budgets

Sensor Accuracy	Algorithm Accuracy
Wavelength dependent albedo calibration Wavelength independent albedo calibration Pixel-to-pixel calibration (includes linearity) Wavelength calibration Wavelength shift Polarization Out-of-field stray light Out-of-band stray light	Rayleigh scattering coefficients Absolute ozone absorption coefficients Temperature dependent ozone absorption coefficients Tropospheric aerosols Cloud top pressure Table pressure interpolation Non-homogenous scene (including clouds vs. snow/ice) Ozone profile shape Multiple scattering Ring effect Interpolation
Sensor Precision	**Algorithm Precision**
Radiance noise Solar calibration noise	Tropospheric ozone Temperature dependent ozone absorption coefficients Cloud-top and surface pressure Cloud fraction (non-homogeneous scene) Ozone profile Tropospheric aerosol correction

3 Algorithm Description

3.1 SDR DATA PRODUCTION

This section describes the contents of and process by which Sensor Data Records (SDRs) are generated from the input Raw Data Records (RDRs). The two basic RDR types, Earth view and calibration, are processed separately by the SDR algorithm. The primary products of calibration processing are calibration SDRs and databases that store the results of calibration analyses. These databases are subsequently used during Earth data processing to adjust the spectral and radiometric calibrations of those data. **Figure 3.1-1** illustrates the major processing components of the SDR algorithm. The basic components of SDR processing: signal correction, calibration analysis, and calibration application, are all automated. Intervention is required for anomalies.

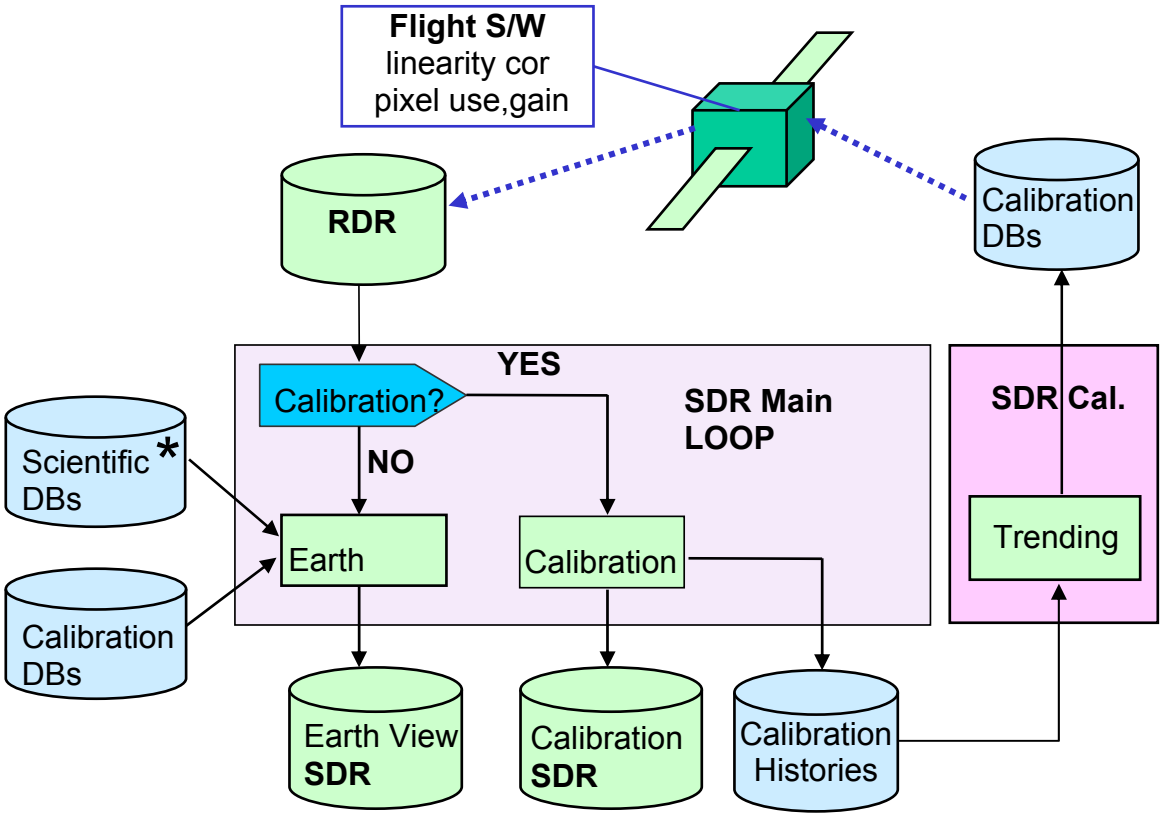

Figure 3.1-1. Schematic Showing SDR Generation

3.1.1 SDR algorithm Inputs and Outputs

The SDR algorithm processes the input RDR data into two separate output SDR files (SDFs): calibration and Earth. The Earth SDF is made available to the EDR algorithm for further processing. The calibration SDF remains as an archival SDR product. An SDF of either data type is a snapshot of the observations and data processing within a particular time.

The SDR algorithm processes individual RDRs of any data type in any data type order, as long the RDRs are time ordered. The SDR algorithm separates the Earth RDRs from the calibration RDRs, processes them separately, and then stores them in separate output calibration and Earth SDFs. The algorithm assumes that all calibration RDRs from a calibration sequence are in the same RDF, though Lamp, Solar, and Dark RDR data can be in separate RDFs from each other, or they can be in the same input RDF. It makes no difference: all calibration RDRs in an RDF are processed and written to a single output calibration SDF. Alternately, the algorithm writes Earth SDRs grouped by day into an SDF for those input RDRs with the same common observation day. Thus, for an orbit spanning two days, the algorithm produces two separate earth SDFs, one for each day.

Each SDF is primarily an archival product containing raw counts, count corrections, measurement precisions, and calibrated values: radiances for Earth and count rate for solar. We designed the earth and calibration SDFs to contain all the information necessary, under normal circumstances, for a retrospective processing of SDF data into EDRs. As such, an SDF contains all calibration factors and identifies the ancillary information needed to convert raw sensor counts to calibrated radiances.

In addition to the two types of output SDFs, the SDR algorithm stores cumulative histories of the calibration observations in a separate set of databases, some of which are used in subsequent SDR processing for trending and signal processing corrections.

The inputs and outputs described in this ATBD are provided in narrative form for a qualitative description of functionality only. For a detailed description of the TC SDR algorithm input and output data files and their contents, please refer to the Operational Algorithm Description Document for the OMPS Total Column SDR algorithm Software (D39310)

3.1.1.1 Inputs to the SDR algorithm

The SDR processing of both calibration and Earth data *together* uses the following input sources:

- RDR headers and data records

- Spacecraft diary ephemeris and attitude with times
- BATC generated databases of utilized pixels (sample tables)
- BATC generated timing pattern table
- Band center wavelength table
- Spectral response bandpass shape table
- CCD pixel look angle table
- Sensor diffuser irradiance goniometry characteristics (BRDFs) table
- Linearity correction table
- Stray-light correction table
- Radiance and irradiance calibration coefficient tables
- Baseline solar irradiance observed by OMPS early in the mission
- Standard high spectral resolution solar flux
- Wavelength fitting parameters and wavelength shift lookup table
- EDR products from other NPOESS sensors, including:
  1. Atmospheric profiles of temperature and pressure – CrIMSS
  2. Cloud cover fraction – VIIRS
  3. Cloud top pressure – VIIRS
  4. Snow/ice fractional surface coverage – VIIRS
     - Sea Ice Characterization - VIIRS
     - Snow Cover/Depth – VIIRS
  5. Quarterly Surface Type Gridded IP - VIIRS

- Climatological databases, including:
  1. Terrain pressure
  2. Cloud top pressure
  3. Snow/ice surface coverage fraction
  4. UV reflectance
  5. Tropospheric ozone column
  6. South Atlantic Anomaly radiation level
  7. TOMS V8 temperature profile climatology
  8. TOMS V8 Ozone profile climatology

External data, either static climatology values or dynamic EDRs from other NPP/NPOESS sensors, are stored in each Total Column SDR record at each spatial location. Actual observed EDR data values, when available, supersede the climatological values. In order for an SDR to be an archival product, the external data, including the EDRs, must be input to the SDR (see Fig. 1.1- 1). The co-location of the external EDRs with OMPS data cells is performed as part of SDR processing and is based on time tags and geolocation. The threshold horizontal and vertical cell sizes specified by the VIIRS, and CrIMSS design documents are sufficient for OMPS resolutions.

3.1.1.2 Outputs from the SDR algorithm

The SDR processing creates two types of products: SDFs, calibration databases. All begin with an ASCII file header containing identifying information. In the case of SDFs, this is known as the major header.

The SDR algorithm writes the following information into the header of each OMPS TC SDR product:

- Spacecraft identification tag
- Sensor identification tag
- SDR product identification tag
- Flight software version
- RDR software version
- SDR software version
- Generation date and time
- Ancillary data file names and version numbers (Timing Pattern and Sample Tables)

3.1.1.2.1 Earth - Sensor Data Files (SDFs)

An SDF can cover any length of time, but because downlinked RDR data must be sorted and ordered sequentially prior to SDR algorithm processing, the nominal coverage of an operational RDR File (RDF) and its associated SDF is one full orbit.

The Earth SDFs contain all of the Earth view data, observation information, and the state of the Nadir Sensor that the TC EDR algorithm needs to produce EDRs. An SDF also contains sufficient information to permit a complete reprocessing by the SDR algorithm, if necessary. Thus, uncorrected radiometric counts are included in the file, as well as calibrated radiances in the Earth SDFs. Conversions of the initial sensor status data and geolocation data are unlikely to be repeated, so their precursors are not saved in the SDF.

Both Earth and calibration SDF files contain a 1) major header, 2) major record data, 3) minor headers, and 4) minor record data. The first two occur once, at the beginning of an SDF. They include information and data that remain constant for the period covered by the file. A sensor data record (SDR) for a particular observation consists of the minor header and minor record data. There are approximately 400 SDRs in each SDF.

SDF MAJOR RECORD DATA – Earth

The following data are written into the major Earth SDF record:

- Number of SDRs in the SDF file
- Bandcenter wavelength registration for the beginning day of the Earth observations in the SDF
- Calculated solar irradiance flux density at the OMPS wavelengths
- Radiance calibration for the current day of the Earth observations
- Dark current correction data
- Electronics Bias data

MINOR RECORD (SDR) HEADER – Earth

The minor record is associated with a group of spatial data cells representing one report period. Each minor record contains a header and data record. The following information is written in the minor record header:

- Unique SDR identification tag
- Logical sequence number
- Operation mode
- Date and time at start & end of period
- CCD integration time
- Input RDR data quality flags
- Input RDR header information
- Subsatellite latitude and longitude at start & end
- Spacecraft altitude at start & end
- Solar right ascension at start & end
- Solar declination at start & end
- Spacecraft-centered solar azimuth at start & end
- Spacecraft-centered solar elevation at start & end
- Spacecraft geocentric position (X,Y,Z) and velocity (V_x, V_y, V_z) at start & end
- Spacecraft attitude (difference from nominal; in Roll, Pitch, Yaw) at start & end

MINOR RECORD (SDR) DATA – Earth

The following data are written into the minor data record:

- Data and processing quality flags
- Radiation anomaly flags (SAA, solar eclipse, and sunglint)
- External data source flags
- Sensor status data
- Intra-orbital spectral shift coefficients (unimplemented)
- Field-of-view (FOV) Latitudes, Longitudes for each spatial cell
- FOV angles for solar zenith, satellite zenith, and relative azimuth
- Terrain pressures – climatology database
- Cloud top pressures – VIIRS *or* climatology

- Cloud coverage fractions – VIIRS *or* flagged as missing
- Snow/Ice coverage – VIIRS *or* climatology database
- UV reflectance – climatology database
- Temperature profiles – CrIMSS or NCEP/climatology
- Pressure profiles – CrIMSS
- Ozone profile amounts - climatology
- Tropospheric Ozone columns – climatology
- Raw RDR sensor counts
- Calibrated Earth radiances
- Smear correction data

3.1.1.2.2 Calibration - Sensor Data Files (SDFs)

An output calibration SDF contains all of the sensor calibration data for one input RDF dataset. Sensor calibrations include solar, lamp, and dark measurements. If one or more of these is contained in an RDF, a single output SDF is produced. The calibration SDF contains sufficient information to permit a complete re-analysis of sensor calibrations. Thus, uncorrected sensor signals are included in the file, as well as corrected calibration signals. Conversions of the initial housekeeping data and geolocation data are unlikely to be repeated, so their precursors are not saved in the SDF.

As with Earth SDF files, calibration SDFs contain a 1) major header, 2) major record data, 3) minor headers, and 4) minor record data. The first two occur once, at the beginning of an SDF. They include information and data that remain constant for the period covered by the file. A sensor data record (SDR) for a particular observation consists of the minor header and minor record data. The number of SDRs in a file varies with the calibration schedule, but is unlikely to exceed 400.

SDF MAJOR RECORD DATA

The following data are written into the calibration SDF major record:

- Bias correction values
- Dark signal correction values
- Pixel map of current good and bad pixels
- Wavelengths currently used
- Flat Field current values
- Current solar count rate
- Reference solar irradiance
- Number of SDRs in the SDF file

MINOR RECORD (SDR) HEADER – solar, dark, or lamp data

The minor record contains data for one report period. Each minor record contains a header and data record. The following information is written in the minor record header:

- Unique SDR identification tag
- Logical sequence number
- Operation mode
- Date and time at start & end of period
- CCD integration time
- Diffuser position code
- Input RDR data quality flags
- Input RDR header information
- Spacecraft geocentric position (X,Y,Z) at start & end
- Spacecraft attitude (difference from nominal; in Roll, Pitch, Yaw) at start & end
- Solar right ascension at start & end
- Solar declination at start & end
- Spacecraft-centered solar azimuth at start & end
- Spacecraft-centered solar elevation at start & end
- Subsatellite latitude and longitude at start & end
- Spacecraft altitude at start & end

MINOR RECORD (SDR) DATA – solar, dark, or lamp data

The following data are written in the minor data record:

- Data and processing quality flags
- Radiation anomaly flags – SAA and solar eclipse
- External data source flags
- Sensor status information
- Raw RDR counts
- Smear data
- Solar-Orbital Plane Beta angle at start & end
- Goniometric correction factors
- Corrected counts

3.1.1.2.3 Databases

The calibration SDR processing produces an extensive set of databases that are used as input to 1) Earth SDR processing, 2) SDR algorithm trending, 3) generating uplink tables to flight software, or 4) off-line data quality and calibration analyses. All are history databases with the newest information appended to the end of a file. If

calibration data is missing from the current RDF, the most recent entries in the calibration databases are used to process the RDR data. The databases are keyed by year and day of year.

Each record of the database histories contains coadded data. When possible, bad pixels are excluded from coadded data, except for dark data, which is used to identify bad pixels. Dark data obtained during the passage of the satellite through the terrestrial SAA are stored separately from other dark data. It is assumed that Lamp data are not acquired through the SAA. Throughout the SDR algorithm description, we refer to these databases by their logical names. The algorithm produces the following direct databases while processing calibration data.

- BIASES – detector electronic offset in counts
- DARKS – detector dark signal in counts
- SAA_DARK – during South Atlantic Anomaly, detected dark signal in counts
- LAMP - lamp signals in counts and count rates
- LINEARITY - detector linearity table
- RAWFLUX - solar signal corrected for detector and normalized by the baseline solar signal
- FLUX - same as RAWFLUX but corrected for detector spectral shifts
- WMON - bandcenter wavelength shifts relative to the baseline solar measurement

The generation of these primary history databases is described more fully in Section 3.1.3.4., but the record entries for all the above databases are created directly from processed calibration RDFs. Both BIASES and DARKS are updated for every input RDF containing coadded dark RDRs. To permit further data trend analyses, the observation time-averages of the sensor status information in the RDR header, are also stored in the listed databases, except for the LINEARITY database. An initial laboratory characterization of the linearity is stored in the LINEARITY database for the first operational processing of flight data. If the initial entry is missing, and if input Lamp RDR data are supplied, the algorithm will correct properly subsequent data, because LINEARITY is updated when Lamp data are processed. The remaining databases are updated when Solar RDR data are processed.

From these primary databases, the SDR algorithm also creates a set of derived databases that contain analysis results such as trending. Due to the infrequency of calibration operations, the algorithm relies upon radiometric and spectral calibration values that are extrapolated from trended fits to the actual calibration observations. The databases contain quantities for each pixel or a binned set of pixels on the CCD image. The generation of these databases is described more fully in Section 3.1.3.5.

- BADPIXELS - bad pixel severity for each pixel on detector
- LINEARITY - detector linearity
- CF_EARTH - radiometric calibration factors for the Earth scene spatial cells
- CF_SOLAR - radiometric calibration factors for the solar illuminated pixels

- WAVELENGTHS - bandcenter wavelengths corrected for solar doppler shift
- FLATFIELDS - relative multiplication factors for each pixel used in binning for an Earth spatial cell. These are locally normalized to unity for each Earth data cell.

3.1.1.2.4 Uplink Files

The SDR algorithm produces two calibration products for use in creating OMPS TC upload tables. The contents of these tables are processed outside of the SDR algorithm for upload to the flight hardware and software and are used for on-board signal corrections and pixel use and rejection. The LINEAR_UPLOAD file is updated concurrently with LAMP calibration databases, whereas the FLAT_UPLOAD file is updated for each change of day of Earth input RDR data. Flight software tables should be generated using these files, with human-in-the-loop, and it remains an operational decision whether or not to upload new ones. In addition, the SDR algorithm produces bad pixel databases containing information of suspected new bad pixels detected from the new calibration data. These databases are reviewed outside of the operational SDR algorithm, and once these suspected bad pixels are confirmed, the EV_sampletable will be updated for uploading to the flight hardware and software.

It should be emphasized that both bad pixel tables and linearity tables used by the operational SDR algorithm should always be checked for consistency with the flight software. An update to the EV_sampletable LUT or the linearity LUT in the ground processing should not happen unless it has been detected from the earth view RDR engineering data that the flight versions of these tables have been updated. The update to these LUTs is a controlled process, and the SDR algorithm is not allowed to update these LUTs on its own.

3.1.2 Earth View Processing

The processing goal is to obtain for each observed Earth spatial data cell, a calibrated Earth radiance spectrum, observation angles, and geolocations, as well as matching NPOESS external data and climatological data. These constitute the set of data needed by the TC EDR algorithm for ozone column calculation. **Figure 3.1-2** shows the flow for processing each raw data file (RDF) containing multiple Earth view RDRs. The description that immediately follows is an overview of the processing. Detailed discussions of the processes, corresponding to the individual elements in Figure 3.1-2, are contained in subsections.

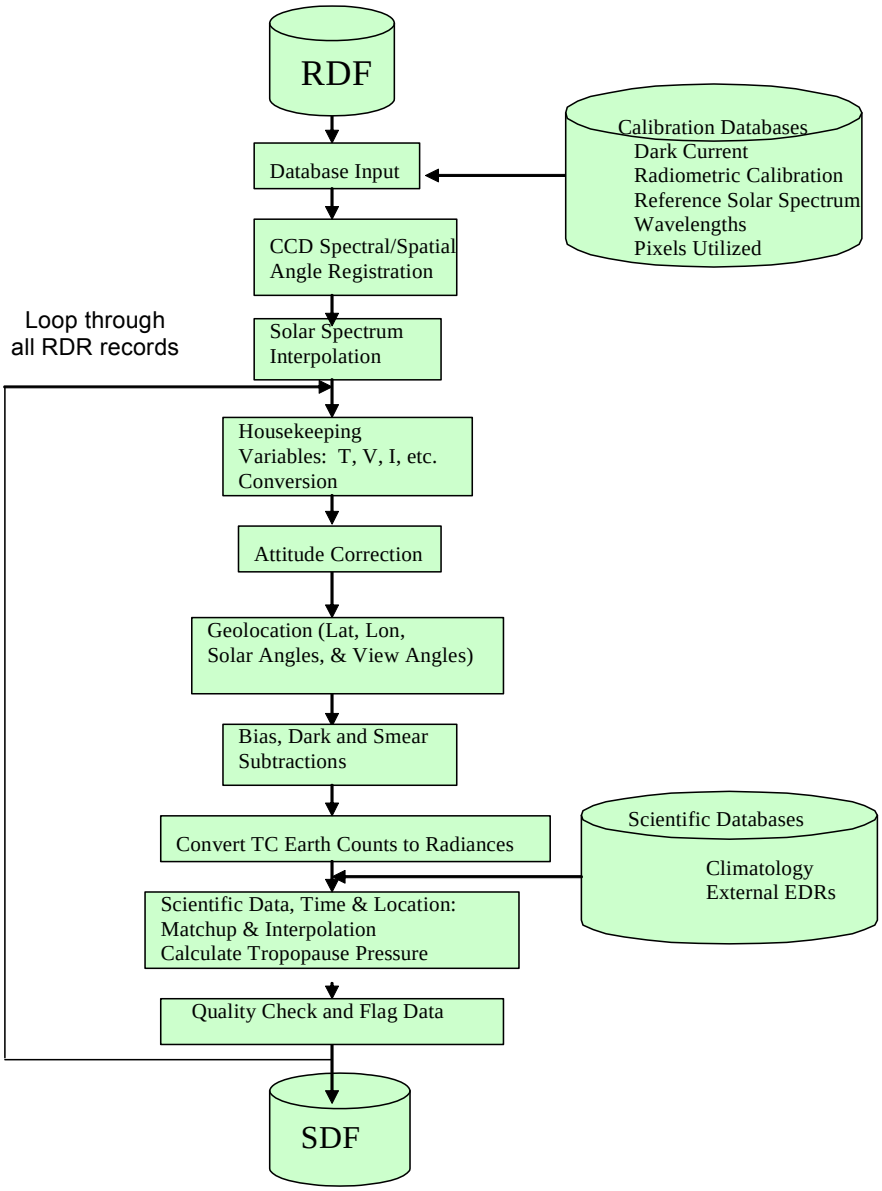

Figure 3.1-2. Schematic showing Earth View SDR generation process

The OMPS TC flight hardware corrects sensor signals for non-linearity and relative pixel response. The TC flight software then bins pixels in the spatial dimension to create a macropixel. A macropixel is typically made up of 20 individual pixels, except when bad pixels are excluded and the two edge macropixels which may have more than 20 pixels. Bad pixel identification is based upon the EV_sampletable LUT. Thus, for each RDF containing Earth data, the algorithm reads the concurrent EV_sampletable, which is always checked to be consistent with the flight software. All ground processing of Earth data excludes bad pixels from the operations, whenever

possible. The remaining signal corrections and calibrations are then applied during ground processing of RDRs into SDRs, using pre-computed databases, except for the exposure smear correction, which uses signals accompanying the earth scene data.

At the start of the Earth SDR processing, the Total Column SDR algorithm reads the CCD map of pixel optical angles, sensor radiometric calibration coefficients, EV sample tables, and ingests an RDF containing the Earth RDRs. Then, for the current day of the Earth RDR data, the SDR algorithm reads both the wavelength database and the Earth radiance calibration factors database, whose values are written into the output SDF major record. Note that the SDR algorithm performs these initial processing steps for different days in an RDF. Therefore, RDFs that contain data from two days are split by day into separate output SDF files.

The remainder of the processing is executed many times: once for each RDR minor record (i.e., set of radiance observations) within an RDF. One input RDR corresponds to one output SDR. After reading the header data from an RDR, the algorithm performs limit checks on both the sensor status data and the CCD data, the flagging results of which are then written into the SDR along with the sensor status data. Next, the algorithm reads the spacecraft diary for attitude and ephemeris and interpolates them to the times of the OMPS RDR observations. With the OMPS mounting angles and attitude deviations, the algorithm obtains the OMPS sensor true attitude, with which it geolocates the Earth spatial data cells by the begin and end observation times. The average geolocation and scattering angles are recorded in each SDR.

Importantly, the SDR algorithm corrects the initial Earth view signal output from the OMPS sensor by removing bias, dark, and smear signals. With the corrected counts, the algorithm then converts the Earth counts to radiance, using binned calibration coefficients and radiance calibration factors, as well as the integration time. It should be pointed out that due to the fine structures in the solar diffuser, calibration factors computed from the solar data may not have the desired accuracy to be used in radiance calibration. Therefore, we have added a switch to the algorithm to allow the operator to decide whether to use the calibration factor or not when converting counts into radiances.

Following the radiance calibration, the algorithm can perform the optional stray-light correction. Details of stray-light correction is discussed in section 3.1.2.8

The next step is to match all external data (climatology and external EDRs.) in time and location to the TC earth view observations and interpolate, if necessary, in time and space. Finally, the algorithm checks and sets quality flags, particularly for the satellite passing through the South Atlantic Anomaly (SAA) radiation zone, viewing the Earth at solar eclipses, and viewing the Earth at sun glint angles. Additional flags for good pixel percentage, as well as wavelength and radiance ranges are checked and set. After the algorithm processes all RDRs within the RDF, it writes the calibrated Earth radiances and all supporting data into the SDF.

3.1.2.1 Database Input

The following database information is read for use during Earth data processing:

- Macropixel sample table LUT – CCD map of EV macropixels
- EV_sampletable LUT – CCD map of EV macropixels including bad pixels
- SC_sampletable LUT – CCD map of solar calibration pixels
- LED_sampletable LUT – CCD map of LAMP pixels
- Timing pattern LUT – integration time, number of co-adds, and number of frames for each data type (EV, DARL, LAMP,SOLAR)
- Bias signals for both image halves (BIASES)
- Most recent dark signals for each macropixel (DARK or SAA_DARK)
- Radiometric calibration factors for current day (CF_EARTH)
- Radiometric calibration constants
- Baseline solar irradiance (RAWFLUX)
- Bandcenter wavelengths of each macropixel for current day (WAVELENGTHS)
- Detector map of pixel optical angles
- Atmospheric and Surface Climatology (monthly, global grids); space radiation SAA map
- Other NPOESS EDRs (VIIRS, CrIMSS)

3.1.2.2 CCD Spectral and Spatial Registration

The goal of the registration is to assign a wavelength and two angles for each data cell. The initial laboratory CCD spectral and spatial maps exist for every illuminated CCD pixel. The SDR algorithm bins and averages the laboratory calibration maps for wavelength into the same data samples as Earth data. Because the spectral calibration excludes bad pixels, the registration does not need to adjust for deleted pixels.

The spatial registration contains CCD pixel look angles and is used to compute the pointing direction (unit vectors) of each individual CCD pixel in the sensor cube coordinates. These unit vectors are then combined according to the EV sample table to calculate the overall Line Of Sight (LOS) for each EV macropixel., which is later used by the common geolocation algorithm to geolocate the EV data location.

The wavelengths of the binned Earth data are read from the WAVELENGTHS database. If calibrated wavelengths are missing, the Earth data are flagged accordingly. Slight distortions of the focal plane on the CCD cause the pixel bandcenter wavelengths to vary slowly across the spatial dimension, resulting in different spectral registration for every Earth macropixel. The spectral registration includes a daily correction for instrument-induced spectral shifts, as well as Doppler shifts caused by OMPS satellite motion toward the Sun. We also anticipate that the spectra will be subjected to uncorrected intra-orbital wavelength shifts due to thermal fluctuations. However, thermal models indicate these shifts are within the spectral

registration error allocation. We have investigated strategies to characterize these additional shifts, but they are not currently part of the baseline algorithm.

3.1.2.3 Housekeeping Data

Sensor housekeeping data generally include information from thermistors as well as any feedback from mechanical systems, command verification, etc. Most housekeeping data, particularly from thermistors, are telemetered in raw form. The SDR algorithm assumes that the NPOESS processing environment uses predetermined conversion factors provided by the OMPS sensor contractor to convert the housekeeping data into sensor status data that resides in each RDR. These status quantities within an RDR are copied and written by the SDR algorithm into the corresponding output SDR.

3.1.2.4 Solar Irradiance Spectrum

Because the TC EDR algorithm uses Earth radiances normalized by solar irradiances as its primary data, each SDF contains a solar irradiance spectrum along with the measured Earth radiances. One should note that neither the SDF radiances nor the SDF irradiances are fully calibrated products. Only the normalized radiances, in which sensor effects and solar flux changes cancel, fulfill that requirement. The SDR algorithm does not compute normalized radiances due to the potential for radiance and irradiance measurements to be measured with different spectral scales. Instead, the algorithm determines the solar irradiance $F^m(\lambda)$ at the time of an Earth observation by correcting the baseline TC solar spectrum $F^m(\lambda^r)$ for subsequent changes in the sensor spectral registration.

During calibration trending the SDR algorithm computes a factor γ for each macropixel in order to estimate $F^m(\lambda)$.

$$F^m(\lambda) = \gamma F^m(\lambda^r) \tag{53}$$

The computation of γ is described in Section 3.1.3.5.9. These factors, registered by day, are read in from the WAVELENGTHS database. The Algorithm computes baseline solar irradiance values $F^m(\lambda^r)$ from pre-launch irradiance calibration constants k^i and values T_o read in from the RAWFLUX database.

$$F^m(\lambda^r) = k^i T_o \tag{54}$$

The SDR algorithm writes the solar irradiance values $F^m(\lambda)$ into the Earth SDF major record.

3.1.2.5 Geolocation

Like other sensors, the geolocation of OMPS SDRs is done in two steps, the sensor specific geolocation and the common geolocation. In the sensor specific geolocation algorithm, which is part of the OMPS TC SDR algorithm implementation, the LOS unit vector in the instrument coordinate is computed from the sensor CCD pixel spatial registration table. Details are discussed in section 3.1.2.5.2. In the second step, the common geolocation algorithm, which is not part of the OMPS SDR algorithm implementation, uses the LOS vectors to compute the projected earth piercing location for each measurement. The actual implementation of the common geolocation algorithm is beyond the scope of this ATBD and if interested, should be referred to the ATBD for the common geolocation algorithm. Nonetheless, the discussion in this section contains information pertinent to the common geolocation and such information is included for reference only.

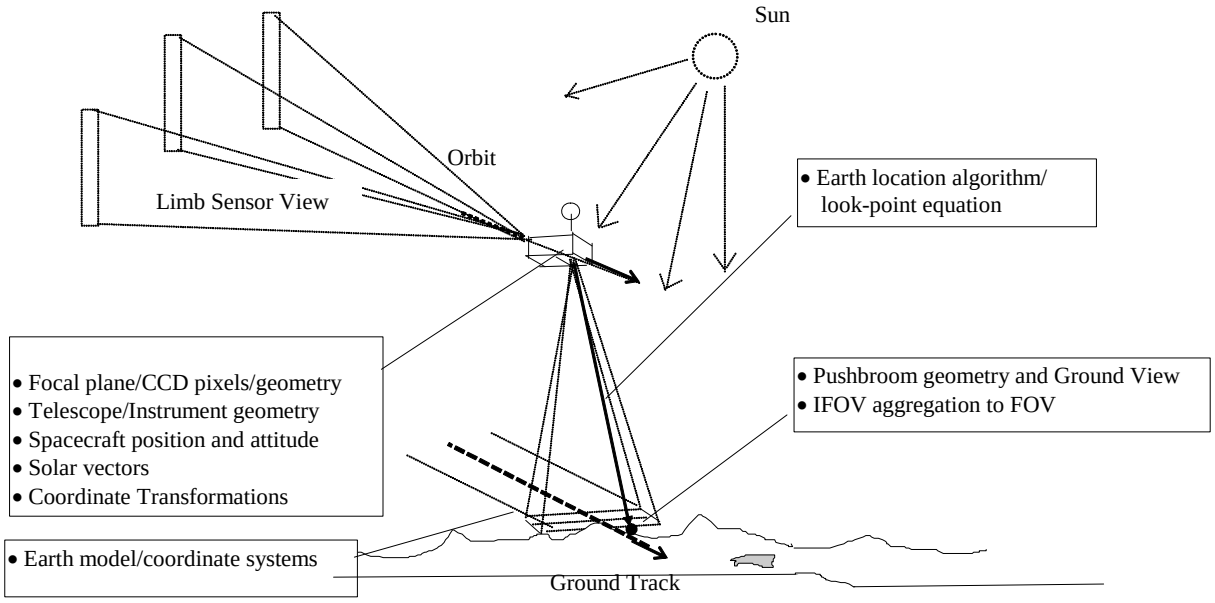

Figure 3.1-3. OMPS geolocation elements

Primary elements of the OMPS geolocation process are shown in Figure 3.1-3. The geolocation algorithm transforms the sensor view angles to the geodetic coordinate system in which geodetic latitude and longitude are expressed. Related parameters, such as solar and satellite zenith angles, used by the SDR and EDR algorithms are calculated within the geolocation algorithm. The following sections describe the theoretical basis for the geolocation algorithm and the implementation approach.

3.1.2.5.1 Coordinate System Definitions

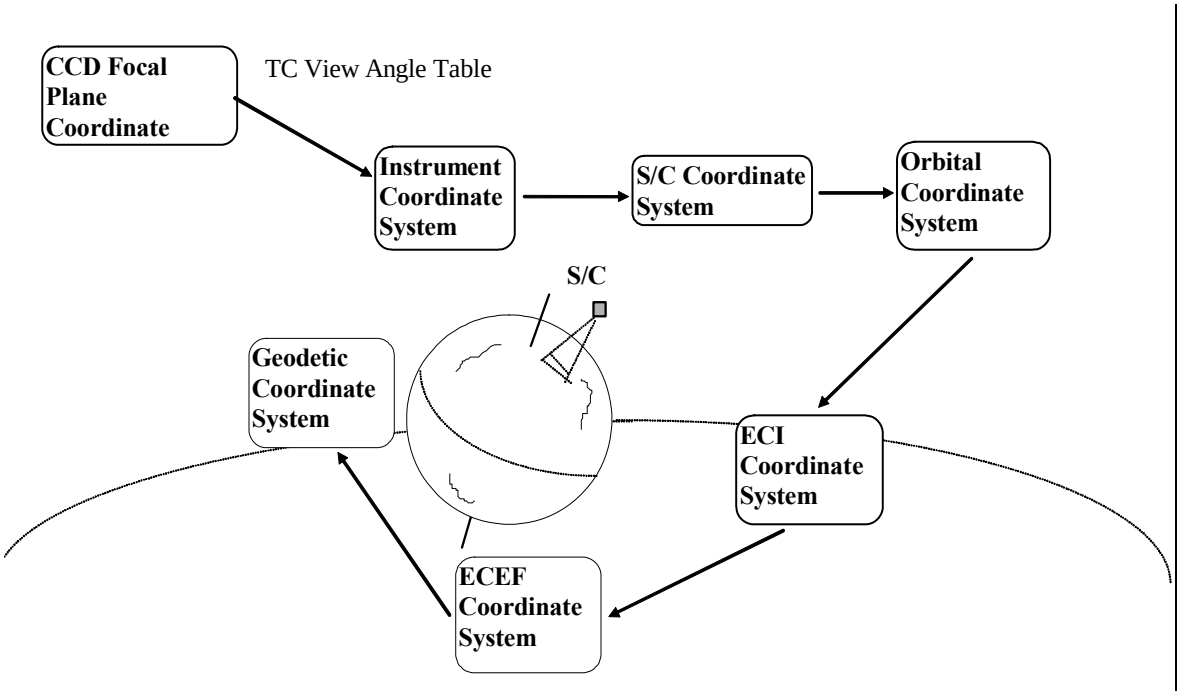

Figure 3.1-4. OMPS geolocation coordinate systems

Figure 3.1-4 displays the coordinate systems used in geolocation along with the typical sequence of coordinate transformations from FOV view angles to geodetic coordinates.

Instrument Coordinate System

The instrument coordinate system (Figure 3.1-5) is the coordinate system in which an image space view vector emanating from the center of a detector or spatial element number and sample time is converted to an object space viewing vector. It is based on the OMPS reference axes defined by the OMPS alignment cube. During preflight testing, the actual alignment of the aft optics/CCD focal plane, and the spacecraft coordinate system to the instrument coordinate system will be measured. This coordinate system is based on preflight measurements of the orientation of the instrument alignment cube.

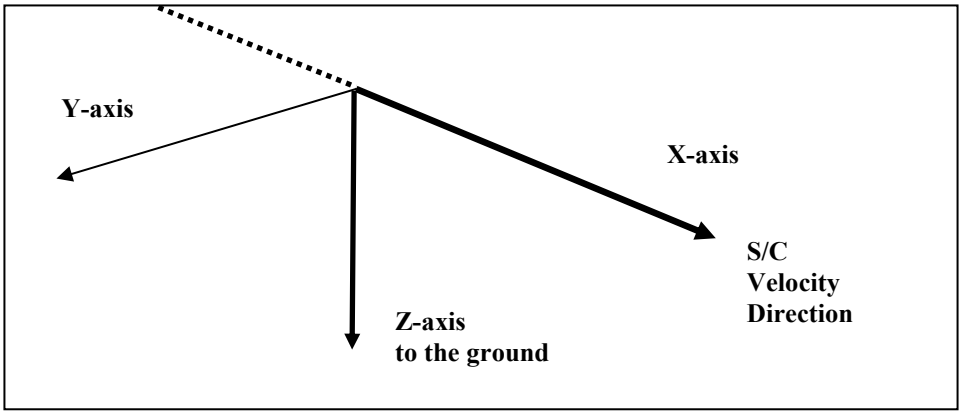

Figure 3.1-5. Instrument Coordinate System

Spacecraft Coordinate System

The spacecraft coordinate system is fixed to the NPOESS spacecraft with its origin at the spacecraft center of mass. The coordinate axes are defined by the spacecraft attitude control system. It is the orientation of this coordinate system relative to the orbital coordinate system that is captured in the spacecraft attitude data.

Orbital Coordinate System

The orbital coordinate system is centered on the satellite and its orientation is based on the spacecraft position in inertial space (Figure 3.1-6). The origin is the spacecraft center of mass with the Z axis pointing from the spacecraft center of mass to the direction perpendicular to the reference ellipsoid. The Y axis is the normalized cross product of the Z axis and the instantaneous (inertial) velocity vector. It corresponds to the direction of the negative of the instantaneous angular momentum vector direction. The X axis is the cross product of the Y and Z axes.

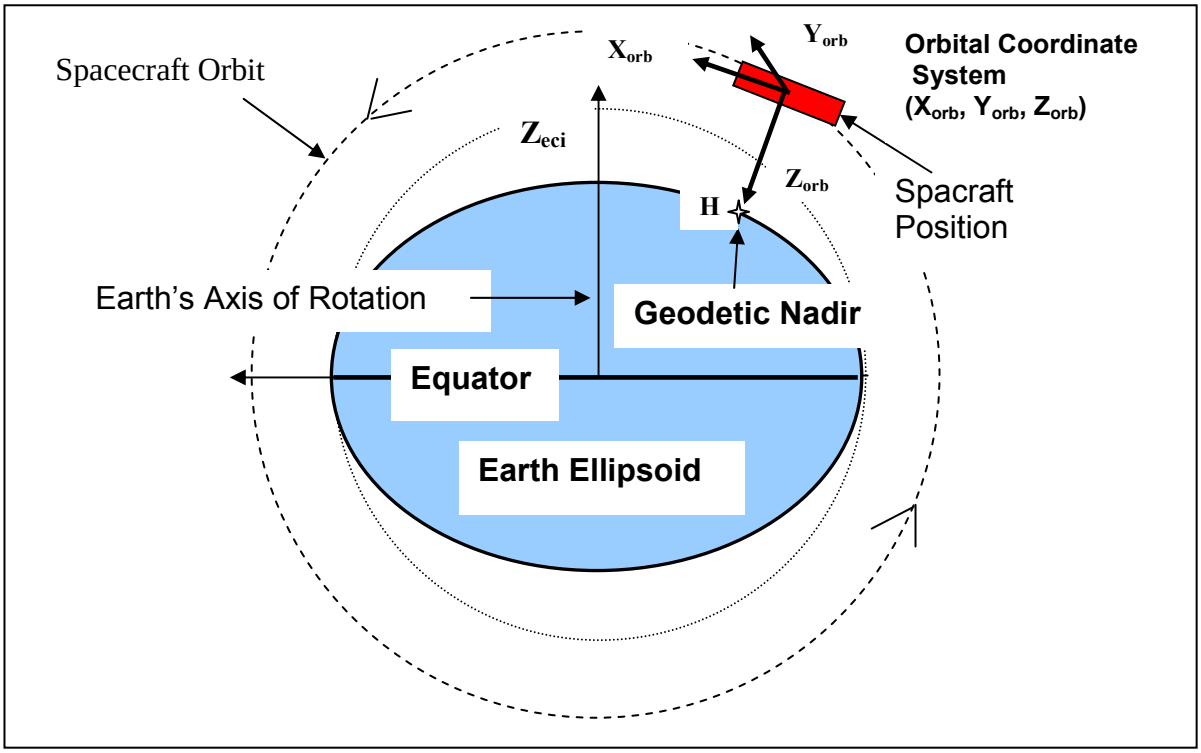

Figure 3.1-6. Orbital Coordinate System

Earth Centered Inertial Coordinate System (ECI)

The Earth Centered Inertial (ECI) coordinate system has its origin at the Earth's center of mass (Figure 3.1-7). The Z axis corresponds to the mean north celestial pole of epoch J2000.0. The X axis is based on the mean vernal equinox of epoch J2000.0. The Y axis is the cross product of the Z and X axes. This coordinate system is described in detail in NIMA, 1997.

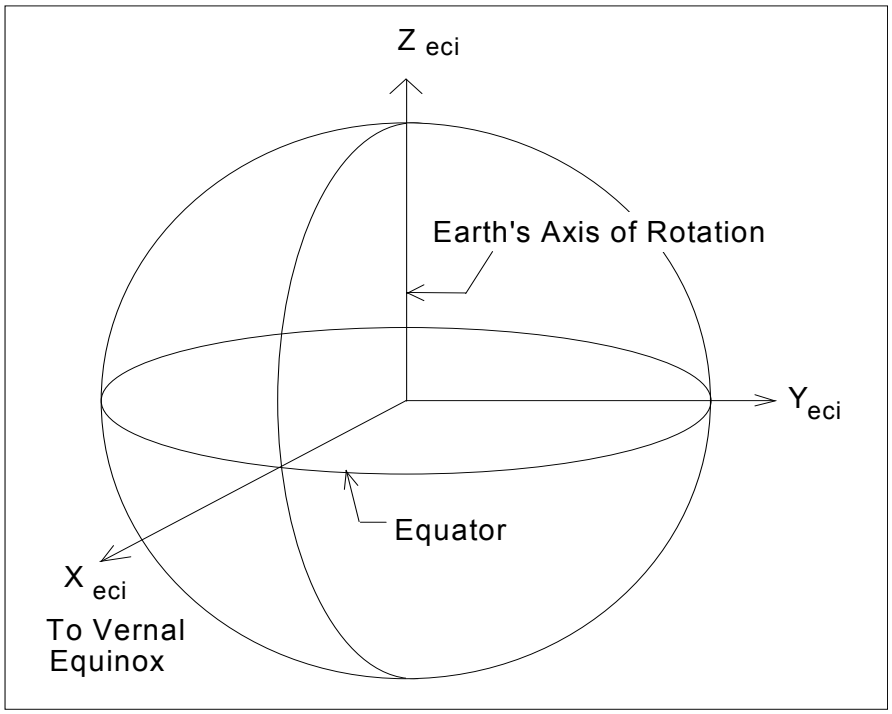

Figure 3.1-7. ECI Coordinate System

Earth Centered Earth Fixed (ECEF)

The Earth Centered Earth Fixed (ECEF) coordinate system has its origin at the center of mass of the Earth (Figure 3.1-8). It corresponds to the Conventional Terrestrial System (CTS) defined by the International Earth Rotation Service (IERS), which is the same as the U. S. Department of Defense World Geodetic System 1984 (WGS84) geocentric reference system. This coordinate system is described thoroughly in NIMA, 1997.

Geodetic Coordinate System

The geodetic coordinate system is based on the WGS84 reference frame with coordinates expressed in latitude, longitude, and height above the reference Earth ellipsoid. No ellipsoid is required by the definition of the ECEF coordinate system but the geodetic coordinate system depends on the selection of an Earth ellipsoid. Latitude and longitude are defined as the angle between the ellipsoid normal and its projection onto the equator and the angle between the local meridian and the Greenwich meridian, respectively. The Earth location data fields in each OMPS SDR will be expressed in the geodetic coordinate system.

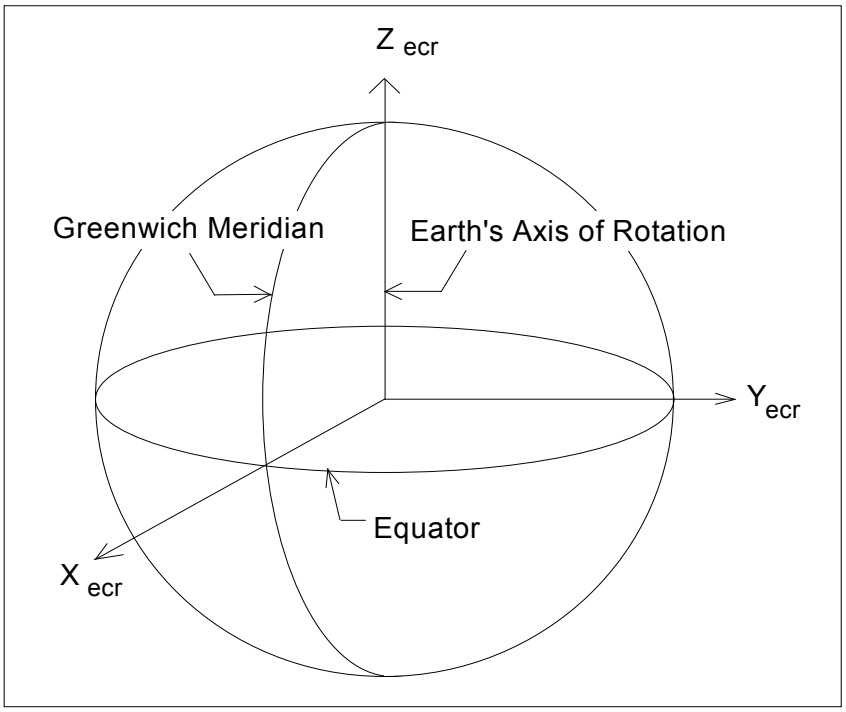

Figure 3.1-8. ECEF Coordinate System

3.1.2.5.2 Coordinate transformations

Focal Plane to Telescope to Instrument Coordinate System

In theory, the view vectors for each of the CCD pixels could be expressed in instrument coordinates with the help of optical ray trace models. Transformation matrices could be developed for each of the optical subassemblies between the focal plane and entrance aperture and then combined to calculate the view vector. This approach is useful when the optical characteristics of a particular subassembly may change on orbit in response to external factors, such as time varying thermal loads. For OMPS, BATC developed a sophisticated sensor/optical model that was used to calculate entrance aperture view angles along with a number of other sensor parameters. While predicted sensor characteristics are useful for SDR and EDR algorithm development and testing, they may lack sufficient fidelity for operational usage. As part of their pre-launch sensor characterization testing, BATC provided view angle pairs for each of the 780 TC CCD pixels expressed in instrument coordinates.

The optical view angles (α, β) provided by BATC are expressed in the form of rotational angles, and the unit exit vectors are calculated as:

$$u_1 = \sin(\beta)$$

$$u_2 = -\sin(\alpha)*\cos(\beta) \quad (56)$$

$$u_3 = \cos(\alpha)\cos(\beta)$$

Here, α is called by BATC as the azimuth look angle (rotation around the x-axis), and β as the elevation look angle (rotation around the y-axis).

Figure 3.1-9 displays a simplified depiction of the sensor (focal plain and curved mirror) and the projection of the view vectors onto the Earth's surface. Predicted view angles from the sensor model are plotted in Figures 3.1-10 and 3.1-11 as a function of pixel number.

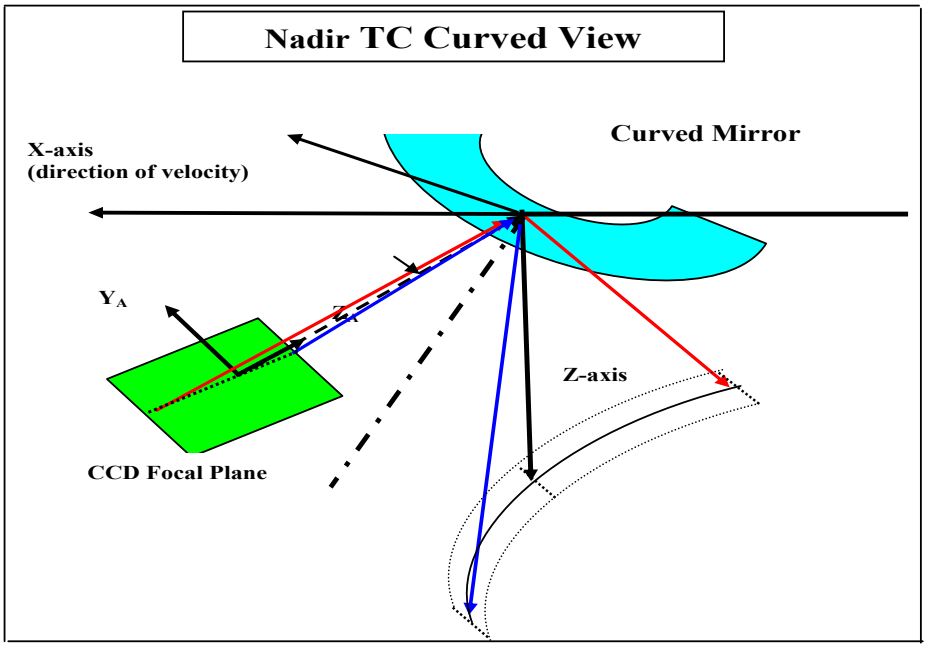

Figure 3.1-9. CCD focal plane to the ground view

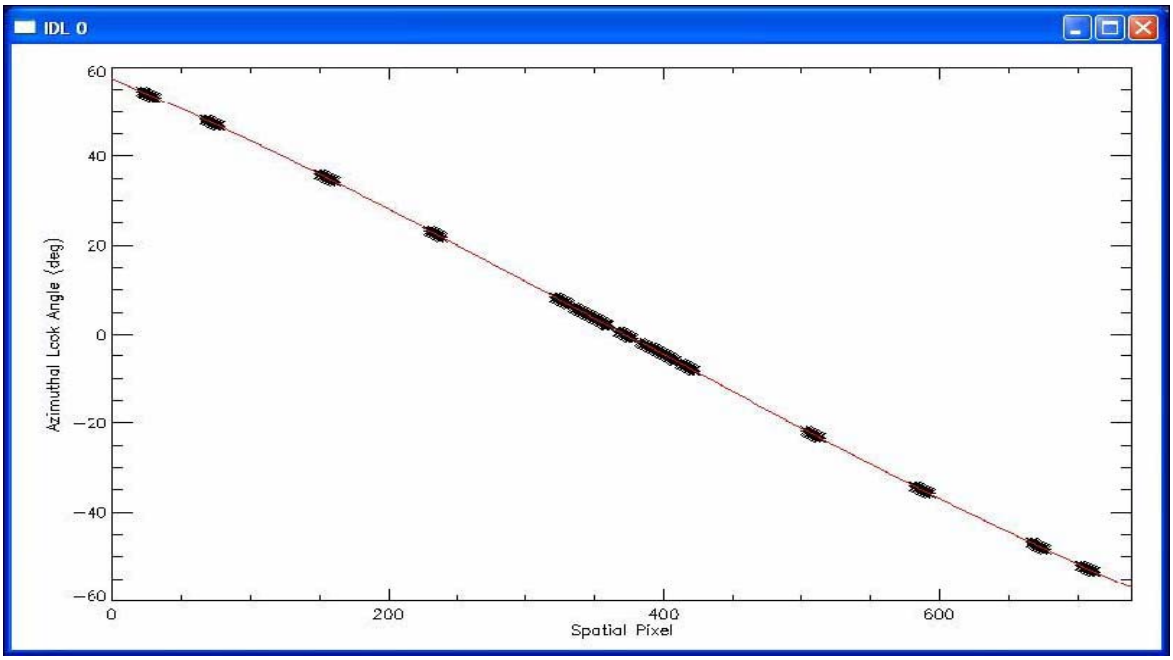

Figure 3.1-10. Cross-Track view angles α (Azimuth)

The cross track view angle is nearly linear. The along track view angle variation is significantly nonlinear as can be seen in Figure 3.1-11.

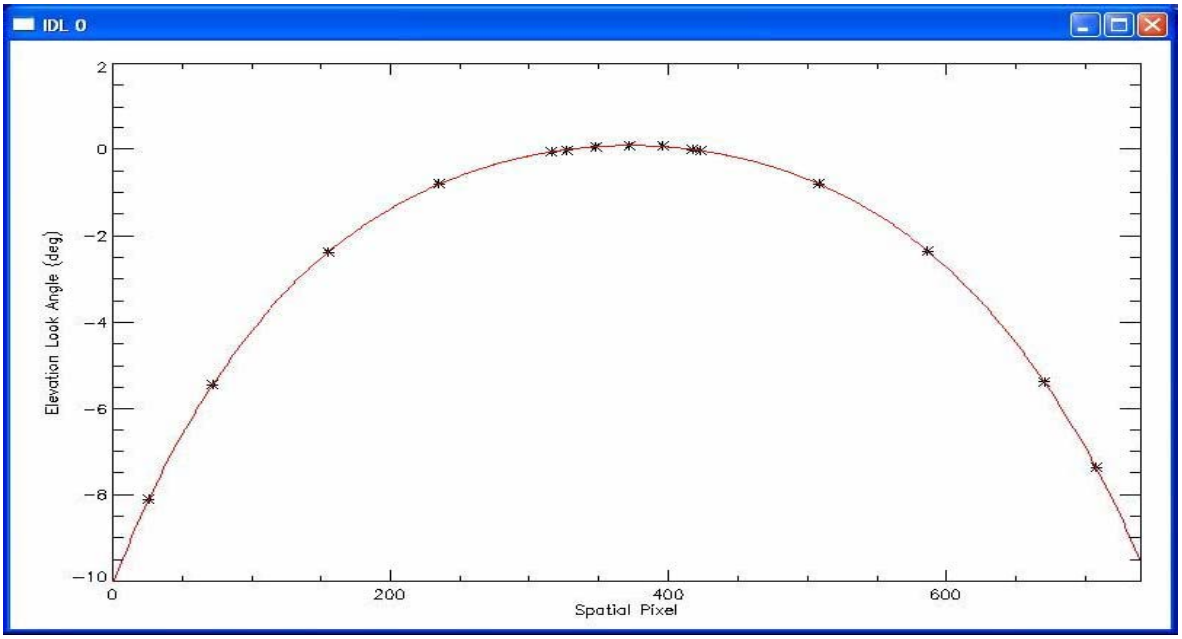

Figure 3.1-11. Along-track view angle β (Elevation)

The along-track view angles in Figure 3.1-11 result in a spatial smile projected on the Earth as shown in Figure 3.1-12.

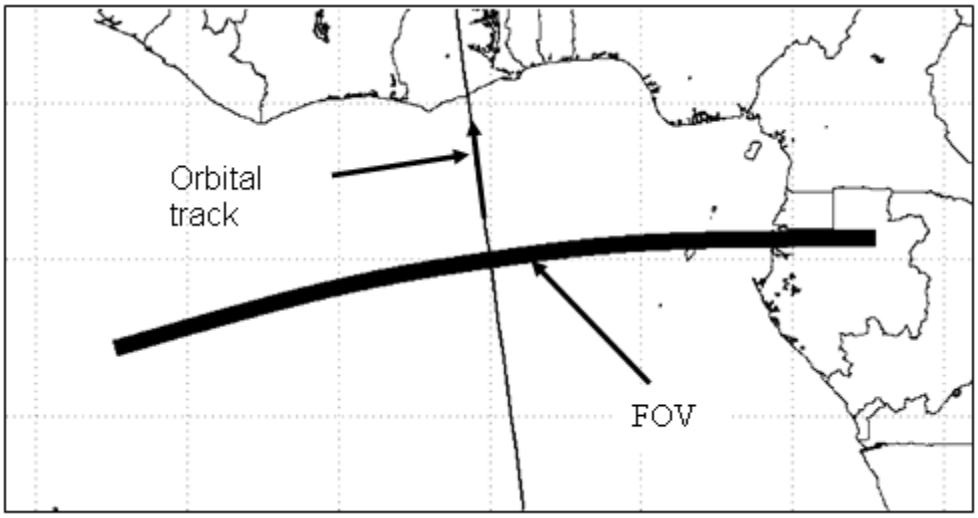

Figure 3.1-12. Ground Trace of TC with respect to spacecraft ground track

Instrument to Spacecraft

For development purposes we assume the transformation matrix between the instrument and spacecraft ($\mathbf{T}_{sc/inst}$) is given by

$$T_{sc/inst} = \begin{bmatrix} 1 & 0 & 0 \\ 0 & 1 & 0 \\ 0 & 0 & 1 \end{bmatrix} \quad (57)$$

These values should be replaced after the sensor has been mounted on the spacecraft and the alignment measured between the sensor and spacecraft reference axes.

Spacecraft to Orbital

The relationship between the spacecraft and orbital coordinate systems is defined by the spacecraft attitude. For NPP and NPOESS attitude information will be provided as a quaternion, which will be converted to Euler angles for use in the SDP Toolkit (ECS Project, 1995). The transformation from spacecraft to orbital coordinates is a three-dimensional rotation matrix, with the components of the rotation matrix being functions of the spacecraft roll, pitch, and yaw attitude angles. The nature of the functions of roll ξr, pitch ξp, and yaw ξy depends on the exact definition of these

angles (i.e. how they are generated by the attitude control system). Wertz (1985) requires the proper rotation order to be yaw, roll, and pitch. Since the spacecraft attitude is constantly changing, this transformation is time varying. The transformation matrix is:

$$\mathbf{T}_{\text{orb/sc}} = \begin{bmatrix} \cos\xi_y & -\sin\xi_y & 0 \\ \sin\xi_y & \cos\xi_y & 0 \\ 0 & 0 & 1 \end{bmatrix} \begin{bmatrix} 1 & 0 & 0 \\ 0 & \cos\xi_r & -\sin\xi_r \\ 0 & \sin\xi_r & \cos\xi_r \end{bmatrix} \begin{bmatrix} \cos\xi_p & 0 & \sin\xi_p \\ 0 & 1 & 0 \\ -\sin\xi_p & 0 & \cos\xi_p \end{bmatrix} \tag{58}$$

$$\mathbf{T}_{\text{orb/sc}} = \begin{bmatrix} \cos\xi_y\cos\xi_p - \sin\xi_y\sin\xi_r\sin\xi_p & -\sin\xi_y\cos\xi_r & \cos\xi_y\sin\xi_p + \sin\xi_y\sin\xi_r\cos\xi_p \\ \sin\xi_y\cos\xi_p + \cos\xi_y\sin\xi_r\sin\xi_p & \cos\xi_y\cos\xi_r & \sin\xi_y\sin\xi_p - \cos\xi_y\sin\xi_r\cos\xi_p \\ -\cos\xi_r\sin\xi_p & \sin\xi_r & \cos\xi_r\cos\xi_p \end{bmatrix}$$

Orbital to ECI

The relationship between the orbital and ECI coordinate systems is based on the spacecraft's instantaneous ECI position and velocity vectors. The rotation matrix to convert from orbital to ECI can be constructed by forming the orbital coordinate system axes in ECI coordinates:

$\mathbf{p}$ - spacecraft position vector in ECI

$\mathbf{v}$ - spacecraft velocity vector in ECI

$\mathbf{H}$ - geodetic nadir location on ellipsoid in ECI

$\mathbf{p'}$ - vector $\mathbf{H} \rightarrow \mathbf{p}$

$\mathbf{T}_{eci/orb}$ - rotation matrix from orbital to ECI

$\hat{\mathbf{b}}_3 = -\mathbf{p}'/|\mathbf{p}'|$ (nadir vector direction)

$\hat{\mathbf{b}}_2 = \hat{\mathbf{b}}_3 \times \mathbf{v} \Big/ \left|\hat{\mathbf{b}}_3 \times \mathbf{v}\right|$ (negative of angular momentum vector direction)

$\hat{\mathbf{b}}_1 = \hat{\mathbf{b}}_2 \times \hat{\mathbf{b}}_3$

$\mathbf{T}_{eci/orb} = \left[\hat{\mathbf{b}}_1 \quad \hat{\mathbf{b}}_2 \quad \hat{\mathbf{b}}_3\right]$

ECI to ECEF

The transformation from ECI to ECEF coordinates is a time varying rotation due primarily to Earth rotation but also containing more slowly varying terms for precession, astronomic nutation, and polar wander. The ECI to ECEF rotation matrix can be expressed as a composite of these transformations:

$$\mathbf{T}_{ecef/eci} = \mathbf{ABCD} \tag{59}$$

A - Polar Motion

B - Sidereal Time

C - Astronomic Nutation

D - Precession

Each of these transformation terms is described in detail in NIMA, 1997.

ECEF to Geodetic

The relationship between ECEF and geodetic coordinates can be expressed simply in its direct form (NIMA, 1997):

$$x = (N + h)\cos(lat)\cos(lon)$$

$$y = (N + h)\cos(lat)\sin(lon)$$

$$z = \left(N\left(1 - e^2\right) + h\right)\sin(lat)$$

$$N = a/\left(1 - e^2 \sin^2(lat)\right)^{\frac{1}{2}}$$

$$e^2 = 1 - \frac{b^2}{a^2}$$

where:

(x, y, z)	- ECEF coordinates
(lat, lon, h)	- Geodetic coordinates
N	- Ellipsoid radius of curvature in the prime vertical
e	- Ellipsoid eccentricity
a, b	- Ellipsoid semi-major and semi-minor axes

Unfortunately, there is no closed form solution for the inverse problem (which is the problem of interest here). Latitude and height must be solved iteratively for points that do not lie on the ellipsoid surface.

3.1.2.5.3 Geolocation algorithm

(Note: Discussion in this section is for reference only, and may not reflect what is implemented in the common geolocation algorithm. In particular, the SDP Toolkit is not used in the operational common geolocation algorithm.)

A basic Earth ellipsoid intersection algorithm yielding geodetic altitude and longitude consists of the following steps.

Given an object viewing vector $\mathbf{u}_{\text{inst}}$ in the instrument coordinate system, (calculated from viewing angles or viewing vectors provided by BATC) and a corresponding time *t*, the algorithm proceeds as follows:

1. Compute the required coordinate transformations:

1a. Get instrument-to-spacecraft alignment matrix $\mathbf{T}_{\text{sc/inst}}$. [Construct the instrument-to-spacecraft alignment matrix based on the time *t* if a time varying model is needed.]

1b. Interpolate the spacecraft attitude to time *t* and construct the spacecraft to orbital coordinate transformation matrix $\mathbf{T}_{\text{orb/sc}}$.

1c. Interpolate the ECI spacecraft position $\mathbf{P}_{\text{eci}}$ and velocity $\mathbf{V}_{\text{eci}}$ to time *t* and construct the orbital to ECI transformation matrix $\mathbf{T}_{\text{eci/orb}}$.

1d. Construct the ECI to ECEF rotation matrix $\mathbf{T}_{\text{ecef/eci}}$ from the sampling time *t*.

1e. Construct the composite transformation matrix:

$$\mathbf{T}_{\text{ecef/inst}} = \mathbf{T}_{\text{ecef/eci}}\mathbf{T}_{\text{eci/orb}}\mathbf{T}_{\text{orb/sc}}\mathbf{T}_{\text{sc/inst}} \tag{60}$$

2. Transform the viewing vector and spacecraft position vector to the ECEF coordinate system:

2a. Rotate the viewing vector $\mathbf{u}_{\text{inst}}$ to the ECEF coordinate system:

$$\mathbf{u}_{\text{ecef}} = \mathbf{T}_{\text{ecef/inst}}\,\mathbf{u}_{\text{inst}} \tag{61}$$

2b. Rotate the spacecraft position vector to the ECEF coordinate system:

$$\mathbf{p}_{ecef} = \mathbf{T}_{\text{ecef/eci}}\,\mathbf{p}_{\text{eci}} \tag{62}$$

3. Intersect the ECEF viewing vector with the WGS84 Earth ellipsoid

Note: These equations do not account for the travel time of light or for aberration due to spacecraft motion or relativistic effects. These effects cause a systematic bias of 7 m at nadir and 14 m at the edges of the scans.

3a. Re-scale the viewing vector $\mathbf{u}_{ecef} = (u_1, u_2, u_3)$ and satellite vector $\mathbf{p}_{ecef} = (p_1, p_2, p_3)$ using the ellipsoid semi-major *a* and semi-minor *b* axis dimensions (*a, a, b*):

$$\mathbf{u}' = \begin{bmatrix} u_1 / a \\ u_2 / a \\ u_3 / b \end{bmatrix} \qquad \mathbf{p}' = \begin{bmatrix} p_1 / a \\ p_2 / a \\ p_3 / b \end{bmatrix}$$

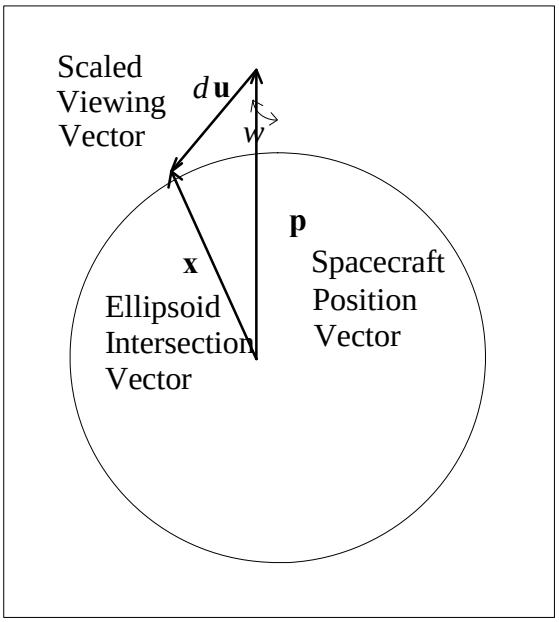

Figure 3.1-13. Ellipsoidal viewing vector intersection

Note:

$$\mathbf{x}' = \begin{bmatrix} x_1 / a \\ x_2 / a \\ x_3 / b \end{bmatrix}$$ - the unknown ground point vector (re-scaled)

3b. Solve for the scaling *d* of $\mathbf{u}'$ which intersects the unit sphere:

From the law of cosines:

$$|\mathbf{x}'|^2 = |d\,\mathbf{u}'|^2 + |\mathbf{p}'|^2 - 2\,|d\,\mathbf{u}'|\,|\mathbf{p}'|\cos(w)$$

Using the dot-product, the cosine of the acute angle *w* between $\mathbf{u}'$ and $-\mathbf{p}'$ is:

$$\cos(w) = -(\mathbf{u}'\cdot\mathbf{p}')/(|\mathbf{u}'||\mathbf{p}'|)$$

By definition $|\mathbf{x}'| = 1$ so:

$$1 = d^2|\mathbf{u}'|^2 + |\mathbf{p}'|^2 + 2d|\mathbf{u}'||\mathbf{p}'|(\mathbf{u}'\cdot\mathbf{p}')/(|\mathbf{u}'||\mathbf{p}'|)$$

Simplifying and rearranging:

$$d^2|\mathbf{u}'|^2 + 2d(\mathbf{u}'\cdot\mathbf{p}') + |\mathbf{p}'|^2 - 1 = 0$$

This can be solved for *d* using the quadratic formula:

$$d = \frac{-(\mathbf{u}'\cdot\mathbf{p}') - \sqrt{(\mathbf{u}'\cdot\mathbf{p}')^2 - |\mathbf{u}'|^2\left(|\mathbf{p}'|^2 - 1\right)}}{|\mathbf{u}'|^2}$$

This is the smaller of the two solutions for *d*, the intersection closest to the satellite. If the solution is not real, then there is no intersection.

3c. Use *d* to compute $\mathbf{x}'$ and $\mathbf{x}$:

$$\mathbf{x}' = \mathbf{p}' + d\,\mathbf{u}'$$

$$\mathbf{x} = \begin{bmatrix} x'_1\,a \\ x'_2\,a \\ x'_3\,b \end{bmatrix} = \begin{bmatrix} (p'_1 + d\,u'_1)a \\ (p'_2 + d\,u'_2)a \\ (p'_3 + d\,u'_3)b \end{bmatrix} = \begin{bmatrix} p'_1\,a + d\,u'_1\,a \\ p'_2\,a + d\,u'_2\,a \\ p'_3\,b + d\,u'_3\,b \end{bmatrix}$$

$$\mathbf{x} = \mathbf{p} + d\,\mathbf{u}$$

4. Convert the ECEF ellipsoid pierce point to geodetic coordinates (special case direct solution):

$$lon = \tan^{-1}\left(\frac{x_2}{x_1}\right) \tag{63}$$

$$lat = \tan^{-1}\left(\frac{x_3/\left(1-e^2\right)}{\sqrt{x_1^2+x_2^2}}\right) \tag{64}$$

$$h = 0 \tag{65}$$

3.1.2.5.3.1 SDP Toolkit application

We adopted and modified the SDP Toolkit (SDPTK) to implement the steps outlined in the previous section. A spacecraft tag was created for the NPOESS series of spacecraft and the orbital simulation program was modified to improve the modeling accuracy of the program for an NPOESS orbit. The majority of the spacecraft platforms SDPTK was designed for employ geocentric pointing with geocentric referenced Euler attitude angles. The TRMM spacecraft is an exception to this in that it employs geodetic pointing and geodetic referenced Euler angles. The SDPTK orbital simulation program is capable of modeling this situation and SDPTK can input geodetic referenced attitude Euler angles and accurately calculate the spacecraft to orbital coordinate transformation with the help of an additional transformation subroutine. NPOESS is a geodetic pointing spacecraft with attitude information provided to the SDR algorithm in the form of an ECI to SC rotation quaternion. Since the Euler angles are not input from an external source, nor do we have any requirements to report Euler angles in any particular form, we are free to chose the Euler angle representation. Selecting the native mode of SDPTK, geocentric referenced Euler angles, simplifies the simulation and geolocation process and reduces the number of computations. Therefore, for NPOESS, the orbital simulation program was modified to simulate geodetic pointing and report attitude as geocentric referenced Euler angles. Attitude angles input to SDPTK in this form can be used without any additional transformations.

Because the TC geolocation process is nearly identical for Earth view and calibration data, it is performed with a single subroutine. A table of sensor view angles representing the view angles at the center of each pixel are input. For Earth view data, which are a spatial average of 20 pixels, view angles corresponding to the center of the 20 pixel average are calculated by averaging the view angles of the two middle pixels (pixels 10 and 11 of the 20). Since calibration data is not spatially averaged, view angle averaging is unnecessary. Viewing vectors are formed from the view angles and the instrument to spacecraft transformation is applied using the nominal mounting matrix. SDPTK subroutine pgs_csc_subsatpoint is called to calculate the sub-satellite latitude and longitude. This call initiates input of the satellite ephemeris (position and velocity) and attitude data that is then interpolated to the requested time. The SDPTK subroutine pgs_csc_getfov_pixel takes as input the unitized view vectors and returns the geodetic latitude and longitude. Other SDPTK subroutines are called to calculate solar right ascension, declination, and elevation angles. These are written into the SDR, but spacecraft-centered solar angles

calculated by the algorithm are *not* written to an Earth SDR because the EDR processing does not require them.

Geolocation is performed for the beginning and ending time of an observation. The final geolocation is an average of the beginning and ending geolocations

3.1.2.5.3.2 Spacecraft diary data conversion

Time

Time tags applied to RDR data and to ephemeris/attitude data are assumed to follow the same definitions and format conventions. It is anticipated that spacecraft time will be reported in CCSDS 301.0-B-2 segmented time code (CDS) with time code epoch January 1, 1958. Generic SDPTK time conversion routines were modified to convert spacecraft time to International Atomic Time (TAI) with a January 1, 1993 epoch (TAI93) and to UTC time. Because the SDPTK native time is TAI93 and the SDR algorithm uses TAI93 internally, the NPOESS time code is converted to TAI93 immediately after the RDR header is input.

Ephemeris

The spacecraft diary ephemeris data, satellite position [meters, ECEF] and velocity {meters/second, ECEF], is converted to units usable by the SDPTK [meters and meters/second, ECI] and in a form acceptable by the standard SDPTK data input routines before RDR processing begins. The conversion is performed with the SDPTK routine pgs_csc_ecrtoeci. The converted ephemeris information is input to the SDR algorithm during RDR processing with the regular SDPTK data input routines.

Attitude

The spacecraft diary attitude information is also converted to a form usable by the SDPTK. The spacecraft diary provides attitude information in the form of a quaternion representing the transformation matrix from J2000 ECI to the spacecraft attitude determination frame approximating the spacecraft body frame. Following the notation for transformation matrices used in preceding sections, the attitude quaternion is expressed as $Q_{\text{sc/eci}}$. Given the time and location of the spacecraft, the SDPTK routine pgs_csc_getorbtoeciquat can be used to calculate $Q_{eci/orb}$. The orbital to spacecraft transformation is computed by multiplying the two quaternions together to yield,

$$Q_{sc/orb} = Q_{\text{sc/eci}} Q_{\text{eci/orb}} \tag{66}$$

The complex conjugate (or inverse) of $Q_{sc/orb}$, yields $Q_{orb/sc}$, which is used with the SDPTK routine pgs_csc_quattoeuler to compute geocentric referenced Euler angles (3-1-2 order).

It is anticipated that for NPP ephemeris data will be reported once per second while NPOESS data will be reported once every ten seconds. For both spacecraft, attitude quaternions will be reported every half second. Because the quaternion to Euler angle conversion requires collocated ephemeris data, the ephemeris data must be time interpolated to the higher resolution attitude time grid. The ephemeris data interpolation is performed with a third order method taken from the SDPTK ephemeris interpolation routine that requires four ephemeris points.

The SDPTK orbsim inputs are currently configured to simulate ephemeris and attitude data in one day granules. SDPTK will accept larger granules, such as a months worth of data or smaller granules, such as a single orbit of data. Larger granules will increase search time within the granule while the smallest granule must contain four points.

3.1.2.6 Signal Corrections

Raw signals from the TC detector require initial corrections prior to radiometric calibration. Corrections to observed macropixel counts O_{Jk} of binned row J (spatial) and column k (spectral) are performed for several instrument characteristics: electronics bias B, CCD dark current D_{jk} for pixel j,k,(rows binned N_D through N_J) for integration time t_D, and observational smear S_k of column k (rows 1 through N_S). Schematically, the corrected counts C_{Jk} for integration time t_E are obtained for each macropixel J,k by:

$$C_{Jk} = O_{Jk} - \sum_{j=N_D,N_J} \frac{t_E}{t_D}(D_{jk} - B) - [S_k - \sum_{j=1,N_S} \frac{t_E}{t_D}(D_{jk} - B)] - B \qquad (67)$$

where all counts except for the bias have been previously corrected for linearity. The algorithm scales dark signal correction counts by the ratio of integration times of the Earth data and the dark data.

Prior to coadding the Earth data, the TC flight software applies linearity corrections based upon results of the lamp calibration processing. Due to the split frame architecture of the CCD, the algorithm calculates and applies separately two distinct biases and two smear corrections. The central (nadir) Earth data cell is comprised of pixels from both halves of the CCD, so the algorithm subtracts an average of the two biases and an average of the two smears from this macropixel, weighted by the number of good pixels determined from the earth view sampletable. Because all CCD

pixels (even the CCD smear rows) contain dark and bias signals, the algorithm must remove the signals prior to any smear correction.

The electronics bias is always present as an addition to the photometric counts. Unlike other data, the bias is independent of image exposure time and is read from special pixels at the edge of the solar RDRs and stored after calibration processing in the BIASES database for each image CCD half. The SDR algorithm during Earth processing reads the BIASES database for the most current values and subtracts the weighted average of the bias values of each image half from the Earth data raw counts. In addition, the bias removal also takes into account the number of image frames co-added before the earth view and calibration images being downlinked to the ground.

The dark signal on an OMPS CCD results when electrons are thermally emitted into the conduction band of pixels in the active and storage regions. The dark signal effectively adds offset counts to the photon-generated pixel counts. Dark signal measurements are normally made during the night side of the orbit with the entrance aperture of the sensor blocked, though the algorithm separates dark data taken outside the SAA from those data taken within the SAA, because the dark current can be expected to increase during an SAA passage. Similarly, the dark current during Earth observations can potentially increase beyond normal. SAA exposure values below 10% of maximum exposure are considered to be normal data for both Earth and dark RDRs.

During calibration processing, and prior to Earth SDR processing, the SDR algorithm characterizes and stores the normal dark signal for each pixel and identifies and stores bad pixel information. To increase the signal to noise, the normal dark data, summed cumulatively in time for the entire RDF duration, are written into a DARK database. Dark SAA data defined as at least the 10% level and greater are not summed, but stored individually in the separate SAA_DARK database along with their SAA exposure values. During Earth data processing, the SDR algorithm reads the latest processed dark data of the appropriate type, even when they were determined from subsequent measurements in the orbit.

For normal Earth data, normal dark data are subtracted. For Earth data acquired during SAA, the SDR algorithm searches and reads the SAA_DARK database for data with a similar level of SAA exposure. If one is lacking, normal dark data are used instead. Whatever the origin of the final dark data used to correct the Earth data, the algorithm bins the dark data pixels into dark macropixels, excluding bad pixels, which were identified in the EV sampletable. The SDR algorithm then subtracts the binned dark data from the corresponding Earth radiometric macropixel value in order to correct the Earth signal for sensor dark current.

At the conclusion of each detector integration period, the CCD quickly shifts the electrons from the active to the storage region (parallel transfer). Photons collected in the active pixels during this transfer period are referred to as the smear signal. For a temporally constant radiance scene, even a spatially heterogeneous one, the

smear signal is the same in all pixels in a column. The smear signal is measured by re-reading multiple edge rows of CCD pixels that were already read fro their primary signal, thereby capturing smear signal produced during the re-reading. These rows are binned to a single row for each CCD half by the flight software. The SDR algorithm subtracts the dark- and bias-corrected smear signal from the observed Earth data to obtain signal-corrected counts, ready for radiometric calibration. The bin sizes for the smear and normal EV macropixels are typically different, so the algorithm first normalize the smear before removing it from the earth view pixels.

3.1.2.7 Radiometric Correction

Following the signal processing, the algorithm computes calibrated radiances using corrected earth-view counts, integration times, pre-launch radiance calibration coefficients, and time-dependent radiometric calibration factors (see Section 3.1.3.5.4). Prior to binning the individual pixels into a spatial cell macropixel, the flight software applies flat field corrections to pixel counts in order to correct for the non-commutative additions of counts from varying pixel sensitivities. Since the mean correction applied to each macropixel is 1, the Earth branch of the SDR algorithm ignores this preliminary calibration by the flight software (see flat field discussion in Section 3.1.3.5.5).

The algorithm computes Earth radiances I^m_{Jk} for each macropixel (*J,k*) by dividing the corrected counts C_{Jk} (Equation 67) by the integration time t_{int} and applying the corrections described in Section 3.1.3.1.

$$I^m_{Jk} = \frac{C_{Jk} k^r_{Jk} A_{Jk}}{t_{\text{int}}} \tag{68}$$

Counts are converted to radiances using pre-launch radiance calibration constants k^r_{jk}. The SDR algorithm sums the constants over the pixels *j,k* in each macropixel *J,k*, including only pixels identified as good in the EV_sampletable. The algorithm then corrects for changes in sensor response using radiometric calibration factors A_{Jk} read from CF_EARTH. These calibration factors have already been corrected for spectral shifts by the calibration SDR processing. If current calibration factors are missing, the latest older calibration factors are used, and this is noted in the Earth data quality flags. If the switch for calibration factor correction is set to false, then the calibration factor is re-set to 1, regardless its value in the CF_EARTH database.

3.1.2.8 Stray Light Correction

Ground test data, analysis and simulations show that the stray light contamination of the OMPS TC sensor is compliant to the < 2% requirement as a global average. Simulations using a data set designed to represent global conditions was conducted by BATC to demonstrate compliance. The results show that the sensor meets the requirement for a global average (weighting various conditions of clear/cloudy, Ozone

amount, Latitude, etc.), however the TC exceeds requirements under conditions of concern to science and the public. Actual performance of the sensor will not be known until on-orbit validation tests are conducted to estimate the levels of stray light contamination present in earth scenes.

As a risk mitigation approach, a stray light correction module has been added to the TC SDR algorithm to remove stray light comtamination if it is confirmed necessary in order to meet the TC EDR performance requirement specifications. The correction is based on the stray light correction approach implemented for the LP SDR algorithm. After the EV counts are converted into radiances, they are binned into 20 spectral regions:

$$I_{JK} = \sum_{k} I_{Jk} \tag{129a}$$

Where J represents the Jth spatial macro pixel, K represents the binned Kth spectral region, and k represents the unbinned kth spectral channel. The binning is mostly for the benefit of reducing computation burden.

The binned signal then multiply with the pre-computed stray light correction matrix to estimate the stray light contamination, ΔI_{lm} in the calibrated radiance I_{lm} for macro pixel (l,m):

$$\Delta I_{lm} = \sum_{J,K} C_{lmJK} I_{JK} \tag{129b}$$

Where the 4-D matrix operator C_{lmJK} is pre-computed from the measured sensor point-spreading-function (psf) and the signal intensities.

For stray light contamination caused by the out of range (OOR) signal, the correction is similar except that one has to estimate the intensity of the OOR signal first because they are not measured directly by the sensor. This can be done using a simple model:

$$I_{OOR} = I^{m}_{370-380nm} \cdot \left[\frac{I^{s}_{OOR}}{I^{s}_{370\sim380nm}} \right] \cdot \left[\frac{I^{m}_{370-380nm}}{I^{m}_{360\sim370nm}} \cdot \frac{I^{s}_{360-370nm}}{I^{s}_{370\sim380nm}} \right]^{k} \tag{129c}$$

Where superscripts m and s denote the actual measured and simulated radiances for the specified wavelength ranges, respectively, and *k* is a scaling factor, pre-determined by simulation.

Once the stray light contamination is computed, it is removed from the measured radiance to get the stray-light corrected radiances for all channels:

$$I^{c}_{lm} = I^{m}_{lm} - \Delta I_{lm} - \Delta I_{OOR} \tag{129d}$$

3.1.2.9 Match-up with Limb Profile EDR

(This section is no longer pertinent to the operational SDR algorithm because the LP SDR and EDR data are not produced in the NPP and NPOESS data product processing system.)

To enable matching LP data with TC data, we have supplied the TC SDR algorithm with a parameter file specifying the TC total cross-track field of view (FOV) angle (110^o), as well as the LP slit separation, LP vertical cell size, and the LP along-track cell size. Because the OMPS LP and TC sensors are co-aligned, the TC SDR algorithm selects the LP data within the same orbit, primarily by the observation time delay (nominally 6.87 minutes) between the two sensors. Assuming that the limb sensor looks aft, the time difference between the LP and TC observations is given by:

$$\tau_{TC} = \tau_{LP} - \frac{d}{v}$$

where *d* is the distance on the earth spanned by the apparent ground track velocity *v*:

$$v = \left(\frac{Gm_e}{R_e + Z_{sat}} \right)^{\frac{1}{2}} \left(\frac{R_e}{R_e + Z_{sat}} \right) \tag{69}$$

The earth centered angle, ECA, in radians that the satellite traverses over

$d = R_e$ * ECA is:

$$ECA = \cos^{-1}[(R_e + Z_{Tan})/(R_e + Z_{Sat})] \tag{70}$$

where R_e is the radius of the earth, Z_{Sat} is the satellite altitude, nominally 833 km for NPOESS, and Z_{Tan} is the tangent altitude. For a tangent altitude of 20 km, close to the ozone profile peak, ECA=27.48^o, the LP and Nadir measurements are separated by 6.87 minutes. Note that because of the time lag and the shift of sub-tangent location with tangent altitude, the limb and total column observations will not align exactly. The match-up between the nadir and limb should use the sub-tangent locations associated with the 20 or 30 km limb radiances, which are close to the ozone peak. Combining the above three equations yields the following:

$$\Delta t_{LP} = \tau_{LP} - \tau_{TC}$$

$$\Delta t_{LP} = \{(R_e + Z_{Sat})^{1.5}/(G \cdot M_e)^{½} \cdot \cos^{-1}(\{(R_e + Z_{tan})/(R_e + Z_{Sat})\}) \tag{71}$$

Data from all three LP slits are read and stored in the output TC SDR for spatial regions overlapping the LP data. In the TC cross-track direction of 35 cells (N_{TC}), the left and right LP slits are nominally 5 TC spatial cells from the center nadir, and the center TC cell is coincident with the LP central slit. No LP data have time coincidences with the TC outside the 10 central TC spatial cells.

Complicating this picture is the rotation of the earth during this time interval (Δt_{LP}) where the TC pixel shift due to the earth's rotation is,

$$\Delta h = \omega \cdot (\Delta t_{LP}), \tag{72}$$

and

$$\omega = (360/k[\text{rev/day} \rightarrow \text{rev/sec}]\} \cdot \cos(\text{latitude}) \quad , \tag{73}$$

and

$$\Delta pix = \text{sign(latitude)}*\omega\cdot(\Delta t_{LP})/(TC\_scale) \tag{74}$$

with,

$$TC\_scale = FOV/ N_{TC} \tag{75}$$

and sign = +1, ascending orbit, whereas sign = -1, descending orbit. Note that we do not correct for satellite attitude differences between the TC and LP observations.

Along the TC sensor track, the LP ozone dominates at the tangent point within 5 continuous sequential TC observations. The third of these 5 TC cells coincides with an actual LP measurement. Thus, to obtain limb ozone profiles at the 4 along-track TC cells that are not coincident, the TC SDR algorithm interpolates in time between two successive LP observations. Finally the ozone profiles are binned to the Umkehr layers defined in Table 2.3-2.

3.1.2.10 External Data Match-up

Each SDR contains EDR information from VIIRS and CrIMSS, if available. The geophysical quantities from each are listed in Section 3.1.1.1. EDR information will overwrite existing climatological values if available. In the event that an EDR parameter has been flagged as having poor quality, those data will not be used. EDR information will require minimal additional processing. Atmospheric profiles, however, are binned to the Umkehr layers defined in Table 2.3-2.

Following geolocation of OMPS TC radiance data, external EDR quantities will be read in for the correct latitude, longitude and time. The threshold horizontal and vertical cell sizes specified for the required VIIRS and CrIMSS EDRs listed in Section 3.1.1.1 are sufficient for OMPS. Because OMPS TC, VIIRS, and CrIMSS are nadir viewing sensors, the data are obtained nearly simultaneously. Thus, measurement collocation is determined solely by spatial considerations.

The CrIMSS swath width encompasses all the TC cells. Cell sizes range from 14 to 40 km. CrIMSS provides profiles of temperature and pressure with varying HCS depending on the observing conditions and varying vertical reporting intervals depending on the pressure level. Table 3.1.2.10-1 lists the CrIMSS EDRs required for use in the TC SDR algorithm. Note that the Horizontal Cell Sizes (HCS) were taken from the NPOESS System Specification, DOC SY15-0007, Rev N, September 12, 2008.

Table 3.1-1. CrIMSS Horizontal Cell Size

EDR	HCS	Measurement Range
Temperature versus Pressure Profile		180 – 335 ºK
Clear – Nadir	14 km	
Cloudy – Nadir	40 km	
Pressure versus Altitude Profile		50 to 1050 mb
	25 km	in 1 km altitude steps

Because there are multiple CrIMSS observations within the TC footprint, the CrIMSS data are selected within the OMPS TC footprint using the criteria described below and then averaged. These selection criteria are as follows:

- For each of the CrIMSS profiles matching the OMPS TC observation time, define a quantity, δlat, as the absolute difference between the latitude of the TC observation and the latitude of the CrIMSS observation. Repeat this analysis for the longitude of the TC and CrIMSS measurements.

- Define an earth-centered angle, ω, in terms of the Total Column (TC) Horizontal Cell Size (HCS). See the Figure 3.1.-14.

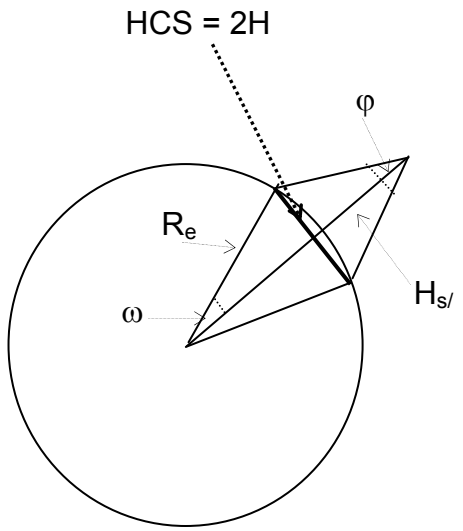

Figure 3.1-14. CrIMSS External Data Match-up

φ = OMPS swath FOV angular coverage/(number of TC horizontal cells)/2

$$\varphi = TC\_scale/2 \quad (76)$$

$$\omega = \sin^{-1}\{ (H_{s/c} \cdot \tan(\varphi/2)) / R_e \} \quad (77)$$

- Define an earth centered angle, β (similar to ω), related to the difference in both longitude and latitude on the earth's surface between two points:

$$\beta = \cos^{-1}\{ \cos(\Delta long) \cdot \cos(\Delta lat) \} \quad (78)$$

- Accept as match all CrIMSS profiles with latitude and longitude satisfying

$$\beta \leq \omega \quad (79)$$

- Repeat for all the CrIMSS profiles, found within the time match.
- Keep track of all the accepted CrIMSS profiles.
- Average the final profiles into corresponding Umkehr layers.
- Average the matching profiles.

Similarly the VIIRS swath width encompasses all the TC cells. The VIIRS cell sizes range from 0.8 to 25 km. Table 3.1.2.10-2 lists the VIIRS EDRs required for use in the TC SDR algorithm. Again note that the Horizontal Cell Sizes (HCS) were taken

from the NPOESS System Specification, DOC SY15-0007, Rev N, 12 September 2008.

Table 3.1-2. VIIRS Horizontal Cell Size

EDR	HCS	Measurement Range
Cloud Cover/Layers		0 – 1.0 HCS
Edge of Swath	25 km	
Nadir	6 km	
Cloud Top Pressure		50 to 1050 mb
Edge of Swath	12.5 km	
Nadir	5 km	
Sea Ice Characterization	Ice Concentration	1/10 to 10/10
Clear	2.4 km	
All Weather	20 km	
Snow Cover		0 – 100% of HCS
Clear – Nadir	0.8 km	
All Weather	20 km	

Since there are multiple VIIRS observations within the TC footprint, the VIIRS data are selected within the OMPS TC footprint using the same criteria as described above for the matching CrIMSS observations within the OMPS TC footprint.

- For each of the VIIRS observations matching the OMPS TC observation time, define a quantity, Δlat, as the absolute difference between the latitude of the TC observation and the latitude of the VIIRS observation. Repeat this analysis for the longitude of the TC and VIIRS measurements.

- Define an earth-centered angle, ω, in terms of the Total Column (TC) Horizontal Cell Size (HCS). See the Figure 3.1-14.

- Define an earth centered angle, β (similar to ω).

$$\beta = \cos^{-1}\{ \cos(\Delta long) \cdot \cos(\Delta lat) \} \quad (80)$$

- Accept as match all VIIRS observations with latitude and longitude satisfying

$$\beta \leq \omega \tag{81}$$

- Repeat for all the VIIRS observations found within the time match.
- Keep track of all the accepted VIIRS observations.
- Average the matching observations.

3.1.2.11 Data Quality Checks

Based on the current bad pixel values, the Earth processing calculates the percentage of good pixels out of the total number of pixels on the fully sampled CCDs image and writes the percentage as a quality flag in the output RDF. This is a basic first assessment of the data quality.

Using the geolocation data for the beginning and end of each observation, the Algorithm relies on NPOESS processing to identify if the satellite ground track during an observation crosses the SAA and to supply the correct value from a static SAA map of relative radiation exposure from maximum. Using this percentage, the OMPS SDR algorithm flags an entire Earth scene FOV for SAA exposure. All other data types are also flagged for SAA level. For example, if the calculated exposure is 45% the data are flagged as exceeding 40% but not 50%. Flagging in 10% exposure gradations with an 80% maximum is adequate.

The SDR algorithm computes a median radiance over all wavelengths for each spatial cell. If the median is greater than a parameterized permitted value, the Algorithm now flags, as a ratio of median value to allowed value, the spatial cell as containing some anomalously bright radiance. The SDR algorithm also should perform more localized transient hot pixel detection by comparison of Earth pixels with nearest neighboring pixels. A cubic spline, or similar smooth regression, should be performed along each row *J* (i.e. spectrally) for each data cell. The splined region should not exceed 2 nm. A gradated flag, similar to that used for the SAA, should be used to indicate the percent by which the measured radiance exceeds that computed from the spline. Macropixels that have lower than expected radiances should not be flagged by this algorithm. Currently, this checking is not implemented in the operational code.

Using an almanac of Solar eclipses by the moon, the algorithm expects the NPOESS processing to check the latitude and longitude of the Earth data for the presence of a solar eclipse at each Earth spatial cell. If the data cell lies within an eclipse, the algorithm flags the entire SDR for eclipses.

Specular reflections of sunlight off water surfaces is a geophysical situation not properly incorporated in the EDR radiance tables. When the sun glint condition is met, water reflects much of the solar irradiation at a solar zenith angle θ_o into the sensor field of view at a satellite zenith angle θ. Waves diffuse the reflection, creating a range of angles for which sun glint produces an error. This includes reflections out of the principal plane, i.e. relative azimuth angle $\varphi \neq 0°,180°$. The SDR algorithm is coded for checks for sun glint using the following equation for the co-scattering angle Φ.

$$\Phi = \cos^{-1}\left[\left(\cos\theta_o \cos\theta + \sin\theta_o \sin\theta\right)\cos\varphi\right] \leq 36^\circ \tag{82}$$

The algorithm identifies the surface type as water using the VIIRS Quarterly Surface Type Gridded IP. If the fractional water surface within an OMPS footprint is over 25%, it is classified as water surface.

The algorithm also compares the minimum and maximum derived wavelengths for each Earth data cell with pre-launch parameterized limits for minimum and maximum. The limits are based on extending, by a parameterized wavelength interval, the extrema of all the wavelengths of the initial laboratory scale. If the current assigned wavelengths for an Earth data cell exceed the extrema, the cell is flagged as suspect.

Data quality checks of the calibration data for the SAA and Eclipse are the same as for Earth data, though sun glint checks are not needed for the calibration data.

3.1.3 Calibration

The calibration concept for the OMPS Total Column sensor follows closely that of TOMS and SBUV/2. The TOMS calibration procedures are described in Jaross, et al.,1995, Seftor et al., 1997, and McPeters, et al., 1998. The implementation for OMPS has been described in ICSR-8092402. The use of diffusers is described in ICSR-8110501.

Backscatter ultraviolet (BUV) instruments measure the response to solar irradiance by deploying a ground aluminum diffuser plate to reflect sunlight into the instrument. The three-diffuser system aboard TOMS reduces the exposure and degradation of the diffuser used for the solar measurements and allows calibration through comparison of signals reflected off diffusers with different rates of exposure. An identical concept is employed on OMPS, but only two diffusers are used because mechanical design differences obviate the need for the third diffuser. The diffusers, designated Working and Reference, are arranged around an annulus so that a given diffuser can be rotated into view on demand. The full CCD is covered with 7 separate diffuser positions. These segments end up in separate RDRs and must be assembled by the SDR algorithm to produce a single solar image.

The Reference diffuser is exposed for one solar measurement sequence every 6 months, and the Working diffuser is exposed every week. The Working diffuser is the primary sensor calibration diffuser. Periodic comparisons with Reference diffuser solar measurements are used to detect changes in the Working diffuser.

3.1.3.1 Theoretical Basis: Radiometric Calibration

Conceptually, the calibration of measured Earth radiance and solar irradiance can be considered separately. We note that they are not separately calibrated quantities for the OMPS TC sensor, because the BUV technique cannot distinguish between solar flux changes and sensor response changes. The measured Earth radiance in a single pixel can be written as a function of the corrected instrument counts in the following way:

$$I^{m}_{jk}(t) = \frac{C^{r}_{jk} k^{r}_{jk}}{\tau_{jk}(t)} \tag{83}$$

where

$I^{m}_{jk}(t)$ = derived Earth radiance for pixel (j,k)

$C^{r}_{jk}(t)$ = radiance counts, corrected by initial signal corrections algorithms

k^{r}_{jk} = radiance calibration constant (from pre-launch calibration)

$\tau_{jk}(t)$ = pixel response changes ($\tau(t=0) = 1$)

The measured solar irradiance, F^{m}_{jk}, can be written as:

$$F^{m}_{jk}(t) = \frac{C^{i}_{jk} k^{i}_{jk}}{g\ \rho(t)\,\tau_{jk}(t)} \tag{84}$$

where

$C^{i}_{jk}(t)$ = irradiance mode counts (corrected) of pixel j,k

k^{i}_{jk} = irradiance calibration constant (from pre-launch calibration)

$\tau_{jk}(t)$ = sensor throughput changes ($\tau(t=0) = 1$)

$\rho(t)$ = solar diffuser plate reflectivity ($\rho(t=0) = 1$)

g = relative angular irradiance response (goniometry) of the sensor

The constants k^{r} and k^{i} are not accurately determined separately in flight. The primary quantity measured by BUV sensors, and from which ozone is derived for the

Total Column sensor, is the normalized radiance $I^m(t)/F^m(t)$. The advantage of this approach is that sensor throughput changes τ affecting both Earth and solar measurements cancel in the ratio. The expression for normalized radiances becomes:

$$\frac{I_{jk}^m}{F_{jk}^m} = K_{jk} \frac{C_{jk}^r}{C_{jk}^i} g\,\rho(t) \tag{85}$$

where K_{jk} is a combined calibration constant for normalized radiances, often referred to as the Albedo Calibration Constant. This constant and g are determined in pre-launch calibrations. Because the sensor changes affecting both the Earth and solar measurements cancel in the ratio, the diffuser plate reflectivity, $\rho(t)$ is the quantity that is critical for the time-dependent calibration of the normalized radiances.

Monitoring of diffuser reflectivity is carried out periodically by deploying the Reference diffuser. The initial deployment frequency will be once every 6 months, and may decrease once adequate statistics of Working diffuser change $\rho(t)$ are obtained. A more detailed discussion of diffuser monitoring follows below. Diffuser deployment frequencies are described in ICSR-8110501 . We expect several percent changes in the Working diffuser. Though we do not expect these changes to significantly affect ozone, our plan is to provide for corrections for diffuser change once the change exceeds a threshold amount. The threshold value will be determined based upon the resulting ozone error.

The expression for normalized radiances $I^m(t)/F^m(t)$, given in Equation 85, implies that time-dependent calibrations (apart from diffuser changes) are obtained by merely computing the ratio of sensor radiance signal to sensor irradiance signal. But this is not possible, since solar irradiance measurements are obtained only once per week. The solution is to characterize changes in the solar signal in order that the ratio can be computed as though irradiance measurements had been simultaneous with Earth radiance measurements. This is performed via trending and extrapolation algorithms.

3.1.3.2 Theoretical Basis: Diffuser Degradation

The multi-diffuser approach to diffuser monitoring relies upon the fundamental assumption that all changes in diffuser reflectance at the sensor wavelengths are a result of solar exposure. No significant changes occur while the diffuser is stowed. Observations of diffuser reflectance change from TOMS, SBUV, and SBUV/2 (Jaross et al. 1998b) show that the primary mechanism for reflectance decreases seems to be photo-deposition of outgassed contaminants. There is no evidence for significant degradation of either a stowed or exposed diffuser surface in the absence of UV radiation. Therefore, the diffuser degradation rate will be a function of the solar measurement frequency. Previous instruments show some evidence that initial rates

depend on the diffuser material (Hilsenrath, 1994), but in the long term, contaminants and UV exposure appear to dominate (Hall, 1994).

In the multi-diffuser approach employed by OMPS for calibration, a quantity derived from solar calibrations is the Working to Reference signal ratio

$$r = \frac{W}{R} \tag{86}$$

where W and R represent the mean signals from the Working and Reference diffusers, respectively, normalized to their baseline (initial post-launch) calibration values. A small fractional change in the value of this ratio, due to the degradation of either surface or a relative goniometric error, is then written as

$$\frac{dr}{r} = \frac{dW}{W} - \frac{dR}{R} \tag{87}$$

The multi-diffuser calibration approach relies on the assumption of exposure-dependent degradation of the flight diffusers. As discussed in ICSR-8110501, almost all evidence indicates that this assumption is valid. This implies

$$W = f(t_W) \qquad\qquad R = f(t_R) \tag{88}$$

where *f(t)* is an arbitrary function of the exposure time *t*. The differential changes are then

$$\frac{dW}{W} = \frac{f'(t_W)}{f(t_W)} dt_W \qquad\qquad \frac{dR}{R} = \frac{f'(t_R)}{f(t_R)} dt_R \tag{89}$$

Since a solar measurement sequence is the same for Working and Reference surfaces, exposure times can be rewritten in terms of the number of Working and Reference measurements, n_W and n_R.

$$\frac{t_R}{t_W} = \frac{dt_R}{dt_W} = \frac{n_R}{n_W} \tag{90}$$

Results from TOMS Cover diffusers indicate that degradation is truly an exponential process (see ICSR-8110501). In the specific case where *f(t)* is an exponential, the change in the working surface reflectance as a function of the change in the quantity *r* is

$$\frac{dW}{W} = \frac{n_W}{n_W - n_R} \frac{dr}{r} \tag{91}$$

For situations where the number of Working measurements far exceeds the number of Reference measurements, as with OMPS, the Working change is nearly equal to the change in the ratio of diffuser surfaces. Any uncertainty ε_r in the value of *r* translates via this relationship to an uncertainty in *W*.

$$\frac{\varepsilon_W}{W} = \frac{n_W}{n_W - n_R}\frac{\varepsilon_r}{r} \tag{92}$$

It is the uncertainty in *W* that ultimately determines the long-term calibration uncertainty.

The value of ε_r is actually a time-dependent quantity because, assuming Gaussian statistics, it varies roughly as $\varepsilon_r = \sigma_r/\sqrt{n_R}$. The current operations schedule calls for Reference measurements every 6 months. Thus there will be 2 values of *r* derived per year. Each data point will have a variance σ^2_r associated with it. We will employ linear regression to these data of the form

$$\ln(r) = b \cdot t_R \tag{93}$$

to determine the Working degradation at a time *t*. An uncertainty ε_W can be estimated (see Bevington, for instance) at a time *t* using σ_r and the proposed exposure schedule.

$$\frac{\varepsilon_W}{W} = \frac{n_W}{n_W - n_R}\sigma_b \cdot t \qquad \sigma_b^2 = \frac{1}{\Delta}\sum^{n_R}\frac{1}{\sigma_r^2} \qquad \Delta = \sum_i^{n_R}\frac{1}{\sigma_r^2}\sum_i^{n_R}\frac{t_R^2}{\sigma_r^2} - \left(\sum_i^{n_R}\frac{t_R}{\sigma_r^2}\right)^2 \tag{94}$$

We note that the uncertainty does not depend on the rate *b* of degradation. Each value σ_r depends upon several factors, but is predominantly related to the errors in the goniometric corrections applied to the solar data. Provided that the relationship

$$\frac{\varepsilon_W}{W} > \frac{dW}{W} \tag{95}$$

holds, we do not intend to apply a correction for Working surface degradation.

3.1.3.3 Theoretical Basis: Wavelength Registration

The algorithm's calibration processing determines spectral shifts of the bandcenter wavelengths during the mission, by periodically comparing the OMPS observed solar

spectrum with a standard solar spectrum. Before fitting the observed spectrum with the model spectrum, the algorithm first corrects the wavelengths for doppler shifts induced by motion between the sun and satellite and convolves the standard solar spectrum by the sensor bandpass wavelength response. The best fit model yields the wavelengths. By extrapolating in time from recent solar wavelength calibrations (see Section 3.1.3.5.6), the algorithm predicts the bandcenter wavelengths for the terrestrial observations until the time of the next solar wavelength calibration. The bandcenters are recorded in each Earth SDF.

The sensor bandpass, often referred to as the slit function, is important in model fitting but also because the EDR algorithm must convolve the slit function with the laboratory ozone spectral cross sections in order to accurately measure ozone column amounts for the terrestrial observations. The SDR algorithm assumes that the slit functions for the TC data cells are properly characterized prior to launch. It also assumes that modal values of those functions, the bandcenter wavelengths, are properly established as of the time of the baseline solar measurement. Thus the initial wavelengths, bandpasses, and observed baseline solar spectrum define the baseline wavelength scale.

During the spectral fitting, the standard solar spectrum is convolved with varying FWHM TC pre-launch slit functions, and then sampled at the initial wavelength map of the CCD, so that all determined wavelength shifts are with respect to the initial baseline wavelengths. The initial TC spectral registration will be performed during pre-launch calibrations and also by comparing the baseline solar measurements with the standard spectrum. This initial OMPS observed, calibrated spectrum is referred to as the reference spectrum. However, because of the higher spectral resolution of the standard solar spectrum, the wavelength monitoring uses it as a comparison to obtain better precision than with the reference spectrum. To establish the accuracy of the initial wavelength baseline, the pre-launch sensor radiometric response is used to compare the observed reference counts with the standard solar spectrum.

The slit functions themselves can change in shape and width during flight, but within the spectral fitting processing, the algorithm derives and compensates for FWHM changes. As a non-parameterized check of the derived wavelength shifts, and as a backup to the spectral fitting in case of poor fitting results, the algorithm uses a subset of solar Fraunhofer absorption lines in the initial standard spectrum in the form of a shift table to gauge wavelength shifts in the observed spectrum during the flight. Slit function changes, though, as they affect the line shift table, must be dealt with through off-line analysis and updates to the shift table.

After a sufficient and parameterized number of wavelength monitorings, the wavelength processing uses the newest sensor radiometric response, rather than the initial radiometric response, to compare the observed solar counts with the model standard irradiances. This accounts for changes in the radiometric response of the pixels (pixel residual non-uniformity: PRNU) that can affect the wavelength monitoring. Thus the wavelength monitoring with fitted model spectra maintains its precision during flight and is the primary wavelength calibrator.

The PRNU changes, however, could pose a challenge for spectral checking using individual lines because the changes can be mistaken for a shift of the Fraunhofer spectrum along a CCD row. Nevertheless, the Fraunhofer structure is well known, so a real spectral shift across the full CCD is well defined and unique. Our line spectral shift checking with approximately ten lines is based on the exceedingly high probability that optical and quantum efficiency changes will not mimic this unique pattern. The result of actual PRNU changes, assuming they are random along rows and columns, is a reduction in the shift resolution precision obtained through the solar Fraunhofer line shift technique.

3.1.3.4 Calibration Record Processing

The processing flow for calibration data shares many elements and proceeds in much the same way as for earth-view data (Section 3.1.2). A fundamental difference is that calibration data are not binned prior to downlink from the spacecraft. Also, several of the data corrections are derived from the calibration data (e.g. dark signals), so these corrections would not always be applied as they are for earth-view data.

There are two basic parts to SDR processing of calibration data: record processing and trending. The former refers to processing of data as it is encountered in the RDR. This data flow is illustrated in **Figure 3.1-15a**. Automated trend analysis of calibration data, shown in **Figure 3.1-15b**, will occur on a routine (at present, weekly) basis. We begin by describing record processing steps.

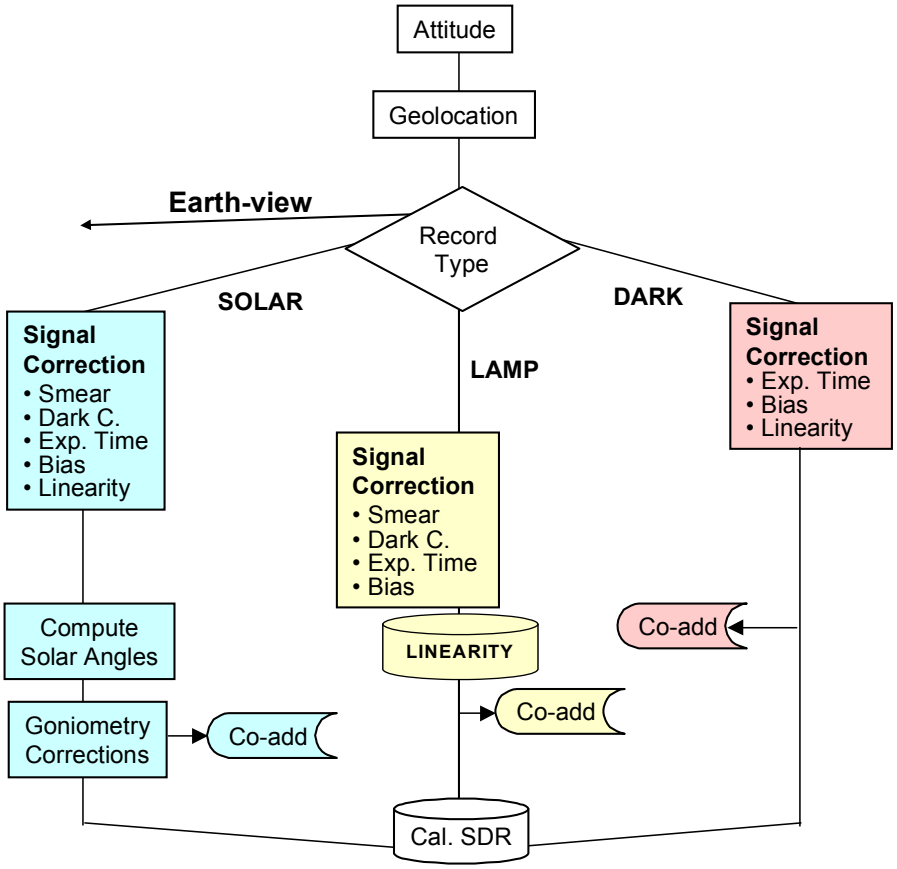

Figure 3.1-15(a). SDR processing flow for calibration records

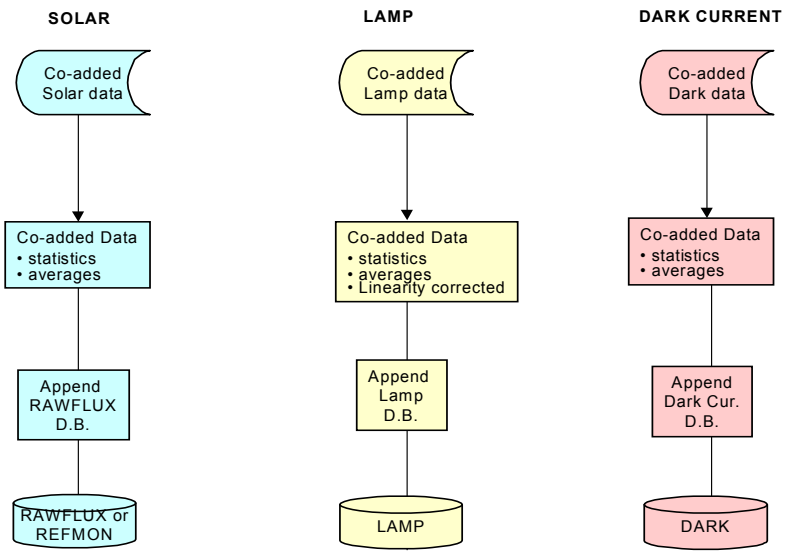

Figure 3.1-15(b). SDR processing flow for calibration records (continued)

3.1.3.4.1 Database Input

Information stored in databases is required for calibration data reduction. Before processing Earth SDR data for each day, these databases are read for the appropriate day and stored in memory for use on all Earth data observed on that day. While Figure 3.1-15 indicates three required databases, in fact dark currents and bad pixels are determined from the current set of calibration RDF dark data if they exist; otherwise the most recent database values are used. The goniometry data are only ingested when calibration data are encountered.

3.1.3.4.2 Limit Checks on Input RDR Data

The RDR header quantities, such as sensor status, are written into the output SDRs for the corresponding input RDR. The sensor status values are also recorded in the appropriate calibration databases, but because a calibration record can span a range of time the sensor status values in the databases are an average over the calibration measurement period represented by the particular database record.

3.1.3.4.3 Initial Signal Corrections

Data corrections will begin once the record type is determined. Section 3.1.2.7 describes these corrections in more detail. These corrections are, for the most part, the same as for Earth-view data except for the linearity correction which is not needed for the EV data. When computing signal corrections, the SDR algorithm scales data counts by the ratio of integration times, data bin size, and number of

image frame coadds to obtain the proper corrections. Bias, dark, and smear corrections are done independently for each CCD half of the image. Table 3.1-3 summarizes the SDR signal corrections performed by the SDR algorithm.

Table 3.1-3. Signal corrections applied to various data types

	Earth	*Solar*	*Lamp*	*Dark*
Bias	X	X		X
Dark	X	X		
Smear	X	X		
Linearity		X		X

3.1.3.4.4 Linearity

The linearity of the sensor radiometric response passing through signal amplifiers, is monitored using a series of lamp exposures of various times, and therefore varying count levels. To assess nonlinearities in the recorded count levels, the SDR algorithm processes and analyzes the RDR lamp calibration data, calculating separately for each image half the linearity response which is stored in the LINEARITY database. The approach to analyzing the LED data and generating the linearity correction table is based on the BATC's LED database algorithm.

The raw lamp data are first corrected for smear, bias, and storage region dark current by subtracting the lowest ramped integration time image, and then averaged to get the average count for each ramped integration time image. A local quadratic fit to the average count levels in the reference integration time frames as a function of time stamp is used to determine the weights to be applied to the ramped integration times (*Tweighted*) to compensate for any lamp intensity instability. This produces the paired values of the corrected average counts (*Qreal*) and the corresponding weighted ramped integration times.

The linearity LUT is constructed from uncorrected ramped integration time data since it is the raw, uncorrected signals that are non-linearity corrected in the on-board software chain using the linearity LUT. To generate the linearity table, two tie points where the measured count levels equal to the ideal count values need to be defined. The lower tie point (Q_{low}), is defined as the count level at the lowest integration time, which is approximately equal to the values of the biases. The upper tie point (Q_{up}), is a tunable algorithm parameter with a default value of 12000 counts, which was chosen to match that used by the OMPS data analysis team. Using all the data points of *Tweighted* vs. *Qreal*, the point in *Tweighted* corresponding to *Qup*, is located using a local quadratic fit. Between these two tie points, *Qup* and *Qlow*, a linear slope is

determined and is used to calculate the *Qideal* values corresponding to the weighted ramped integration times.

Once the array of *Qideal* corresponding to *Qreal* has been calculated, the LUT is constructed by using a local quadratic fit to each 3-point neighborhood [*Qideal*[i-1], *Qideal*[i], *Qideal*[i+1]] surrounding the interval *Qideal*[i] ≤ IndexLUT ≥ *Qideal*[i+1], where IndexLUT are the indices of the LUT (i.e. values from 0 to 16,383). For values of *Qideal* above 16383, the LUT will contain values of 16,383 since this is the 14-bit limit of the analog to digital converter.

The linearity tables created from the new calibration data will be reviewed and verified outside of the operational SDR algorithm. Once approved, it will be converted to the appropriate format for uploading to the spacecraft. The switch to the new linearity tables will occur in the ground SDR algorithm processing only when the earth view data to be processed are produced with the new linearity tables. Similarly, the calibration data is corrected for nonlinearity effects using the equivalent LUT of the flight version of the linearity table. The LUT is read at the beginning of the processing and is not automatically updated by the new calibration data.

3.1.3.4.5 Geolocation

Sensor geolocation (Section 3.1.2.5) is the same for Earth-view and calibration data, except that azimuthal and zenith scattering angles are not computed for the calibration data. Spacecraft-centered sun angles are needed for the goniometric correction of solar data. The SDR algorithm computes and stores the average subsatellite position separately for each kind of calibration data. It also calculates and stores the geocentric position and velocity vectors of the sun. Satellite velocity is subsequently used for computing the satellite-sun radial velocity used in spectral monitoring.

3.1.3.4.6 Goniometric solar corrections

A correction $1/g(\alpha,\beta)$ is applied that accounts for variations in irradiance sensitivity as the spacecraft-centered solar angles α and β change. This is a dimensionless quantity with a value of 1 at the angle at which radiometric calibrations were performed prior to launch. It will vary from pixel to pixel, i.e. spatially and spectrally. The pixel dependence of the correction can be established from pre-launch characterizations. If $C^i(t_{rep})$ represents the signal-corrected counts during report period t_{rep} with signal corrections applied, then the quantity $T(t_{rep})$ is written for each pixel into each SDR.

$$T\left(t_{rep}\right) = \frac{1}{T_o}\frac{C^i\left(t_{rep}\right)}{g\, t_{rep}} \tag{98}$$

In the equation, $T_o = C^i(0)/gt_{rep}$ refers to the fully corrected signal averages from the baseline solar measurement. The quantities T_o are stored as the first record in RAWFLUX.

Operational implementation

TC sensor has 2 diffusers – work and reference. Each diffuser may take one of 7 positions during a solar calibration. Pre-launch characterization covers both diffusers and their nominal positions, as well as the range of solar angles, which may be seen during calibration on a given orbit. Characterization is done in the sensor coordinates.

The goniometry database input consists of these 2x7=14 BRDF tables, of corresponding solar angle tables, of actual diffuser positions for the measurement in the motor counts, and of the sensor on spacecraft mounting matrix. The database is preprocessed by transforming the BRDFs in the local diffuser coordinate system. This streamlines data processing and makes possible a fusion of BRDF data in order to better cover the solar angle range.

The goniometry algorithm gets information about the kind of diffuser used and about the diffuser position for a particular solar frame (RDR provides information about actual position of diffuser in the form of the motor counts; it may differ from the nominal position). Using this information, the algorithm transforms the solar angles in the spacecraft coordinates into the local diffuser coordinates and selects an appropriate BRDF table. It does the table interpolation and applies the goniometry correction to the flux_data and flux_err files. Applied goniometry coefficients are stored in gon_par file in order to make possible a backprocessing of the flux data if necessary.

Flag information

The goniometry routine populates 2 flag variables. It also skips correction if sun was occulted by diffuser and passes the information to SDR algorithm to ignore this solar frame.

The variable occult_flag checks for the occultation of sun by the rotor and by Earth (night time calibration). It may have values 0, 1, 2, and 3 for each solar frame. 0 means that there is none of the above occultations, 1 means that the occultation by Earth takes place (night time), 2 means that the occultation by rotor occurred, and 3 means presence of both kinds of occultation. If this flag is set, the solar frame is ignored by SDR algorithm

The second variable, diff_incid_angle, passes the value of the solar incidence angle on diffuser to SDR algorithm. SDR algorithm may issue a warning if the solar rays are almost parallel to diffuser surface, because BRDF data may be too noisy at such angles or an extrapolation may occur.

3.1.3.4.7 Data co-addition and statistics

(***The measured data are co-added onboard the spacecraft before downlinking to the ground. As a result, there is no need for co-adding the signal by the ground SDR processing. More importantly, it is no longer possible to calculate the statistics (e.g., standard deviation) from these effectively single measurements. Nevertheless, this section (3.1.3.4.7) is kept for the sole purpose of reference.***)

Following the completion of signal processing of all RDRs of each data type in an RDF, the SDR algorithm coadds independently all SDRs of each data type: solar, dark, and lamp. The dark data $C^d(t)$ are summed and averaged to obtain a coadded dark calibration image.

$$D_{j,k} = \frac{1}{n_{rep}} \sum_{1}^{n_{rep}} \mathbf{L}\left(C^d_{j,k}\right)\ C^d_{j,k}\left(t_{rep}\right) \tag{99}$$

for an average exposure time of:

$$t_D = \frac{1}{n_{rep}} \sum_{1}^{n_{rep}} \left(t_{rep}\right) \tag{100}$$

The factor $\mathbf{L}(\ C^d)$ is the linearity correction read from the LINEARITY database. Lamp data $C^l(t)$ are coadded for each different integration time to obtain lamp count rates

$$L_{j,k} = \sum_{1}^{n_{rep}} \mathbf{L}\left(C^l_{j,k}\right)\ C^l_{j,k}\left(t_{rep}\right) / \sum_{1}^{n} t_{rep} \tag{101}$$

Solar data are coadded separately for each diffuser position *d*. Since diffuser positions probably will overlap slightly, this will likely result in multiple database entries for some pixels. The summation follows from Equation 98.

$$T\left(d\right)_{j,k} = \frac{1}{n_{rep} t_{rep}\, T_o} \sum_{1}^{n_{rep}} \frac{C^i_{j,k}\left(t_{rep}, d\right)}{g_{j,k}\left(d\right)} \tag{102}$$

A linearity correction $\mathbf{L}$ should be applied in Equation 102 as in Equation 99, if none is applied in the flight hardware (see discussion in Section 3.1.3.4.3).

Co-added calibration data are averaged and standard deviations are calculated. Lamp results L_{jk} are appended to the LAMP database and dark results D_{jk} are

appended to the DARK database. Solar results T_{jk} are appended to RAWFLUX after multiple diffuser positions have been combined. All records are uniquely identified by pixel location, orbit number, day, and year. Of the three databases, only RAWFLUX contains normalized quantities. In particular, the entries representing the baseline solar measurement, *T(t=0)*, are all 1.

3.1.3.4.8 Combine solar diffuser segments

After the SDR algorithm goniometrically corrects the individual solar segments, the algorithm assembles them into one solar image by masking the CCD pixels in each segment and averaging data from multiple images so as to include only the desired pixels that are fully illuminated by the sun. Also, transient high pixels in a solar segment are flagged by statistically comparing the median counts in a spectral row to individual pixel counts in that row. If good pixel data is not available from another solar segment taken at the same diffuser position, the pixel is excluded from further calibration analysis of the current set of calibration, but because it is a transient, the pixel is not identified as bad in the bad pixel databases. Results per pixel for the solar data are appended to the RAWFLUX database, which contains the full, combined solar data over the whole CCD field. If a majority of diffuser segments are present but others are missing, the SDR algorithm reads the newest existing solar diffuser segments from the RAWFLUX database and substitutes these for the missing one in the current solar calibration.

3.1.3.4.9 Solar spectral correction

Each record of the RAWFLUX database contains the normalized, averaged, corrected solar signal for every pixel during a single calibration sequence. This quantity *T(t)*, defined in Equation 98, can be expressed in terms of the variables in Equation 84, where *t* refers to the calendar time of the calibration sequence.

$$T(t) = \frac{C^i(t)}{T_o\, g(t)} = \rho(t)\ \tau(t) \frac{F^m(t,\lambda)}{F^m\left(0,\lambda^r\right)} \tag{103}$$

The quantity *T(t)* represents two distinct components of solar measurements, sensor change and irradiance change. We emphasize this separation by re-writing the RAWFLUX entries as

$$T(t) = \rho(t)\ \tau(t)\ \gamma \frac{F^m\left(t,\lambda^r\right)}{F^m\left(0,\lambda^r\right)} \tag{104}$$

where the factor γ is an estimate of the following ratio.

$$\gamma(\lambda,\lambda^r) \approx \frac{F^m(\lambda)}{F^m(\lambda^r)} \tag{105}$$

This factor, defined in Equation 105, describes the apparent change in solar irradiance resulting from spectral shifts of pixel bandcenter wavelengths. The quantity γ is estimated during wavelength trending and written in the WAVELENGTHS database. If the wavelength determination is imprecise, or very few wavelength monitoring exists, the trending sets γ = 1 so as to avoid corrupting the fluxes. Using estimates of γ(t) and ρ(t) (see discussion in Section 3.1.3.5.3 and 3.1.3.5.9), the SDR algorithm creates a second database called FLUX, which contains the quantity

$$T'(t) = \tau(t)\frac{F_m(t,\lambda^r)}{F_m(0,\lambda^r)} = \frac{T(t)}{\rho(t)\,\gamma(t)} \tag{106}$$

for each pixel. The values T'jk(t) nearly describe the response change of each pixel τjk(t) because the solar output varies little above 300 nm. It is these values that are the basis for radiometric trending. If the wavelength trending is too imprecise, as parameterized by a threshold uncertainty, then the correction factors are set to 1.0, effectively keeping FLUX vales equivalent to RAWFLUX values for that calibration.

3.1.3.5 Calibration Trending

Calibration data are analyzed in more detail upon completion of the calibration SDR processing using results stored in the LAMP, RAWFLUX, and DARK databases. No information from the RDF or SDF is utilized. It is important to note that for this reason calibrations of a particular type cannot be split across multiple RDFs. The flow for trending is shown in Figure 3.1-16. The purpose of trending is to provide an estimate of the calibration information at the time the earth observation is made. The process of extrapolating existing calibration results into the future has the added benefit of smoothing out random variations in those data.

3.1.3.5.1 Bad pixel update

The bad pixel database BADPIX is updated based on information from dark data. Potential bad pixels are output based on threshold values. These threshold values are tunable and set the upper and lower bounds of acceptable values (nominally set at 0 and 600). After HITL (human in the loop) review, pixels from this potential list can be accepted or rejected as bad. If accepted as bad, the EV_sampletable will be updated to exclude the newly determined bad pixels from both onboard and ground data processing.

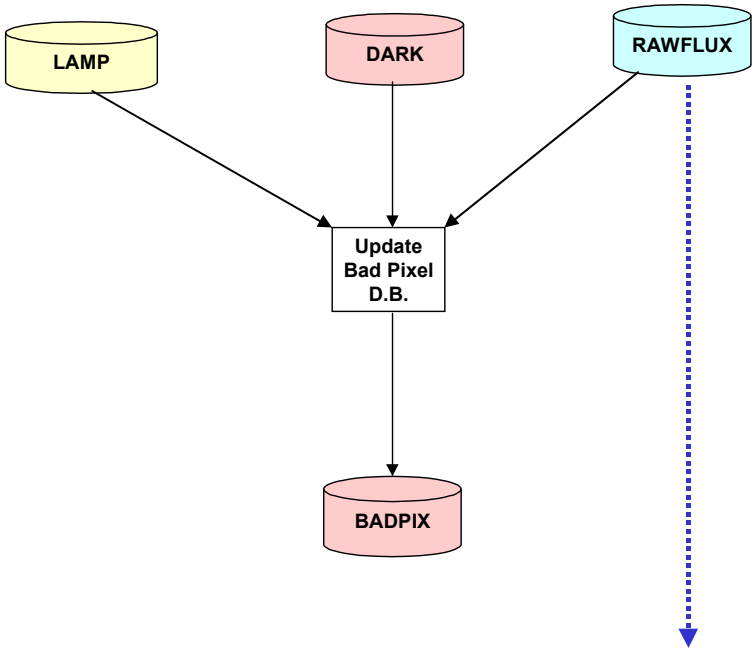

Figure 3.1-16 (a). SDR flow for trending calibration data

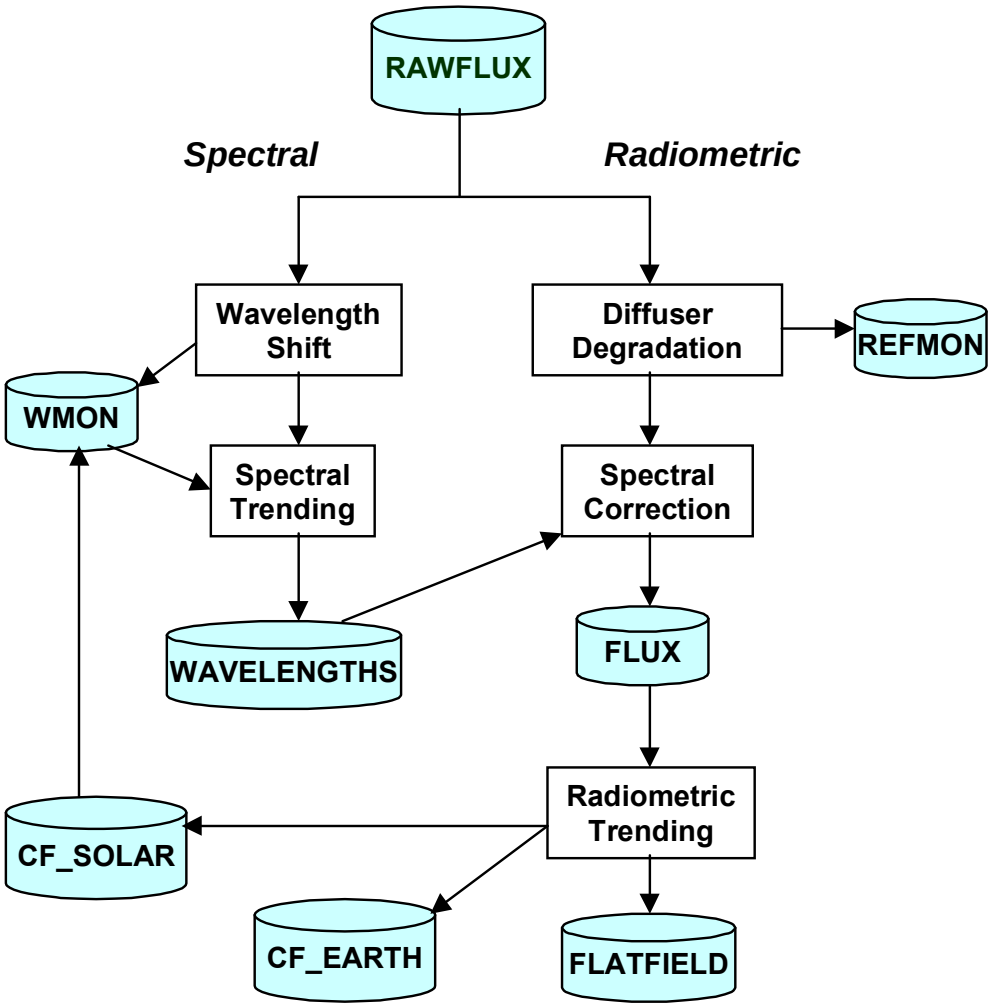

Figure 3.1-16 (b). SDR flow for trending calibration data

3.1.3.5.3 Diffuser Degradation

The basic approach for determining Working diffuser changes is described in Section 3.1.3.2, where the Working to Reference signal ratio

$$r_{jk} = \frac{W_{jk}}{R_{jk}}$$

(107)

was introduced. W_{jk} and R_{jk} represent the individual pixel signals from the Working and Reference diffusers, respectively. The operational algorithm will compute the values of W_{jk} and store them in RAWFLUX. R_{jk} is computed in an off-line process from the reference solar calibration data. Each pixel along a row (spectral dimension) measures a unique diffuser change. Since the solar diffusers are near a sensor aperture, each pixel's view of the diffuser surface overlaps that of adjacent pixels. Consequently, the values r_{jk} from many pixels along a column k can be combined without loss of information. Since optical degradation is thought to be a smooth, monotonic function of wavelength, r_{jk} values can also be combined in the spectral direction. The width of these spectral and spatial bins will depend upon the actual sensor performance.

$$r_{JK} = \frac{1}{n_{row} n_{col}} \sum_{j} \sum_{k} r_{jk} \tag{108}$$

The resulting averages r_{JK} would be used for off-line analysis of diffuser change. This analysis should ultimately produce an estimate for $\rho(t)$, determined by

$$\rho(t,\lambda) = 1 - \left(\frac{dW}{W} \right) \tag{109}$$

where dW/W is determined via Equation 91. The value of $\rho(t,\lambda)$ should be sampled at the appropriate band center wavelengths and entered into a database. The values ρ_{jk} are initially all set to 1. With the proposed weekly solar measurement schedule, we do not expect significant degradation of the Working diffuser. The historical TOMS sensor diffuser data suggest the degradation that does occur has a linear wavelength dependence. The result is that EDR ozone products, computed using a triplet formulation, are insensitive to these changes. Should the need arise, the algorithm described above can be easily implemented.

It should be pointed out that the above analysis designed to monitor and characterize the solar diffuser degradation is not implemented in the operational algorithm. Instead, the analysis will be performed off-line by the cal/val and long term monitoring team. Once the solar diffuser surface degradation has been quantitatively characterized, the solar diffuser BRDF values of the working diffuser will be adjusted to bring the baseline working solar measurement into agreement with the baseline reference solar measurement.

3.1.3.5.4 Radiometric calibration

The radiometric calibration of the earth-view radiances, described in Equation 83, amounts to multiplying corrected counts by an initial calibration constant and dividing by an estimate of the pixel response change $\tau_{jk}(t)$. The values $T'_{jk}(t)$, stored in FLUX, are a close approximation of response change, differing only when the solar output changes. In the BUV technique it is not possible, nor is it necessary, to separate sensor and solar changes. However, the resulting radiance $I^m_{jk}(t)$ (Equation 83) is in error by the amount that the solar output changed at the wavelength in question. Only the normalized radiance, in Equation 85, is a properly calibrated quantity.

Experience with TOMS (see ICSR-8110501) has demonstrated that a linear time dependence is quite adequate for trending over one week intervals. The number of previous data values included in the regression is typically less than ten. But the optimum number depends upon how the sensor response actually changes with time. Each regression is extrapolated in time to yield estimates of $\tau_{jk}(t+i)$, where *i* is the day number following the last solar measurement. For a weekly measurement schedule, *i* begins at 0 and need not exceed 7, though it is safer to generate more values and simply overwrite them as new solar measurements are made.

The SDR trending algorithm derives the calibration factors $\tau_{jk}(t+i)$ from $T'_{jk}(t)$ in an indirect manner. The temporal variations in TOMS solar data exhibited a significant degree of correlation between channels, with the result that channel ratios were less noisy than single channels. It follows, and was verified in the TOMS data, that the extrapolated channel ratios will remain closer to the true ratios than will the ratios of extrapolated single channels. With this in mind, the TC radiometric trending also operates on pixel ratios (along a row). To be precise, it operates on the pairs and triplets chosen for use in the EDR algorithm (Section 2.4.9). That algorithm constructs a triplet radiance (see Equation 143) from a linear combination of three radiances. The SDR trending algorithm performs an equivalent combination of T'_{jk} values for use in trending. Let *s*, *m*, and *l*, represent short, middle and long wavelength values of T'_{jk}. Then the pair and triplet values, *p* and *t*, are defined as

$$p = \frac{m}{l} \tag{110}$$

$$t = \frac{s/l}{1-\alpha(1-p)} \qquad \text{where} \qquad \alpha = \frac{\lambda_l - \lambda_s}{\lambda_l - \lambda_m} \tag{111}$$

Following the trending, a simple inversion of the combination described in Equations 110 and 111 yields the trended channels *s′*, *m′*, and *l′* (*l′* is simply the trended value of *l*) of $\tau_{jk}(t+i)$.

$$m' = l'\ p' \tag{112}$$

$$s' = l'\ t'\left[1-\alpha\left(1-p'\right)\right] \tag{113}$$

Of the tremendously large number of triplets possible with 192 spectral channels, the EDR algorithm uses only 48. These are defined in Section 2.4.9 and specifically in Table 2.4-1. The SDR must trend exactly those 48 combinations. For the remaining channels, the choice is arbitrary. The following prescription should be used for combining the remaining pixels.

Short: λ< 330 nm

Middle: 330 nm < λ < 340 nm

Long: λ> 340 nm

All remaining pairs might use a single long wavelength, and all remaining triplets might use a single pair.

The algorithm computes calibration factors $A_{Jk}(t+i)$ by binning the extrapolated responses $\tau_{jk}(t+i)$ in each of the macropixel:

$$A_{Jk}\left(t+i\right) = \frac{1}{nmacro}\sum_{j}\tau_{jk}\left(t+i\right) \tag{114}$$

where *nmacro* is the number of pixels made up of the *Jth* macropixel, as derived from the macropixel sampletable. The binning is fewer than *nmacro* if the EV_sampletable indicates that the flight software will have excluded specific pixels in its binning. The daily values of A_{Jk} for each macropixel are stored in the database CF_EARTH. These daily values can be overwritten if a better estimate is obtained, but only prior to their use in the Earth SDR processing.

As mentioned earlier, the SDR algorithm has the flexibility built in either to apply or not to apply calibration factor correction during calibration, depending on the accuracy of the calibration factor computed from trending the solar data.

3.1.3.5.5 Flat Field update

The flight hardware sums the signals from *nmacro* pixels along a CCD column in a process referred to as binning. The radiance calibration constants k^r and calibration factors *A*, which are derived per pixel, are similarly binned in the SDR algorithm (see Equation 68). However, a significant radiometric error can occur if the individual pixel signals are binned prior to radiometric correction. This follows because

$$\sum_j k_j C_j \neq \sum_j k_j \sum_j C_j \tag{115}$$

To correct this error, a flat field correction is applied in the flight hardware prior to binning earth-view signals. The correction η_{jk} equalizes the pixel signals using the relative photon response non-uniformity (PRNU) as a weight.

$$\eta_{jk} = \frac{\frac{k^r_{jk}}{\tau_{jk}}}{\frac{1}{nmacro}\sum_j \frac{k^r_{jk}}{\tau_{jk}}} \tag{116}$$

The PRNU is estimated as k^r/τ where τ is obtained from an unbinned version of the CF_EARTH database. Similar to calibration, the SDR algorithm has the flexibility built in either to apply or not to apply calibration factor correction when computing the flat filed table, depending on the accuracy of the calibration factor computed from trending the solar data. As before, the sum is over fewer than nmacro when EV_sampletable indicates a flight hardware pixel rejection. An important point concerning η_{jk} is it does not alter the binned signal, so the calibrations applied to the data cell by the Earth SDR algorithm need not be altered. Also, it does not alter the relative calibration between binned rows and columns.

The algorithm computes a full set of η_{jk} and appends the results to the FLATFIELD database. Thus there is a one-to-one correspondence with records in the RAWFLUX database. The contents of the FLATFIELD database can be periodically loaded into tables for uplink to the flight hardware as deemed necessary. Since changes in PRNU are primarily the result of optical degradation, which has a broad spectral dependence, weekly uplinks to flight hardware are more than adequate.

3.1.3.5.6 Wavelength Registration - Operational

The operational algorithm computes bandcenter wavelength shifts by varying the standard solar irradiances using several model parameters, and then minimizing the differences between these model irradiances and the observed irradiance changes over the entire usable spectrum. The algorithm is based on Caspar and Chance

(1997) [Caspar, C. and Chance, K., GOME Wavelength Calibration Using Solar and Atmospheric Spectra, Proc. 3rd ERS Symposium (ESA SP-414), p. 609, 1997.]

Additive spectral shifts and multiplicative shifts are primary spectral parameters that are applied to the standard spectrum to obtain a model spectrum. The derived shifts are relative to the wavelength scale that includes the grating dispersion. The fitting parameters account for grating rotations and focal plane shifts in the dispersion direction. The latter two effects are non-linear in wavelength, as given by the dispersion relation. But the change in the dispersion from the short to long wavelengths is about two percent, so a linear approximation is valid.

To account for broad, spectrally dependent diffuser and sensor response changes, one can vary multiplicative parameters for a cubic scaling in wavelength of the reference spectra by a polynomial.

$$P(\lambda) = a + b\lambda + c\lambda^2 + d\lambda^3 \tag{117}$$

In practice, the implemented Algorithm fitting as initially configured uses a linear subset of the parameters. To compute optimal additive and multiplicative spectral shifts that are actually present in the observed OMPS TC spectrum, the algorithm calculates a minimum chi-squared statistic over all wavelengths in common between the shifted F^s and model F^r spectra with noise σ.

$$\chi^2(\delta,\beta) = \sum_{\lambda} \left\{ \frac{F^s(\lambda) - P(\lambda)\cdot F^r(\lambda[1+\beta]+\delta)}{\sigma} \right\}^2 \tag{118}$$

$$\Delta_{\min} = \arg\min_{\delta}\{\chi^2(\lambda[1+\beta]+\delta)\} \tag{119}$$

$$\mathrm{B}_{\min} = \arg\min_{\beta}\{\chi^2(\lambda[1+\beta]+\delta)\} \tag{120}$$

where $\Delta_{\min}$ and $\mathrm{B}_{\min}$ are the resulting additive and multiplicative shifts, respectively.

The model spectrum F^r used in the regression is the convolved standard spectrum sampled at the baseline TC bandcenter wavelengths. At t=0, this should be equivalent to what is termed the reference solar flux. The current shifted spectrum containing radiance changes due shifts and not changes in the sensor response can be expressed in terms of the reference spectrum, the newest solar measurement ratio, and calibration.

$$F_{jk}^{s}(t) = T_{jk}(t)\, F_{jk}^{r}(0) k_{jk}^{i} / \tau_{jk}(t) \qquad (121)$$

By radiometrically calibrating the measured solar signal, the sensor fixed pattern noise and radiometric response are removed. The SDR algorithm processes solar data in the beginning of the flight with $\tau_{jk}(t)$=1 . After processing a parameterized number of wavelengths monitorings during flight to attain the required precision, the Algorithm then uses the newest previous *radiometric* calibration $\tau_{jk}(t-1)$ to account for the sensor response, independent of wavelength shifts. The wavelength monitoring obtains the radiance calibration factors by reading them from the CF_SOLAR database, which is based on the radiometric database FLUX.

Before performing the shift analysis, previously identified bad pixels are interpolated across or excluded by weighting them by an uncertainty equal to their value. The wavelength algorithm computes spectral shifts, additive and multiplicative, separately for each spatial row of the unbinned solar RDR data. In order to reduce the effect of sensor noise and the aliasing of PRNU changes into spectral shifts, the algorithm spatially averages the resultant shift information across the 20 pixels in a terrestrial data cell before storing it in the shift monitoring database WMON. Thus, each spatial region on the CCD, as defined by the Earth-view binning prescription, has a spectral registration determined using the measured solar spectrum in that region. Stored uncertainties in the shifts are also calculated as the standard deviations across the spatially averaged region.

3.1.3.5.7 Discrete Spectral Lines

As a non-parametric measure of the wavelength shifts, the algorithm also calculates shifts of narrow spectral absorption lines at discrete wavelengths across the solar spectrum. This has the advantage that no assumptions are needed regarding the nature of the sensor spectral dispersion. In contrast to the parametric shifts derived from the continuum, shifts are derived by comparing the observed irradiance changes with a set of irradiance changes stored in a pre-computed reference shift table $M_{j\kappa\delta}$, where δ identifies the grid of shifts and κ refers to detector columns associated with specific Fraunhofer line. The row index *j* is introduced because of the slight spectral smile (row dependence) at the TC focal plane.

A response change, $d_{j\kappa}$, is determined from the RAWFLUX entries $T_{j\kappa}$ according to

$$d_{j\kappa}(t) = 1 - T_{j\kappa}(t) \qquad (122)$$

To remove broad spectral changes in diffuser and sensor response, the observed changes on each side of a line with center at pixel κ are subtracted from each other.

$$D_{j\kappa} = d_{j\kappa-1} - d_{j\kappa+1} \tag{123}$$

The contents of the table $M_{j\kappa\delta}$ are the computed column signal differences D for absorption lines κ with varying wavelength shifts S_{δ}. Linear interpolation of the observed difference in the shift table yields the estimated spectral shift $S_{j\kappa}$ at each pixel j,κ.

$$S_{j\kappa} = \frac{D_{j\kappa} - M_{j\kappa\delta-1}}{M_{j\kappa\delta} - M_{j\kappa\delta-1}} \cdot \left(S_{\delta} - S_{\delta-1}\right) + S_{\delta-1} \tag{124}$$

As with the parametric method, small-scale changes in diffuser and sensor response are removed by spatially averaging the shift results over rows *j*. The shift linearity with wavelength is checked with a linear regression fit to the line shifts. Individual line shifts, group shift values, uncertainties, and linear fitting parameters are stored in the WMON database. The linear regression and individual line shifts thus provide a comparison for the assumed linear shift that was derived previously in the operational algorithm.

3.1.3.5.8 Wavelength Trending in Time

For every day of the year, the wavelength trending algorithm predicts the spectral wavelengths for each Earth-view data cell. Bandcenter wavelengths are determined by adding a derived shift to the baseline wavelength scale. Trending is only performed on results from the operational method described above. If the wavelength fitting produces poor fits, as parameterized by a χ^2 threshold, the SDR algorithm substitutes the wavelength shift parameters that were derived from the discrete line-shift method.

Following updates to the WMON database, the algorithm performs individual regressions in time for the additive and multiplicative shift terms (see Equations 119 and 94) at each of the 35 spatial locations. Regression results are extrapolated and the wavelengths are evaluated daily for at least 2 weeks into the future. The Earth SDR algorithm reads these predicted values from the WAVELENGTHS database to provide spectral registration of Earth data cells in each Earth SDF. Once a WAVELENGTHS value is actually used for the output SDRs, the value in the database remains unchanged to serve as an additional history of the SDR spectral calibration. However, when the WMON database is subsequently updated, the trending algorithm overwrites outdated predicted values in WAVELENGTHS that were never used.

Regressions of the additive and multiplicative shift terms take the following forms.

$$\Delta_{Jk}(t) = \delta_{Jk} + \delta'_{Jk}t \tag{125}$$

$$B_{Jk}(t) = b_{Jk} + b'_{Jk}t \tag{126}$$

The daily values λ_{Jk} appended to the WAVELENGTHS database take the form

$$\lambda_{Jk} = \lambda^r_{Jk} + S_{Jk} \tag{127}$$

where

$$S_{Jk}(i) = \delta_{Jk} + b_{Jk}\lambda^r_{Jk} + \left(\delta'_{Jk} + b'_{Jk}\lambda^r_{Jk}\right)\cdot(t+i) \tag{128}$$

and λ^r_{Jk} are the baseline bandcenter wavelengths of the macropixels. As with the radiometric trending, the time *i* refers to the day number beyond the most recent calibration, denoted by *t*. The SDR algorithm computes wavelength precisions by propagating errors in root of the mean square minus the covariance of the linearly dependent additive and multiplicative parameters.

Alternatively, the shifts S_{Jk} can be averaged over spatial locations *J* provided they have no spatial dependence. The resulting values S_k would then be used for all *J* in Equation 127. Recall that the discrete method results are stored as a means of checking spatial and spectral dependence of the shifts.

In addition to long-term drifts and annual cycles in spectral registration, the TC sensor will also experience intra-orbital shifts. These arise from the approximately 1°C thermal cycle of the sensor during the course of an orbit. Such short-term shifts present a challenge to the sensor calibration because they cannot be tracked using solar data. However, the estimate for typical shifts is within acceptable margins if left uncorrected. The baseline SDR algorithm does not register these additional shifts.

We recognize the uncertainty in predicting post-launch behavior, particularly with regards to thermal response. Consequently, we have investigated methods for deriving intra-orbital spectral shifts from Earth-view radiance data. With the exception of minor NO_2 absorption, the O_2-O_2 collisional complex, and the Ring Effect, radiances between 340 nm and 380 nm are spectroscopically similar to the extraterrestrial solar spectrum. If needed, these data can be used to monitor shifts and to provide an adjustment to the database bandcenters. Given the larger uncertainties involved with monitoring earth radiances, the best results will be obtained by parameterizing measured shifts with such variables as sensor temperature. The recommended SDR content contains place holders for these parameters (see Section 3.1.1.2.1).

3.1.3.5.9 Irradiance Shift Factors

Following the bandcenter wavelength prediction, the algorithm computes a set of solar shift factors. In order to derive normalized radiances, as represented in Equation 85, the EDR algorithm must be provided measured irradiances $F^m(\lambda)$ on the same spectral scale as earth radiances. The irradiances are estimated in Equation 83 by scaling the baseline solar irradiances $F^m(\lambda^r)$. The scale factors $\gamma(t)$ describe the change in measured solar irradiance arising from shifts $\lambda(t)$-λ^r, and are defined as follows for each macropixel *J,k*.

$$\gamma_{Jk}\left(\lambda,\lambda^r\right)=\frac{F^r_{Jk}\left(\lambda\right)}{F^r_{Jk}\left(\lambda^r\right)} \tag{129}$$

The irradiances $F^r(\lambda)$ are the standard spectrum convolved with the sensor spectral functions and evaluated via interpolation at the bandcenter wavelengths $\lambda(t)$. The bandcenters are those written in the WAVELENGTHS database. The irradiances $F^r(\lambda^r)$ are the reference spectrum, which uses the baseline spectral registration λ^r. The shift factors γ_{Jk}, registered by day, are stored in WAVELENGTHS database along with the bandcenter wavelengths.

3.2 EDR PRODUCTION

The following sections describe the process of how the total column ozone EDR is produced from the OMPS total nadir column sensor measurements. **Figure 3.2-1** identifies the flow of the algorithm's modules as detailed below. **Table 3.2-1** identifies all the variables used in this algorithm flow-chart. The assumptions contained in the algorithm, data checks, and assessments that are performed in the algorithm are also discussed.

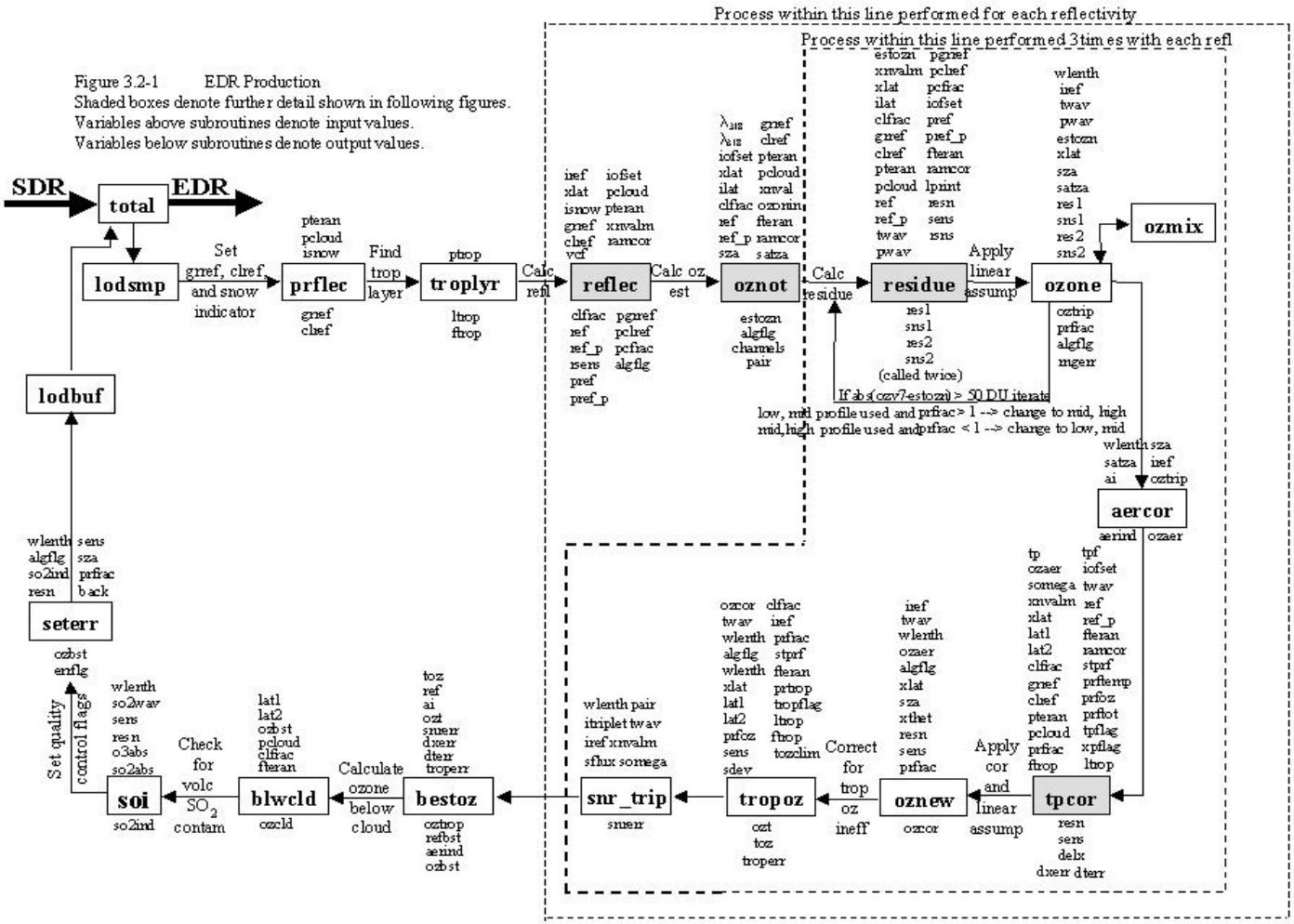

Figure 3.2-1. EDR Production

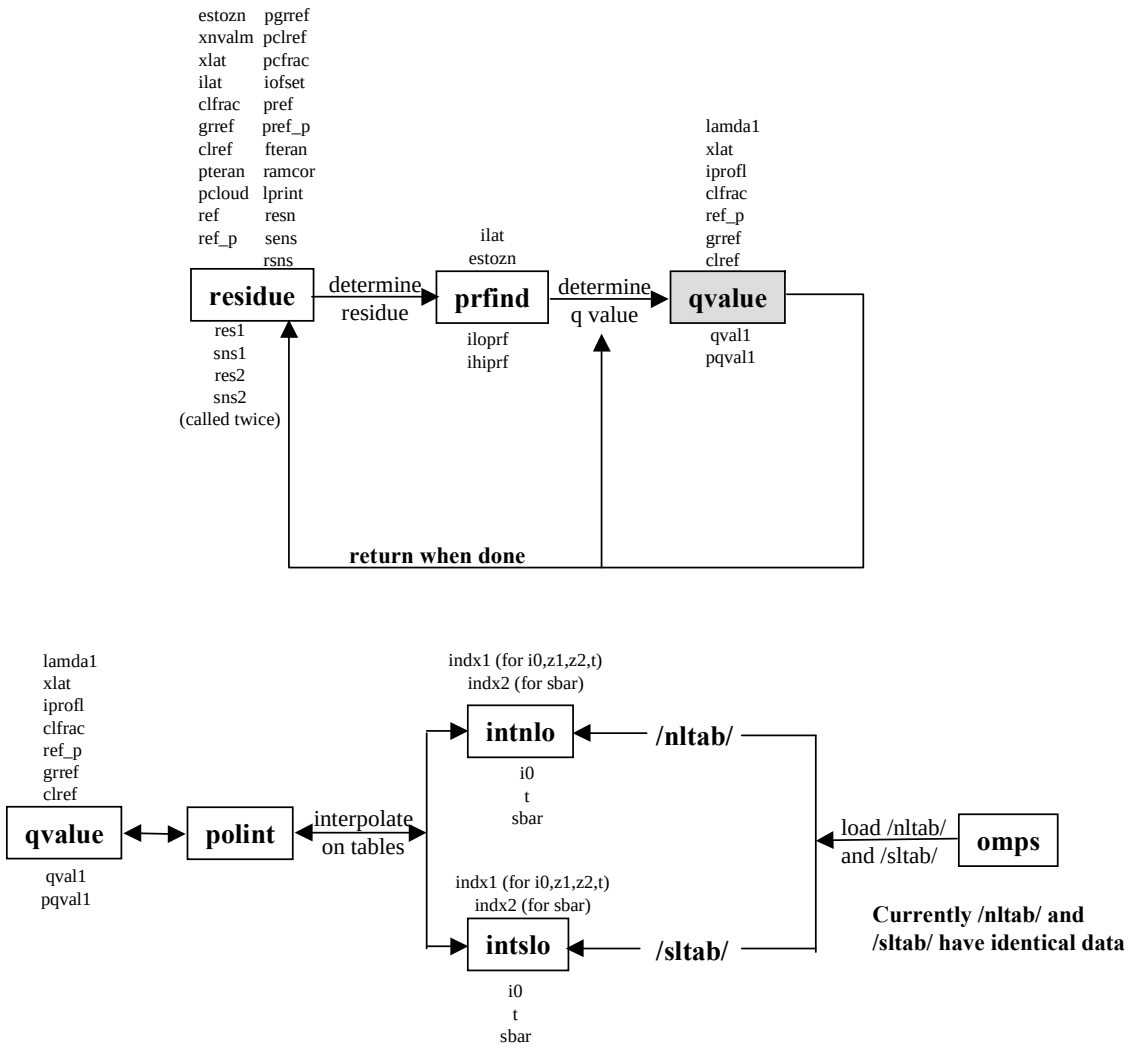

Figure 3.2-1. EDR Production (cont)

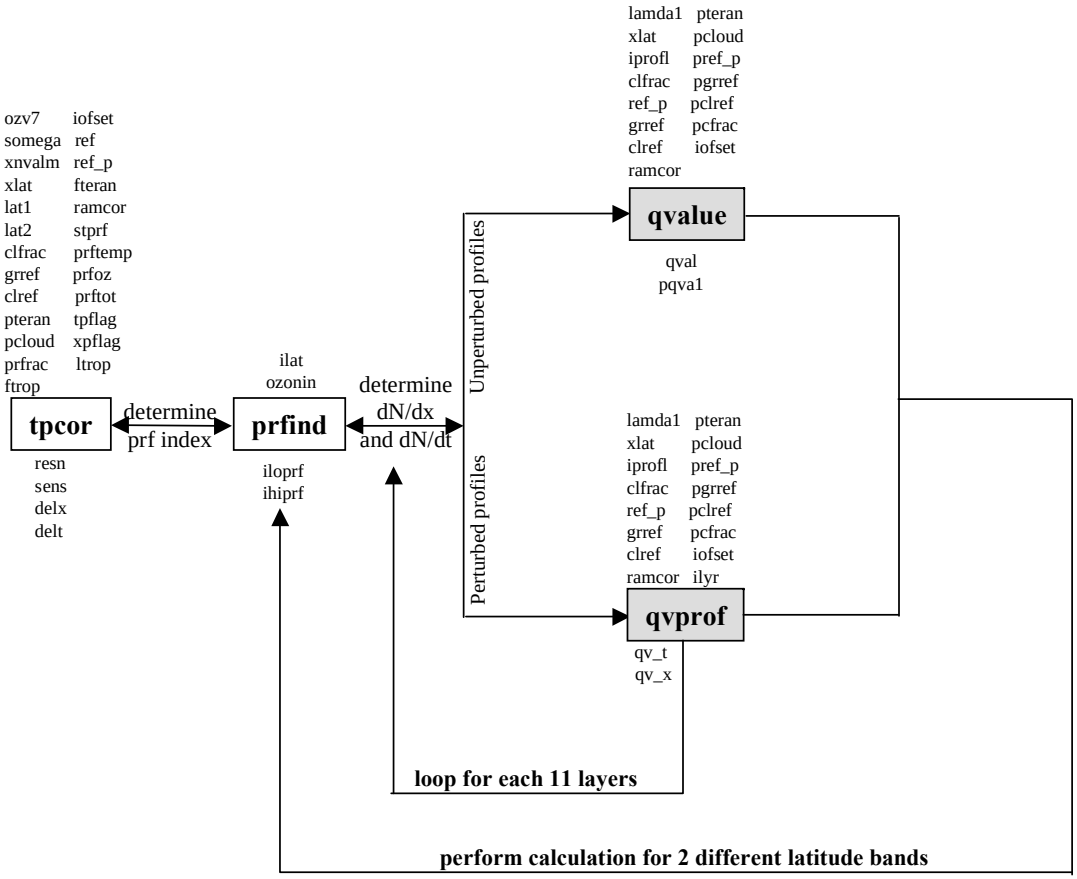

Figure 3.2-1. EDR Production (cont)

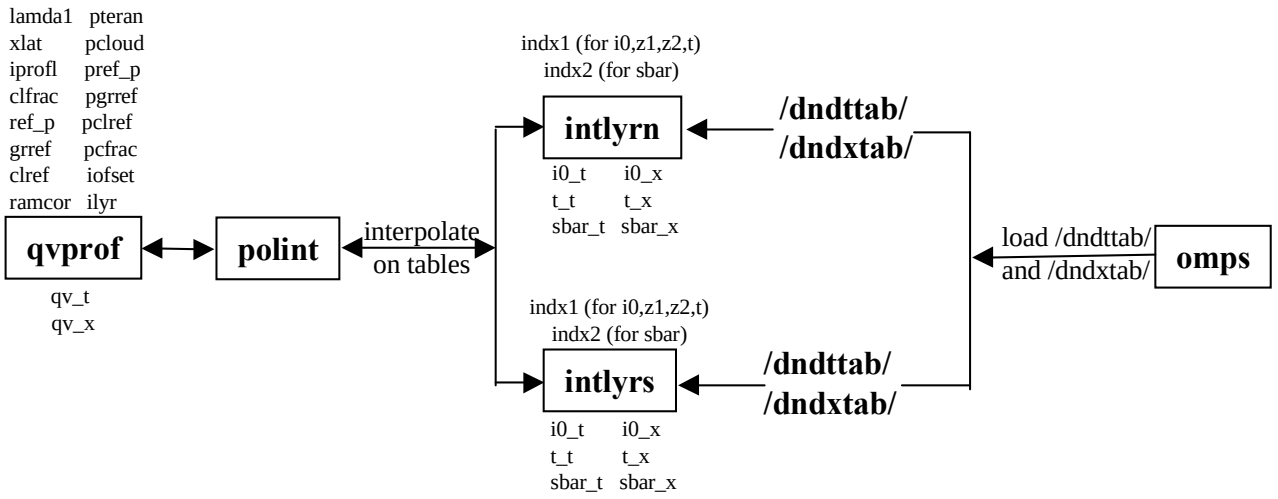

Figure 3.2-1. EDR Production (cont)

Table 3.2-1. List of Variables Used in the Algorithm Flow Diagrams

Variable Name	Variable Type	Variable Dimension	Description
aerind	real	1	Aerosol Index (as defined for TOMS: 331-360 nm residue diff)
ai	real	12	336-337 nm residue diff (“aerosol index” for OMPS)
algflg	integer	1	Algorithm flag indicating which triplets are used
Back	logical	1	Ascending/descending flag (if false, ascending)
clfrac	real	4	Cloud fraction
clref	real	1	Cloud reflectivity
day	integer	1	Julian day of year for measurement
dxerr	real	12	Error calculated for ozone profile shape correction for each triplet
dterr	real	12	Error calculated for temp profile shape correction for each triplet
estozn	real	1	Estimated ozone from 318/336 pair calculation
errflg	integer	1	Error flag
fteran	real	1	Terrain fraction (1 at 1 atm, 0 at 0.4 atm)
ftrop	real	1	Interpolation factor used in determining how much of a layer is below/above tropopause
grref	real	1	Ground reflectivity
ilat	integer	1	Latitude index (1 for low, 2 for mid, 3 for high)
iofset	integer	1	Angular offset index for table pointer
iref	integer	1	Wavelength number used in reflectivity calculation in reflec. reflec uses wavelengths 19-22 to determine 4 different reflectivities, so iref can be between 19 and 22
isnow	integer	1	Snow/ice indicator (from ext EDR or database)
lat1	integer	1	Index corresponding to 1st latitude band used
lat2	integer	1	Index corresponding to 2nd latitude band used
Ltrop	integer	1	Index representing layer in which tropopause resides
o3abs	real	4	Ozone absorption coefficients (needed for soi)
Ozaer	real	1	Ozone value after being corrected for tropospheric aerosols
Ozbst	real	1	Final ozone value after all corrections (weighted average of toz)
Ozcld	real	1	Ozone below cloud
Ozcor	real	1	Ozone value after being corrected for temp and oz profile shape
Ozonin	real	1	Ozone estimate at beginning of algorithm (260 DU for low lat, 350 for mid, 360 for hi at beginning of day, previous measurement for rest of day)
Ozt	real	12	Ozone values below 13 km determined from enhanced residual correction for all 12 triplets
Oztrip	real	1	Ozone determined from a triplet of wavelengths
Oztrop	real	1	Ozone value below 13 km (weighted average of ozt)
Pcloud	real	1	Cloud pressure from external EDR or database
Pclref	real	1	Perturbed cloud reflectivity
Pcfrac	real	1	Perturbed cloud fraction
Pgrref	real	1	Perturbed ground reflectivity
Pref	real	4	Perturbed reflectivity for 4 wavelengths interpolated using pref_p
pref_p	real	4x4	Perturbed reflectivity for 4 wavelengths from 1.0, 0.7, 0.4, and 0.1 atm tables
Prfrac	real	1	Profile mixing fraction
Pteran	real	1	Terrain (ground) pressure from external EDR or database
Ptrop	real	1	Tropopause pressure

pwav	integer	2	Array contains indices corresponding to wavelength pair used in determining ozone from perturbed N values. pwav wavelengths matched with iref wavelengths to form triplet
qval	real	1	Albedo
ramcor	real	22x4	Raman scattering correction for 22 wavelengths at 1.0, 0.7, 0.4, and 0.1 atm
ref	real	4	Reflectivity for 4 wavelengths interpolate using ref_p
refbst	real	1	Average of ref
ref_p	real	4x4	Reflectivity from 1.0, 0.7, 0.4, and 0.1 atm tables
rsens	real	22	Reflectivity sensitivity (dN/dR) for 22 wavelengths
res1	real	6	Residues for 1st latitude band used in calculation
res2	real	6	Residues for 2nd latitude band used in calculation
resn	real	22	Final residues
rngerr	real	1	Range error (true if ozone < 0, > 750 DU)
sens	real	18	Ozone sensitivities
sns1	real	6	Sensitivities for 1st latitude band used in calculation
sns2	real	6	Sensitivities for 2nd latitude band used
snrerr	real	12	SNR error calculated for each triplet
so2abs	real	4	SO_2 absorption coefficients (needed for soi)
so2wav	real	4	SO_2 wavelength indices
sza	real	1	Solar zenith angle
toz	real	12	Total ozone values for all 12 triplets after all corrections applied
tp	integer	22	There are 7 sensor tables, calculated with different sets of 22 wavelengths that span the range of the spectral smile. Tp contains the index of the table corresponding to the wavelength set below the wavelengths fed to the edr from the sdr
tpf	real	22	Interpolation factor between sensor wavelength tables (using tp as the low value and tp+1 as the higher value)
troperr	real	12	Ozone error below 13 km calculated for each triplet
twav	integer	2	Array contains indices corresponding to wavelength pair used in determining ozone. twav wavelengths matched with iref wavelengths to form triplet
wav1	Real	1	Strongly ozone sensitive wavelength used for estimate (318 nm)
wav2	real	1	Weakly ozone sensitive wavelength used for estimate (332 nm)
wlenth	real	22	OMPS wavelengths
xlat	real	1	Latitude
xnvalm	real	22	Measured normalized radiances for 22 wavelengths
vcf	real	1	Cloud fraction from VIIRS

3.2.1 Retrieval Algorithm Description

The following is a step-by-step description of the algorithm. It is limited to a description of the modules necessary to convert information in the SDR into the EDR ozone value and omits any references to the I/O and other routines.

A) omps

The main program **omps** performs the following preliminary tasks:

1) Reads in the SDR.
2) Produces normalized radiances from radiances and solar flux provided by the SDR. Calculates interpolation factor. It reads in entries contained in the main table as well as those for the dN/dx and dN/dt tables ($\log_{10}I_0$, Z_1/I_0, Z_2/I_0, T/I_0, and S_b).
3) Determines linear factors needed to interpolate sensor table values between wavelength sets that bracket the wavelength values provided by the SDR.
4) Since the denominators of the Lagrange functions $L_i(X)$ and $L_j(Y)$ do not depend upon satellite measured quantities, these are computed for each sequential 4-point segment of tabular θ_0 and θ values.

5) It reads in the Raman scattering correction factors for each of the 22 wavelengths.

6) It determines on which side of the CCD the macropixel is located.

B) total

The subroutine **total** is the main driver for the scientific algorithm. This subroutine obtains total ozone and determines SO_2 contamination for each OMPS measurement.

1) Using satellite latitude at the beginning of the first scan in the orbit, select an initial ozone estimate, Ω_{init}, based upon latitude as follows:

$|lat| < 45°$ $\Omega_{init} = 260$ DU

45°< |lat| < 60° Ω_{init} = 340 DU

|lat| > 75° Ω_{init} = 360 DU

2) lodsmp

Load satellite observed quantities.

Unpack θ, θ_0, ϕ, latitude, longitude, and day number.

If θ > 80° skip this measurement.

Set latitude flag for this sample:

|lat| < 15° lLAT = 1

45°< |lat| < 60° lLAT = 2

|lat| > 75° lLAT = 3

Screen sample for possible contamination by an eclipse.

Read the cloud pressure p_c, the presence of snow or ice, and the surface category from the SDR. These are either values from external EDRs or, if not available, values from climatological databases. Read the terrain pressure and surface reflectivity from climatological databases.

Read in radiances for each of the 22 wavelengths.

Calculate angular quantities necessary to determine calculated N values:

$Y = \ln(\sec\theta_0)$, $s = \sec\theta + \sec\theta_0$, $\cos\phi$, $\cos 2\phi$, Q_1, and Q_2.

Find the 4 tabular values of $\theta_{0j}(j=l,l+3)$ that bracket the observed solar zenith angle and determine $L_j(X)$, $l = l+3$ (use n=4). Do the same for $L_j(Y)$ using the bracketing values of $\theta_l(l=k,k+3)$ (also with n=4).

3) prflec

Set R_t = surface reflectivity (from N7/TOMS UV surface ref database)

$R_c = 0.80$ (cloud reflectivity)

4) troplyr

Calculate the tropopause layer from external EDR temperature information.

The following steps (5 – 15) are performed for each of 3 different triplet for each of the 4 reflectivity wavelengths.

5) reflec

For each of the 4 ozone-insensitive reflectivity wavelengths (364, 367, 372, and 377 nm):

1) Compute an effective cloud fraction, f^*, and an effective reflectivity, R^*.

2) Compute the terrain value of the normalized radiance, I_t, using R_t

$$I_c = I_0 + I_1 \cos\phi + I_2 \cos 2\phi + \frac{R_c T}{1 - R_c S_b} \tag{130}$$

$$I_t = I_0 + I_1 \cos\phi + I_2 \cos 2\phi + \frac{R_t T}{1 - R_t S_b} \tag{131}$$

and the cloud value of the normalized radiance, I_c, for the 1.0, 0.7, 0.4, and 0.1 atm tables:

Lagrange interpolation is used to obtain the calculated quantities I_0, Z_1, Z_2, T, and S_b; I_1 and I_2 are obtained using Z_1, Z_2, Q_1, and Q_2 values calculated in **omps.** A correction for Raman scattering (which is not accounted for in the radiative transfer tables) is applied to the normalized radiance (NR) at all 4 pressure levels and for both R_t and R_c. Lagrange interpolation is then used between the 1.0, 0.7, 0.4, and 0.1 atm parts of the table to obtain I_t and I_c for the correct terrain and cloud pressures.

If $I_{meas} \leq I_t$

1) Compute R^* for the 1.0, 0.7, 0.4, and 0.1 atm tables:

$$R^*(P) = \frac{I^{\lambda}_{meas} - I^{P}_{a}}{T + S_b (I^{\lambda}_{meas} - I^{P}_{a})} \tag{132}$$

where

$$I_a^P = I_0^P + I_1^P \cos\phi + I_2^P \cos 2\phi \quad (133)$$

2) Use Lagrange interpolation to determine R^* for the given terrain pressure.

3) Set the cloud fraction , f^*, equal to 0.

If $I_t < I_{meas} < I_c$:

1) Calculate cloud fraction according to:

$$f^* = \frac{I_{meas}^{\lambda} - I_t}{I_c - I_t} \quad (134)$$

2) If there is snow or ice on the ground

a) assume there are no clouds

b) calculate a reflectivity for the 1.0, 0.7, 0.4, and 0.1 pressure tables using

$$R^* = \frac{I_{meas}^* - I_a}{T + S_b(I_{meas}^* - I_a)} \quad (135)$$

c) Use Lagrange interpolation and the terrain pressure to get the terrain reflectivity

If $I_{meas} > I_c$:

1) Compute R* for the 1.0, 0.7, 0.4, and 0.1 atm tables:

$$R^* = \frac{I^{\lambda}_{meas} - I_a}{T + S_b(I^{\lambda}_{meas} - I_a)} \tag{136}$$

where

$$I^P_a = I^P_0 + I^P_1 \cos\phi + I^P_2 \cos 2\phi \tag{137}$$

2) Use Lagrange interpolation to obtain R*

3) Set f* = 1.

4) If snow or ice is present

a) assume there are no clouds

b) calculate a reflectivity for the 1.0, 0.7, 0.4, and 0.1 pressure tables using

$$R^* = \frac{I^{\lambda}_{meas} - I_a}{T + S_b(I^{\lambda}_{meas} - I_a)} \qquad (138)$$

c) Use Lagrange interpolation and the terrain pressure to get the terrain reflectivity

Subroutines called by **reflect:**

intnlr: perform table look-ups for the Northern Hemisphere

intslr: perform table look-ups for the Southern Hemisphere

plint: perform Lagrange interpolations

(Note: the tables for the Northern and Southern Hemisphere are currently the same).

The following steps (6 – 15) are performed for each of 3 different triplets for each of the 4 reflectivity wavelengths.

6) oznot

Compute Ω_0 using the 318.0/336.0 pair of wavelengths and the partial cloud algorithm. A single set of ozone profiles (low for |lat| $\leq$ 15°, mid for 15°$\leq$ |lat| $\leq$ 60°, high for |lat| $\geq$ 60°) are used.

Start with the initial guess of ozone appropriate for latitude zone ILAT or, for measurements other than the first one, the result from the previous measurement.

Using the 1.0 atm tables and R_t find I_0, Z_1 (and, from it, I_1), Z_2 (and, from it, I_2), T, and S_b and calculate I_t(1.0 atm). Apply a correction for Raman scattering (which is not accounted for in the radiative transfer code) to the NR. Do the same thing with the 0.7, 0.4, and 0.1 atm tables. Use Lagrange interpolation on the calculated NRs at the 4 pressure levels to determine I_t at the terrain pressure. In a similar manner, determine I_c using the cloud pressure instead of the terrain pressure.

Use the cloud fraction, f*, calculated in Step 4 to interpolate between I_t and I_c to produce I_{calc}. Calculate $N_{calc} = N_{318} – N_{336}$ from $I_{calc} = I_{318}/I_{336}$.

If N_{calc} is lower than the measured N value, N_{meas}, perform the above calculation for the next higher ozone value in the table, If N_{calc} is higher than N_{meas}, go to the next lower ozone value. Continue searching through the profiles in the latitude zone designated by ILAT to find the two values of ozone, Ω_L and Ω_U, whose corresponding pair N values, N_L and N_U, bracket N_{meas} at the observed solar zenith angle, satellite zenith angle, and azimuth angle and for the reflectivity calculated previously.

The ozone amount between 1.0 and 0.4 is contained in a table for each of the 26 profiles. The terrain pressure is used to calculate the fraction of this ozone amount that is below the ground and this amount is subtracted from both Ω_L and Ω_U.

Linearly interpolate to obtain an estimate of ozone for the latitude zone:

$$\Omega_0 = \Omega_L + \frac{N_{meas} - N_L}{dN/d\Omega} \tag{139}$$

Where dN/dΩ is the ozone sensitivity given by

$$\frac{N_U - N_L}{\Omega_U - \Omega_L} \tag{140}$$

Using the procedure above, calculate ozone for two temperature sensitive triplets (including the 316/321 and 318/329 nm pairs).

Subroutines called by **oznot:**

nvbrac: determines whether N_{calc} is above or below N_{meas} in order to determine bracketing values;

prfind: determines profile index (the pointer that indexes the correct profile in the table);

qvalue: determines table values (**qvalue** calls **intnlr** and **intslr**)

7) residue

Compute two sets of residues and sensitivities for wavelengths comprising from two sets of profiles (low and mid for |lat| < 45°, mid and high otherwise). Also calculate residues for the 336 nm and 377 nm wavelengths.

For each of the two latitude bands and wavelengths, use Ω_0 to determine I_0, I_1 (from Z_1), I_2 (from Z_2), T, and S_b for the 1.0, 0.7, 0.4, and 0.1 atm tables. Using f*, R_t*, R_c* and reversing the calculations in Step 5, determine N_{calc}.

Calculate residues:

$$r = N_{meas} - N_{calc} \tag{141}$$

Calculate the OMPS "aerosol index" ($R_{336\text{-}377}$).

Subroutines called by residue:

prfind: determines profile index (the pointer that indexes the correct profile in the table);

qvalue: determines table values (**qvalue** calls **intnlr** and **intslr**)

8) ozone

Compute new ozone estimate for each of the 3 wavelength triplets.

Determine which three triplets to use by calculating the optical path length:

$$somega = \frac{\Omega_{est} \cdot (\sec\theta_0 + \sec\theta)}{1000} \tag{142}$$

For each of the 3 triplets:

Compute two separate values of Ω at two latitudes using the two sets of residues and sensitivities obtained in Step 6 and the following formula:

$$\Omega_{profile} = \Omega_0 + \frac{r_1\Delta\lambda_2 - r_2\Delta\lambda_1}{\eta_1\Delta\lambda_2 - \eta_2\Delta\lambda_1};\ \Delta\lambda_i = \lambda_i - \lambda_R \quad (143)$$

where subscripts refer to two selected wavelengths, η is the sensitivity, and r is the residue.

To account for the change in calculated ozone value, adjust residues using the following formula:

$$r_{adj} = \lfloor r_{prf1} \cdot (1 - f_m) + r_{prf} \cdot f_m \rfloor - (\Omega_{profile} - \Omega_0) \cdot \eta \quad (144)$$

Call **ozmix** to determine select mixing fraction between low- and mid- or mid- and high-latitude profiles.

Subroutines called by **ozone:**

ozmix

For somega $\leq$ 1.5, mix Ωs to get Ω using the latitude mixing fraction, f_m:

$$\Omega_{mix} = (1 - f_m) \cdot \Omega_{prf1} + f_m \cdot \Omega_{prf2} \quad (145)$$

where prf1 and prf2 are low- and mid- or mid- and high-latitude profiles, respectively, and

f_m = 0 for |lat| $\leq$ 15°,

f_m = (|lat|-15)/30 for 15° < |lat| < 45°,

fm = (|lat|-45)/30 for 45° < |lat| < 75°, and

fm = 1 for |lat| ≥75°.

For somega > 1.5 ***AND*** $R_{336\text{-}377}$ > 1, use the following procedure.

1) For each triplet chosen in Step 7, use a 4th wavelength that is sensitive to ozone profile shape to select mixing fraction between low- and mid- or mid- and high-latitude profiles. For example, if the optical path length of the measurement is 1.7, the 3 triplets chosen in Step 7 are formed by using one of the 4 reflectivity wavelengths with the 312.5/321.0, 314.0/321.0, and 318.0/336.0 nm pairs. For these 3 triplets, the 308.5 nm wavelength is used to select ozone profile shape.

2) Calculate a residue for the 4th wavelength, r_4.

3) For each of the two profile sets, calculate the "triplet residue":

$$r_{trip} = r_4 - r_2 \frac{\lambda_4 - \lambda_R}{\lambda_2' - \lambda_R} \qquad (146)$$

where r_2 is the middle wavelength of the wavelength triplet.

4) Calculate the mixing fraction:

$$f_m = \frac{r_{trip}(lower)}{r_{trip}(lower) - r_{trip}(higher)} \quad (147)$$

Calculate ozone using this mixing fraction:

$$\Omega_{mix} = (1 - f_m) \cdot \Omega_{prf1} + f_m \cdot \Omega_{prf2} \quad (148)$$

and readjust residues

$$r = \lfloor r_{prf1} \cdot (1 - f_m) + r_{prf} \cdot f_m \rfloor - (\Omega_{mix} - \Omega_0) \cdot \eta \quad (149)$$

5) Recalculate r_{trip}. If it is greater than 0.1, iterate once using Ω_{mix} determined in 4 above.

Ω_{mix} corresponds to the heritage V7 ozone amount, Ω_{V7}.

9) To account for the change in calculated ozone value, adjust residues using the following formula:

$$r_{adj} = \lfloor r_{prf1} \cdot (1 - f_m) + r_{prf} \cdot f_m \rfloor - (\Omega - \Omega_{mix}) \cdot \eta \quad (150)$$

10) aecor

Correct Ω_{mix} for tropospheric aerosols and sea glint using Equations (26) and (27):

$$\Omega_{aercor} = \Omega_{V7} + 0.75 R_{336-377} - 0.011 R_{336-377}^2 \text{ for PL} \leq 4.5 \quad (151)$$

$$\Omega_{aercor} = \Omega_{V7} + 0.80\, R_{336-377} \text{ for PL > 4.5} \quad (152)$$

Convert to aerosol index using Equation (28) and report out:

$$Aerosol\ Index = \frac{331-360}{336-377} R_{336-377}\,. \quad (153)$$

11) tpcor

Correct for differences between actual ozone and temperature profiles and standard ozone and temperature profiles

1) Calculate dN/dx and dN/dt using the dN/dx sensitivity table.

Unperturbed profile

For each of the two latitude bands and wavelengths, use Ω_{aercor} to determine I_0, I_1 (from Z_1), I_2 (from Z_2), T, and S_b for the 1.0, 0.7, 0.4, and 0.1 atm dN/dx tables. Use the following formula to determine dn/dt from dn/dx:

$$\sum_x \left(\frac{\Delta N}{\partial T}\right)_x = \sum_x \left(\frac{\partial N}{\partial x}\right)_x \frac{x}{\alpha_x}\frac{\partial \alpha}{\partial T} = \sum_x \left(\frac{\partial N}{\partial x}\right)_x \frac{x}{\alpha_x}\left[\alpha(T_x^{stdprf}) - \alpha(T_x^{measured})\right] \quad (154)$$

where

$$\alpha = c_0 + c_1 T + c_2 T^2 \quad (155)$$

and c_0, c_1, c_2 are located in the file abs_coef.dat as a function of wavelength. $T^{measured}$ for each layer is obtained from the external EDR.

Using f_m, f^*, R_t^*, R_c^* and reversing the calculations in Step 5, determine N_{calc}.

Perturbed Profiles

For each of the two latitude bands and wavelengths, use Ω_{V7} to determine I_0, I_1 (from Z_1), I_2 (from Z_2), T, and S_b for each of the 11 perturbed profiles for the 1.0, 0.7, 0.4, and 0.1 atm dN/dx and dN/dt tables. Again, use f_m, f^*, R_t^*, R_c^* and reverse the calculations in Step 5 to determine N_{calc} for each of the perturbed profiles.

2) Using N values calculated for the unperturbed profile and the N values calculated for the perturbed profiles, calculate 11 dN/dx and dN/dT values (one for each of the 11 layer perturbations).

3) Using Ω_{aercor} and f_m, determine the standard ozone and temperature profile used in the table lookup.

4) Use the EDR external temperature profile to determine the difference between the actual and standard temperature, Δt, for all 11 layers.

5) Use the limb retrieved ozone profile to determine the difference between the actual and standard ozone profile, Δx, for all layers for which there is a limb retrieval.

6) Form the two sums:

$$\sum_{layer}(t_{layer}-t^{0}_{layer})\frac{dN}{dt_{layer}}$$
$$\sum_{layer}(x_{layer}-x^{0}_{layer})\frac{dN}{dx_{layer}} \qquad (156)$$

Calculate dxerr (error in ozone profile shape correction) and dterr (error in temperature shape correction (to be used in weighted average to obtain final ozone amount)

12) oznew

Form the equation

$$r = N_m - N_{aercor} = (\Omega - \Omega_{aercor})\eta + \sum_{layer}(t_{layer}-t^{0}_{layer})\frac{dN}{dt_{layer}} + \sum_{layer}(x_{layer}-x^{0}_{layer})\frac{dN}{dx_{layer}} + a + b\lambda \qquad (157)$$

and solve for Ω:

$$\Omega_{cor} = \Omega_{aercor} + \frac{r_1\Delta\lambda_2 - r_2\Delta\lambda_1}{\eta_1\Delta\lambda_2 - \eta_2\Delta\lambda_1}. \qquad (158)$$

13) resadj

To account for the change in calculated ozone value, adjust residues using the following formula:

$$r_{adj} = \left\lfloor r_{prf1} \cdot (1 - f_m) + r_{prf} \cdot f_m \right\rfloor - (\Omega - \Omega_{aercor}) \cdot \eta \quad (159)$$

14) tropoz

Calculate the climatological amount of tropospheric ozone in standard profile used to determine Ω down to 13 km.

Calculate efficiencies for layers below 13 km:

$$\xi_{layer} = \frac{dN_{triplet}/dx}{dN_{triplet}/d\Omega} \quad (160)$$

where the numerators are obtained from Step 9 and the denominators are obtained from Step 7.

Calculate the amount of retrieved ozone below 13 km and subtract the amount from the standard profile corresponding to Ω_{cor}.

$$X_{13} = \Omega_{cor} - \sum_{13}^{60} x_{limb} - X_{13}^{0} \quad (161)$$

Use the values above to correct ozone for measurement inefficiency below 13 km:

$$\Omega = \Omega_{cor} - X_{13}^{0} + X_{13} = \Omega_{tpcor} + (1+\xi)\frac{X_{retr} - X_{13}^{0}}{\xi} \tag{162}$$

Calculate troperr (to be used in weighted average to get final ozone amount)

15) snr_trip

Calculate snr error for the triplet from the following formula:

$$\frac{\sigma_{\Omega}}{\Omega} = \sqrt{\frac{(\lambda_2 - \lambda_3)^2 e_1^{\,2} + (\lambda_1 - \lambda_3)^2 e_2^{\,2}}{\left[(\lambda_2 - \lambda_3)s_1 - (\lambda_1 - \lambda_3)s_2\right]^2}} \tag{163}$$

where e_n is the normalized standard deviation of the albedo random noise.

The previous steps (6 – 15) are performed for each of 3 different triplets for each reflectivity wavelength.

The previous steps (5 – 15) are performed for each of the 4 reflectivity wavelengths.

15) bestoz

Calculate best ozone from a weighted average of all of the triplets, using snrerr, dxerr, dterr, and troperr using the following formulas:

$$\Omega_{best} = \frac{\sum_i W_i \Omega_i}{\sum_i W_i} \quad \textit{where i is a triplet value} \tag{164}$$

$$W_i = \sqrt{snrerr^2 + dterr^2 + dxerr^2 + troperr^2} \tag{165}$$

Calculate best reflectivity by averaging together reflectivity amounts from 4 reflectivity wavelengths.

Calculate best aerosol index from a weighted average of all of the triplet values using snrerr, dxerr, dterr, and troperr.

16) blwcld

Calculate ozone beneath the cloud for both appropriate latitude bands.

If the cloud pressure is greater than 0.5 atm, the cloud is in layer 1. Determine the fraction of ozone in layer 1 that is below the cloud for the bracketing ozone values (since pressure scales with height exponentially use logarithmic interpolation):

$$f_{cloud} = \frac{\log(1.013 / p_{cloud})}{\log(1.013/0.5)} \tag{166}$$

$$\Omega_{cld}^{prflo} = f_{cloud} \cdot \Omega_{layer1}^{prflo} \tag{167}$$

$$\Omega_{cld}^{prfhi} = f_{cloud} \cdot \Omega_{layer1}^{prfhi} \tag{168}$$

If the cloud pressure is less than 0.5, the cloud is in layer 2 (which ends at 0.253 atm). Determine the fraction of ozone in layer 2 that is below the cloud and add to the ozone in layer 1 (which is totally below the cloud):

$$f_{cloud} = \frac{\log(0.5 / p_{cloud})}{\log(0.5/0.253)} \tag{169}$$

$$\Omega_{cld}^{prflo} = f_{cloud} \cdot \Omega_{layer2}^{prflo} + \Omega_{layer1}^{prflo} \tag{170}$$

$$\Omega_{cld}^{prfhi} = f_{cloud} \cdot \Omega_{layer2}^{prfhi} + \Omega_{layer1}^{prfhi} \tag{171}$$

Mix ozone below cloud from bracketing profiles for the two latitude bands:

$$f_{\Omega} = \frac{\Omega - \Omega_{prflo}}{\Omega_{prfhi} - \Omega_{prflo}} = \frac{\Omega - \Omega_{prflo}}{50}, \tag{172}$$

$$\Omega_{cld}^{lat} = \Omega_{cld}^{prflo} \cdot (1 - f_{\Omega}) + \Omega_{cld}^{lat2} \cdot f_{\Omega}. \tag{173}$$

Mix Ω_{cld} using the profile mixing fraction:

$$\Omega_{cld} = (1 - f_m) \cdot \Omega_{cld}^{lat1} + f_m \cdot \Omega_{cld}^{lat2}. \tag{174}$$

Finally, multiply by the cloud fraction:

$$\Omega_{cld} = f_{cld} \cdot \Omega_{cld}. \tag{175}$$

17) soi

Determine if SO_2 is present.

For each reflectivity wavelength

Calculate the ratio, Rat, of ozone to SO_2 absorption coefficients for the 317, 331 and 336 nm wavelengths.

Calculate SO_2 sensitivities:

$$\frac{dN}{d(SO_2)} = Rat \cdot \frac{dN}{d\Omega}. \tag{176}$$

Calculate the SO_2 index using

$$SO_2 = \frac{r_{23} \cdot s_{13} - r_{13} \cdot s_{23}}{so_{23} \cdot s_{13} - so_{13} \cdot s_{23}}, \tag{177}$$

where

$$s_{13} = \left(\frac{dN}{d\Omega}\right)_{310.5} \cdot (321.0 - \lambda_R) - \left(\frac{dN}{d\Omega}\right)_{321.0} \cdot (310.5 - \lambda_R), \tag{178}$$

$$s_{23} = \left(\frac{dN}{d\Omega}\right)_{312.0} \cdot (321.0 - \lambda_R) - \left(\frac{dN}{d\Omega}\right)_{321.0} \cdot (312.0 - \lambda_R), \quad (179)$$

$$so_{13} = \left(\frac{dN}{dSO_2}\right)_{310.5} \cdot (321.0 - \lambda_R) - \left(\frac{dN}{dSO_2}\right)_{321.0} \cdot (310.5 - \lambda_R), \quad (180)$$

$$so_{23} = \left(\frac{dN}{dSO_2}\right)_{312.0} \cdot (321.0 - \lambda_R) - \left(\frac{dN}{dSO_2}\right)_{321.0} \cdot (312.0 - \lambda_R), \quad (181)$$

$$r_{13} = r_{310.5} \cdot (321.0 - \lambda_R) - r_{321.0} \cdot (310.5 - \lambda_R), \text{ and} \quad (182)$$

$$r_{23} = r_{312.0} \cdot (321.0 - \lambda_R) - r_{321.0} \cdot (312.0 - \lambda_R). \quad (183)$$

Average the 4 reflectivity wavelengths to obtain the final SO_2 value. Rename SOI and use to flag data if larger than 4σ.

17) seterr

Assess the quality of the data. This assessment will include:

1) checks on the residues for deviation from linearity;
2) checks for volcanic SO_2 contamination; and
3) comparison of ozone determined from the 2 temperature sensitive triplets (see Table 2.4-1) with the 318/336 nm ozone estimate to determine large-scale temperature deviations from the standard profile

4 Assumptions

Table 4-1 summarizes the assumptions described in Sections 2.3, 2.4, and 3.2.1.

Table 4-1. List of Assumptions Made in Forward Model and in Retrieval

Forward Model
The atmosphere can be represented by a simplified Beer's Law, which includes Rayleigh scattering and ozone absorption.
The atmosphere's lower bound consists of two Lambertian reflecting surfaces, one for the ground and one for clouds.
Raman scattering can be treated as being independent of solar and satellite zenith angle.
Retrieval
The NR for an entire scene can be treated as coming from a point source with viewing conditions given by those at the center of the FOV.
The cloud fraction can be determined by linearly interpolating the measured normalized radiance of an ozone-insensitive wavelength between a normalized radiance calculated for the surface and one for the cloud.
The cloud's reflectivity is 0.8.
The surface's reflectivity is obtained by a table look-up.
A correction factor linear with wavelength corrects for most non-Rayleigh scattering atmospheric effects.
Tropospheric aerosols and sun glint can be corrected by requiring a reflectivity dependence that is linear with wavelength.
A correction factor independent of viewing angles can be used to correct calculated normalized radiances for Raman scattering.

5 Input Data Requirements

5.1 PRIMARY SENSOR REQUIREMENTS

Table 5.1-1 outlines what the baseline algorithm needs and sensor allocations.

Table 5.1-1. Sensor Parameters and Performance Requirements

Parameter	Baseline Algorithm Needs	Baseline Sensor Allocation	Comments
Wavelength range	308-377 nm	300-380 nm	Ozone and path length range
Bandwidth	1 nm	1 nm	Pair/triplet approach
Samples/FWHM	1 min.	2.4	λ shift, Ring effect
Number of channels	22*	192	Triplets, over-sampling, aerosols
Horizontal cell size	50 km @ nadir	50 km @ nadir	
Horizontal coverage	> 2800 km	> 2800 km	
SNR	> 1000 for SZA < 80 at specified radiances	> 1000 for SZA < 80 at specified radiances	Precision
λ registration	< 0.01 nm	< 0.01 nm	Ozone cross-section error
Albedo calibration	2%	2%	Accuracy and stability
Pixel to pixel calibration (includes linearity)	0.5% max.	0.5% max.	Accuracy
Albedo deviation error	< 1%	< 1%	Accuracy and stability

* The 22 wavelengths are: 308.5, 310.5, 312.0, 312.5, 314.0, 315.0, 316.0, 317.0, 318.0, 320.0, 321.0, 322.5, 325.0, 328.0, 329.0, 331.0, 332.0, 336.0, 364.0, 367.0, 372.0, and 377.0 nm

5.2 OTHER OMPS SENSOR DATA REQUIREMENTS

OMPS LP data is no longer a required input to the TC Ozone algorithms (both SDR and EDR). The table is retained for the sole purpose of reference

Table 5.2-1 specifies other OMPS data required by the total column ozone algorithm.

Table 5.2-1. Other OMPS Data Required by the Total Column Ozone Algorithm

Sensor	Data	Form	Use
UV/Vis limb	Ozone profile	Co-located in 11 Umkehr layers Dobson Units	Ozone profile shape Tropospheric ozone correction
UV/Vis limb	Aerosol profile	Co-located	P^3I

5.3 OTHER NPOESS SENSOR DATA REQUIREMENTS

Table 5.3-1 specifies data from other NPOESS sensors required by the total column ozone algorithm.

Table 5.3-1. Data Products from Other NPOESS Sensor Systems That Are Used by the Total Column Ozone Algorithm

Sensor	Data	Form	Use
CrIMSS	Temperature - pressure profile	Co-located in 11 Umkehr layers Kelvin	Temperature profile shape
VIIRS	Cloud top pressure	Co-located Atm	Partial cloud algorithm Calc of normalized radiances
VIIRS	Snow and ice cover	Co-located Percent	Snow/ice indication Calc of normalized radiances
VIIRS	Cloud Fraction	Co-located and regridded percent of OMPS footprint covered	Cloud fraction, used when snow/ice in field of view

5.4 CLIMATOLOGY DATA REQUIREMENTS

Table 5.4-1 specifies climatological data required by the total column ozone algorithm (note: some of the databases are only used if external EDRs are not available).

Table 5.4-1. Climatology Databases Used by the Total Column Ozone Algorithm

Data	Form	Source	Use
Surface pressure*	0.5° x 0.5°grid In mbars	TUG87 geophysical model (see Weiser, 1987)	Calculation of normalized radiances
Cloud pressure*	1° x 1° x 12 month In mbars	ISCCP	Partial cloud algorithm Calculation of normalized radiances
Snow/ice*	1° x 1° x 12 month In percent probability	Air Force	Snow/ice indication Calculation of normalized radiances
Surface reflectivity	1° x 1° x 12 months	Herman and Celarier, JGR, 1997	Calculate radiances
Eclipse	Areal coverage	Astronomical almanac	Flag data
SAA	Areal Coverage	TBD	Flag Data
Temperature profile*	3-D monthly zonal mean for 11 Umkehr layers	TOMS V8 climatology	Calculation of normalized radiances
Ozone profile	4-D total column dependent monthly zonal mean for 11 Umkehr layers	TOMS V8 climatology	Calculation of normalized radiances

* Used if external EDR not available

6 Output Data Description

6.1 EDRS

Ozone total column is defined as the amount of ozone in a vertical column of the atmosphere measured in Dobson Units (milli-atm-cm). The specifications and specified performance for the EDR are given in **Table 6.1-1**.

Table 6.1-1. Total Column Ozone EDR Specifications

SS Paragraph No.	Description	Allocated (Assured) Performance
SS3.2.1.1.1.1-1	Horizontal Cell Size	50 km @nadir
SS3.2.1.1.1.1-3	Horizontal Reporting Interval	50 km @ nadir
SS3.2.1.1.1.1-4	Vertical Cell Size	60 km
SS3.2.1.1.1.1-10	Horizontal Coverage	SZA < 80 degrees
SS3.2.1.1.1.1-11	Vertical Coverage	0 – 60 km
SS3.2.1.1.1.1-12	Measurement Range	50 – 650 m-atm-cm
SS3.2.1.1.1.1-15	Measurement Accuracy	15 m-atm-cm, 480 < Ω < 650 m-atm-cm 12 m-atm-cm, 250< Ω<450 m-atm-cm 9 m-atm-cm, Ω < 250 m-atm-cm
SS3.2.1.1.1.1-19	Measurement Precision	3 m-atm-cm + 0.5%, 450 m-atm-cm $\leq \Omega$ m-atm-cm + 0.5%, 250< Ω<450 m-atm-cm 2.5 m-atm-cm + 0.5%, Ω < 250 m-atm-cm
SS3.2.1.1.1.1-24	Long term Stability	1%
SS3.2.1.1.1.1-26	Mapping Uncertainty	5 km
SS3.2.1.1.1.1-28	Mapping Local Average Revisit Time	24 hours

6.2 ADDITIONAL DATA PRODUCTS

Table 6.2-1 specifies additional algorithm outputs that are not part of our baseline as verified data products but are available as P^3I.

Table 6.2-1. Additional, Non-Baseline Data Products Available from the Total Ozone Algorithm

Data	Form	Reference
Cloud fraction	$0.0 < f_{cld} < 1.0$	Section 2
Reflectivity	Percent	Section 2
Volcanic SO_2	Dobson Units	Section 2, ICSR 8091101
Aerosol index	Index	Section 2, ICSR 8100101

6.3 EDR CONTENT

The output records of the Total Column Ozone EDRs will include the information listed in Table 6.1-1 and Table 6.2-1. (The additional, non-baseline P^3I data products are flagged as bold-italicized parameters.) These are organized into a header record followed by a number of Earth view data records. The recommended content of these records follows:

Header record with:

- EDR identification
- Spacecraft identification
- Sensor identification
- Date and time of EDR generation
- Date and start time of data in file
- Date and end time of data in file
- Earth view data records (approximately 14,000 IFOV per orbit) with:
  - Orbit number
  - Date and time of data
  - Data acquisition orbit number
  - Data transmission orbit number
  - Ascending node Julian date and time tag
  - Spacecraft altitude
  - Identification of SDR calibration parameters
  - EDR algorithm identification number
  - EDR algorithm version number
  - Channel identification
  - Latitude of scene
  - Longitude of scene
  - Solar zenith angle
  - Satellite zenith angle
  - Azimuth angle (the angle between the sun and the satellite IFOV)
  - Calibrated albedo (ratio of radiance to irradiance) per channel
  - Total ozone (from the OMPS Total Column Ozone Algorithm)
  - Total ozone (from the heritage TOMS Version 7 Algorithm)
  - Residue, defined as the difference between measured and modeled N-values per channel
  - Ozone sensitivity per channel (defined as $dN/d\Omega$)
  - Reflectivity sensitivity per channel (defined as dN/dR, where R is the scene reflectivity)
  - ***Cloud fraction***
  - ***Scene reflectivity***
  - ***Surface category***

- ***Cloud pressure***
- ***Aerosol index***
- ***SOI (SO2 index)***
- Updated tropospheric ozone value for scene (if cloud free)
- Data quality flags

7 System Accuracy and Precision

This section is out of date. The analysis on system accuracy and precision will likely be moved to error-budget documentation and therefore has not been updated here.

Accuracy and precision in total column retrievals are allocated to the sensor and the algorithms. In this section, error sources are identified along with estimates of the error we expect to achieve based on our design.

7.1 SYSTEM ACCURACY

Total column ozone retrieval accuracy is allocated to sensor and algorithm systematic errors. The NPOESS requirements for accuracy are given in **Table 7.1-1** below.

Table 7.1-1. OMPS System Accuracy Requirements

Ozone Range	Requirement
50 < Ozone ≤ 250 DU	9.5 DU
250 < Ozone ≤ 450 DU	13 DU
450 < Ozone ≤ 650 DU	16 DU

The combined allocation of sensor and algorithm accuracy (not including margin which is carried at the system level) is shown in **Figure 7.1-1** as a function of total ozone, along with the system requirements shown above. The plots are curved due to the combination of driving errors such as the linear dependence from cross section errors and a constant contribution from wavelength-dependent calibration errors.

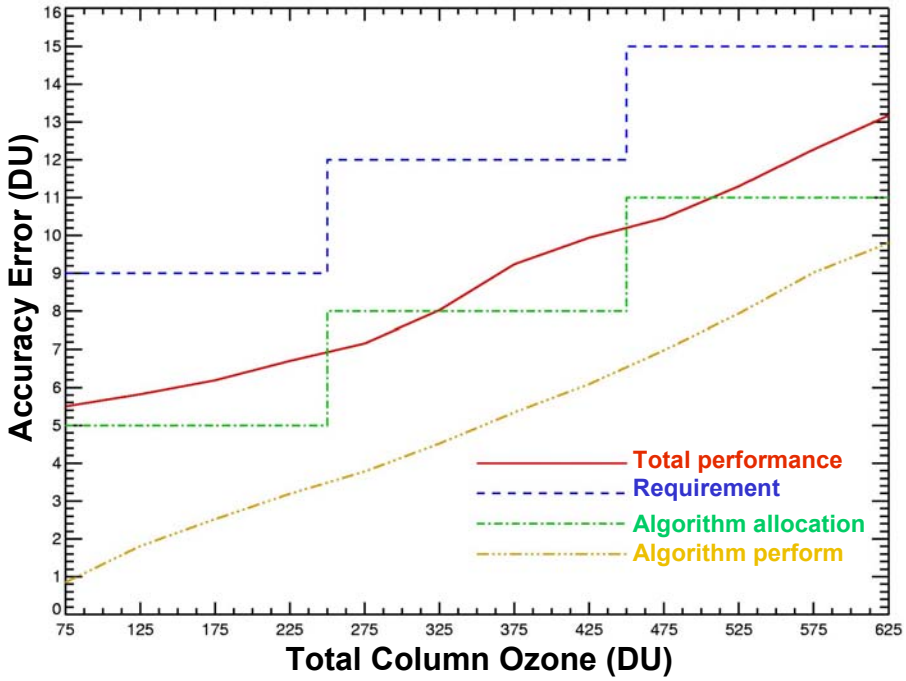

Figure 7.1-1. OMPS Total Column accuracy error allocations and performance.

The "total" performance curve indicates a combination of sensor and algorithm errors.

7.1.1 Sensor Accuracy

The sensor accuracy allocations for retrieved total column ozone values are given in **Table 7.1-2.** Derivations of the allocations are given in the text and plots that follow the allocation tree.

Table 7.1-2. Allocation for sensor contributions to retrieved ozone accuracy

Total Ozone	Initial Albedo Cal (WL ind.)	Long Term Albedo Cal	Inital Albedo Cal (WL dep.)	Long Term Albedo Cal (WL dep)	Pix-Pix Rad. Cal	Polariz. Sens	OOF stray light	OOB stray light	Wave Cal. Acc.	On- orbit WL shift	Intra- orbit WL stability	RMS Total
50	0.14	0.04	3.50	2.10	2.50	0.02	0.03	0.41	0.15	0.10	2.52	5.43
125	0.36	0.09	3.50	2.10	2.50	0.05	0.07	1.02	0.38	0.25	2.52	5.54
175	0.50	0.13	3.50	2.10	2.50	0.07	0.10	1.42	0.53	0.35	2.52	5.65
225	0.64	0.16	3.50	2.10	2.50	0.09	0.13	1.83	0.68	0.45	2.70	5.89
275	0.79	0.20	3.50	2.10	2.50	0.12	0.16	2.24	0.83	0.55	2.70	6.08

325	0.93	0.23	3.50	2.10	2.50	0.14	0.19	2.64	0.98	0.65	3.42	6.63
375	1.07	0.27	3.50	2.10	2.50	0.16	0.21	3.05	1.13	0.75	4.64	7.54
425	1.21	0.30	3.50	2.10	2.50	0.18	0.24	3.46	1.28	0.85	4.77	7.85
475	1.36	0.34	3.50	2.10	2.50	0.20	0.27	3.86	1.43	0.95	4.23	7.79
525	1.50	0.38	3.50	2.10	2.50	0.22	0.30	4.27	1.58	1.05	4.18	8.05
575	1.64	0.41	3.50	2.10	2.50	0.24	0.33	4.67	1.73	1.15	4.14	8.32
625	1.86	0.46	3.50	2.10	2.50	0.27	0.37	5.28	1.95	1.30	4.14	8.79

7.1.1.1 Initial Albedo Calibration, Wavelength-Independent

Albedo calibration is the ratio of sensor sensitivity to spectral radiance (nadir scene) and spectral irradiance (solar calibration). In that ratio, absolute scales and sensor efficiency cancel out leaving only the spectral efficiency and geometry of the solar diffuser.

Our allocation of 2% accuracy of initial, wavelength-independent albedo calibration is based upon experience with similar calibrations of SBUV/2. In this uncertainty we include both the pre-launch albedo calibration uncertainty and potential errors in transferring this calibration into orbit. Ordinary in-flight solar calibration does not detect or correct errors in the pre-flight baseline calibration, however, vicarious calibrations and data justification will allow evaluation of, and possible correction to, the pre-flight wavelength-independent baseline.

In deriving the column ozone uncertainty associated with wavelength independent albedo calibration, we used a retrieval algorithm sensitivity of 1% ozone for 7% calibration error as discussed in Jaross et al. (1998a). Studies of TOMS/Nimbus data (Wellemeyer et al., 1996) show that no simple relationship exists between ozone retrieval errors and wavelength-independent calibration errors. A sensitivity of 7:1 represents a mean over all viewing conditions.

7.1.1.2 Initial Albedo Calibration, Wavelength-Dependent

The OMPS TC ozone retrieval is much more sensitive to relative channel errors than it is to errors that are the same in all channels. This follows from the use of triplets of channels in the retrieval rather than single channels. For TOMS, sensitivity of ozone to albedo variations depends strongly on total column and path length. For a well designed instrument with many wavelengths, such as OMPS, we select triplets to essentially keep the sensitivity constant (**Table 2.4-1**). Thus the value of $s\Delta\alpha\Omega$ varies by no more than a factor of 2 over the full range of measurements. By

Monte Carlo analysis we find that a 1% wavelength-dependent (but uncorrelated) albedo calibration error will result in about 7 DU ozone error. This value is essentially independent of total column amount, by design.

The initial wavelength-dependent albedo calibration uncertainty is estimated at 0.5%. It is driven primarily by the uncertainty in the reflectance uncertainty of the radiometric standard used in pre-launch calibrations (Jaross et al., 1998a). It also includes the estimated error in transferring this ground calibration to orbit. It does not, however, include pixel-to-pixel sensor errors that will also degrade inter-channel calibration. Detector characterization uncertainties are considered separately.

7.1.1.3 Long-term Albedo Calibration

Long-term radiometric stability is specified at the system level separately from accuracy. However, an accuracy specification applies at the end of the mission as well as at the beginning. Establishment of sensor calibration at the end logically divides into the initial calibration and any changes from that. We therefore account for uncertainty in calibration drift under both accuracy and long-term stability. These uncertainties are discussed more completely in Section 7.2.

7.1.1.4 Pixel-to-Pixel Radiometric Calibration

This contribution includes the uncertainty of the initial detector flat-fielding and system linearity calibrations. The sensitivity to this uncertainty is the same as to wavelength-dependent albedo calibration.

7.1.1.5 Wavelength Calibration Accuracy

We allocate an initial wavelength calibration accuracy of 0.015 nm and an uncertainty for measuring bandcenter wavelength shifts in orbit of 0.01 nm. The allocations for both are based upon analysis, the results of which are shown in **Table 7.1-2**. The technique for monitoring spectral registration shifts in flight using solar Fraunhofer lines is discussed in Section 3.1.3.3. Pre-launch spectral calibrations will utilize laboratory spectral line sources. However, we anticipate that the most accurate initial spectral registration will come from the baseline solar measurements in flight. For the shift sensitivity analysis, the assumed sensor characteristics were 0.1% irradiance measurement noise and 1 nm FWHM sensor resolution. In order to derive the results, GOME 0.2 nm solar data were degraded to 1 nm FWHM resolution and the sensitivity using single absorption lines was determined. The result is that we expect better than 0.005 nm shift resolution from solar measurements.

The sensitivity of the Nadir Total Column sensor retrieved ozone to wavelength registration errors occurs predominantly via the absorption

coefficients. A sensitivity study was performed as part of channel selection (see Section 2). The sensitivities of triplet-derived ozone to 0.02 nm wavelength registration errors is shown in Figure 2.4-5 for all triplet combinations. The results indicate less than 1% retrieval errors for most of the triplets (5% per 0.1 nm). Those triplets with greater sensitivity are not intended for standard ozone retrievals. For instance, triplets were chosen with maximum temperature sensitivity as a monitoring tool. These same triplets will also have large sensitivities to wavelength registration. We use the 5% per 0.1 nm as the sensitivity for the wavelength calibration allocations.

We also performed end-to-end simulations of wavelength registration errors in the Nadir ozone retrieval. For this study we selected three triplets which will cover the full range of atmospheric slant paths encountered during ozone retrieval: 1) A triplet (312.0 nm, 321.0 nm, 364.0 nm), 2) B triplet (316.0 nm, 329.0 nm, 364.0 nm), and 3) C triplet (322.5 nm, 336.0 nm, 364.0 nm)

For each triplet, the forward model was run assuming the nominal wavelengths. Ozone was then retrieved from the generated radiances using a modified ozone table. This modified table was created by shifting the band centers of all channels 0.1 nm from nominal. The retrieved ozone was then compared to the original input amounts. The differences are shown in **Figure 7.1-5** as a function of total ozone amount. For each triplet a solar zenith angle (SZA) and satellite zenith angle (SatZA) were chosen to maximize the error. The resulting sensitivities are approximately 1.5%, 4%, and 3% per 0.1 nm for the A, B, and C triplets, respectively. These sensitivities are all less than the maximum 5% per 0.1 nm shown in Figure 2.4-5 for triplets used in ozone retrievals.

Finally, a study was performed using a multiple-triplet retrieval. A mid-latitude 325 DU profile was chosen because of its large weight toward the 318 nm, 336 nm triplet. This triplet has the greatest sensitivity, of those listed in Table 2.4-2, to spectral shifts: 7% per 0.1 nm. Upon inclusion as part of the multiple triplet retrieval, the sensitivity became 2% per 0.1 nm. We view this as the worst case OMPS TC spectral sensitivity.

Based on the above analysis, we make a conservative allocation of 0.01 nm shift sensitivity. The accuracy allocation accounts for the calibration transfer uncertainty from wavelength standards to the reference solar spectrum.

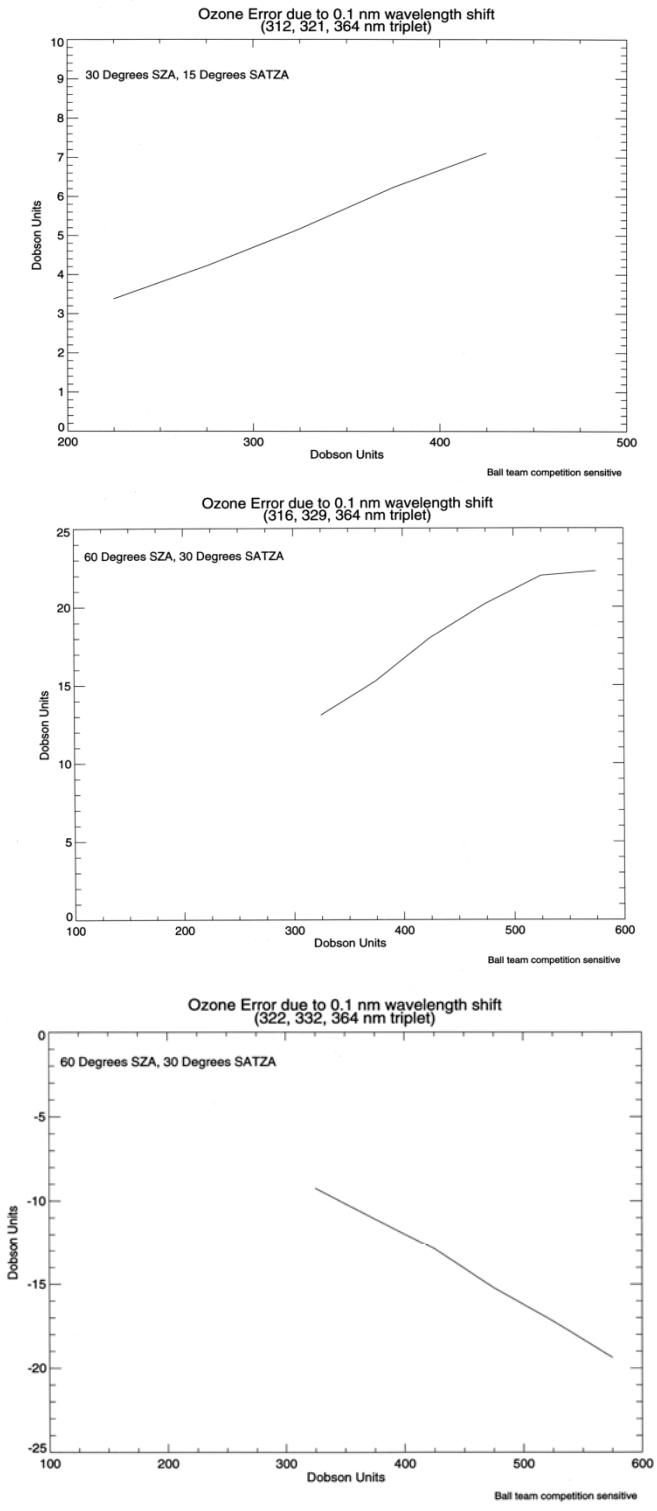

Figure 7.1-2. Simulated Retrievals of Ozone

The simulated retrievals of ozone are shown using an ozone table with 0.1 nm sensor wavelength errors. The percent error for each triplet varies little with viewing conditions or with total ozone amount.

7.1.1.6 Intra-orbital Wavelength Shift Sensitivity

Thermal changes to the sensor throughout the orbit cause shifts in wavelengths of up to 0.018 nm in radiances measured by the sensor with respect to the bandcenter wavelength predicted from weekly solar flux measurements. Since the algorithm uses tables of NRs where the radiance and solar flux measurements are not shifted with respect to each other, this intra-orbital shift leads to both accuracy and precision errors in the retrieval. To estimate the accuracy component, simulations using the OMPS algorithm were performed with input NRs constructed of radiances shifted in wavelength 0.018 nm with respect to the solar flux. This represents the worst case situation. The resulting errors range from 0.72% at high ozone values to 1.5% at low ozone values.

7.1.1.7 Polarization Sensitivity

We have estimated the sensitivity of the Nadir Total Column retrieval algorithm to polarized radiances. Polarization of backscattered radiation poses a particular problem in the near UV where Rayleigh scattering cross sections are high and single scatters predominate. Reflective surfaces in the sensor can enhance incident radiation of one polarization state more than the other. This in itself is not a problem, except that the relative amplitudes, S and P, of polarized light will vary with viewing conditions. The result would be cross-track and latitude dependences in the retrieved ozone amounts. BUV sensors typically use polarization scramblers or depolarizers in the fore-optics to reduce the polarization sensitivity of the sensor to acceptable levels. The Nadir sensor is designed with a polarization scrambler at its entrance aperture.

We took advantage of existing radiative transfer simulations to first estimate the percent polarization in each of the two polarization states for backscattered UV radiation. This information is available from the Dave forward model, which has been used to generate radiances for TOMS and OMPS viewing conditions and at TOMS wavelengths. To compute the sensitivity to polarized light, we make the assumption that radiances will be in error by the percentage of polarization present in the incoming radiances. For our studies, we also assumed that the Nadir scrambler reduces the linear polarization sensitivity to 5%. Thus, if 20% of the incoming radiation is plane polarized, we say in our conservative model that radiances have a 1% error. The optical designs have no scanning optics and fairly small apertures, making polarization scrambling very effective at reducing polarization sensitivity; expected polarization sensitivity of the sensor will actually be 1% or less.

We computed radiance errors at three TOMS wavelengths under a variety of viewing conditions. The wavelengths, 313 nm, 331 nm, and 360 nm, correspond to the TOMS A triplet and are not far from A triplet wavelengths on the Nadir sensor. The triplet formulation, discussed in Section 2, forms a linear combination of the N values from the three measured radiances. We express an error in the N values, ΔN_λ, in terms of an error in the radiances, ΔI_λ:

$$\Delta N_\lambda = \ln\left(\frac{I_\lambda + \Delta I_\lambda}{I_\lambda}\right) \tag{192}$$

The effective radiance error in the A triplet is the difference between the true error at 313 nm and the error predicted by the linear extrapolation of the two longer wavelengths,

$$\Delta N_A = \Delta N_{313} - \left[f\left(\Delta N_{331} - \Delta N_{360}\right) + \Delta N_{360}\right] \tag{193}$$

where f is a ratio of wavelength separations from 360 nm of the two short channels. The ozone error $\Delta\Omega$ is then simply computed using the sensitivity, $dN_A/d\Omega$=0.135 DU^{-1}.

$$\Delta\Omega = \frac{\Delta N_A}{dN_A/d\Omega} \tag{194}$$

These formulas state that no ozone errors will exist due to polarization if the fractional radiance error caused by sensor polarization sensitivity varies at most linearly in wavelength. This fact can be used to explain, in large part, the simulation results shown in **Figure 7.1-3**. These results indicate that, under the worst viewing conditions, ozone errors do not exceed 0.02 DU. The 0.1% error allocation is therefore conservative.

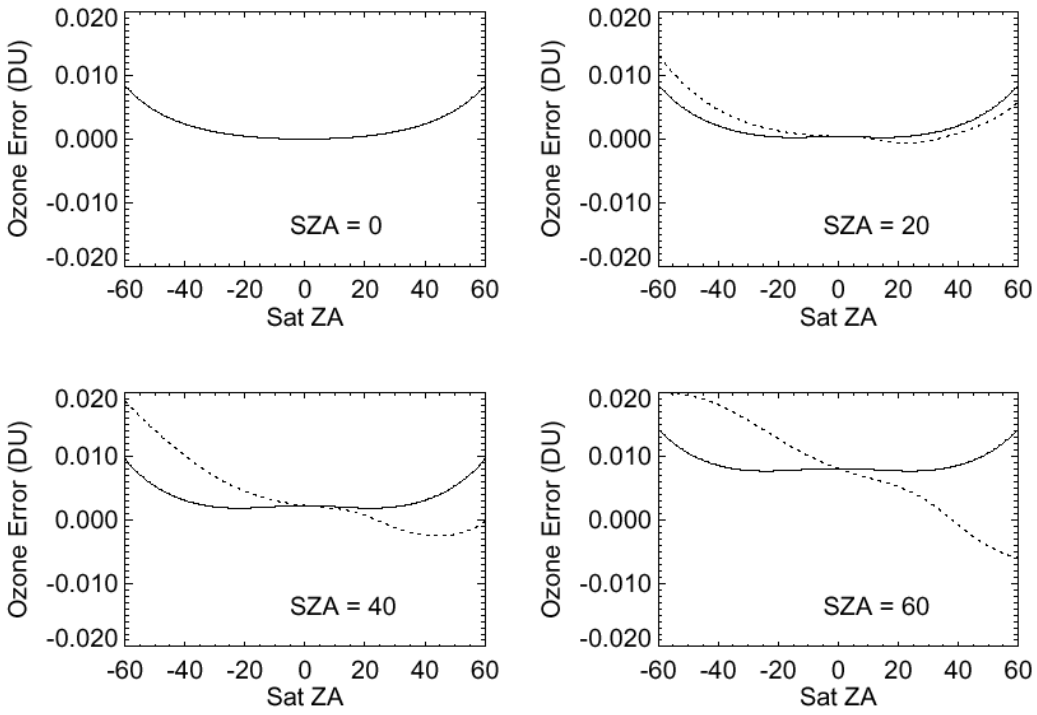

Figure 7.1-3. Ozone Error Due to Polarization Sensitivity

Plots of ozone error due to polarization sensitivity are shown as a function of satellite zenith angle for four solar zenith angles. Errors are for A-triplet ozone. A 5%-residual depolarizer is assumed for the sensor. The solid line represents the situation in a near-noon orbit (relative azimuth = ±90°), and the dotted line is for a 4PM or 8AM orbit (relative azimuth = 30°, 150°)

In this analysis we have used TOMS wavelengths and ozone sensitivities. Because the ozone errors are so small, we hypothesize that the slight changes in these quantities for OMPS wavelengths will make little difference. Also, we have neglected triplet combinations other than the A triplet. These other triplets, which tend to be used at higher latitudes, all use wavelengths longer than 313 nm to decrease ozone sensitivity. Thus the linear extrapolation of radiance errors in wavelength should work even better. On OMPS, the values of $dN/d\Omega$ are the same within a factor of 2 for all triplets.

7.1.1.8 Stray Light, Out of Field

Out-of-field stray light has three sources: off-axis scatter into the telescope's field-of-regard, scatter within the telescope (before the slit), and scatter within the spectrometer (after the slit). We expect that this error is predominantly wavelength-independent before and after the slit. The ozone sensitivity to out-of-field scatter is therefore similar to that of a wavelength-independent albedo calibration error. Current analysis of the sensor optical scatter indicates worst-case off-axis and telescope stray light equivalent to 0.4% of the measured albedo This led to a sensor allocation of 1%. The allocation for total out of field stray light in Table 7.1-2 couples this radiometric allocation with the 7:1 ozone sensitivity discussed above for wavelength-independent albedo errors.

7.1.1.9 Stray Light, Out of Band

The effect of out-of-band stray light on the total column algorithm is detailed in ICSR E8093001 (titled "Explanation of the ozone total column algorithm's linear wavelength assumption and its use in stray light analyses", 30 Sep 98). There it is shown that stray light increases almost exponentially below approximately 317 nm. The result is that short wavelength triplets can have a significant radiance error. The stray light error is defined as the difference between the expected and actual short wavelength signal. Sensor stray light studies indicate that 1% stray light at 312.5 nm is achievable. Using the sensitivity of ozone error to radiance error defined in Equation 38 we see the largest ozone errors occur at the smallest sensitivity values in Table 2.4-2. The allocations entered in Table 7.1-2 are derived using a sensitivity of 1.23% radiance change per 1% ozone change from the 312.5 nm triplet. This sensitivity results in large ozone allocations at the large total column amounts. We expect performance to be much better than this for high column amounts

because longer wavelengths are used for those retrievals. Sensor studies have indicated that stray light levels are less than 0.5% for wavelengths longer than approximately 317 nm.

7.1.2 Algorithm Accuracy Errors

The algorithm accuracy allocations for retrieved total column ozone values are given in the tree shown in **Table 7.1-3**. Derivations of the allocations are given in the text and plots that follow the allocation tree.

Table 7.1-3. Allocation for algorithm contributions to retrieved ozone accuracy

DU	Ray. Scat.	O3 Abs. Coef.	AVTP	Aersol Cor.	Ring Eff.	Cloud Top	Press. Table	Non-Hom. Scene	O3 Profile Shp.	Mult. Scat.	O2-O2	RMS Total
50	0.02	0.50	0.50	0.25	0.10	0.14	0.25	0.20	0.14	0.10	0.10	0.86
125	0.04	1.25	0.50	0.63	0.25	0.35	0.63	0.50	0.35	0.25	0.25	1.81
175	0.05	1.75	0.50	0.88	0.35	0.56	0.88	0.70	0.56	0.35	0.35	2.52
225	0.07	2.25	0.50	1.13	0.45	0.68	1.13	0.90	0.68	0.45	0.45	3.19
275	0.08	2.75	0.50	1.38	0.55	0.55	1.38	1.10	0.55	0.55	0.55	3.78
325	0.10	3.25	0.50	1.63	0.65	0.85	1.63	1.30	0.85	0.65	0.65	4.53
375	0.11	3.75	0.50	1.88	0.75	1.28	1.88	1.50	1.28	0.75	0.75	5.34
425	0.13	4.25	0.50	2.13	0.85	1.53	2.13	1.70	1.53	0.85	0.85	6.09
475	0.14	4.75	0.50	2.38	0.95	2.04	2.38	1.90	2.04	0.95	0.95	6.98
525	0.16	5.25	0.50	2.63	1.05	2.63	2.63	2.10	2.63	1.05	1.05	7.94
575	0.17	5.75	0.50	2.88	1.15	3.34	2.88	2.30	3.34	1.15	1.15	9.02
625	0.19	6.25	0.50	3.13	1.25	3.63	3.13	2.50	3.63	1.25	1.25	9.80

7.1.2.1 Rayleigh Scattering Coefficients

We allocate the 0.3% accuracy for total column given by Fleig et al. (1990, Table 7.2).

7.1.2.2 Ozone Absorption Coefficients, Absolute

We allocate 1.0% based on analysis by C. Wellemeyer comparing Bass-Paur and French measurements of ozone absorption coefficients.

7.1.2.3 Ozone Absorption Coefficients, Temperature Dependence

The allocation is based on the selection of temperature-insensitive wavelengths (Section 2.4.10) and the use of the external atmospheric vertical temperature profile (AVTP) EDR. We allocate constant 0.5 DU error for both precision and accuracy. The derivation is given in the section on the precision allocation.

7.1.2.4 Tropospheric Aerosol Correction

The quadratic fits of the percent error in ozone with $R_{335-377}$ remove most of the systematic error due to aerosols. We expect stray light to affect the tropospheric aerosol correction, with an ozone error of no more than 0.3% (ICSR E8093001, 30 Sep 98). We conservatively allocate 0.5% ozone error.

7.1.2.5 Cloud Top Pressure

The accuracy allocation for cloud top pressure (CTP) is based on the global amount derived for the VIIRS CTP EDR precision listed in section 7.3.2. The global weighted average is 0.38% based on the 25 mb threshold precision at 400 mb; consequently, for the 50 mb threshold CTP accuracy, the allocation is 0.76%.

7.1.2.6 Pressure Table Interpolation

This allocation accounts for the greatly reduced error due to interpolation in pressure when using the new OMPS radiative transfer tables. This improvement over TOMS is due to the availability of the external cloud top pressure data from VIIRS. The fidelity of the table is enhanced by increasing the number of pressure node points from 2 to 4 and changing from linear to Lagrangian interpolation. The improvement is demonstrated in **Figure 7.1-4**. The largest error occurs for extremely high clouds with pressure above 0.2 atm. To be conservative, we set the allocation at 0.5% to account for this extreme case.

The radiative transfer interpolation errors in solar and satellite zenith angles are the same as heritage and are negligible (<0.1%, Klenk et al., 1982).

7.1.2.7 Non-Homogeneous Scene (Snow/Ice/Cloud Cover)

Non-homogenous scenes can occur either due to snow or ice on the ground or cloud cover within the field of view. Simulations using the OMPS algorithm have been performed to determine the effect of non-homogenous scenes on the retrievals. All of the simulations assumed one 20-pixel scene at nadir viewing conditions. In the case of snow/ice cover, the simulation used the high-latitude 125 DU standard profile to represent the worst case (highest radiance) situation encountered by the algorithm.

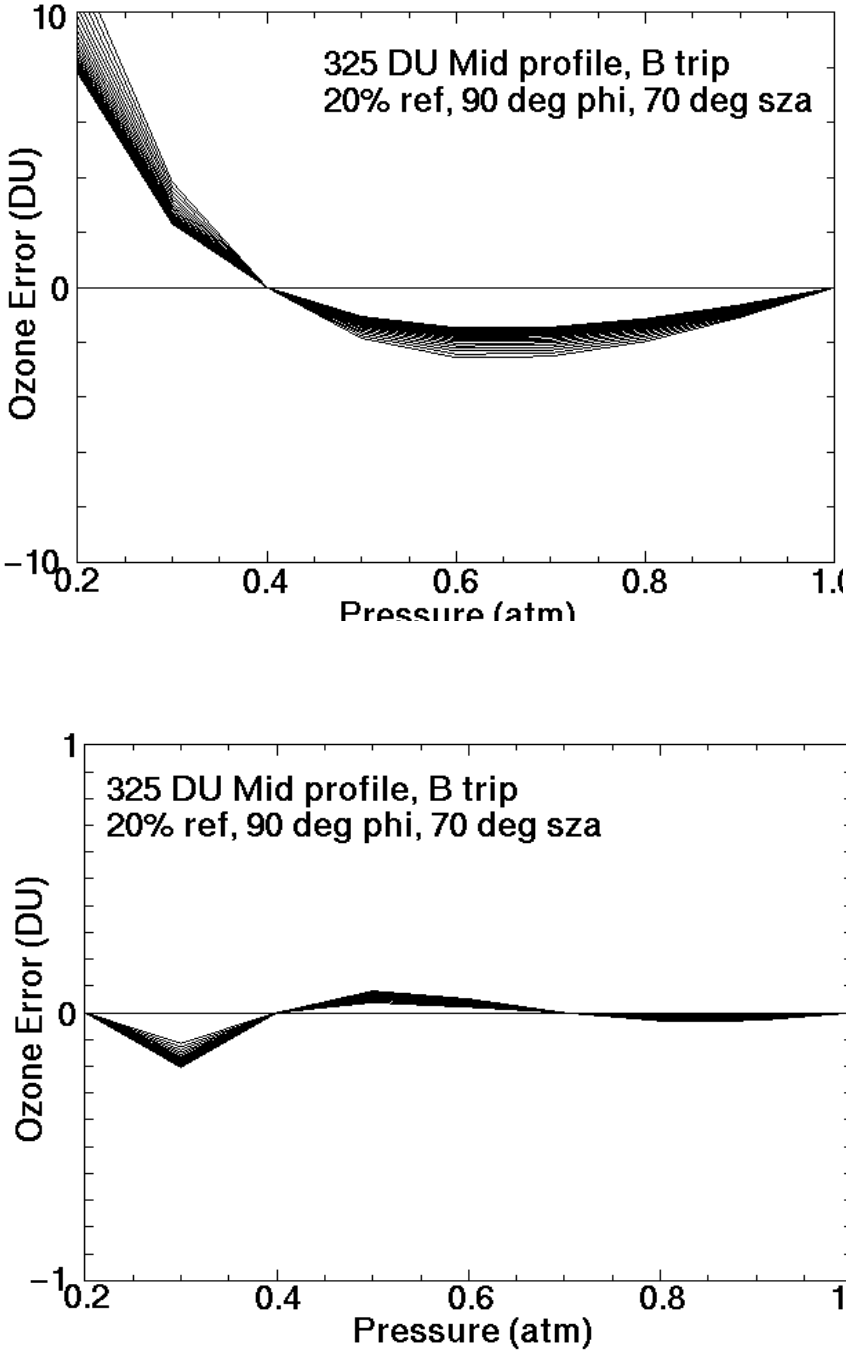

Figure 7.1-4. Ozone error in DU using the TOMS pressure node points (TOP) and the new OMPS pressure node points (BOTTOM). Note the difference in the vertical scales.

The simulations included mixed snow/ice scenes ranging from a clear scene with snow/ice cover from one to ten pixels to a snow/ice scene with

ground cover from one to ten pixels. The average error from all of the simulations was 1.7%. To determine the fraction of 125 DU scenes that contain mixed scenes, the number of 125 DU (+/1 5 DU) retrievals from TOMS for a year were combined with the probability of mixed snow/ice scenes occurring. When this result (2%) was folded in, the error reduced to 0.03% for a global ensemble of 125 DU measurements. For partly cloudy scenes, simulations used the low-latitude 225 DU standard profile to represent the highest radiance scene the algorithm will encounter for these conditions. Partly cloudy scenes were simulated all the way from almost clear (a clear scene with one cloudy pixel) to almost fully clouded (a cloudy scene with one clear pixel) and resulted in errors between 1 and 2%. When both the cloud fraction and cloud pressure distributions were folded into these results, the error reduced to 0.38%. Clearly, the cloudy component of the non-homogenous scenes dominates this term. The allocation was therefore set at 0.4% to reflect this situation.

7.1.2.8 Ozone Profile Shape Errors

The uncertainty due to assumed ozone profile shape reaches 1% at 80 SZA (Wellemeyer et al., 1997). We allocate improved performance (0.5%) through the use of measured profiles from limb and nadir in place of the climatology used in previous retrievals from other instruments.

7.1.2.9 Multiple Scattering

Klenk et al. (1982) report <0.2% error in multiple scattering using six iterations of Dave's auxiliary equation solution to the radiative transfer equation.

7.1.2.10 Ring Effect Correction

We allocate a 0.2% systematic error based on the following considerations.

TOMS V7 makes a Ring effect (rotational Raman scattering) correction based on the work of Joiner et al. (1995). The following angular assumptions are made: SZA = 45 deg, scan angle = 0. Dependences on solar and scan angles are neglected but are small under most conditions (a major exception is SZA > 80 deg). Corrections are calculated for two boundaries: surface (1 atm, R = 0.08) and cloud (0.4 atm, R = 0.8). The magnitude of the correction is <1%. The two N7 TOMS wavelengths most sensitive (~–0.9% radiance correction at 1 atm, R = 0.08) are 317.35 nm and 359.88 nm. We have not selected 360 nm as an ozone insensitive wavelength for OMPS, but we have included 317 nm in our set of ozone sensitive wavelengths for the purpose of measuring our sensitivity to the Ring effect, as described below. The correction is 0.27% for 312.34 nm, which is close to our 312.5 nm baselined wavelength for ozone retrievals.

We have included this correction in our baseline total column retrieval algorithm. Accuracy concerns are twofold: wavelength errors and the incomplete angular modeling described above. C. Wellemeyer selected triplet wavelengths for the operational retrievals that are insensitive to temperature and minimize sensitivity to Raman scattering. He also selected some triplets that are particularly sensitive to Raman scattering. Retrievals using the sensitive and insensitive wavelengths were compared not only to estimate the magnitude of the error but also to provide an additional correction. A talk by J. Joiner at NASA Code 916 in 1994 showed that wavelengths that are insensitive to Raman scattering are also insensitive to the angular dependence of radiance error.

7.2 LONG TERM STABILITY

The long term stability of the total column ozone depends upon the schedule of on-orbit solar calibrations and the solar measurement uncertainty. This section contains a discussion of the planned calibration operations and the anticipated change in diffuser reflectances and its effect on retrieval algorithms. While the long-term stability requirement is 0.1% per year over 7 years of operation, all allocations are based upon a 0.5% stability goal over 7 years.

Spectral stability will contribute to the long-term stability of the EDR products. However, we have no allocation for long-term spectral stability, since we foresee no mechanism for drifts in OMPS spectral knowledge using the solar Fraunhofer technique. Indeed, the sensor spectral registration will drift, and the knowledge of that drift will be uncertain. But the uncertainty of each weekly wavelength calibration will be smaller than 0.1% in ozone (<0.005 nm shift resolution per solar cal. $\times$ 2% ozone per 0.1 nm shift). Assuming a smooth long-term wavelength drift, the uncertainty after only one year of solar measurements will be of the order 0.01%.

7.2.1 Reference Deployment Schedule

Sensor calibration is based upon solar measurements using the Working diffuser. Our baseline schedule for Working measurements means this diffuser will degrade. The Reference diffuser is employed to monitor changes in the Working diffuser through periodic comparison of the two sets of measurements. The Reference measurement frequency is ultimately determined by the lifetime of the sensor and the uncertainty in the comparison between Working and Reference measurements. We will apply regressions to the Working/Reference measurement ratios in order to determine the correction required for Working diffuser degradation. Since the uncertainty in this correction will decrease with time, the Reference deployment frequency can also decrease as the mission progresses.

As discussed in Section 3.1.3.2, it is not the rate of diffuser degradation but our ability to measure the change that determines the radiometric calibration trend uncertainty. Equation 94 gives the uncertainty of the Working diffuser response relative to the Reference diffuser at any point during mission life. The diffuser deployment schedule and solar measurement noise are the only contributing factors in determining this uncertainty.

We have used TOMS Working and Reference solar data to estimate measurement noise in order to determine the optimum diffuser deployment schedule necessary to meet long-term stability requirements. Figure 7.2-1 contains a plot of the A triplet (312.5nm, 331.2nm, 360 nm) combination (see Equation 111) of the TOMS Earth Probe Working/Reference diffuser signal ratio. A regression of these data indicate an individual Working/Reference ratio uncertainty of σ=0.00128. The actual Working signal uncertainty alone is approximately $\sqrt{2}$ times this number. Applying the 312.5 nm triplet sensitivity 1.23% radiance per 1% ozone from Table 2.4-2 yields an ozone uncertainty of σ=0.15% due to Working reflectance uncertainty. Clearly, repeated diffuser comparisons will reduce this ozone uncertainty still further. We need only have a single Working/Reference comparison in order to satisfy radiometric stability requirements. But this measurement would have to occur just prior to end of the OMPS mission.

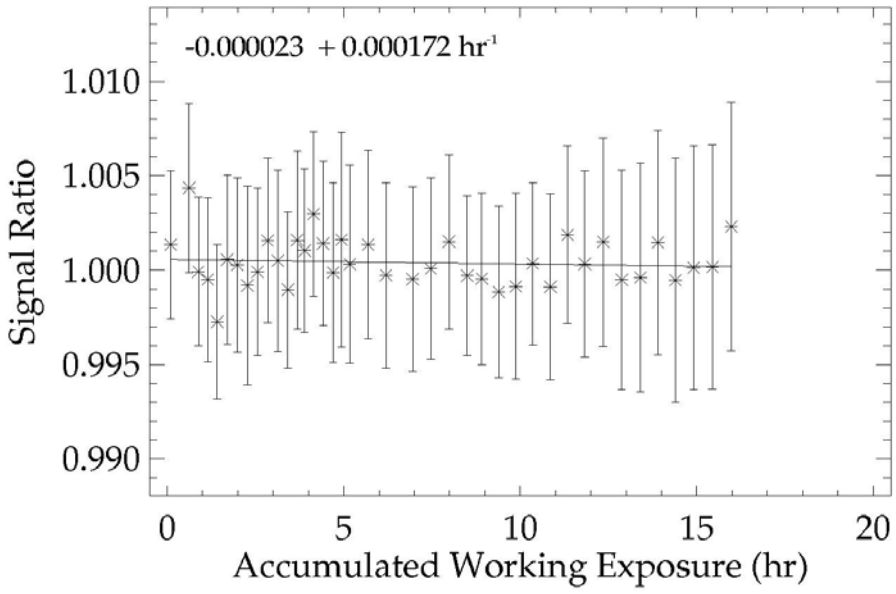

Figure 7.2-1. TOMS Earth Probe Working/Reference solar measurement ratio

The TOMS Earth Probe Working/Reference solar measurement ratio is plotted for the A triplet combination (313 nm, 331 nm, 360 nm) of wavelengths as a function of Working diffuser exposure. Error bars are $\pm 1\sigma$ and represent the estimated uncertainty of a single Working/Reference ratio measurement. A 1st order regression applied to the data indicate that no statistically significant change has occurred in the Working diffuser (relative to the Reference) for the A triplet combination.

A single Reference diffuser measurement just prior to the end of the mission is impractical because it is impossible to predict when the end will be. If there were no Reference diffuser at all, the uncertainty in Working diffuser change would be the maximum expected change over 7 years. Similarly, we can establish a Reference deployment frequency by limiting the maximum expected Working diffuser change in one deployment period.

We base our assumptions concerning OMPS diffuser degradation on the results from TOMS/ADEOS, the BUV sensor with the greatest diffuser degradation rate. The multi-diffuser monitoring system on that instrument indicated rates with equivalent exponential time constants of 500 hr at 360 nm and 300 hr at 309 nm. Assuming weekly solar measurements each with an equivalent solar exposure of 0.05 hr, the reflectance of the OMPS Working diffuser will have decreased by about 3.5% at 360 nm after 7 years.

We can estimate the effect of Working diffuser degradation on ozone by assuming that the 309 nm change represents a triplet radiance change, and by applying the maximum short-wavelength sensitivity from Table 2.4-2, 1.06% radiance change per 1% ozone change. With a degradation time constant of 300 hr, ozone errors would remain below 0.5% if the Working diffuser is exposed for no more than 1.6 hr. At 0.05 hr per solar sequence, the maximum number or weekly Working deployments is then 32. Being even more conservative, we propose a Reference diffuser deployment period of 6 months. This period can decrease or increase depending upon whether actual OMPS degradation rates are greater or less than TOMS/ADEOS and whether solar measurement noise is greater or less than observed on TOMS. The period can also be decreased as more Working/Reference comparisons are accumulated.

In the foregoing discussion we have ignored Reference diffuser change over the 7 year lifetime. We do not expect significant Reference diffuser change, and what change does occur should not introduce additional long-term errors. The exposure-dependent model of diffuser degradation allows us to estimate Reference diffuser change (see discussion in Section 3.1.3.2) once a reasonable number or Working/Reference

comparisons have been made. Furthermore, any Reference diffuser change should introduce negligible errors in ozone trends. The degradation rate assumptions we made to determine the deployment frequency were very conservative. Assuming the 309 nm degradation is the same as A triplet degradation is equivalent to saying that no degradation occurs at the other two wavelengths of the triplet. If, which is closer to reality, diffuser degradation varies linearly with wavelength, there will be no resulting triplet-derived ozone error. In fact, the TOMS triplet approach was developed primarily to deal with diffuser degradation. As **Figure 7.2-2** demonstrates, the wavelength dependence of BUV diffuser reflectance time constants has been nearly linear for wavelengths longer than 300 nm. This spectral relationship holds for moderate degradation (<10%). **Figure 7.2-1** contains a plot of the A triplet degradation of the TOMS Earth Probe Working diffuser. There is no statistically significant change in the Working/Reference ratio after over 15 hours of Working exposure. The total expected Reference exposure time is less than 1 hour. We can therefore argue with some confidence that any Reference diffuser degradation will have no effect on triplet-derived ozone.

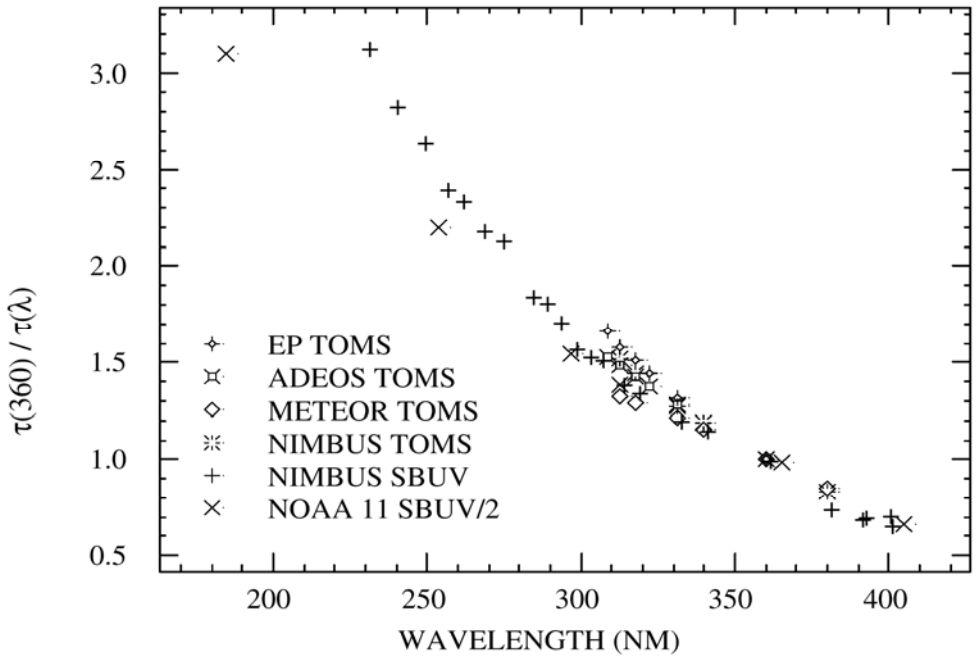

Figure 7.2-2. Diffuser degradation rates for TOMS and SBUV instruments.

This figure contains the diffuser degradation rates (1/time constant) for several TOMS and SBUV instruments plotted as a function of wavelength. The data, which have been normalized to the time constant at 360 nm,

demonstrate the similarity in spectral dependence of diffuser degradation in the UV. The data also show that this dependence is nearly linear for wavelengths longer than 300 nm.

We note that the data contained in the Figure 7.2-1 represent more than 6 years of solar measurements. It could be concluded, based upon these results, that there is no need to correct for Working diffuser change either. Indeed this is our baseline approach, as discussed in Section 3.1.3.5.3.

7.2.2 Radiometric Uncertainty Allocation

In order to allocate an uncertainty for long-term radiometric stability, we simply divide our 0.5% ozone stability goal by the sensitivity of ozone change to radiometric change. For a single wavelength change, i.e. only one of the three triplet wavelengths, a sensitivity of 1.23% radiance per 1% ozone was used in the preceding section. This would result in a wavelength-dependent radiometric stability requirement of 0.62%. Using a wavelength-independent sensitivity of 7% radiance per 1% ozone yields a 3.5% wavelength-independent radiometric stability requirement.

As discussed in the previous section, these allocations are far larger than what can currently be achieved from TOMS solar measurements. Figure 7.2-3 contains a prediction for the radiometric trend uncertainty using the following TOMS Earth Probe solar measurement precisions: 0.1% wavelength-dependent and 0.2% wavelength-independent. We assume that Working/Reference comparisons are made semi-annually and that uncertainties are of the same magnitude and uncorrelated for both diffusers. Uncertainty calculations are made using Equation 94. Each point in the plot represents the drift uncertainty at the time of the diffuser comparison. Since the stability requirement may be met after the complete dataset is acquired, only the final points in the plot are relevant to the requirement. Based upon these results, we set the allocation for long term stability at 0.5% for wavelength-independent errors and 0.3% for wavelength-dependent radiometric changes. These values are roughly twice what can currently be achieved based upon TOMS solar measurement precisions..

This figure contains estimated radiometric drift uncertainties, for both wavelength-dependent and wavelength-independent changes, following each of the semi-annual Working/Reference diffuser comparisons. Calculations are based upon estimated solar measurement precisions from TOMS Earth Probe data. The 0.3% and 0.5% allocations, respectively, are also shown.

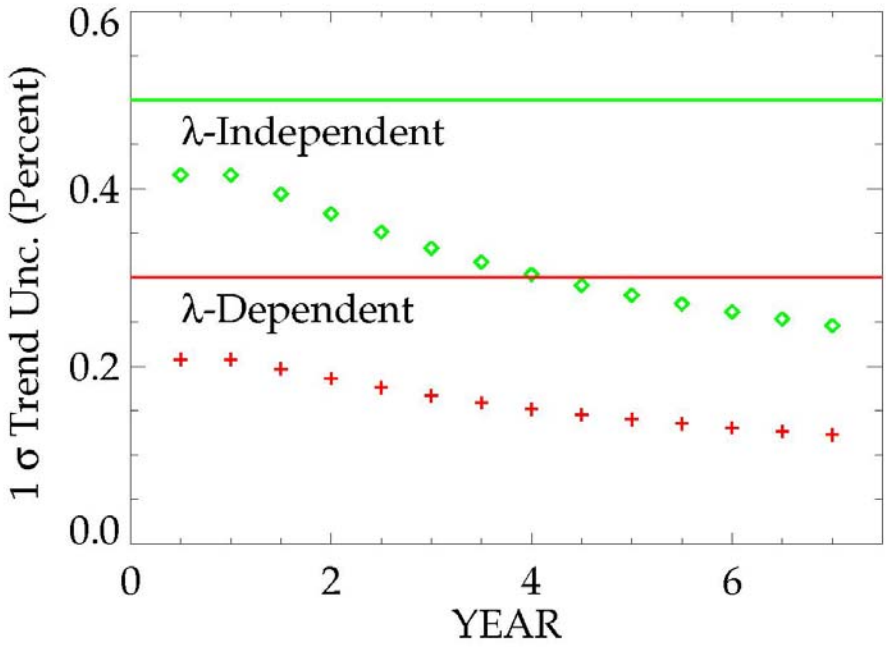

Figure 7.2-3. Estimated Radiometric Drift Uncertainties

7.3 SYSTEM PRECISION

The allocated precision performance is shown in **Figure 7.3-1**. We assure precision performance at or better than threshold, depending on the measured total column amount. As with accuracy, total column precision applies to a global ensemble of measurements having the same total column amount (IPO ICSR 3999, 29 Jan 99). Therefore, this allocation applies to a global ensemble.

Section 7.3.1 describes the allocations to sensor noise. Section 7.3.2 describes the allocations to algorithm precision errors. Section 7.3.3 describes how the global ensemble is estimated.

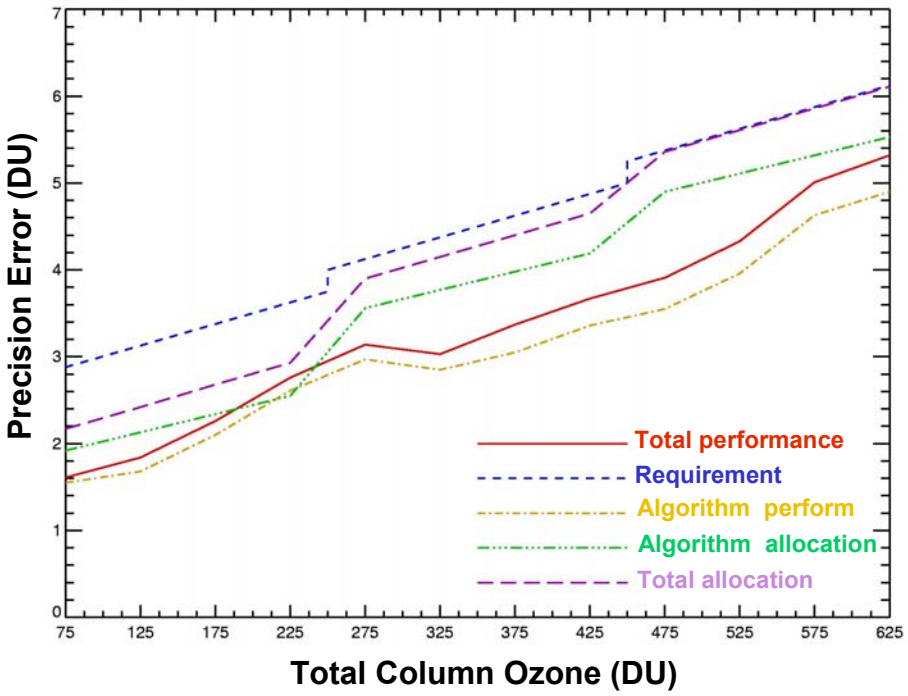

Figure 7.3-1. OMPS Total Column precision error allocations and performance.

The “total” allocation and performance curves indicates a combination of sensor and algorithm errors.

7.3.1 Sensor Precision Errors

There are two basic components of sensor precision: radiometric and spectral. The only pure noise sources that contribute to sensor precision are detector shot noise and electronic readout noise. However other errors, such as thermal sensitivity and calibration accuracy, appear random in a global ensemble.

7.3.1.1 Sensor Noise

The sensor uncertainties contributing to precision errors are just due to the signal to noise ratios of the wavelength channels used in the retrieval. Improving the signal-to-noise ratio (SNR) of the sensor can reduce the effect of sensor noise. The precision error due to random noise in the earth radiances and solar irradiances observed by the spectrometer is derived from equation (21) of McPeters et al. (1996):

$$\frac{\sigma_\Omega}{\Omega} = \sqrt{\frac{(\lambda_2 - \lambda_3)^2 e_1^{\,2} + (\lambda_1 - \lambda_3)^2 e_2^{\,2}}{\left[(\lambda_2 - \lambda_3)s_1 - (\lambda_1 - \lambda_3)s_2\right]^2}} \tag{195}$$

where e_n is the normalized standard deviation of the albedo random noise:

$$e_n^{\,2} = \left(\frac{\sigma_A}{A}\right)^2 = \left(\frac{\sigma_I}{I}\right)^2 + \left(\frac{\sigma_F}{F}\right)^2 \tag{196}$$

and s_n is the sensitivity at wavelength n to ozone (percent albedo per percent ozone).

We have allocated SNR = 1000 for radiance and for irradiance noise due to the sensor. **Figure 7.3-2** shows the sensitivity to SNR = 1000 for a wide range of cases. The solid curves represent bright cases (low ozone, cloudy scene) while the dashed curves represent dark cases (high ozone, clear scene). Based on these results, the allocations are 0.20% for 0 < SZA < 60 deg, 0.25% for 60 < SZA < 70 deg, and 0.33% for 70 < SZA < 80 deg.

Irradiance noise is dominated by goniometric errors associated with the solar diffuser. The noise is reduced (yielding SNRs of 1000) by 1 week extrapolations based on the previous 10 weekly calibrations, as shown in Figures 3.1-15 and 7.2-2.

The solid curves represent bright cases (low ozone, cloudy scene) while the dashed curves represent dark cases (high ozone, clear scene). The curves for 0 < SZA < 60 deg include two cases for low SZA and two cases for moderate SZA. The cases for low SZA are Ω = 300 DU, R = 0 and Ω = 200 DU, R = 1. The cases for moderate SZA are Ω = 450 DU, R = 0.2 and Ω = 200 DU, R = 1. The two curves for 60 < SZA < 80 deg represent Ω = 75 DU, R = 1 and Ω = 650 DU, R = 0. Clearly, the cases for SZA < 60 deg are similar. The cases for higher SZAs show larger errors, with the error largest for edge of scan (SZA = 80 deg).

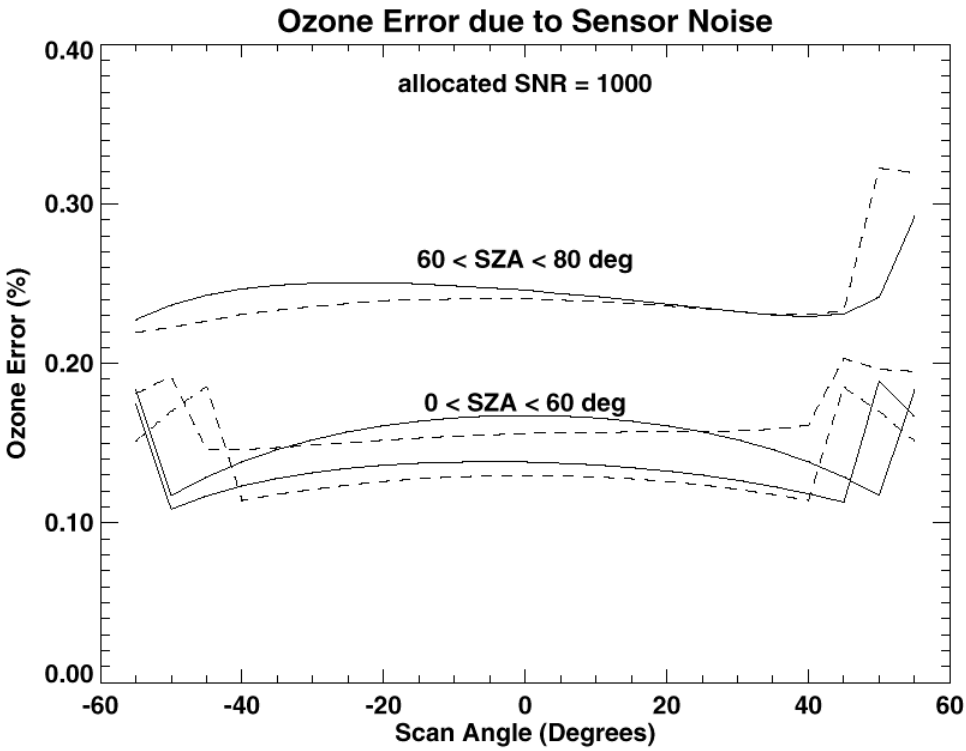

Figure 7.3-2. Ozone error due to sensor SNR = 1000 for a wide range of scenes.

7.3.1.2 Spectral Calibration

Like radiometric calibration, spectral calibration results are trended and extrapolated to yield predicted bandcenter wavelengths for all macropixels. The process is described in more detail in Sections 3.1.3 and 3.1.3.5.6. The precision error associated with bandcenter wavelength assignments will be a function of the wavelength measurement uncertainty and the number of measurements included in a trend. We estimate the precision of individual measurements to be 0.005 nm or smaller. If we assume the wavelength drift is a smooth, monotonic function of time, then the trended values should have even smaller deviations with respect to true bandcenter wavelengths. Our baseline regression period is 10 measurements, so we might expect 0.002 nm or better precision in the trended values. With a sensitivity of 2% ozone per 0.01 nm wavelength error (see Section 7.1), this results in less than 0.05% ozone error.

However, wavelength shifts in flight, specifically those of the OMPS Total Column sensor, do not change monotonically with time. In particular, temperature cycles in the sensor result in shifts in spectral registration on

the focal plane. The dominant cycles are orbital (approximately 1 °C) and annual.

The estimated annual cycle in spectral registration is shown in Figure 7.3-3. This result was obtained from a sensor thermal model coupled with a mechanical model, and assumes end-of-life performance. We have correlated the spectral variation with solar beta angle, which often has the greatest effect on sensor heating, though we can't be certain of this correlation.

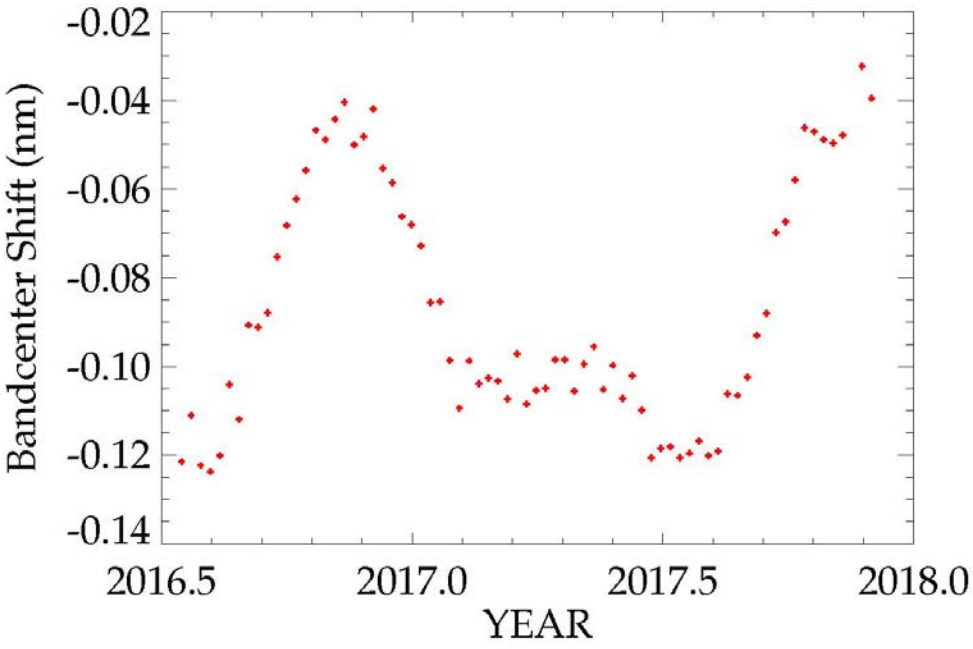

Figure 7.3-3. Results of Thermal and Mechanical Modeling on Spectral Registration

The results of thermal and mechanical modeling on spectral registration is shown. The time dependence was chosen to match that of the solar beta angle. Measurement deviations of σ=0.005 nm about the nominal registration were introduced.

Using our baseline regression of 10 measurements we performed a trend analysis and compared the predicted shift with the actual (nominal) shift on every measurement date. The resulting errors are plotted in Figure 7.3-4. Their standard deviation is 0.008 nm, poorer than the measurement precision itself. However, the thermal sensitivity of these spectral shifts should remain constant once the sensor is in orbit. Once this sensitivity is determined, soon after launch, it can be as a first order correction for such shifts, in effect smoothing out Figure 7.3-3. It only

remains for the wavelength trending to remove residual drifts. While it is difficult to estimate the precision with which such a technique will perform, it is easy to imagine final bandcenter wavelength precisions below the 0.005 nm mark.

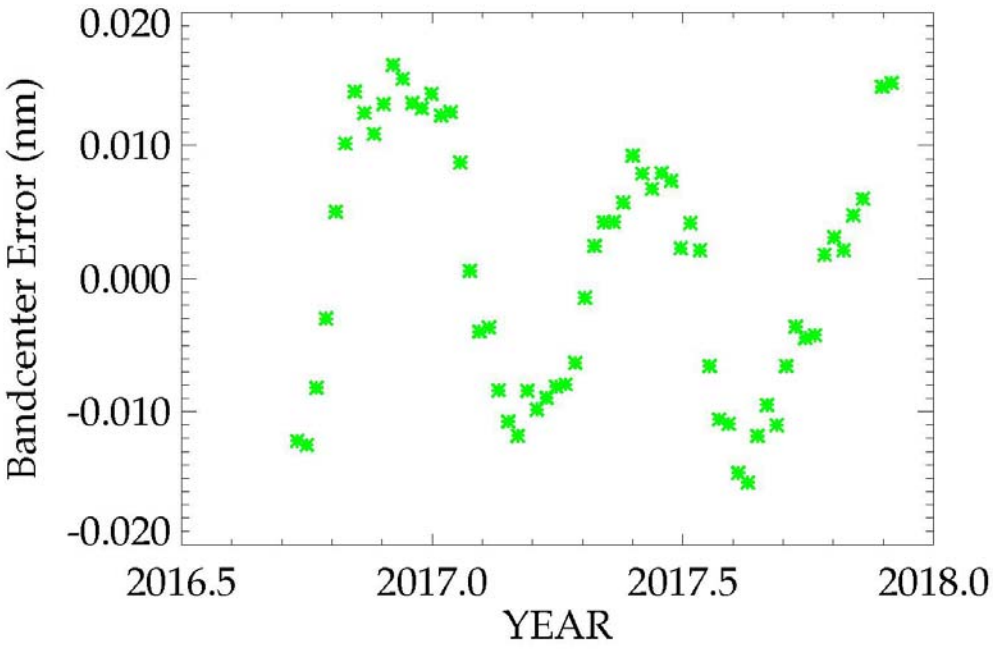

Figure 7.3-4. Deviations From Actual Wavelength Shifts

The deviations from actual wavelength shifts (Figure 7.3-3) following trending are shown. The trending fits 10 measurements prior to the measurement of interest. The standard deviation is 0.008 nm.

As discussed in Section 7.1, thermal changes to the sensor throughout the orbit causes shifts in bandcenter wavelengths of up to 0.018 nm with respect to the values predicted from weekly solar flux measurements. To estimate the precision component, simulations using the OMPS algorithm were performed with input NRs constructed of radiances shifted 0.006 nm with respect to the solar flux. This number is slightly larger than the standard deviation of the modeled wavelength variation throughout the OMPS orbit. The resulting errors range from 0.2% at high ozone values to 0.65% at low ozone values. These errors have been applied to the sensor precision allocations.

A correction, similar to that proposed for annual spectral registration cycles, can be applied to reduce the error associated with intra-orbital

spectral shifts. The thermal sensitivity of these shifts would probably be different than for annual cycles because the sensor is no longer in thermal equilibrium. Section 3.1.3.5.8 contains a discussion of strategies for determining the thermal coefficient.

7.3.1.3 Radiometric Calibration

Our recommended SDR algorithm relies upon the current TOMS calibration approach for operational processing (see Section 3.1.3). In order to obtain sensor calibrations for operational processing, the OMPS solar measurements are fit to a low order polynomial and extrapolated for a short period. This regression is updated as new solar data are obtained. An example of the resulting sensor calibration is shown in Figure 7.3-5 for the A-triplet combination of solar data. For an operating OMPS, a plot or plots analogous to Figure 7.3-5 will exist for each spatial channel. An estimate of the true TOMS measurement is obtained by smoothing through the solar data, and is shown in Figure 7.3-6. It is worth noting that the standard deviation of the solar data about “truth” is 0.085% whereas the standard deviation of the predicted values is about 0.055%. The implication is that the predicted calibration introduced less ozone error than a calibration based on the most recent solar measurement (0.3 DU). The prediction error is a function of the amount of solar data included in the regression. We investigated the optimal number of measurements in a regression for the operational calibration of TOMS. The results, shown in Figure 7.3-7, measure the standard deviation of the predicted solar measurement with respect to the actual measurement. The optimum number of measurements is the result of a trade between following changes in sensor throughput and not following individual solar measurements. TOMS does not currently use the optimum interval.

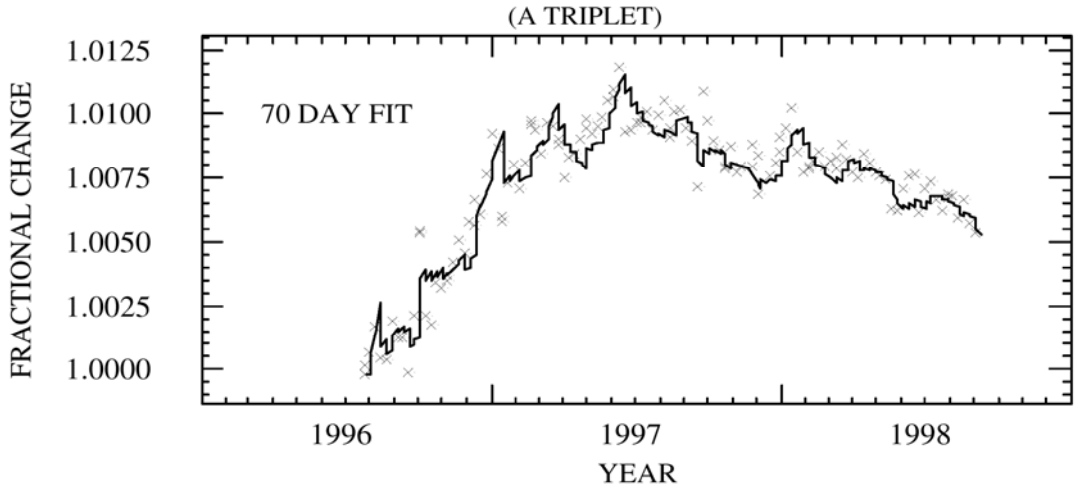

Figure 7.3-5. TOMS Earth Probe operational calibration for the A triplet

The TOMS Earth Probe operational calibration for the A triplet is shown superimposed over the solar data. Predicted calibrations for 1 week into the future are determined from a 1st order regression of the previous 10 Working diffuser measurements

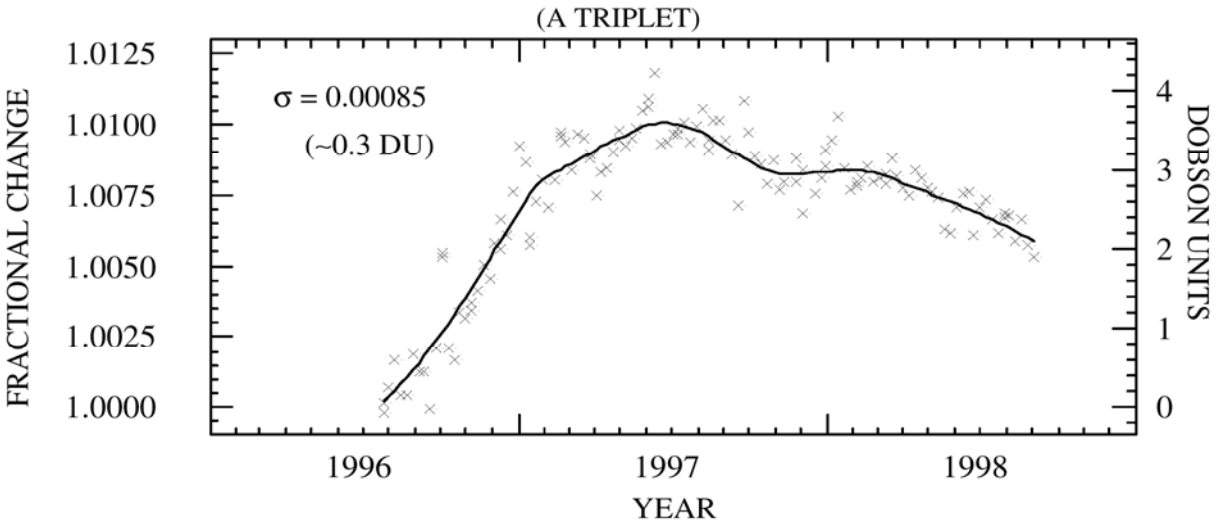

Figure 7.3-6. TOMS Earth Probe Working diffuser solar signal

A plot of TOMS Earth Probe Working diffuser solar signal (corrected for goniometry and sun/earth distance) is shown for the A triplet combination of wavelengths (313nm, 331nm, 360 nm). A smooth fit indicates an estimate of the true instrument calibration. The standard deviation about the fit is translated into an ozone uncertainty of ~0.3 DU via the A triplet sensitivity of 0.3%/DU.

The standard deviation of predicted calibrations (translated into column ozone) about the “true” sensor calibration of Figure 7.3-6 is shown. The variance depends on the amount of solar data included in the regression. The plot indicates that an optimum data selection exists for a given sensor. This optimum period will depend on the specific sensor response and the solar measurement uncertainty.

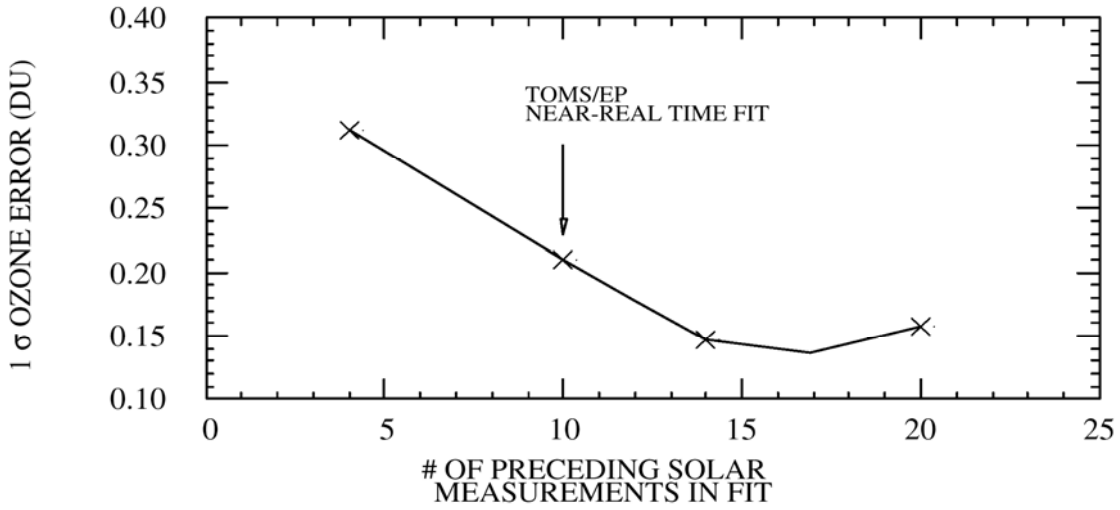

Figure 7.3-7. Standard Deviation of Predicted Calibrations About the "True" Sensor Calibration of Figure 7.3-6

One effect that will tend to increase the precision of radiometric calibrations is the annual thermal cycle of the sensor. As discussed in the previous section, the thermal cycle of the sensor results in a spectral registration shift of approximately 0.085 nm peak-to-peak that probably correlates with solar beta angle. As the spectral registration of the sensor varies throughout the year, each pixel's bandcenter will slide along the Fraunhofer structure. This irradiance change is as much as 4.5% at 359 nm, the worst affected channel. The SDR algorithm corrects for these shifts when reporting solar irradiances (see Section 3.1.2.4). The final error will be approximately 1% peak-to-peak at 359 nm, and will have the time dependence shown in Figure 7.3-4. The EDR algorithm uses these erroneous irradiances to compute theoretical radiances for the sensor tables. But following these computations, it divides by the same solar irradiance to compute normalized radiances, NR. This is a fundamental feature of the BUV technique: *spectral shifts, provided they are the same for radiance and irradiance measurements, do not affect normalized radiances*. The erroneous bandcenter wavelengths reported in the SDF are also used by the EDR algorithm in determining ozone absorption cross sections. The effect of this error was discussed in the previous subsection.

The statement that spectral shifts cancel when computing normalized radiances is true in principle, but in practice there are mitigating circumstances. As we showed with wavelength monitoring in the previous section, an additional error results when trending on a cyclical function. To investigate the magnitude of this error, we took the result shown in Figure 7.3-4 and multiplied it by the 359 nm sensitivity: 0.52% irradiance

change per 0.01 nm shift. We then added a random σ=0.1% noise to this, corresponding to the wavelength-independent solar measurement uncertainty. We performed a 10 measurement trend on this result and compared it to the original cyclic irradiance without noise. The result is shown in Figure 7.3-8. The standard deviation is 0.2%.

We note that the 359 nm shift sensitivity is quite easily twice that of other near-UV wavelengths, so most irradiance errors should have a standard deviation within 0.1%. Also, wavelengths such as 359 nm were specifically avoided in selecting triplet wavelengths because of the Fraunhofer structure. Finally, we have yet to consider the mitigation strategy outlined in the previous section for spectral trending. A thermal correction that reduces spectral registration trending errors will also reduce resulting irradiance trending errors. As a result, we do not believe that the annual spectral registration cycle will have a significant effect on radiometric calibration.

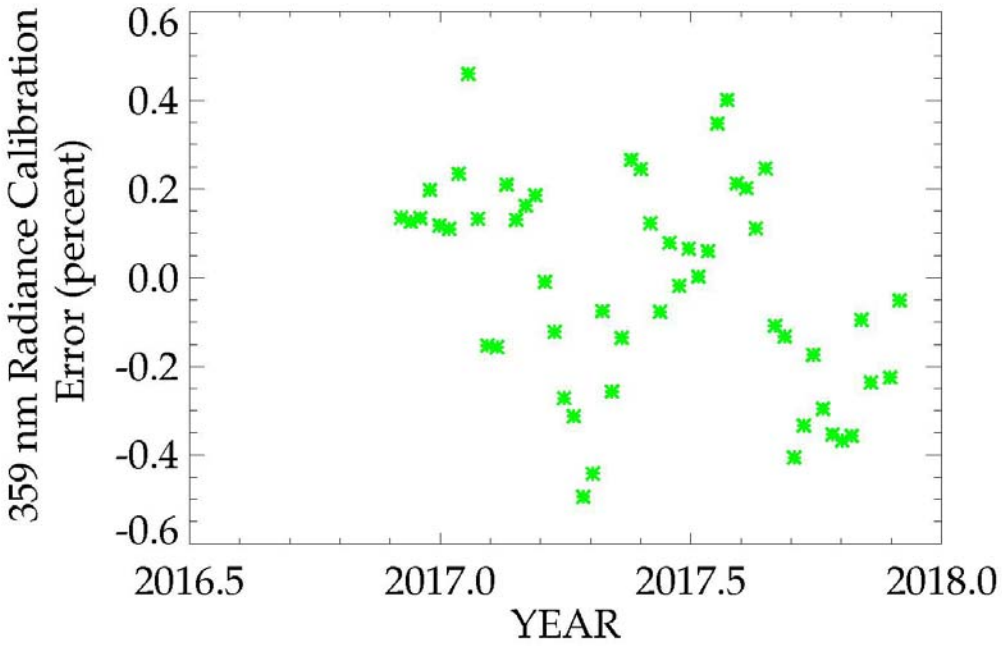

Figure 7.3-8. Trended irradiance errors resulting from the spectral trend errors of Figure 7.3-4

The trended irradiance errors resulting from the spectral trend errors of Figure 7.3-4 are shown. The standard deviation of these points is 0.2%.

7.3.2 Algorithm Precision Allocations

7.3.2.1 Ozone Absorption Coefficients, Temperature Dependence

In the SBUV and TOMS heritage algorithms, the variation of the actual temperature profile about the climatological profiles used in the forward model causes a precision error. Fleig et al. (1990) and McPeters et al. (1996) give it as 1%. For the OMPS baseline design, the allocation for this error is based on the selection of temperature-insensitive wavelengths (Section 2.4.10) and the use of the external atmospheric vertical temperature profile (AVTP) EDR from CrIMSS. We allocate constant 0.5 DU error for both precision and accuracy based on assumed 10K temperature variation simulations shown in **Figure 7.3-9**. The largest error in DU is for 425 DU at low SZAs (0.4 DU), so this constant allocation should account for the required measurement range (50-650 DU) and horizontal coverage (SZA < 80 deg).

7.3.2.2 Cloud Top/Surface Pressure

In general, a terrain pressure database is sufficient for our uses. However, surface pressure can vary by more than 100 mb from ambient. Since such a deviation corresponds to a 0.3% total column ozone error (significant in the context of a 3 DU + 0.5% threshold), we baseline the use of the pressure profile EDR (ICSR E7121806, 19 Dec 97). The precision threshold for this EDR is 4 mb, corresponding to ~0.01% error, so we allocate 0.05% ozone precision due to surface pressure for totally clear scenes.

For totally cloudy scenes, our allocations are based on simulation results shown in **Figure 7.3-10**. The uncertainty in the cloud top pressure (CTP) causes two errors that cancel to some degree but not entirely: the error in the ozone estimated to be beneath the cloud, and the error in the ozone measured above the cloud by the BUV technique. For example, if the algorithm places a cloud at a lower pressure than it actually is, the amount of ozone estimated beneath the cloud for the assumed CTP will be larger than it should be (independent of other errors in the estimate). At the same time, with the higher altitude, the algorithm expects less backscatter and hence less ozone absorption above the cloud to match the measured radiances than it should. The magnitude of the former error is larger than the latter.

The results in Figure 7.3-10 are for low, mid, and high latitude scenes, assuming clouds at 0.4 atm (>7 km) and a cloud top pressure precision of 30 mb. The effect on the reflectivity is included self-consistently. The most serious error was 0.7% for low-mid latitude ozone and 0.9% for high latitude ozone (both corresponding to high ozone amounts). The allocations are based on the use of the external CTP EDR. For 25 mb (the

VIIRS threshold above ~7.5 km), the allocations are 0.6% and 0.75% for low-mid and high latitude ozone, respectively. The most serious error was 0.7% for low-mid latitude ozone and 0.9% for high latitude ozone (both corresponding to high ozone amounts). The allocations are based on the use of the external CTP EDR. For the 25 mb threshold precision, the allocations are 0.6% and 0.75% for low-mid and high latitude ozone, respectively.

7.3.2.3 Cloud Fraction (Non-Homogeneous Scene)

This allocation is driven by the case when there is snow or ice cover on the ground. Based on the same reasoning as the accuracy allocation, for the the ozone column precision allocation is 0.4%.

7.3.2.4 Ozone Profile Shape Errors

As the SZA increases, the incident solar irradiance penetrates less into the atmosphere. Consequently, the sensitivity to the shape of the ozone profile increases. A correction technique based on profile climatology and total column radiances can achieve about 1% precision at 80 deg SZA, using the Nimbus 7 and Meteor TOMS wavelengths (Wellemeyer et al., 1997, Figure 5). We expect to improve this performance from 1% to 0.5% by using the ozone profile measured by our limb sensor. We allocate 0.5% for 70 < SZA < 80 deg, and 0.1% for lower SZAs.

7.3.2.5 Tropospheric Aerosol Correction

There are two sources of precision error in the aerosol correction. The first is due to sensor and algorithm noise. A unit of N value is equal to a 2.3% change in albedo (Torres et al., 1998). Consequently, for SNR = 1000, we expect the equivalent N value noise to be 0.14/2.3 = 0.06 N-value. The combined algorithm and sensor noise is about 0.1 N-value in the aerosol index. The algorithm error is probably associated with errors in the forward model. Based on **Figure 7.3-11**, this error is equivalent to about 0.1% ozone error.

The dominant source of error is due to the scatter of actual ozone error about $R_{336\text{-}377}$. **Figure 7.3-11** (from Torres et al., 1998) shows the scatter due to different aerosol types, layer heights, and optical depths, and different relative azimuth angles and satellite zenith angles. To account for the scatter as well as the noise effects, we allocate 0.5% precision for an aerosol-laden scene after the aerosol correction.

7.3.2.6 Tropospheric Ozone

This section is no longer relevant as this correction is no longer done with data from the limb profiler.

Since the OMPS correction for the inefficiency of the BUV technique to tropospheric ozone depends on the stratospheric ozone profile determined by the OMPS limb-retrieval system, this error is dominated by the precision of the limb retrieval in determining individual layer ozone amounts, given in Table 7.3.-1.

Table 7.3-1. Limb retrieval precision

PRESSURE (ATM)	Error(%)
Tropopause – 15 km	10
15 – 28 km	3
28 – 60 km	10

In order to minimize this contribution (and to avoid the complicating effect of clouds) the tropospheric technique uses limb-retrieved profiles above 13 km. Also, the total ozone above 13 km is assumed to be constant above the nadir mapper's FOV, meaning the 3 profiles retrieved by the limb sensor above the FOV can be averaged together to further reduce the limb sensor's contribution to by a factor of 1.7. This assumption is generally valid except in areas where weather fronts cause changes in air mass across the air mass. This technique must therefore check to make sure the assumption is valid before applying this technique.

The contribution of the limb-retrieved ozone profile above 13 km was estimated by randomly varying the total column standard profiles layer amounts within the limb precision errors given in Table 7.3-1, summing up the total ozone above 13 km, and determining the standard deviation about the true amount above 13 km. These values were then combined with corresponding efficiencies of the BUV technique to measure ozone below 13 km (determined using the dN/dx sensitivity table described in Section 2.3.2) to arrive at the total column's precision error estimates corresponding to the tropospheric ozone technique.

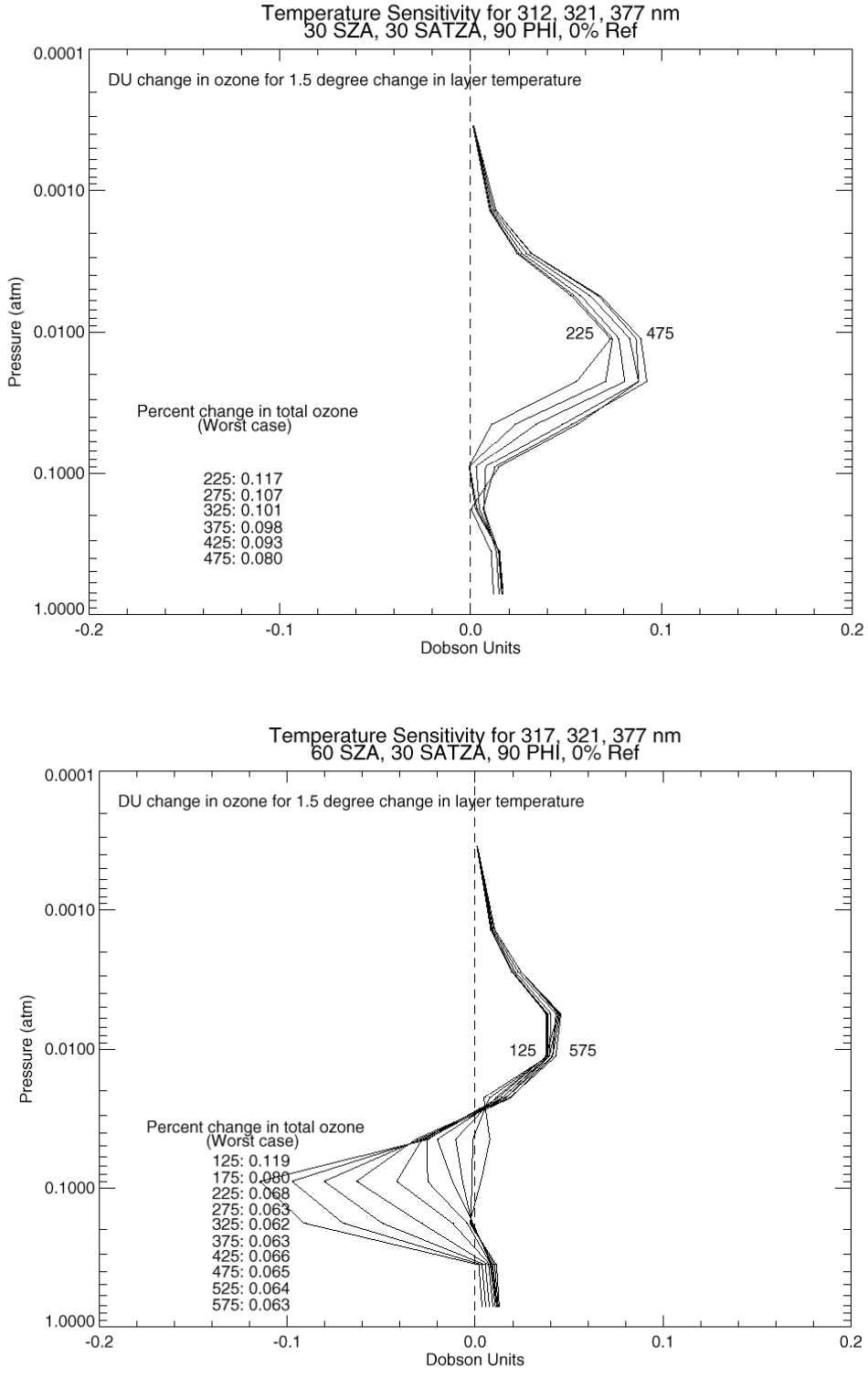

Figure 7.3-9 (a),(b). Temperature Sensitivity for (a) Low and (b) mid

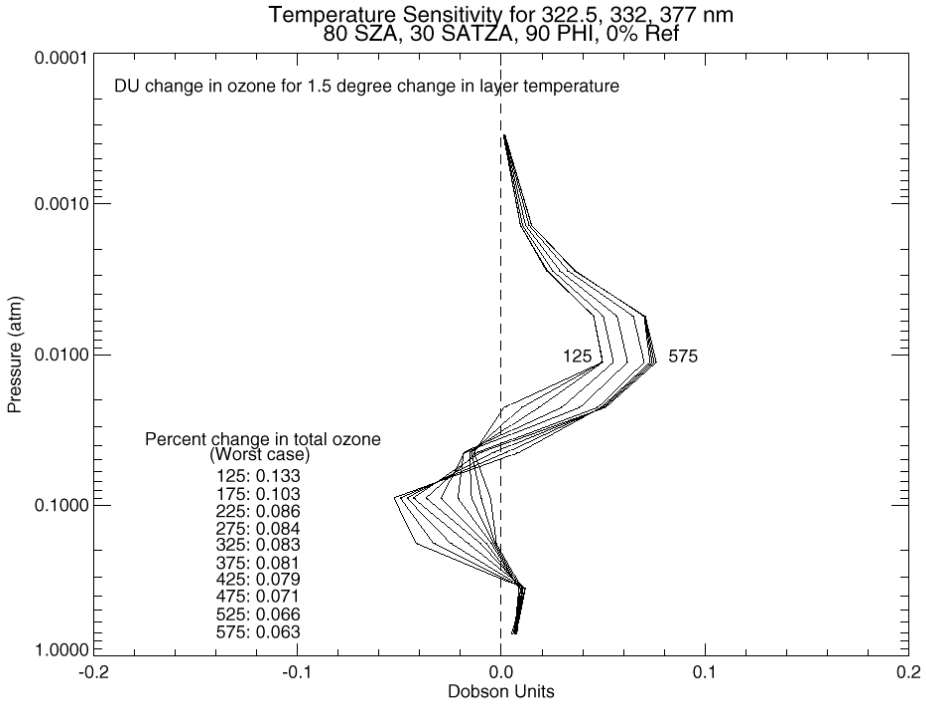

Figure 7.3-9(c). Ozone Temperature Sensitivity for (c) High

Ozone temperature sensitivity for (a) low, (b) mid, and (c) high solar zenith angles as a function of altitude for the TOMS standard ozone profiles. The total column error for a 1.5 K temperature precision is given in each figure in the lower left hand corner. The largest error in DU is for 425 DU at 30 deg SZA (0.4 DU). The allocations account for the 3.5 K temperature threshold above the 1 mb level.

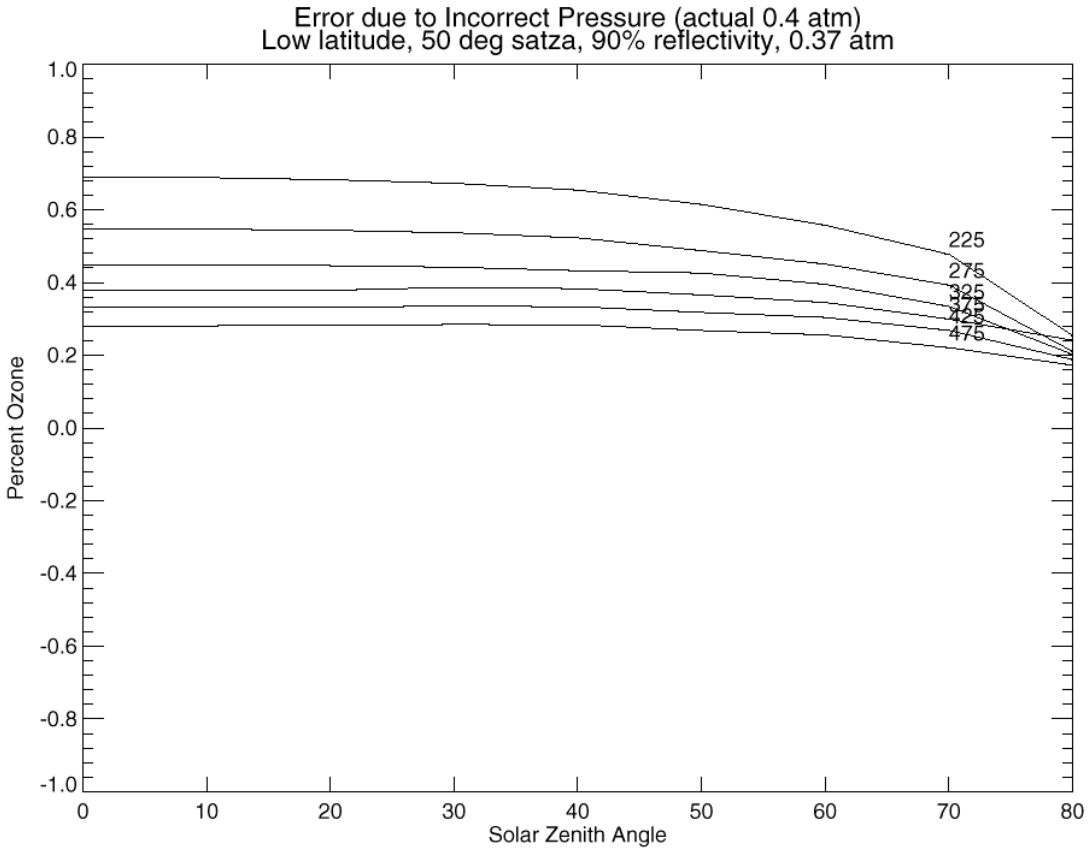

Figure 7.3-10 (a).

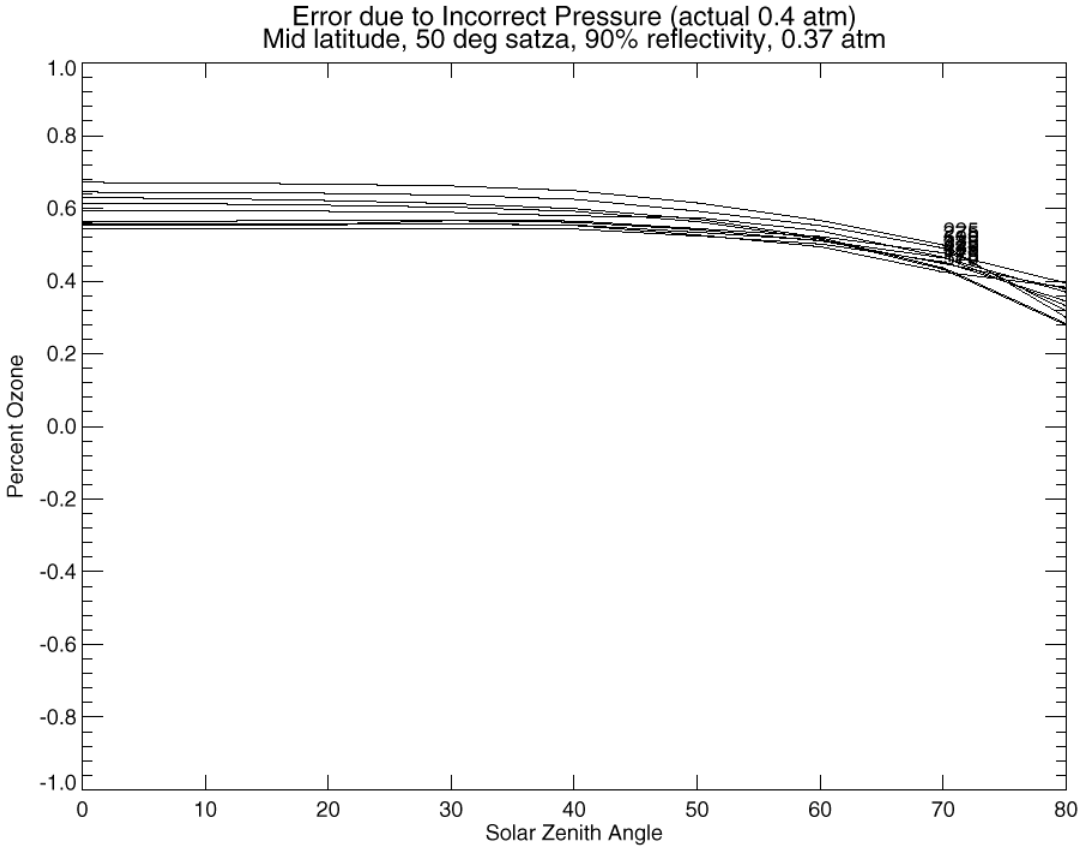

Figure 7.3-10 (b).

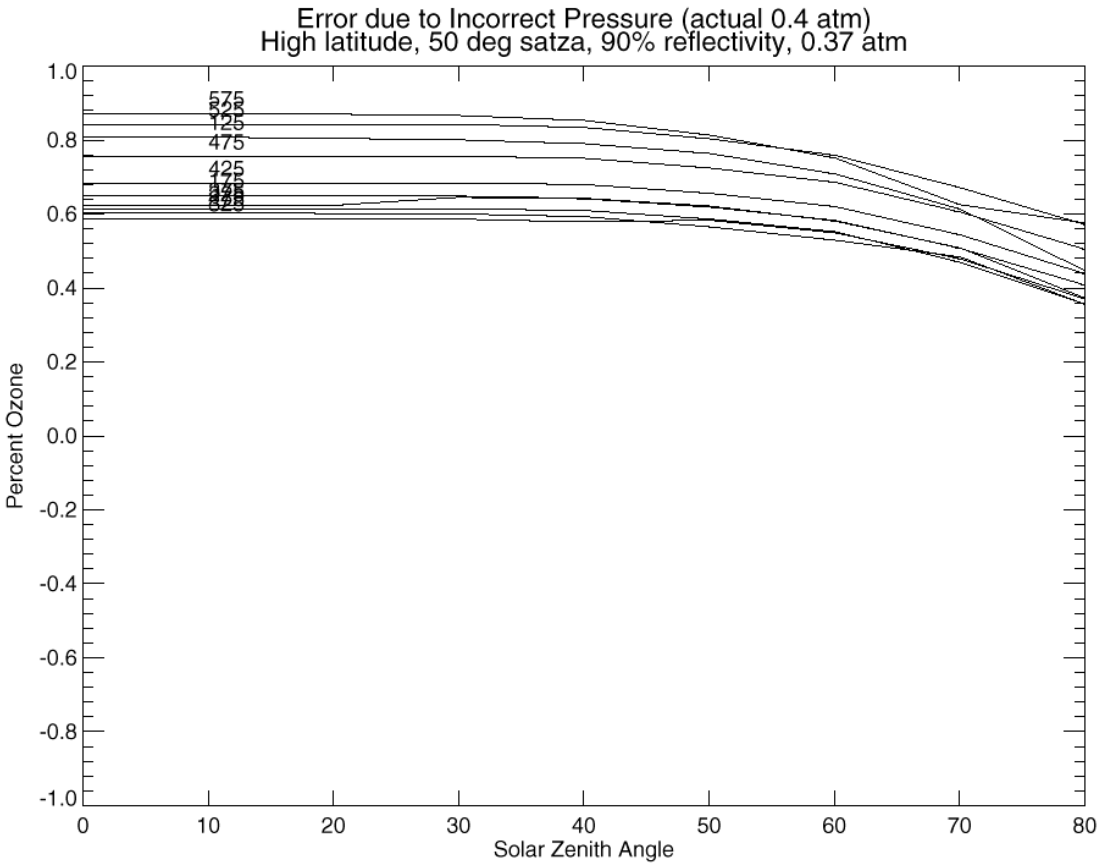

Figure 7.3-10 (c).

Figure 7.3-10. Error due to cloud top pressure error for (a) low, (b) mid, and (c) high latitude ozone.

The curves are parametric in total column ozone in Dobson Units.

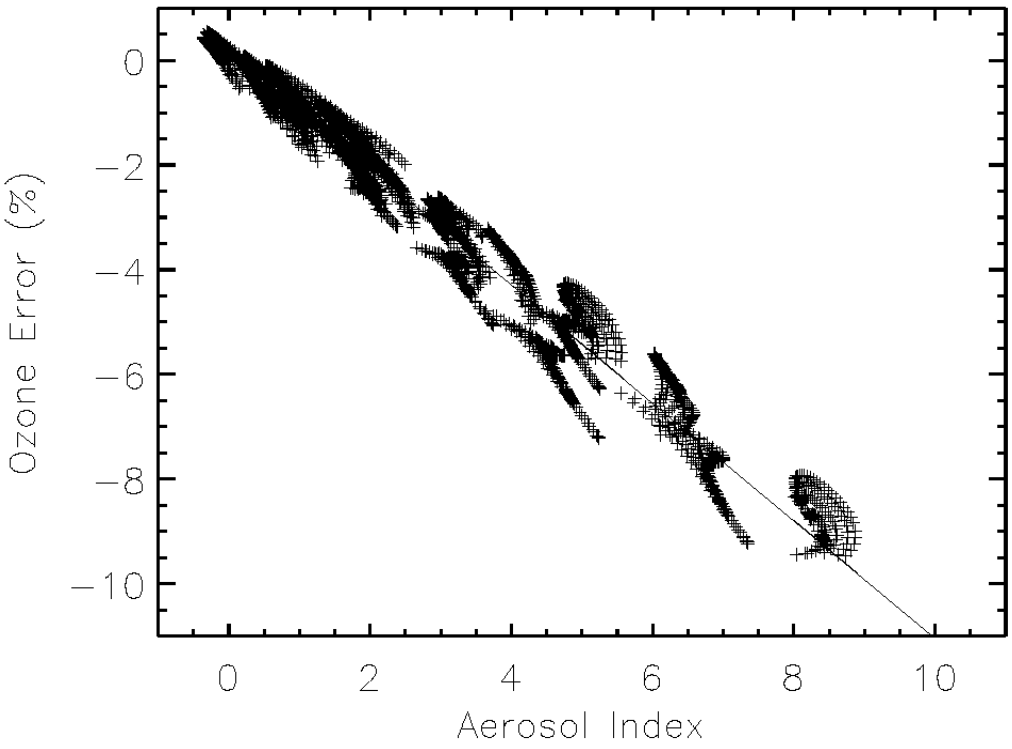

Figure 7.3-11. Systematic Ozone Error

Systematic Ozone Error shown as a function of aerosol index and the linear ozone correction developed by Torres et al. (1998). [after Torres et al., 1998]

7.3.3 Global Distribution of Total Column Precision Errors

For allocation purposes, we estimate the precision of a global ensemble of total column retrievals (as a function of total column) based on a distribution of solar zenith angles and of cloud fraction.

The global allocations are calculated as follows. Given two ensembles of M and N elements with standard deviations σ_M and σ_N:

$$\sigma_M^2 = \frac{1}{M-1}\sum_{i=1}^{M}(x_i - \bar{x})^2 \quad (197)$$

$$\sigma_N^2 = \frac{1}{N-1}\sum_{j=1}^{N}(x_j - \bar{x})^2 \quad (198)$$

The variance of the combined ensembles can be estimated as

$$\sigma_{M+N}^2 = \frac{1}{M+N-1}\sum_{k=1}^{M+N}(x_k - \bar{x})^2 = \frac{1}{M+N-1}\sum_{k=1}^{M}(x_k - \bar{x})^2 + \frac{1}{M+N-1}\sum_{k=M+1}^{M+N}(x_k - \bar{x})^2 \quad (199)$$

$$= \frac{1}{M+N-1}\left[(M-1)\sigma_M^2 + (N-1)\sigma_N^2\right] \cong \frac{M}{M+N}\sigma_M^2 + \frac{N}{M+N}\sigma_N^2 \quad (200)$$

This can be generalized to the combination of more than two ensembles. The individual standard deviations σ_N were derived in sections 7.3.1 and 7.3.2. How they are weighted in a global ensemble (i.e., the derivation of N/(M+N)) is derived as follows.

7.3.3.1 Global Allocations for Temperature Dependence, Cloud Fraction, and Tropospheric Aerosols

The temperature dependence and cloud fraction error are assumed to be the same under all conditions.

Based on results by Herman et al. (1997), tropospheric aerosols are assumed to cover 10% of the Earth's surface. This corresponds to peak conditions of tropospheric aerosol coverage.

7.3.3.2 Global Allocations for Sensor Noise and Profile Shape

The distribution of solar zenith angles is based on what would be observed on average along a 0930 orbit. Geographic latitudes are mapped to solar zenith angles based on this local time. The latitude divisions correspond to the profile mixing regimes of the total column algorithm. Ozone amounts are weighted by latitude. This permits an appropriate distribution of ozone column amounts (i.e., 50 and 650 DU total columns are not observed at low latitudes), shown in **Table 7.3-2**.

Table 7.3-2. Distribution of total column ozone amount

	L (lat < 15)	L/M (15 < lat < 45)	M/H (45 < lat < 75)	H (75 < lat)

	SZA < 60		60 < SZA	
125 - 175	0	0	0.75	0.25
225 - 475	0.1875	0.375	0.375	0.0625
525 - 575	0	0	0.75	0.25

This distribution is used to allocate errors based on solar zenith angle (sensor noise and ozone profile). The three columns on the left of **Table 7.3-3** are the allocations derived in sections 7.3.1 and 7.3.2, and the three columns on the right are the global allocations.

Table 7.3-3. Solar zenith angle distributions

	SZA < 60	60 < SZA < 70	70 < SZA < 80	125 – 175	225 - 475	525 - 575
Solar Radiance SNR	0.20%	0.25%	0.33%	0.29%	0.24%	0.29%
Solar Calibration	0.20%	0.25%	0.33%	0.29%	0.24%	0.29%
Ozone profile	0.10%	0.10%	0.50%	0.36%	0.25%	0.36%

7.3.3.3 Global Allocations for Cloud Top / Surface Pressure and Tropospheric Ozone

Based on all Nimbus 7 TOMS data from 1990 data, the distribution of cloud fraction amounts is shown in **Table 7.3-4.**

Table 7.3-4. Cloud fraction distribution

Cloud Fraction	Percent of Measurements
clfrac = 0.0	13
0.0 < clfrac <= 0.2	40
0.2 < clfrac <= 0.4	18
0.4 < clfrac <= 0.6	12
0.6 < clfrac <= 0.8	9
0.8 < clfrac < 1.0	5
clfrac = 1.0	3

Similar results were derived from 1988 data.

The global cloud top / surface pressure allocation shown in **Table 7.3-5** is calculated based on this distribution of cloud fraction and the errors derived in section 7.3.2 by simulation.

Table 7.3-5. Cloud fraction distribution

	Cloud Fraction							
	0	0.0 < f <= 0.2	0.2 < f <= 0.4	0.4 < f <= 0.6	0.6 < f <= 0.8	0.8 < f < 1.0	f = 1.0	
CF	**0**	**0.1**	**0.3**	**0.5**	**0.7**	**0.9**	**1**	**All**
prob.	0.13	0.4	0.18	0.12	0.09	0.05	0.03	**1**
125 - 175	0.05%	0.23%	0.38%	0.49%	0.58%	0.66%	0.70%	**0.38%**
225 - 475	0.05%	0.21%	0.35%	0.45%	0.54%	0.61%	0.64%	**0.35%**
525 - 575	0.05%	0.23%	0.38%	0.49%	0.58%	0.66%	0.70%	**0.38%**

Because the efficiency of the buv technique in detecting tropospheric ozone goes to zero when the ozone is under clouds, the tropospheric ozone allocations are weighted in the same way as the cloud top / surface pressure. The basic allocations in the second and third column of **Table 7.3-6** are derived as described in section 7.3.2.

Table 7.3-6. Distribution of errors in tropospheric ozone

	Trop oz error		Cloud Fraction						
Total Oz	**Clear**	**Cloudy**	**0**	**0.0 < f <= 0.2**	**0.2 < f <= 0.4**	**0.4 < f <= 0.6**	**0.6 < f <= 0.8**	**0.8 < f < 1.0**	**f = 1.0**	**All**
125	0.87	1.59	0.87	1.59	1.14	1.28	1.41	1.53	1.59	**1.38**
175	1.14	1.96	1.14	1.96	1.44	1.60	1.75	1.89	1.96	**1.72**
225	0.91	2.61	0.91	2.61	1.62	1.95	2.24	2.49	2.61	**2.17**
275	1.10	2.89	1.10	2.89	1.83	2.19	2.49	2.76	2.89	**2.42**
325	1.28	2.27	1.28	2.27	1.64	1.84	2.02	2.19	2.27	**1.98**
375	1.32	2.19	1.32	2.19	1.63	1.81	1.97	2.12	2.19	**1.93**
425	1.48	2.30	1.48	2.30	1.77	1.93	2.09	2.23	2.30	**2.05**

475	1.31	2.11	1.31	2.12	1.59	1.76	1.91	2.04	2.11	**1.88**
525	1.47	2.28	1.47	2.28	1.75	1.92	2.07	2.21	2.28	**2.04**
575	2.02	2.92	2.02	2.92	2.33	2.51	2.68	2.84	2.92	**2.64**

Based on these weightings, the global sensor and algorithm allocations, in Dobson Units, are shown in **Table 7.3-7**

Table 7.3-7. Global sensor and algorithm precision error allocations

Error	75	125	175	225	275	325	375	425	475	525	575	625
Radiance SNR	0.14	0.24	0.33	0.38	0.46	0.55	0.63	0.71	0.80	0.99	1.08	1.18
Solar Calibration	0.14	0.24	0.33	0.38	0.46	0.55	0.63	0.71	0.80	0.99	1.08	1.18
Intra-orbital shift	0.41	0.68	0.70	0.70	0.77	0.68	1.13	1.06	1.19	1.05	1.15	1.25
Temp Dependence	0.50	0.50	0.50	0.50	0.50	0.50	0.50	0.50	0.50	0.50	0.50	0.50
Cloud Top / Surface Pres	0.18	0.30	0.26	0.22	0.34	0.47	0.46	0.45	0.46	0.51	0.55	0.59
Cloud Fraction	0.23	0.38	0.53	0.68	0.83	0.98	1.13	1.28	1.43	1.58	1.73	1.88
Ozone Profile	0.11	0.18	0.27	0.28	0.21	0.34	0.56	0.70	0.96	1.28	1.63	1.77
Aerosol Correction	0.38	0.63	0.88	1.13	1.38	1.63	1.88	2.13	2.38	2.63	2.88	3.13
Tropospheric Ozone	1.38	1.38	1.72	2.17	2.42	1.98	1.93	2.05	1.88	2.04	2.64	2.64
Total Precision	**1.61**	**1.84**	**2.26**	**2.76**	**3.14**	**3.03**	**3.37**	**3.67**	**3.91**	**4.33**	**5.01**	**5.32**
OMPS Requirement	**2.88**	**3.13**	**3.38**	**3.63**	**4.13**	**4.38**	**4.63**	**4.88**	**5.38**	**5.63**	**5.88**	**6.13**

These allocations correspond to the curve “Allocation, Sensor and Algorithms” in Figure 7.3-1.

7.4 MAPPING UNCERTAINTY

The mapping uncertainty of the nadir total column ozone is derived from sensor and spacecraft specifications and from the geometry of the observation. The allocation of uncertainties is summarized in **Figure 7.4-1**.

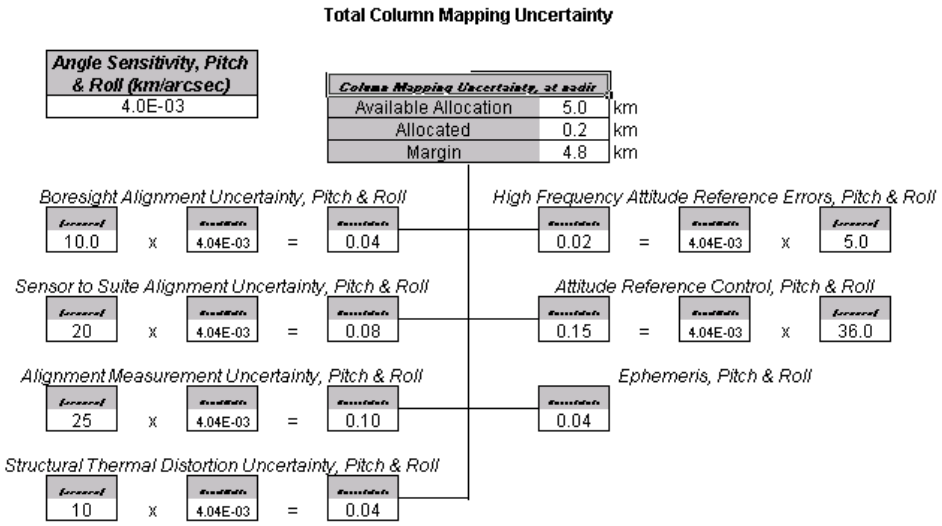

Figure 7.4-1. Error tree addressing the mapping uncertainty of the nadir total column measurements

7.5 VERIFICATION AND VALIDATION

A set of test have been performed to verify and validate that the performance of the algorithm meets or exceed the allocations presented in this section and that the total accuracy and precision errors meet or exceed the total allocations presented here. The results of those test are presented in a companion document titled “Algorithm Test Results: 1. Total Column Ozone.”

8 References

Ahmad, Z., and P. K. Bhartia, Effect of molecular anisotropy on backscattered ultraviolet radiance, Appl. Opt., 34, 8309-8314, 1995.

Bass, A.M., and R. J. Paur, The ultraviolet cross-sections of ozone: II. The measurements, in Proceedings of the Quadrennial Ozone Symposium, ed. C.S. Zerefos and A. Ghazi, D. Reidel Publishing, 661-671, 1984.

Dave, J.V., Meaning of successive iteration of the auxiliary equation in the theory of radiative transfer, Astrophys. J., 140, 1292-1303, 1964.

Dave, J. V., Effect of aerosols on the estimation of total ozone in an atmospheric column from the measurement of its ultraviolet radiance, J. Atmos. Sci., 35, 899-911,1978.

ECS Project, 1995. Theoretical Basis of the SDP Toolkit Geolocation Package for the ECS Project, Technical Paper, 445-TP-002-002.

Fleig, A.J., et al., Nimbus 7 Solar Backscatter Ultraviolet (SBUV) Ozone Products User's Guide, NASA Reference Publication 1234, 1990.

Gurevich, G.S. and A.J. Krueger, Optimization of TOMS wavelength channels for ozone and sulfur dioxide retrievals, Geophys. Res. Lett., 24, 2187-2190, 1997.

Hall, D. F., Flight measurement of molecular contaminant deposition, Proc. SPIE, 2261, 58-71, 1994.

Herman, J.R., P.K. Bhartia, O. Torres, N.C. Hsu, C.J. Seftor, and E. Celarier, Global distribution of absorbing aerosols from Nimbus-7/TOMS data, J. Geophys. Res., 102, 16911, 1997.

Herman, J.R. and E.A. Celarier, Earth surface reflectivity climatology at 340-380 nm from TOMS data, J. Geophys. Res., 102, 28003, 1997.

Hilsenrath, E., H. Herzig, D. E. Williams, C. J. Brugge, and A. E. Stiegman, Effects of Space Shuttle flight on the reflectance characteristics of diffusers in the near-infrared, visible, and ultraviolet regions, Opt. Eng., 33, 3675-3682, 1994.

Jaross, G., et al., Calibration and postlaunch performance of the Meteor 3/TOMS instrument, J. Geophys. Res., 100, 2985—2995, 1995.

Jaross, G., A. J. Krueger, and C. G. Wellemeyer, Sensitivity of Total Ozone Mapping Spectrometer products to diffuse reflectance measurements, Metrologia, 35, 663-668, 1998a.

Jaross, G., R. Cebula, M. DeLand, R. McPeters, E. Hilsenrath, and A. Krueger, Backscatter ultraviolet instrument solar diffuser degradation, Proc. SPIE, 3427, 432-444, 1998b.

Joiner, J., P. K. Bhartia, R. P. Cebula, E. Hilsenrath, and R. D. McPeters, Rotational-Raman Scattering (Ring Effect) in Satellite Backscatter Ultraviolet Measurements, Appl. Opt., 34, 4513-4525, 1995.

Klenk, K.F. , P.K. Bhartia, A.J. Fleig, V.G. Kaveeshwar, R.D. McPeters, and P.M. Smith, Total ozone determination from the backscattered ultraviolet (BUV) experiment, J. Appl. Meteorol. 21, 1672-1684, 1982.

McPeters, R.D., et al., Earth Probe Total Ozone Mapping Spectrometer (TOMS) Data Product User's Guide, NASA/TP-1998-206895, November 1998.

McPeters, R.D., P.K. Bhartia, A.J. Krueger, J.R. Herman, B.M. Schlesinger, C.G. Wellemeyer, C.J. Seftor, G. Jaross, S.L. Taylor, T. Swissler, O. Torres, G. Labow, W. Byerly, and R. P. Cebula, Nimbus-7 TOMS Ozone Mapping Spectrometer (TOMS) Data Products User's Guide, NASA Reference Publication 1384, April 1996.

NIMA, 1997. NIMA TR8350.2: Department of Defense World Geodetic System 1984, Its definition and Relationship with Local Geodetic Systems, Third Edition, prepared by the NIMA WGS84 Development Committee.

Seftor, C.J., G. Jaross, J.R. Herman, X. Gu, L. Moy, S.L. Taylor, and C.G. Wellemeyer, The Meteor 3/total ozone mapping spectrometer version 7 data set: Calibration and analysis, J. Geophys. Res., 102, 19247-19256, 1997.

Torres, O., P.K. Bhartia, J.R. Herman, Z. Ahmad, and J. Gleason, Derivation of aerosol properties from satellite measurements of backscattered ultraviolet radiation: Theoretical Basis, J. Geophys. Res., 103, 17099, 1998.

Wellemeyer, C.G., S.L. Taylor, G. Jaross, M.T. Deland, C.J. Seftor, G. Labow, T.J. Swissler, and R.P. Cebula, Final report on Nimbus-7 TOMS Version 7 calibration, NASA Contractor Report 4717, March 1996.

Wellemeyer, C. G., S. L. Taylor, C. J. Seftor, R. D. McPeters, and P. K. Bhartia, A correction for total ozone mapping spectrometer profile shape errors at high latitude, J. Geophys. Res., 102, 9020, 1997.

Weiser, M., The global digital terrain model TUG87, Internal Report on Set-up, Origin and Characteristics, Institute of Mathematical Geodesy, Technical University of Graz, Austria, 1987.

Wertz, J.R. (ed.) 1985, Spacecraft Attitude Determination and Control, D. Reidel Publishing Co., Vol. 73.

Woods, T.N., et al., Validation of the UARS Solar Ultraviolet Irradiances: Comparison with the ATLAS 1 and 2 Measurements, J. Geophys. Res., 101, 9541-9569, 1996.

Ziemke, J. R., S. Chandra, and P. K. Bhartia, Two new methods for deriving tropospheric column ozone from TOMS measurements: Assimilated UARS MLS/HALOE and convective-cloud differential techniques, J. Geophys. Res., 103, 22,115-22,127, 1998.